Mechanism of Phase Transition in Vanadium Oxides and Its Applications

By
Raktima Basu

Enrolment No: PHYS 02 2015 04 013

Indira Gandhi Centre for Atomic Research, Kalpakkam

A thesis submitted to the

Board of Studies in Physical Sciences
In partial fulfillment of requirements
for the Degree of

DOCTOR OF PHILOSOPHY

of

HOMI BHABHA NATIONAL INSTITUTE

November, 2019

Homi Bhabha National Institute

Recommendations of the Viva Voce Committee

As members of the Viva Voce Committee, we certify that we have read the dissertation prepared by **Raktima Basu** entitled **"Mechanism of Phase Transition in Vanadium Oxides and Its Applications"** and recommend that it may be accepted as fulfilling the thesis requirement for the award of Degree of Doctor of Philosophy.
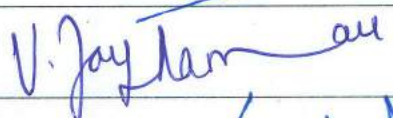
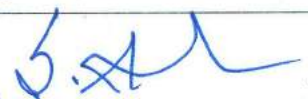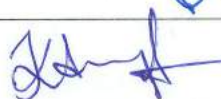|	
Chairman - Dr. M. Kamruddin	
Guide - Dr. Sandip Kumar Dhara	
Examiner - Dr. Ajay Kumar Sood	
Member 1- Dr. V. Jayaraman	
Member 2- Dr. S. Amirthapandian	
Member 3- Dr. Arun K Prasad	

Final approval and acceptance of this thesis is contingent upon the candidate's submission of the final copies of the thesis to HBNI.

I hereby certify that I have read this thesis prepared under my direction and recommend that it may be accepted as fulfilling the thesis requirement.

Date: January 24, 2020

Place: Kalpakkam

Dr. Sandip Kumar Dhara

(Guide)

STATEMENT BY AUTHOR

This dissertation has been submitted in partial fulfillment of requirements for an advanced degree at Homi Bhabha National Institute (HBNI) and is deposited in the Library to be made available to borrowers under rules of the HBNI.

Brief quotations from this dissertation are allowable without special permission, provided that accurate acknowledgement of source is made. Requests for permission for extended quotation from or reproduction of this manuscript in whole or in part may be granted by the Competent Authority of HBNI when in his or her judgment the proposed use of the material is in the interests of scholarship. In all other instances, however, permission must be obtained from the author.

Raktima Basu

DECLARATION

I, hereby declare that the investigation presented in the thesis has been carried out by me. The work is original and has not been submitted earlier as a whole or in part for a degree / diploma at this or any other Institution / University.

Raktima Basu

List of Publications arising from the thesis

Journals

1. Polarized tip-enhanced Raman spectroscopy in understanding metal to insulator and structural phase transition in VO_2, **R. Basu**, A. Patsha, S. Chandra, S. Amirthapandian, K. G. Raghavendra, A. Dasgupta, S. Dhara, *J. Phys. Chem. C* **2019**, *123*, 11189.

2. Phase-pure VO_2 nanoporous structure for binder-free supercapacitor performances, **R. Basu**, S. Ghosh, S. Bera, A. Das, S. Dhara**,** *Sci. Rep.* **2019**, *9*, 4621.

3. Spectroscopic study of native defects in the semiconductor to metal phase transition in V_2O_5 nanostructure, **R. Basu**, and S. Dhara, *J. Appl. Phys.* **2018**, *123*, 161550.

4. VO_2 microcrystals as advanced smart window material at semiconductor to metal transition, **R. Basu**, P. Magudapathy, M. Sardar, R. Pandian, S. Dhara, *J. Phys. D: Appl. Phys.* **2017**, *50*, 465602.

5. Role of 1-D finite size Heisenberg chain in increasing metal to insulator transition temperature in hole rich VO_2, **R. Basu**, M. Sardar, S. Bera, P. Magudapathy, S. Dhara, *Nanoscale* **2017**, *9*, 6537.

6. Role of vanadyl oxygen in understanding metallic behavior of V_2O_5 (001) nanostructure, **R. Basu**, A. K. Prasad, S. Dhara, A. Das, *J. Phys. Chem. C* **2016**, *120*, 26539.

7. Probing phase transition in VO_2 with the novel observation of low-frequency collective spin excitation, R. Basu, V. Srihari, M. Sardar, S. Bera, S. Dhara, *Sci. Rep.* **2020** *(In Press)*.

Communicated:

1. Near room temperature CH_4 sensing and role of oxidation states for phase pure Wadsley V_nO_{2n+1} nanostructures, **R. Basu**, P. R. Reshma, A. K. Prasad, S. Dhara (*Communicated*).

2. Phase Transitions in VO_2 under extreme conditions **R. Basu**, V. Srihari, T. R. Ravindran, S. Chandra, S. Dhara (*Communicated*).

Conference Proceedings:

1. VO_2 micro-crystals as blue light filter at semiconductor to metal transition, **R. Basu**, S. Dhara, *Proc. Intl. Conf. Adv. Funct. Mater.* (ICAFM) Chennai, India (2017) 241-243.

2. Origin of Phase Transition in VO_2, **R. Basu**, M. Sardar, S. Dhara, *AIP Conf. Proc.* **2018**, *1942*, 030003.

3. High pressure spectroscopic studies of phase transition in VO_2, **R. Basu**, K. K. Mishra, T. R. Ravindran, S. Dhara, *AIP Conf. Proc.* **2018**, *1951*, 030012.

Conference Presentations:

1. Study of phase transition in VO_2 using Tip-Enhanced Raman Spectroscopy, **R. Basu**, A. Patsha, S. Chandra, S. Dhara, National conference on Light Matter Interaction at Nanoscale (LMIN-2019, July 15-17) IGCAR, Kalpakkam (*Best oral presentation award*).

2. Polarized Raman studies on VO_2 micro-crystals, **R. Basu**, S. Amirthapandian, S. Dhara, Research Scholars Meet HBNI-On Materials Science and Engineering of Nuclear Materials (RSM-MSENM-2018, May 7-9) Tamil Nadu, India (*Best research contribution award*).

3. Polarized TERS Studies on VO_2 Single Nanorod in the Sub-Diffraction Limit, **R. Basu**, A. Patsha, and S. Dhara, International Conference on Nano Science and Technology (ICONSAT-2018; March 21-23) Bengaluru, India.

4. Pressure Dependent Structural Phase Transition in VO_2, **R. Basu**, V. Srihari, S. Dhara, American Physical Society (APS) March Meeting 2018 (March 5-9, 2018) Los Angeles, USA (*Contributory Talk*).

5. Origin of Phase Transition in VO_2**, R. Basu**, M. Sardar, S. Dhara, 62nd DAE Solid State Physics Symposium (DAE SSPS-2017; December 26-30) Mumbai, India (*Contributory Talk*).

6. High pressure spectroscopic studies of phase transition in VO_2, **R. Basu**, K. K. Mishra, T. R. Ravindran, S. Dhara, 9th National Conference on Thermo-physical Properties (9th NCTP-2017; *Nov 6-8*) Tamil Nadu, India (*Best Poster Award*).

7. VO_2 micro-crystals as blue light filter at semiconductor to metal transition, **R. Basu**, S. Dhara, *Intl. Conf. on Advances in Functional Materials* (ICAFM-2017; *Jan 6-8*) Chennai, India (*Contributory Talk*).

8. Raman Spectroscopic analysis of V_2O_5 nanostructures deposited by vapour transport process, **R. Basu**, A. K. Prasad, S. Dhara, *Emerging Trends in Adv. Func. Mater.* (ETAFM-2016, *January 18-21*), Buhbaneswar, India.

Other Journal Publications (Not Included in the Thesis):

1. Unique identification of phonon modes using polarized Raman studies of SnO (001) crystals, **R. Basu**, D Sornadurai, S Amirthapandian, S. Dhara, *Bull. Mater. Sci.* 42 (2019) 83.

2. Modulation of thermal conductivity and thermoelectric figure of merit by anharmonic lattice vibration in Sb_2Te_3 thermoelectrics, D. Das, K. Malik, S. Das, P. Singha, A. K. Deb, V. A. Kulbachinskii, **R. Basu**, S. Dhara, A. Dasgupta, S. Bandyopadhyay, A. Banerjee, *AIP Advances* 8 (2018) 125119.

3. Local inversion symmetry breaking and spin-phonon coupling in perovskite $GdCrO_3$, S. Mahana, B. Rakshit, **R. Basu**, S. Dhara, B. Joseph, U Manju, S. D Mahanti, D. Topwal, *Phys. Rev. B* 96 (2017) 104106.

4. Evolution of phonon anharmonicity in Se-doped Sb_2Te_3 thermoelectrics, D. Das, S. Das, P. Singha, K. Malik, A. K. Deb, A. Bhattacharyya, V. A. Kulbachinskii, **R. Basu**, S. Dhara, S. Bandyopadhyay, A. Banerjee, *Phys. Rev. B* 96 (2017) 064116.

5. Site-substitution in $GdMnO_3$:effects on structural, electronic and magnetic properties S. Mahana, B. Rakshit, P. Nandi, **R. Basu**, S. Dhara, U. Manju, S. D. Mahanti, D. Topwal, *arXiv preprint arXiv:1908.02307*, 2019.

6. Role of polarized tip-enhanced Raman spectroscopy in the enhancement of interface optical phonon modes in AlGaN multi-quantum wells, A.K. Sivadasan, P. Dhara, **R. Basu**, S. Parida, C. Singha, A. Bhattacharyya, K. K. Madapu, S. Dhara, *J. Mat. NanoSci.* 7 (2020) 19.

7. Understanding structural changes to Y_2O_3 dispersoids and effect of Ti during mechanical milling and high-temperature annealing in $Fe-Y_2O_3-Ti$ model ODS alloy, P. K. Parida, A. Dasgupta, V. Srihari, C. Ghosh, **R. Basu**, R. Mythili, S. Dhara, *Adv. Powder Technol.* (Under review).

Raktima Basu

Raktima Basu

Dedicated to

My beloved Parents and Family

&

The Future Generation of Women in Science

Acknowledgments

First of all, I would like to express my sincere gratitude to my research supervisor Prof. Sandip Dhara for his continuous support, motivation and encouragement in my PhD work. Besides my advisor, my sincere thanks to the doctoral committee chairman Dr. M. Kamruddin, and members Dr. V. Jayaraman, Dr. S. Amrithapandian and Dr. A. K. Prasad for providing me helpful feedback and evaluating my work at each stage. I convey my gratitude to Dr. R. Rajaraman, Dean, Physical Sciences, Dr. G. Amarendra, Director, MSG and Dr. A. K. Bhaduri, Director, IGCAR for providing me the opportunity to continue the research work. I would like to thank Dept. of Atomic Energy, Govt. of India for financial assistance.

I convey my deep gratitude to my research collaborators Dr. Manas Sardar, Dr. T. R. Ravindran, Dr. V. Srihari, Dr. Arindam Das, Dr. Santanu Bera, Dr. R. Pandian, Dr. Sharat Chandra, Dr. Sachin K Srivastava, Mr. P. Magudapathy, Dr. Subrata Ghosh, Dr. Arup Dasgupta and Dr. K. G. Raghavendra for their help in many stages of the research.

I want to thank the reviewers of my thesis and manuscripts for their valuable comments and suggestions which helped in the improvement of the research articles. I deeply express my heart full thanks to my seniors Dr. Avinash Patsha, Dr. A. K. Sivadasan, Dr. Kishore K. Mudupu, Dr. Santanu Parida who had immensely helped in learning various stages of Ph.D. career. I would also like to thank my colleagues Mr. Binaya Kumar Sahu, Mr. Gopinath Sahoo, Ms. Reshma P. R., and Mr. C. Abinash Bhuyan for their help at the laboratory and sharing our scientific adventures.

Above all, I will never have the words of appreciation for my Parents and family members as well as my teachers and friends for their constant encouragements and supports.

CONTENTS

SUMMARY

The Thesis principally described the phase transition in vanadium oxides nano and micro-structures (VO_2 and V_2O_5), the mechanism behind the phase transitions and finally the applications of the materials in the light of phase transformation. The correlation between the metal to insulator (MIT) and structural phase transitions (SPT) is studied in detail to resolve the long-lasting debate on the physical origin behind the phase transition.

After brief introduction of both the oxides, the conflicts on the phase transition mechanism, change in the structure and properties around the transition are discussed. There exists a controversy to use the term 'MIT' in case of V_2O_5, as the mechanism behind the metallic behavior is under conflict. The role of vanadyl O_I oxide in initiating the MIT of V_2O_5 nanostructures and the post-transition structural relaxation of the sample are deliberated. The breakdown of $pd\pi$ bonds due to reduction of vanadyl O_I helps in accumulating electrons towards neighbouring V atom to occupy the partially filled V *3d* bands [16], leading to the increase in the number of carriers in the conduction band, which is finally made responsible for the observed metallic behavior in V_2O_5.

On the other hand, the association of a structural phase transition (SPT) with the MIT in VO_2 (at 340K) has led to a '*chicken-and-egg*' debate on the driving mechanism of the phase transition. The structural change from a low-temperature monoclinic, M1 to a high-temperature rutile tetragonal, R is also assisted via another two metastable phases of monoclinic, M2 and triclinic, T. The stabilization of stable and metastable phases of VO_2 is made possible in a novel technique by introducing defects in the system, for the first time, via two ways: (i) hole doping by native vacancy creation and (ii) Mg doping with optimal proportions. The structural transitions M2 →T and T→M1 is found to be second order

continuous phase transitions from the continuous change in the volume and a discontinuity in the bulk modulus with hydrostatic pressure. However, the temperature-driven M2→R phase transition is found out as first order from the coexistence of both the phases for a narrow span of temperature. The assignment of phonon frequencies corresponding to each lattice vibration is made possible by density functional theory calculations of phonon density of states. The phonon mode responsible for the structural phase transition is also identified using the polarized and high-temperature tip-enhanced Raman spectroscopy (TERS) measurements. The origin of the MIT and SPT in VO_2 and the correlation between them is analyzed by both phenomenological model and experimental evidence along with spinon mode-frequency calculation. The effect of defects in changing the transition temperature of VO_2 is discussed by invoking dimensional reduction in V chains. The role of vanadium vacancy in increasing the transition temperature is argued by introducing finite-size 1-D Heisenberg spin ½ chain model in the hole rich system. The correlation between MIT and SPT is analyzed by the observation of collective spin-excitation in VO_2. The shift in the frequency of collective spin excitation mode and simultaneous increase in the transition temperature in the absence of any structural change confirms that SPT does not prompt MIT in VO_2. The MIT is found out as a correlation driven Mott-transition which prompts a simultaneous SPT with reduction of temperature.

The applications of VO_2 are also explained in light of its phase transition. Along with MIT, significant changes also take place in the optical and structural properties of VO_2. The three imperative applications of VO_2 are investigated (i) Binder free supercapacitor, (ii) Advanced smart window, and (iii) Methane sensing near room temperature.

LIST OF FIGURES

LIST OF TABLES

CHAPTER 1

INTRODUCTION

"Words do not create transition. Ideas do."

— Peter Jacobi

1.1 Phase Transition in Vanadium Oxides:

Vanadium (V) was discovered by del Rio in 1801 and was rediscovered by Sefstrom in 1831. Sefstrom named the element after the Scandinavian goddess Vanadis, due to its attractive multicoloured compounds [1]. V is a transition metal ($[Ar]3d^34s^2$) having valences ranging between +2 to +5 with colourful principal oxides in the form of VO (lavender), V_2O_3 (Green), VO_2 (Blue), and V_2O_5 (Yellow), respectively [2]. However, the V-O phase diagram includes mixed-valence oxides containing two oxidation states, such as V_4O_9, V_6O_{13}, V_8O_{15}, V_7O_{13}, V_6O_{11}, and others allowing easy conversion between oxides of different stoichiometry [3]. The oxides of vanadium are categorized into two groups, (i) Magneli phases (V_nO_{2n-1}) and (ii) Wadsley phases ($V_{2n}O_{5n-2}$ or, V_nO_{2n+1}) [4]. Most of the oxides of V undergo a metal to insulator transition (MIT) as a function of temperature along with changes in their optical, electrical, thermal, and magnetic properties. The transition temperatures for various vanadium oxides are listed in table 1.1 [3,5].

Table 1.1 Vanadium oxides with corresponding MIT temperatures

Vanadium oxides	Transition temperature	Vanadium oxides	Transition temperature
V_2O_3	168±2K	V_6O_{11}	170K
VO_2	340K	V_8O_{15}	70K
V_3O_5	430K	V_9O_{17}	70K
V_4O_7	250K	V_6O_{13}	150K
V_5O_9	130K	V_2O_5	530K

The V-O system not only gains wide applications due to the MIT but also grabs attention for the mechanism behind the phase-transition. The phase transitions in vanadium oxides have been inspected for a long time as the physical mechanisms behind the phase transitions vary widely [3]. In the present thesis, we have explored the phase transition behavior of the end member of each class, VO_2 ($VO_{2-1/n}$; n=∞), and V_2O_5 ($V_2O_{5-2/n}$; n=∞).

1.2   Phase Transition in V_2O_5:

1.2.1   Structural properties of V_2O_5

V_2O_5 stabilizes in various phases including α-V_2O_5, β-V_2O_5, δ-V_2O_5, γ′-V_2O_5, ζ-V_2O_5, and ε′-V_2O_5 [6]. The most well-known phase is α-V_2O_5, which crystallizes into an orthorhombic structure composed of weakly Van der Walls bonded layers of VO_5 pyramids sharing their vertices and corners [7,8]. The unit-cell parameters are $a = 11.51$ Å, $b = 3.56$ Å, and $c = 4.37$ Å [7]. It has space group Pmmn, (D_{2h}^{13}) with distorted square-pyramidal coordination symmetry around each vanadium (Fig. 1.1). There are three non-equivalent oxygen atoms in each unit cell (denoted as O_I, O_{II}, and O_{III}).
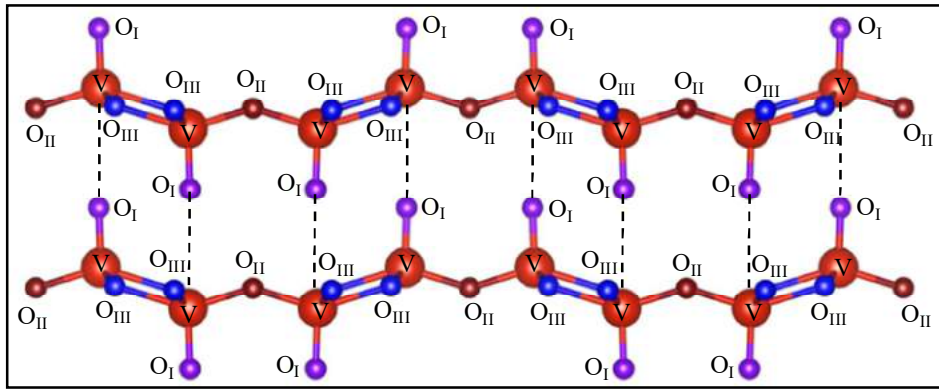
Figure 1.1 Schematic diagram of the V_2O_5 layered structure. Red ball denotes V atoms; purple, wine, and blue balls represent O_I, O_{II} and O_{III} atoms, respectively.

2

O_I is the terminal (vanadyl) oxygen with two different bond lengths. One of them is a strong and short V-O_I bond with a length of 1.577 Å (d_1). Another one is large and weak Van der Waals type, which connects the two adjacent layers in the V_2O_5 structure, with a bond length of 2.793 Å (showed by dotted lines in fig. 1.1). Both of these vanadyl oxygen atoms orient almost along the c-axis. The two-fold coordinated bridging oxygen (O_{II}) connects two adjacent V atoms with V-O_{II} bond length of 1.78 Å (d_2). The ladder-shaped O_{III} atoms are the three-fold coordinated oxygen with three different V-O_{III} bond lengths of 1.88 (d_3), 1.88 (d_3), and 2.02 Å (d_4) [7].

1.2.2 Electronic properties of V_2O_5

V_2O_5 is reported as a semiconductor of a large energy gap (3.3 eV) with the Fermi energy lying between O $2p$ and V $3d$ bands. Within this gap, however, there exist two localized split-off bands about 0.6 eV below the main V $3d$ band due to the layer-structure of this material [9]. The schematic diagram of the electronic band structure of V_2O_5 is shown in figure 1.2.
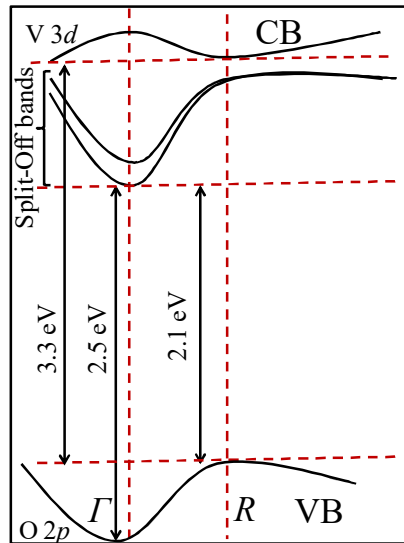
Figure 1.2 Schematic electronic band structure of V_2O_5 indicating possible transitions.

3

The indirect bandgap value of 2.1 eV due to transition from R to Γ point and direct bandgap ~2.5 eV at Γ point are reported in the first Brillouin zone corresponding to the energy between the top of the O $2p$ valence band and the split-off part of the V $3d$ band [10,11]. The absorption band-edge of the V_2O_5 crystals are reported to vary between 2.15 and 2.22 eV depending on the orientation of the sample [12]. The split-off bands with a narrow bandwidth (~ 0.7 eV) below the conduction band at Γ point are reported to originate from the overlapped O $2p$ and V $3d$ bands ($pd\pi$ bonds) [12,13]. If the split-off band is filled, the bandgap would correspond to the transition between the top of the O $2p$ band and the bottom of the main part of the V $3d$ band, since transitions between the two parts of the V $3d$ band are parity forbidden [14].

Table 1.2 Raman mode frequencies of the V_2O_5 lattice with their symmetry assignments and specific atomic vibrations

Raman frequency (cm^{-1})	Symmetry assignment	Corresponding atomic vibration
993	A_g	Displacements of O_I atoms along Z-axis
850	B_{1g}	Antiphase stretching of V-O_{II} bonds
701	either B_{1g} or B_{3g}	Anti-phase stretching of the V-O_{III} bonds along Y-axis
523	A_g	*S*tretching vibration of the V-O_{II} bonds along X-axis
483	A_g	Bending of V-O_{II}-V along Z-axis
403	A_g	Oscillation of O_I atoms along X-axis
301	A_g	Displacement of O_{II} atoms along Z-axis
283	either B_{1g} or B_{3g}	Oscillation of O_I atoms along Y-axis
195	either A_g or B_{2g}	Displacements of V-atoms along X-axis
144	either B_{1g} or B_{3g}	Displacements of the whole chain of V, O_{II}, and O_{III} in XY plane
102	A_g	Displacements of the whole chain of V-O_{II} bonds along Y-axis

1.2.3 Vibrational properties of V_2O_5

Space and point symmetric group for V_2O_5 are Pmmn (D_{2h}^{13}). Group theoretical analysis predicts twenty-one Raman active modes at Γ point, $7A_g+7B_{2g}+3B_{1g}+4B_{3g}$ [15]. The Raman mode frequencies of V_2O_5, with proper symmetry assignments [15,16] and particular atomic vibrations, are presented in table 1.2. The Raman mode at 850 cm^{-1} is reported not to be observed experimentally due to the pseudo-centrosymmetric nature of the V-O_{II}-V bond [16].

1.2.4 Phase transformation in V_2O_5

V_2O_5 undergoes a transition from insulating to metallic phase around 530±5K [17]. However, reversible surface metallicity for (001) facets around 340 to 400K and bulk metallicity for a polycrystalline film at 553K are also reported [18,19]. However, it is quite contentious to use the term 'MIT' in case of V_2O_5 [20]. The origin of metallic behavior is still not fully resolved. The metallic transition was reported because of the reduction of V_2O_5 to other lower ordered stoichiometric or non-stoichiometric oxides without any structural change [17,21]. There also exists a dispute in the identification of the particular O responsible for the reduction, as all three O_I [18,22], O_{II} [23], and O_{III} [24] are suggested to be the eligible candidates. A structural phase transition from α-V_2O_5 to metastable γ´-V_2O_5 [25], however, is also proposed with the increase in temperature to explain metallicity above the transition temperature, as the later resembles conductive Wadsley phase of V_4O_9 [26].

1.3   Phase Transition in VO_2:

1.3.1 Structural properties of VO_2

VO_2 is known to be stabilized in different polymorphs, including VO_2(A), VO_2(B), VO_2(C), VO_2(D), etc. [27]. Among the VO_2 polymorphs, VO_2(B) has been paid much attention for its well known MIT at a technologically important temperature of 340K, which is very close to

room temperature [28]. VO$_2$(B) crystallizes in rutile tetragonal (R; space group $P4_2/mnm$) and monoclinic (M1; space group $P2_1/c$) structure above and below the transition temperature, respectively [29,30]. In the high-temperature R phase, V atoms are equally spaced, forming linear chains along the c_R axis with each V atom surrounded by an oxygen octahedron (Fig. 1.3a) [31]. The lattice parameters are c_R = 2.85 Å, and $a_R = b_R$ = 4.55 Å. Whereas in the low-temperature monoclinic phase the volume of the unit cell becomes double than that of R phase with lattice parameters a_{M1} = 5.70 Å, b_{M1} = 4.55 Å, c_{M1} = 5.38 Å, and β_{M1} = 123° [32]. The approximate crystallographic relationship between M1 and R phase is $a_{M1} \leftrightarrow 2c_R$, $b_{M1} \leftrightarrow a_R$, and $c_{M1} \leftrightarrow b_R$ - c_R [33]. In the M1 phase there are significant differences in the arrangement of V along c_R axis. The V atoms form pair, and the pairs tilt along the c_R axis making the surrounding octahedron deformed (Fig. 1.3b). Besides M1, another two metastable phases of monoclinic M2 (space group $C2/m$) and triclinic T (or monoclinic M3; space group $C\overline{1}$) are also reported to evolve during the phase transition from M1 to R [34].
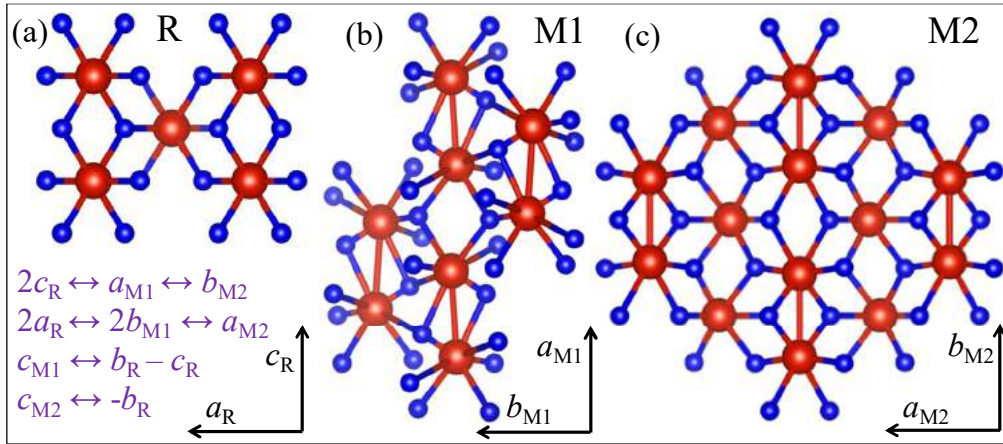
Figure 1.3 The schematic structures for (a) rutile, R (b) monoclinic, M1 and (c) monoclinic, M2 phases of VO$_2$. Red and blue balls denote V and O atoms, respectively.

In the M2 phase, the one set of V chains along the c_R axis pair without twisting, while the V ions in the nearest neighbor V chains, do not pair but twist away from c_R axis (Fig. 1.3c). The lattice parameters for M2 phase are: a_{M2} = 9.07 Å, b_{M2} = 5.797 Å, c_{M2} = 4.53 Å, and β_{M2} = 91.88° with crystallographic relationship with the R phase $b_{M2} \leftrightarrow 2c_R$, $a_{M2} \leftrightarrow 2a_R$, and $c_{M2} \leftrightarrow$ -b_R [32,34]. The triclinic T phase is intermediate between the M1 and M2 phases, in which paired V chains in the M2 phase are reported to be twisted slightly [35].

1.3.2 Electronic properties of VO$_2$

The electronic structures of VO$_2$ before and after the transition were reported long ago by Goodenough [33]. The O $2p$ orbitals stay 2.5 eV below the Fermi level [36,37], and form the valence band with π and σ bonds. In VO$_2$, there is one d electron per V atom, and the d levels of the V ions split into two states, namely, the lower-lying triply degenerate t_{2g} and higher-lying doubly degenerate e_g^σ states (schematic in Fig. 1.4).
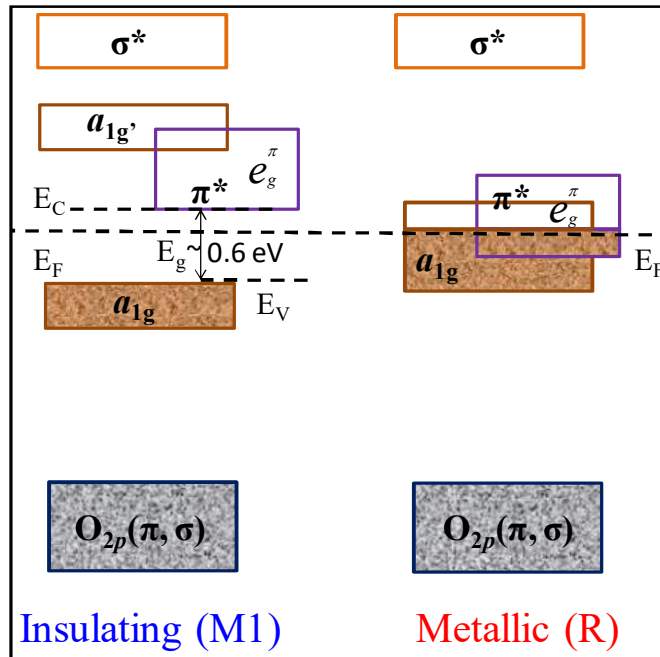
Figure 1.4 Schematic electronic band structures for the insulating and metallic phases of VO$_2$.

The t_{2g} multiplet splits again into an a_{1g} state (d_{xy}) and an e_g^π (d_{xz}, d_{yz}) doublet due to the tetragonal crystal field [33]. In the low-temperature semiconducting phase, V atoms form pairs in the c_R direction and split the a_{1g} bands into lower (bonding, a_{1g}) and upper (antibonding, $a_{1g'}$) bands. Moreover, the V-V pairs twist and thereby enhance the Vd-Op hybridization, which leads to a rise in the e_g^π band above the Fermi level. Thus, a gap of ~ 0.7 eV opens up to stabilize the insulating phase [33,35]. It is important to note that the density functional theory (DFT) with local density approximation (LDA) [35], however, fails to open the band gap between a_{1g} and e_g^π bands. On the other hand, LDA along with cluster dynamical mean field theory (C-DMFT) does manage to open up an energy gap of correct magnitude by taking account the correlation effects (Hubbard U) [38]. However, the energy gap collapses in the metallic phase, and the Fermi level crosses partially filled a_{1g} and e_g^π bands.

1.3.3   Vibrational properties of VO$_2$

Above the transition temperature (T_c), VO$_2$ stabilizes in R phase with space group $P4_2/mnm$ (D_{2h}^{13}). Whereas below the T_c, the most stable phase is M1 with space group $P2_1/c$ (C_{2h}^5) [31,32]. The other two low-temperature metastable phases have space group $C2/m$ and $\overline{C}1$ for M2 and T, respectively. Group theoretical analysis predicts five Raman active modes (A_{1g}, B_{1g}, B_{2g}, and E_g) for the high-temperature R phase and eighteen Raman modes for all three low-temperature phases of VO$_2$ (for M1: $9A_g+9B_g$, and for M2 and T: $10A_g+8B_g$) at Γ point [34,39]. Former Raman studies in the metallic phase showed four broad Raman peaks at 240, 390, 510, and 615 cm^{-1} with line-width larger than 100 cm^{-1} [40]. However, we were unable to observe any Raman mode at the metallic phase due to the screening effect. For the

M1 phase, there are several reports on the Raman studies with different symmetry assignments [40-44]. A comparison of the observed frequencies with the mode assignments is given in Table 1.3.

Table 1.3 Comparison of the assignments of the Raman modes of previous studies on low-temperature insulating M1 phase of VO_2.

Chen et al. 300K [41]		Schilbe et al. 83K [40]		Aronov et al. 100K [42]		Srivastava et al. 300K [43]		Vikhnin et al. 300K [44]	
-	-	149	A_g	149	-	-	-	144	-
-	-	199	A_g	200	A_g	208	B_{1g}	194	A_g
226	A_g	225	A_g	226	A_g	236	-	226	A_g
262	A_g	259	B_g	259	A_g	-	-	260	A_g
264	B_g	265	B_g	-	-	-	-	-	
311	B_g/A_g	313	A_g	313	A_g	-	-	311	A_g
339	A_g	339	B_g	340	A_g	-	-	337	A_g
390	A_g	392	A_g	392	A_g	-	-	389	A_g
395	B_g	395	B_g	-	-	-	-	-	
444	B_g	444	B_g	436	A_g	450	E_{1g}	438	A_g
454	B_g	453	B_g/A_g	-	-	-	-	-	
483	B_g	489	B_g	-	-	-	-	-	
500	A_g	503	A_g	501	A_g	-	-	493	A_g
591	B_g	595	A_g	594	B_g	-	-	595	A_g
618	A_g	618	A_g	620	A_g	655	A_{1g}	615	A_g
662	B_g	670	B_g	-	-	-	-	627	A_g
826	B_g	830	B_g	-	-	850	B_{2g}	-	-

Marini et al. [39] in their study of O isotope substitution in VO_2 showed that the Raman modes ~195 and 225 cm^{-1} correspond to the V-V vibration, while the mode at ~ 618 cm^{-1} is associated with V-O vibration. The Raman spectra for the T and M2 phases are of similar pattern like M1 and are reported for Cr and Al-doped VO_2 [39]. The phonon frequency ~618 cm^{-1} (V-O vibration) of the M1 phase shifts the maximum in T and M2 phases of VO_2. The mode frequency splits into two peaks at ~572 and 636 cm^{-1} in T phase and shifts to 650 cm^{-1}

in M2 phase, and thereby known as the signature mode for identifying the corresponding phase of VO_2 [34, 39].

1.3.4 Phase diagram of VO_2

The metastable M2 and T phases of VO_2 are reported to be stabilized at room temperature by doping with metals of lower valency than V^{4+}(e.g., Al^{+3}, Ga^{+3}, Cr^{+3}) [32,45,46]. The phase stabilization of the metastable phases is alternatively reported by applying tensile strain along the c_R axis [47,48]. Doping in $M_xV_{(1-x)}O_2$ is reported to decrease [49] in the T_c value for M = W^{+6}, Mo^{+6}, Ta^{+5}, $Nb^{+5,}$ and an increase is reported in the T_c value for M = Al^{+3}, Ga^{+3}, Cr^{+3} [32,45,46]. The observations point out that tensile (compressive) stain along the c_R axis is equivalent to doping with metals having valency less (more) than V^{4+}. Figure 1.5 shows (reproduced from Ref. [47] and [48]) strain or doping vs. temperature phase diagram of VO_2.
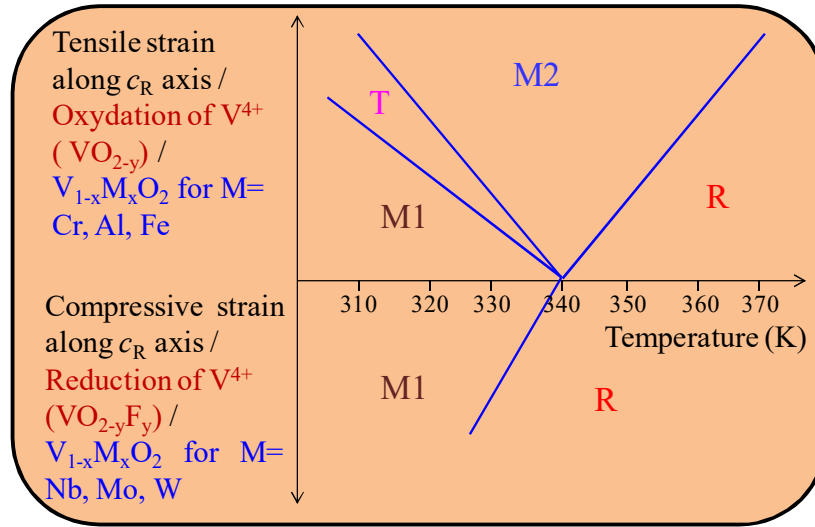
Figure 1.5 Strain or doping vs. temperature phase diagram of VO_2

1.3.5 Phase transition mechanisms in VO_2

Mott transition:

Mott transition describes the transition from insulating to metallic state of a material considering the electron-electron interaction and electron screening effect. Due to electric

field screening (the negative electrons closer to a nucleus shielding it's potential such that the potential energy peaks exponentially around the equilibrium position of the atom), the electrons become localized and can no longer conduct a current. Mott observed this phenomenon in nickel oxide in 1949 [50], and he argued that the important parameter is the electron density (n_c). If n_c is high enough and the ground state wave functions of the electrons of neighbouring atoms overlap the material undergoes a Mott transition. The critical value of n_c for undergoing a Mott transition is $n_c^{1/3} \times a_H \sim 0.2$, where a_H is the effective Bohr radius.

The Hubbard Hamiltonian is used to calculate the band structure of the correlated electronic systems. The Mott-Hubbard theorem tells the balance between two energy terms; (i) The electron hopping or tunneling (t), which is directly related to the kinetic energy of electrons, and (ii) The correlated electron-electron interaction or, the Coulomb repulsion (U). When the ratio $U/t > 4$, the electronic band splits into lower and upper Hubbard band leading to localized electronic wave functions. On the other hand, when the value of the hopping term (t) conquers the Coulomb repulsion (U), electrons become delocalized and can conduct current.

Peierls transition:

Peierls' theorem states that 'a one-dimensional equally spaced chain with one electron per ion is unstable.' This theorem was first espoused in the 1930s by Rudolf Peierls. Above the Peierls temperature (T_P), the atoms are all equally spaced with the lattice constant ***a***. Whereas below the T_P, a distortion occurs due to electron-phonon interactions in the conduction band, and the periodicity changes to 2***a***. This process is known as dimerization and happens when the metal is cooled down. However, doubling the periodicity introduces new band gaps located at multiples of ***ka***$=\pm\pi/2$. The electrons in the distorted chains move to

the lower energy than that of a perfect crystal due to the introduction of the new bandgap, which makes this lattice distortion energetically favorable. In the absence of lattice distortion, however, the one-dimensional chain is in the metallic phase with the half-filled band.

1.3.6 Phase transformation in VO_2

The MIT in VO_2 was first observed by Morin in 1959 [28]. VO_2 undergoes a first-order MIT between low-temperature M1 to high-temperature R phase at 340K [29,30], sometimes via two other metastable phases of T and M2 [48]. Around the transition, the resistivity changes by four orders of magnitude [51], and the material reflects the electromagnetic radiation in the infrared (IR) region at high-temperature metallic phase, whereas it transmits IR at low-temperature semiconducting phase [52-54]. However, the associations of SPT with the MIT have led to a '*chicken-and-egg*' debate on the driving mechanism of the phase transition, whether the residual lattice strain and dynamical electron (spin)-phonon coupling (Pierls) or strong electron-electron correlation (Mott-Hubbard) trigger the MIT [35,55]. Biermann *et al*. [38] argued that VO_2 should be considered as a renormalized Peierls insulator (band-insulator) where the opening of the bonding-antibonding gap is driven by dimerization and renormalized down by interactions. Insulating and nonmagnetic nature of the M1 phase of VO_2 suggests that it may be a typical Peierls insulator with all the V chains dimerized [45]. However, it is also found that uniaxial strain [8], or doping of trivalent metals in VO_2 [32,45,46], leads to another monoclinic phase of VO_2 (M2), where V ions in alternate chains are only dimerized. Since the M2 phase with alternative non-dimerized V chains is also insulating, dimerization alone can not drive the MIT. According to Zylbersztejn and Mott [31], Sommers and Doniach [56], and Rice *et al.* [57], Coulomb repulsion is responsible for opening the energy gap in the semiconducting phases of VO_2. A qualitative proposal of

electronic structures of VO_2 was reported long ago by Goodenough [33]. He considered an antiferroelectric-to-paraelectric transition at a higher temperature than the homopolar to metallic V-V bonding (MIT) transition. The pairing of V atoms traps the d electrons in the V-V homopolar bands at the low-temperature phase of VO_2. Whereas, tilting of V-V pairs from the c_R axis increases the electric dipole of V-V homopolar bonds. Since the net electric dipole is zero, tilting is considered to be an antiferroelectric transition. The compression of V-V pairing along the c_R axis is expected to increase the splitting between bonding and anti-bonding orbitals and thereby increases the bandgap. Berglund et al. [58] showed experimentally that with an increase in hydrostatic pressure, the energy gap of VO_2 decreases. Goodenough pointed out the observation of Berglund et al. and anticipated that V-V dimerization is not the driving force for the MIT in VO_2. It is important to note that the DFT with LDA [35] does not find any gap between a_{1g} and overlapped $a_{1g'}$, π^* bands, even including structural distortion in the calculation as imagined by Goodenough [33]. On the other hand, LDA along with DMFT [38] does manage to open up a gap, which increases with local Coulomb correlation strength. Zhensheng et al. [59] found a new monoclinic metal phase lying between the insulating monoclinic phase and the metallic rutile phase and could separate the SPT and MIT by changing substrate. Muraoka et al. [60] reported that the tensile (compressive) strain along the c_R direction increases (decreases) the T_c of VO_2. Moreover, the T_c is also reported to be tuned by altering carrier density [61], varying stoichiometry [62], or doping [63] with significant change in the optical, thermal and electrical properties of VO_2.

1.4   Application of VO_2:

Along with MIT at 340K, VO_2 also undergoes several changes in its structural and optical properties. These characteristics along with multi-valency and catalytic properties make VO_2 a promising material for various electrical, thermal, and optical devices such as smart windows [64,65], gas sensors [66], electrical switches [67], energy storage devices [68] and cathodes for Li-ion batteries [69].

Vanadium oxides are attractive candidates as supercapacitor (SC) electrode owing to their catalytic nature as well as low-cost and abundant storage on earth [70-72]. There are several reports on SC properties of VO_x composites [73,74]. VO_2 is found out as a good choice for electrode because of its higher electronic conductivity and structural stability due to the increased edge-sharing and the consequent resistance to lattice shearing during cycling, as reported by Lampe-Onnerud *et al.* [75]. Issues related to the presence of multiple valence states of V, as well as its stability affecting capacitance retention and efficiency, is found to impede further utility in SCs. However, VO_2 undergoes several structural phase transitions as a function of temperature, external electric field, hydrostatic pressure, intense illumination, and strain. So, the influence of each structural phase and corresponding oxidation states of VO_2 has to be probed on its supercapacitive behaviour.

VO_2 is reported to transmit IR at a low-temperature semiconducting phase and reflect IR at high-temperature metallic phase [52-54], whereas it is known to be transparent in the visible region [76]. This phase transition property makes VO_2 an attractive material for smart windows [53]. However, there are only a few reports for enhancing the transmittance in the visible region by doping with F and Mg [76,77].

The identification of methane (CH_4), the second-largest contributor to global warming after CO_2 [78], is difficult at temperatures lower than 200 $^{\circ}$C due to its high thermodynamic stability [79]. However, being a catalytic materials vanadium oxides form an interesting group of materials in this field because of their varying oxidation states between V^{2+} and V^{5+}. VO_2 is particularly attractive because it exhibits a first-order metal to insulator phase transition (MIT) near room temperature (340K) [28-30]. The resistance drops by four orders above the transition temperature [51]. As most of the metal-oxide gas-sensors works by resistance-based mechanism, a systemic study of CH_4 sensing behavior of VO_2 around the transition temperature needs to be probed. As VO_2 is extremely susceptible to change its oxidation state and forming various metastable phases in the presence of air, we extended the sensing study for the higher-order oxides of V than VO_2 (V_nO_{2n+1}). As most of the resistance-based gas sensors work at high temperatures in air background, the chance of oxidation is very high, especially for multivalent oxide sensors [80]. Thus, the possibility of oxidation at a higher temperature and sensing behavior of the corresponding phase for V_nO_{2n+1} in the complete temperature range of gas sensing should be investigated systematically.

1.5   Objective and Overview of the Thesis:

The prime objective of the thesis is to found out the origin of the MIT as well as SPT of the vanadium oxides especially VO_2 and V_2O_5, and the applications of the materials in the light of phase transition. VO_2 and V_2O_5 nano and micro-structures were grown by a custom-built atmospheric pressure chemical vapor deposition technique. Localized spectroscopic studies using tip-enhanced Raman spectroscopy (TERS) along with proper polarization conditions were carried out to find the orientation of the nanostructures. The reason behind the metallic nature of V_2O_5 and the post-transition structural relaxation of the sample are conferred by

electrical activation energy calculations along with temperature-dependent Raman, photoluminescence and UV-Vis spectroscopic studies. The stabilization of various stable and metastable phases of VO_2 by doping and transformation between the phases by external stimuli like temperature and pressure are carried out to analyze the SPT in VO_2. The reason behind the MIT and SPT in VO_2 and the correlation between them is studied to resolve the long-lasting debate on the origin of phase transition in this material. The application of VO_2 in the light of phase transition has also been probed.

1.6 References:

1. Weckhuysen, B. M.; Keller, D. E. Chemistry, Spectroscopy and the Role of Supported Vanadium Oxides in Heterogeneous Catalysis. *Catal. Today* **2003,** *78*, 25-46.

2. Haber, J. Fifty Years of My Romance with Vanadium Oxide Catalysts. *Catal. Today* **2009**, *142*, 100-113.

3. Liu, K.; Lee, S.; Yang, S.; Delaire, O.; Wu, J. Recent Progresses on Physics and Applications of Vanadium Dioxide. *Mater. Today* **2018**, *21*, 875-896.

4. Bahlawane, N.; Lenoble, D. Vanadium Oxide Compounds: Structure, Properties, and Growth from the Gas Phase. *Chem. Vap. Depos.* **2014**, *20*, 299-311.

5. Kachi, S.; Kosuge, K.; Okinaka, H. Metal-Insulator Transition in V_nO_{2n-1}. *J. Solid State Chem.* **1973**, *6*, 258-270.

6. Balog, P.; Orosel, D.; Cancarevic, Z.; Schön, C.; Jansen, M. V_2O_5 Phase Diagram Revisited at High Pressures and High Temperatures. *J. Alloys Compd,* **2007**, *429*, 87-98.

7. Enjalbert, R.; Galy, J. A Refinement of the Structure of V_2O_5. *Acta Cryst.* **1986**, *C42*, 1467-1469.

8. Bachmann, H. G.; Ahmed, F. R.; Barnes, W. H. The Crystal Structure of Vanadium Pentoxide. *Z. Kristallogr.* **1961**, *115*, 110-131.

9. Khan, G. A.; Hogarth, C. A.; Electron Spin Resonance Studies of Evaporated V_2O_5 and Co-Evaporated V_2O_5/B_2O_3 Thin Films. *J. Mater. Sci.* **1991**, *26*, 2707-2710.

10. Clauws, P.; Broeckx, J.; Vennik, J. Lattice Vibrations of V_2O_5. Calculation of Normal Vibrations in a Urey-Bradley Force Field. *phys. stat. sol. (b)* **1985**, *131*, 459-473.

11. Chakrabarti, A.; Hermann, K.; Druzinic, R.; Witko, M.; Wagner, F.; Petersen, M. Geometric and Electronic Structure of Vanadium Pentoxide: A Density Functional Bulk and Surface Study. *Phys. Rev. B* **1999**, *59*, 10583-10590.

12. Eyert, V.; Höck, K. H. Electronic Structure of V_2O_5: Role of Octahedral Deformations. *Phys.l Rev. B* **1998**, *57*, 12727-12737.

13. Atzkern, S.; Borisenko, S. V.; Knupfer, M.; Golden, M. S.; Fink, J.; Yaresko, A. N.; Antonov, V. N.; Klemm, M.; Horn, S. Valence-Band Excitations in V_2O_5. *Phys. Rev. B* **2000**, *61*, 12792-12798.

14. Díaz-Guerra, C.; Piqueras, J. Thermal Deposition Growth and Luminescence Properties of Single-Crystalline V_2O_5 Elongated Nanostructures. *Cryst. Growth Des.* **2008**, *8*, 1031-1034.

15. Abello, L.; Husson, E.; Repelin, Y.; Lucazeau, G. Vibrational Spectra and Valence Force Field of Crystalline V_2O_5. *Spectrochim. Acta, Part A: Mol. Spectrosc.* **1983**, *39***, 641-651.

16. Baddour-Hadjean, R.; Pereira-Ramos, J. P.; Navone, C.; Smirnov, M. Raman Microspectrometry Study of Electrochemical Lithium Intercalation into Sputtered Crystalline V_2O_5 Thin Films. *Chem. Mater.* **2008**, *20*, 1916-1923.

17. Kang, M.; Kim, I.; Kim, S. W.; Ryu, J.-W.; Park, H. Y. Metal-Insulator Transition without Structural Phase Transition in V_2O_5 Film. *Appl. Phys. Lett.* **2011,** *98*, 131907-3.

18. Blum, R. –P.; Niehus, H.; Hucho, C.; Fortrie, R.; Ganduglia-Pirovano, M. V.; Sauer, J.; Shaikhutdinov, S.; Freund, H.-J. Surface Metal-Insulator Transition on a Vanadium Pentoxide (001) Single Crystal. *Phys. Rev. Lett.* **2007**, *9*, 226103-4.

19. Nadkarni G. S.; Shirodkar, V. S. Experiment and Theory for Switching in Al/V$_2$O$_5$/Al Devices. *Thin solid films* **1983**, *105*, 115-129.

20. Pergament, A.; Stefanovich, G.; Andreev, V. Comment on "Metal-Insulator Transition without Structural Phase Transition in V$_2$O$_5$ Film" [Appl. Phys. Lett. 98, 131907 (2011)] *Appl. Phys. Lett.* 2013, *102*, 176101.

21. Xie, S.; Iglesia, E.; Bell, A. T. Effects of Temperature on the Raman Spectra and Dispersed Oxides. *J. Phys. Chem. B* 2001, *105*, 5144-5152.

22. Lambrecht, W.; Djafari-Rouhani, B.; Vennik, J. Electronic Structure of Bulk and Surface Vanadyl Oxygen Vacancies in the Layer Compound V$_2$O$_5$. *Surf. Sci.* **1983**, *126*, 558-564.

23. Eon, J. G.; Olier R.; Volta, J. C. Oxidative Dehydrogenation of Propane on γ-Al$_2$O$_3$ Supported Vanadium Oxides. *J. Catal.* **1994**, *145*, 318-326.

24. Ramirez, R.; Casal, B.; Utrera, L.; Ruiz-Hitzky, E. Oxygen Reactivity in Vanadium Pentoxide: Electronic Structure and Infrared Spectroscopy Studies. *J. Phys. Chem.* **1990**, *94*, 8960-8965.

25. Rubin Aita, C. Additional Comment on "Metal-Insulator Transition without Structural Phase Transition in V$_2$O$_5$ Film" [Appl. Phys. Lett. 98, 131907 (2011)]. *Appl. Phys. Lett.* **2014**, *104*, 176101-2.

26. Wilhelmi, K. A.; Walterson, K. On the Crystal Structure of a New Vanadium Oxide, V$_4$O$_9$. *Acta. Chem. Scand.* **1970**, *24*, 3409-3411.

27. Srivastava, A.; Rotella, H.; Saha, S.; Pal, B.; Kalon, G.; Mathew, S.; Motapothula, M.; Dykas, M.; Yang, P.; Okunishi, E.; Sarma, D. D.; Venkatesan, T. Selective

Growth of Single Phase VO_2 (A, B, and M) Polymorph Thin Films. *APL Mater.* **2015**, *3*, 026101.

28. Morin, F. J. Oxides Which Show a Metal-to-Insulator Transition at the Neel Temperature. *Phys. Rev. Lett.* **1959**, *3*, 34.

29. Haverkort, M. W.; Hu, Z.; Tanaka, A.; Reichelt, W.; Streltsov, S. V.; Korotin, M. A.; Anisimov, V. I.; Hsieh, H. H.; Lin, H. -J.; Chen, C. T.; Khomskii, D. I.; Tjeng, L. H. Orbital-Assisted Metal-Insulator Transition in VO_2. *Phys. Rev. Lett.* **2005**, *95*, 196404.

30. Kim, H. -T.; Lee, Y. W.; Kim, B. -J.; Chae, B. -G.; Yun, S. J.; Kang, K. -Y.; Han, K. -J.; Yee K. -J.; Lim, Y. -S. Monoclinic and Correlated Metal Phase in VO_2 as Evidence of the Mott Transition: Coherent Phonon Analysis. *Phys. Rev. Lett*. **2006**, *97*, 266401.

31. Zylbersztejn, A.; Mott, N. F. Metal-insulator Transition in Vanadium Dioxide. *Phys. Rev. B,* **1975**, *11*, 4383.

32. Marezio M.; Dernier, P. D. Twinning in Cr-Doped VO_2, *Acta Cryst*. **1973,** *A29*, 618.

33. Goodenough, J. B. The Two Components of the Crystallographic Transition in VO_2. *J. Solid State Chem.* **1971**, *3*, 490-500.

34. Strelcov, E.; Tselev, A.; Ivanov, I.; Budai, J. D.; Zhang, J.; Tischler, J. Z.; Kravchenko, I.; Kalinin S. V.; Kolmakov, A. Doping-based Stabilization of the M2 Phase in Free-standing VO_2 Nanostructures at Room Temperature. *Nano Lett.* **2012**, *12*, 6198-6205.

35. Eyert, V. The Metal-Insulator Transitions of VO_2: A Band Theoretical Approach. *Ann. Phys. (Leipzig),* **2002**, *11*, 650-702.

36.   Verleur, H. W.; Barker, Jr. A. S.; Berglund, C. N. Optical Properties of VO_2 between 0.25 and 5 eV, *Phys. Rev.* **1968**, *172*, 788.

37.   Powell, R. J.; Berglund, C. N.; Spicer, W. E. Photoemission from VO_2, *Phys. Rev.* **1969**, *178*, 1410.

38.   Biermann, S.; Poteryaev, A.; Lichtenstein, A. I.; Georges, A. Dynamical Singlets and Correlation-Assisted Peierls Transition in VO_2, *Phys. Rev. Lett*. **2005**, *94*, 026404.

39.   Marini, C.; Arcangeletti, E.; Castro, D. D.; Baldassare, L.; Perucchi, A.; Lupi, S.; Malavasi, L.; Boeri, L.; Pomjakushina, E.; Conder K.; Postorino, P. Optical Properties of $V_{1-x}Cr_xO_2$ Compounds under High Pressure. *Phys. Rev. B* **2008**, *77*, 235111.

40.   Schilbe, P. Raman Scattering in VO_2, *Phys. B : Condensed Matter* **2002**, *316*, 600-602.

41.   Chen, X.-B. Assignment of the Raman Modes of VO_2 in the Monoclinic Insulating Phase. *J. Korean Phys. Soc.* **2011**, *58*, 100-104.

42.   Aronov, A.; Mirlin, D. Reshina, L. 1.; Chudnovskii, Fa. *Sov. Phys. Solid State* **1977**, *19*, 110.

43.   Srivastava R.; Chase, L. Raman Spectrum of Semiconducting and Metallic VO_2, *Phys. Rev. Lett.* **1971**, *27*, 727.

44.   Vikhnin, V.; Goncharuk, I.; Davydov, V. Y.; Chudnovskii, F.; Shadrin, E. Raman Light Scattering of Vanadium Dioxide High-Temperature Phase and the Model of Structural Transformations near Metal-Semiconductor Phase Transition. *Fizika Tverdogo Tela* **1995**, *37*, 3580-3596.

45.   Villeneuve, G.; Drillon, M.; Hagenmuller, P.; Nygren, M.; Pouget, J. P.; Carmona F.; Delhaes, P. Magnetic and Structural Properties of Stoichiometric and Non-Stoichiometric (V, Al) O_2 Alloys, *J. Phys. C: Solid State Phys*. **1977**, *10*, 3621.

46.   Brückner, W.; Gerlach, U.; Moldenhauer, W.; Brückner, H. P.; Mattern, N.; Oppermann H.; Wolf, E. Phase Transitions and Semiconductor-Metal Transition in $V_{1-x}Ga_xO_2$ Single Crystals, *Phys. Status Solidi A* **1976**, *38*, 93-102.

47.   Pouget, J. P.; Launois, H.; D'Haenens, J. P.; Merenda, P.; Rice, T. M. Electron Localization Induced by Uniaxial Stress in Pure VO_2, *Phys, Rev. Lett.* **1975**, *35*, 873-875.

48.   Park, J. H.; Coy, J. M.; Kasirga, T. S.; Huang, C.; Fei, Z.; Hunter S.; Cobden D. H. Measurement of a Solid-State Triple Point at the Metal-Insulator Transition in VO_2, *Nature* **2013**, *500*, 431-434.

49.   Fisher, B. Electrical and Seebeck Effect Measurements in Nb Doped VO_2. *J. Phys. Chem. Solids* **1982**, *43*, 205-211.

50.   Mott, N. F. The Basis of the Electron Theory of Metals, with Special Reference to the Transition Metals. *Proc. Phys. Soc. A* **1949**, *62*, 416-422.

51.   Kim, D. H.; Kwok, H. S. Pulsed Laser Deposition of VO_2 Thin Films, *Appl. Phys. Lett*. **1994**, *65*, 3188.

52.   Mlyuka, N.; Niklasson, G.;. Granqvist, C. –G. Mg Doping of Thermochromic VO_2 Films Enhances the Optical Transmittance and Decreases the Metal-Insulator Transition Temperature, *Appl. Phys. Lett.* **2009**, *95*, 171909.

53.   Roach, W. R. Holographic Storage in VO_2, *Appl. Phys. Lett.* **1971** *19*, 453.

54.   Lu, S.; Hou, L.; Gan, F. Preparation and Optical Properties of Phase-Change VO_2 Thin Films, *J. Mater. Sci.* **1993**, *28*, 2169.

55.   Belozerov, A. S.; Korotin, M. A.; Anisimov, V. I.; Poteryaev, A. I. Monoclinic M1 Phase of VO_2: Mott-Hubbard Versus Band Insulator. *Phys. Rev. B* **2012**, *85*, 045109.

56.   Sommers, C.; Doniach, S. First Principles Calculation of the Intra-Atomic Correlation Energy in VO_2. *Solid State Communications* **1978**, *28*, 133-135.

57.   Rice, T. M.; Launois, H.; Pouget, J. P. Comment on "VO_2: Peierls or Mott-Hubbard? A View from Band Theory". *Phys. Rev. Lett.* **1994**, *73*, 3042-3042.

58.   Berglund, C. N.; Jayaraman, A. Hydrostatic-Pressure Dependence of the Electronic Properties of VO_2 near the Semiconductor-Metal Transition Temperature. *Phys. Rev.* **1969**, *185*, 1034-1039.

59.   Tao, Z.; Han, T.-R. T.; Mahanti, S. D.; Duxbury, P. M.; Yuan, F.; Ruan, C.-Y.; Wang, K.; Wu, J. Decoupling of Structural and Electronic Phase Transitions in VO_2. *Phys. Rev. Lett.* **2012**, *109*, 166406.

60.   Muraoka, Y.; Hiroi, Z. Metal-Insulator Transition of VO_2 Thin Films Grown on TiO_2 (001) and (110) Substrates. *App. Phys. Lett.* **2002**, *80*, 583-585.

61.   Chen, C.; Zhao, Y.; Pan, X.; Kuryatkov, V.; Bernussi, A.; Holtz M.; Fan, Z. Influence of Defects on Structural and Electrical Properties of VO_2 Thin Films. *J. Appl. Phys.* **2011**, *110*, 023707.

62.   Atkin, J. M.; Berweger, S.; Chavez, E. K.; Raschke, M. B.; Cao, J.; Fan, W.; Wu, J. Strain and Temperature Dependence of the Insulating Phases of VO_2 Near the Metal-Insulator Transition. *Phys. Rev. B* **2012**, 85, 020101.

63. Lee, S.; Cheng, C.; Guo, H.; Hippalgaonkar, K.; Wang, K.; Suh, J.; Liu, K.; Wu, J. Axially Engineered Metal–Insulator Phase Transition by Graded Doping VO_2 Nanowires. *J. Am. Chem. Soc.* **2013**, *135*, 4850-4855.

64. Mjejri, I.; Rougier, A.; Gaudon, M. Low-Cost and Facile Synthesis of the Vanadium Oxides V_2O_3, VO_2, and V_2O_5 and Their Magnetic, Thermochromic and Electrochromic Properties. *Inorg. Chem.* **2017**, *56*, 1734-1741.

65. Mlyuka, N.; Niklasson, G.; Granqvist, C. -G.; Mg Doping of Thermochromic VO_2 Films Enhances the Optical Transmittance and Decreases the Metal-Insulator Transition Temperature, *Appl. Phys. Lett.* **2009**, *95*, 171909.

66. Prasad, A. K.; Amirthapandian, S.; Dhara, S.; Dash, S.; Murali, N.; Tyagi, A. K. Novel Single Phase Vanadium Dioxide Nanostructured Films for Methane Sensing Near Room Temperature. *Sens. Actuators B* **2014**, *191*, 252-256.

67. Rajeswaran, B.; Umarji, A. M. Effect of W Addition on the Electrical Switching of VO_2 Thin Films. *AIP Adv*. **2016**, *6*, 035215.

68. Jampani, P. H.; Velikokhatnyi, O.; Kadakia, K.; Hong, D. H.; Damle, S. S.; Poston, J. A.; Manivannan, A.; Kumta, P. N. High Energy Density Titanium Doped-Vanadium Oxide-Vertically Aligned CNT Composite Electrodes for Supercapacitor Applications. *J. Mater. Chem. A* **2015**, *3*, 8413-8432.

69. Nethravathi, C.; Rajamathi, C. R.; Rajamathi, M.; Gautam, U. K.; Wang, X.; Golberg, D.; Bando, Y. N-Doped Graphene-VO_2 (B) Nanosheet-Built 3D Flower Hybrid for Lithium Ion Battery. *ACS Appl. Mater. Interfaces* **2013**, *5*, 2708-2714.

70.   Yan, Y. ; Li, B.; Guo, W.; Pang H.; Xue, H. *J.* Vanadium Based Materials as Electrode Materials for High Performance Supercapacitors. *Power Sources* **2016**, *329*, 148-169.

71.   Man, P.; Zhang, Q.; Sun, J.; Guo, J.; Wang, X.; Zhou, Z.; He, B.; Li, Q.; Xie, L.; Zhao, J.; Li, C.; Li, Q.; Yao, Y. Hierarchically Structured VO_2@Ppy Core-Shell Nanowire Arrays Grown on Carbon Nanotube Fibers as Advanced Cathodes for High-Performance Wearable Asymmetric Supercapacitors, *Carbon* **2018**, *139*, 21-28.

72.   Zhang, Q.; Wang, X.; Pan, Z.; Sun, J.; Zhao, J.; Zhang, J.; Zhang, C.; Tang, L.; Luo, J.; Song, B.; Zhang, Z.; Lu, W.; Li, Q.; Zhang, Y.; Yao, Y. Wrapping Aligned Carbon Nanotube Composite Sheets around Vanadium Nitride Nanowire Arrays for Asymmetric Coaxial Fiber-Shaped Supercapacitors with Ultrahigh Energy Density, *Nano Lett*. **2017**, *17*, 2719-2726.

73.   Huang, G.; Li, C.; Sun X.; Bai, J. Fabrication of Vanadium Oxide, with Different Valences of Vanadium, Embedded Carbon Fibers and Their Electrochemical Performance for Supercapacitor. *New J. Chem.* **2017**, *41*, 8977-8984.

74.   Tang, K.; Li, Y.; Li, Y.; Cao, H.; Zhang, Z.; Zhang, Y.; Yang, J. Self-Reduced VO/VO_x/Carbon Nanofiber Composite as Binder-Free Electrode for Supercapacitors. *Electrochim. Acta* **2016**, *209*, 709-718.

75.   Lampe-onnerud, C.; Thomas, J. O.; Hardgrave, M.; Yde-Andersen, S. The Performance of Single-Phase in the Lithium/Polymer Electrolyte Battery. *J. Electrochem. Soc.* **1995**, *142*, 3648-3651.

76.   Zhou, J.; Gao, Y.; Liu, X.; Chen, Z.; Dai, L.; Cao, C.; Luo, H.; Kanahira, M.; Sun, C.; Yan, L. Mg-doped VO_2 Nanoparticles: Hydrothermal Synthesis, Enhanced Visible

Transmittance and Decreased Metal–Insulator Transition Temperature, *Phys. Chem. Chem. Phys.* **2013**, *15*, 7505.

77. Burkhardt, W.; Christmann, T.; Meyer, B. K.; Niessner, W.; Schalch, D.; Scharmann, A. W- and F-Doped VO_2 Films Studied by Photoelectron Spectrometry. *Thin Solid Films* **1999**, *345*, 229-235.

78. Wetchakun, K.; Samerjaia, T.; Tamaekonga, N.; Liewhiran, C.; Siriwong, C.; Kruefu, V.; Wisitsoraat, A.; Tuantranont, A.; Phanichphant, S. Semiconducting Metal Oxides As Sensors for Environmentally Hazardous Gases, *Sens. Actuators B* **2011**, *160* 580-591.

79. Das, A.; Bonu, V.; Prasad, A. K.; Panda, D.; Dhara, S.; Tyagi, A. K. The Role of SnO_2 Quantum Dots in Improved CH_4 Sensing at Low Temperature, *J. Mater. Chem. C* **2014**, *2* 164-171.

80. Kang, Y. B. Critical Evaluation and Thermodynamic Optimization of the $VO-VO_{2.5}$ System, *J. Eur. Ceram. Soc.* **2012**, *32*, 3187-3198.

CHAPTER 2

PHASE TRANSITION IN V$_2$O$_5$

"In knowledge that man only is to be condemned and despised who is not in a state of transition"

— Michael Faraday

2.1   Introduction:

Vanadium is a transition metal ([Ar]$3d^3 4s^2$) with multiple oxidation states leading to various stoichiometric and non-stoichiometric oxides. Vanadium pentoxide (V$_2$O$_5$), which is essentially a semiconductor at room temperature, is the most stable oxide of V [1,2]. Although, most of the vanadium oxides such as VO$_2$, V$_2$O$_3$, V$_6$O$_{13}$ exhibit metal-to-insulator transitions (MITs) as a function of temperature, it is quite contentious to use the term 'MIT' in case of V$_2$O$_5$ [3]. However, there are few reports about the transition to the metallic phase of V$_2$O$_5$ films around 530 to 553K and surface metallicity of (001) facet around 340 to 400K [4-6]. The MIT is also reported to be reversible [6]. The catalytic behavior makes V$_2$O$_5$ applicable as gas sensors [7,8], thermochromic devices [9,10], optical and electrical switches [11] around the transition temperature. The origin of the metallic behavior, however, is still not fully understood. The metallic transition was reported because of the reduction of V$_2$O$_5$ to other lower ordered stoichiometric or non-stoichiometric oxides without any structural change [5,12]. In the structure of V$_2$O$_5$, there are three differently coordinated O atoms, namely, O$_I$ (vanadyl), O$_{II}$ (bridging), and O$_{III}$ (chain) [13]. There is also a dispute in the identification of the O responsible for the reduction, as all three O$_I$ [6,14], O$_{II}$ [15], and O$_{III}$ [16] are suggested to be the eligible candidates. A structural phase transition from α-V$_2$O$_5$ to metastable γ′-V$_2$O$_5$ [17], however, is also proposed with the increase in temperature to

explain metallicity above the transition temperature, as the later resembles conductive Wadsley phase of V_4O_9 [18].

The present chapter is devoted to the growth of (001) oriented V_2O_5 nanostructures by vapour transport process using atmospheric pressure chemical vapor deposition (APCVD) technique and to study the MIT in V_2O_5. A transition from insulating to metallic behavior was recorded in the temperature-dependent I-V measurement. The reason behind the metallic behavior is discussed considering the observed emission peaks above transition temperature in the temperature-dependent photoluminescence (PL) spectroscopic studies. The newly evolved PL emission above the transition temperature is understood in terms of creation of defect states leading to the modification of conduction bands in the V_2O_5 electronic structure invoking metallicity in the system. The reversible temperature-dependent Raman spectra were analyzed for the allowed vibrational modes of semiconducting and metallic V_2O_5 phases to identify the particular defect state responsible for the transition as well as to understand the relaxed structure after the transition. The change in electronic band structure after the reduction of V_2O_5, prompting the metallicity in the sample, is discussed using temperature-dependent ultraviolet-visible (UV-Vis) absorption spectroscopic studies and thermal activation energy calculations.

2.2 Growth of V_2O_5 Nanostructures:

2.2.1 Thermal evaporation

One of the widespread methods of physical vapor deposition (PVD) technique is thermal evaporation [19]. This is a procedure for coating pure materials (mostly metals) in the thickness range of few angstroms to few microns on various substrates. The coatings can be a single material or can be multiple layers of different materials. Thermal evaporation

technique undergoes three major steps; generation, transport, and condensation under high vacuum ($\sim 10^{-6}$ mbar) [19]. The required temperature for evaporation of the metal is delivered by a heating element (W filament or Mo boat) through electrical resistive heating. The Au deposition on the Si substrate, required for growth of V_2O_5, was carried out by thermal evaporation system (HINDHIVAC Vacuum Coater-12A4D) at high vacuum with in-situ thickness monitor facilities.

2.2.2 Atmospheric pressure chemical vapor deposition

Chemical vapor deposition (CVD) is a common industrial process for depositing high-quality crystalline materials as it operates in the thermodynamical equilibrium condition. In a typical CVD process, the wafer is exposed to one or more volatile precursors, which react and decompose on the substrate surface to produce the desired deposit. Frequently, volatile byproducts are also produced, which are removed by gas flow through the reaction chamber. There are a great number of variants within the CVD technique. However, all CVD deposition processes undergo the following steps.

- ✓ Generation of gaseous precursors.

- ✓ Transportation of gaseous reactants into the reaction chamber.

- ✓ Formation of intermediates following the gas-phase reaction of the gaseous reactants.

- ✓ Deposition of material onto the substrate.

- ✓ Diffusion of deposited material across the substrate resulting in the formation of crystallization centers.

- ✓ Transportation of gaseous by-products away and out of the reaction chamber.

CVD is a promising method for its cost-effectiveness and large-scale growth of nanostructures [20]. Additionally, CVD enables high levels of control over uniformity,

thickness, and structure, while also maintaining phase purity of the deposit. Due to its non-line-of-sight deposition capabilities, low cost, and high throughput, we preferred CVD for the growth of V_2O_5 nanostructures. We have used APCVD, where the chamber is maintained at atmospheric pressure during the deposition. The experimental setup arranged for the growth of V_2O_5 nanostructures is shown in figure 2.1.
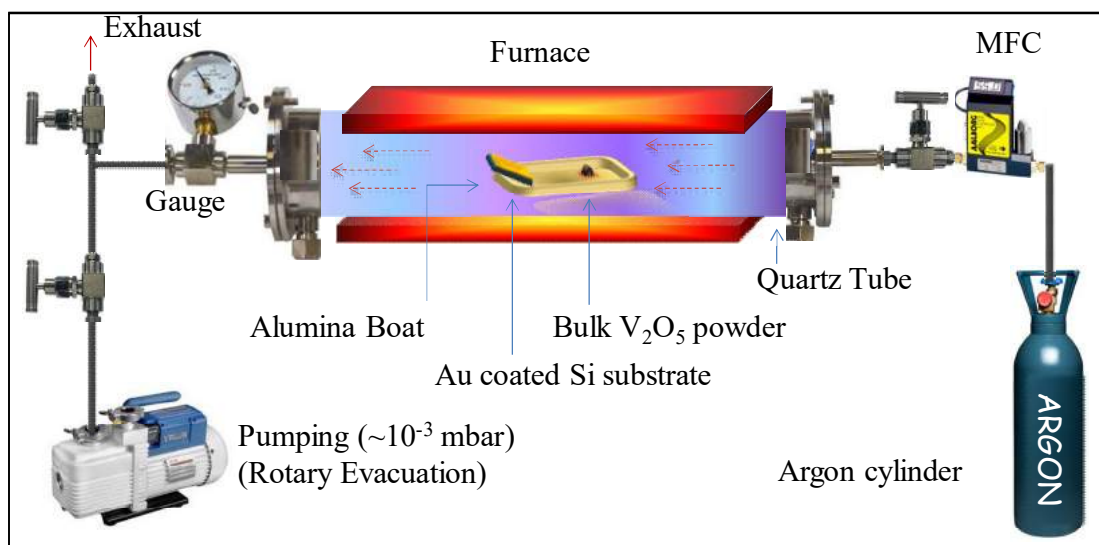
Figure 2.1 Schematic representing the APCVD system used for the growth of V_2O_5 nanostructures.

The major components of the custom-built APCVD system are listed below with the specific functionalities.

A. Horizontal high temperature tubular furnace (MTI-OTF-1200X-III)

(i) Maximum temperature: 1200 ^{o}C; Optimized temperature: 900 ^{o}C

(ii) Temperature control: Proportional-integral-derivative (PID); Temperature accuracy: ±1 ^{o}C.

(iii) Heating element: SiC; Thermocouple: S-type.

B. Vacuum system and reaction chamber:

(i) Mechanical rotary pump for pre-evacuation (Edwards, RV12, 1×10^{-3} mbar)

(ii) Vacuum gauge for measuring chamber-pressure (Pirani Gauge; Maximum vacuum: 2×10^{-3} mbar).

(iii) Reaction chamber: A quartz tube of length ~100 cm and diameter of 2.5 cm inside which the solid precursor was kept using a high pure (99.99%) alumina boat.

C. Gas delivery and control system:

The flow rate of carrier gas (Commercial Ar; 99.9%) was controlled by the mass flow controller (MFC).

2.2.3 Vapour transport process and the optimized experimental condition

In the vapour transport process a condensed phase (source), typically a solid, is vaporised in the presence of carrier gas (transport agent) and gets deposited on the substrate in the form of crystals. V_2O_5 nanostructures were synthesized on Au coated SiO_2/Si (100) substrate by vapor transport process using bulk V_2O_5 powder (Sigma-Aldrich, 99%) as source and commercial Ar as the carrier gas. Au film of 2 nm was deposited on SiO_2/Si (100) using thermal evaporation technique at 10^{-6} mbar as described in section 2.2.1. The bulk V_2O_5 powder was placed in a high pure (99.99%) alumina boat at the center of the quartz tube reaction chamber, kept in a thermoelectrically controlled furnace. The substrate was kept 5 cm away from the source and perpendicular to the stream of Ar. The reaction chamber was evacuated up to 10^{-3} mbar with the help of a rotary pump. The temperature of the quartz tube was programmed to rise up to 773K and was stabilized at that temperature for 10 min to form Au islands on the substrate (shown later in section 2.3.1) with the introduction to carrier gas reaching atmospheric pressure in the reactor chamber. Then the temperature was increased to the optimized growth temperature of 1173K with a ramp rate of 15 °C min^{-1}. The synthesis was carried out at 1173K flowing 20 sccm of Ar as the carrier gas for 60 min.

2.3 Characterizations of the Pristine Sample:

2.3.1 Morphological analysis

The morphological studies of the V_2O_5 nanostructures were carried out using a field emission scanning electron microscope (FESEM, SUPRA 55 Zeiss) with 30 kV source from a tungsten field emission tip.
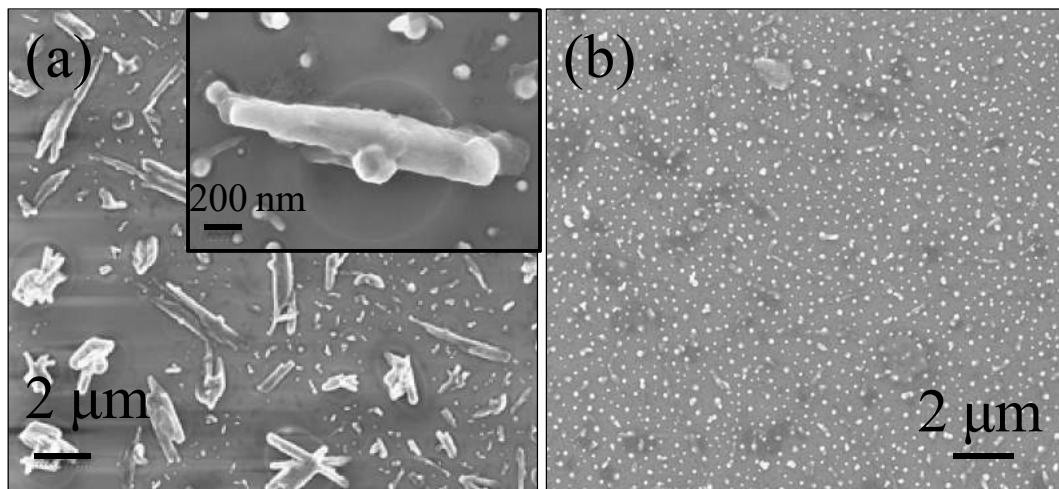
Figure 2.2 (a) FESEM image of as-grown nanostructures. Inset shows a typical single V_2O_5 nanorod of diameter ~ 200-300 nm and spherical Au nanoparticles (NPs) (b) FESEM image of the Au NPs in the early nucleation of oxide phase.

The typical FESEM image (Fig. 2.2a) of the as-grown sample shows rod-like structures with an average diameter of 200-300 nm. The region with the early nucleation of oxide phase with Au nanoparticle (NPs) is also recorded in the typical FESEM image (Fig. 2.2b). The inset of figure 2.2a shows a high magnification image of a typical single nanorod along with Au NPs. The average diameter of the Au particles is found out ~ 40 nm (Fig. 2.2b).

2.3.2 Structural analysis

The crystal structure and phase of the as-grown material was analyzed by glancing incidence x-ray diffraction (GIXRD) studies. In GIXRD, the diffraction pattern is collected from a

depth of ~10-100 Å of the sample where the contribution from the substrate is negligible. The crystallographic structural studies were carried out with the help of GIXRD (Bruker D8) using a Cu Kα radiation source ($\lambda = 1.5406$ Å) with a glancing angle (θ) of 0.5°. The GIXRD pattern obtained from the sample is compared with the ICDD database.
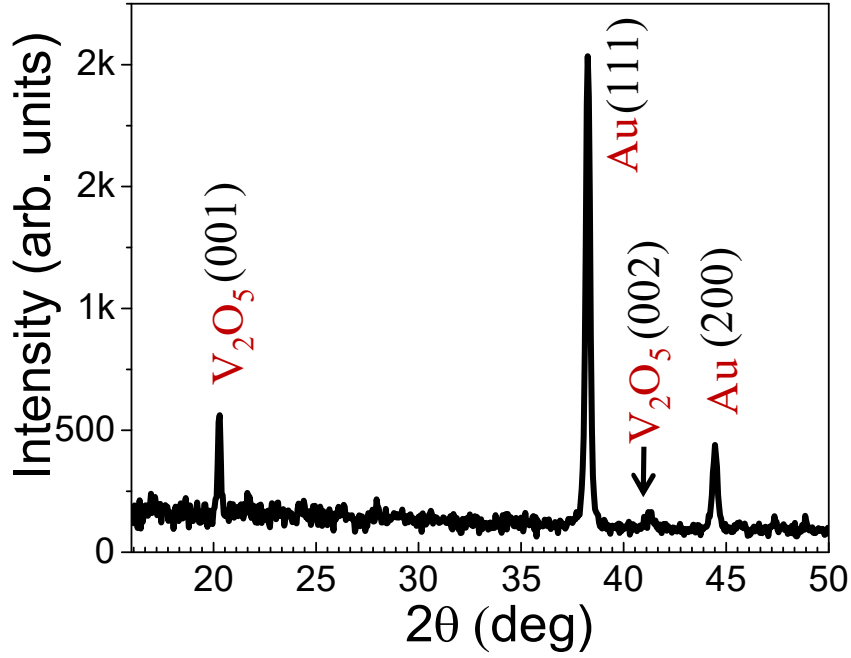
Figure 2.3 GIXRD pattern of the as-grown sample indicating crystalline planes corresponding to phases present.

The GIXRD pattern (Fig. 2.3) confirms the presence of pure V_2O_5 phase (ICCD 00-041-1426) [13] with peaks corresponding to the (*hkl*) planes of (001) and (002) along with peaks corresponding to (111) and (200) planes for Au (ICCD 00-004-0784).

2.3.3 Raman spectroscopic analysis

The space group of V_2O_5 is P_{mmn} $\left(D_{2h}^{13}\right)$. Group theoretical analysis predicts twenty one Raman active modes for V_2O_5 at Γ point, $7A_g+7B_{2g}+3B_{1g}+4B_{3g}$ [21]. We used micro-Raman spectrometer (inVia, Renishaw, UK), in the backscattering configuration to study the

vibrational modes of the synthesized sample using Ar^+ laser (514.5 nm) as an excitation source. The spectra were collected using a 50x objective with numerical aperture of 0.45 along with diffraction gratings of 1800 gr.mm^{-1} as a monochromator, and a thermoelectric cooled charged coupled device (CCD) as detector.

We observed eleven Raman modes for as-grown nanostructures (Fig. 2.4), which match with the reported data for V_2O_5 [21,22]. The Raman peaks at 102 (A_g), 144 (either B_{1g} or B_{3g}; B_{1g}/B_{3g}), 195 (A_g/B_{2g}), 283 (B_{1g}/B_{3g}), 301 (A_g), 403 (A_g), 483 (A_g), 523 (A_g), 701 (B_{1g}/B_{3g}), 850 (B_{1g}) and 993 (A_g) cm^{-1} confirm the presence of pure V_2O_5 phase [21].
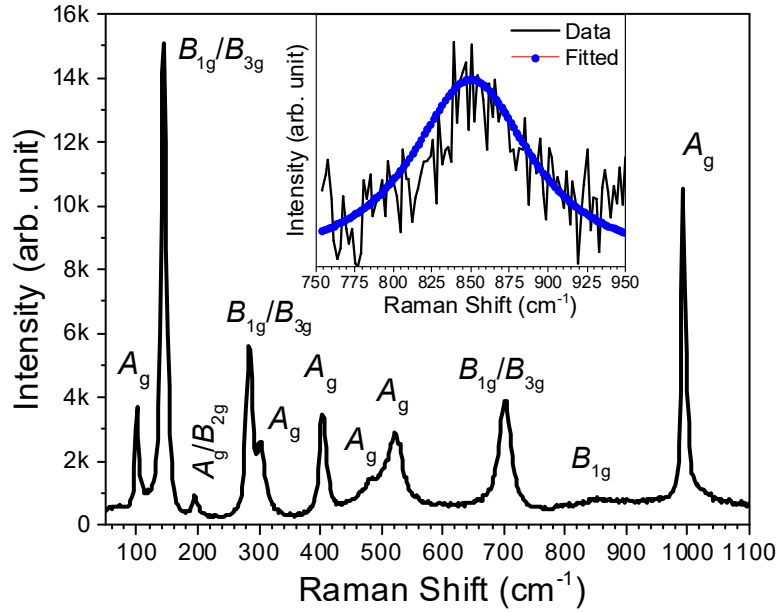
Figure 2.4 Raman spectrum of the pristine V_2O_5 nanostructures at room temperature with proper symmetry notations. The inset shows fitted peak at 850 cm^{-1} corresponding to B_{1g} mode.

Orthorhombic V_2O_5 is made of distorted VO_5 pyramids sharing edges and corners [23]. A schematic diagram of V_2O_5 unit cell is shown in the inset of figure 2.5. There are three structurally different oxygen atoms in each unit cell which are denoted as O_I, O_{II}, and O_{III}, as shown in the figure 2.5.
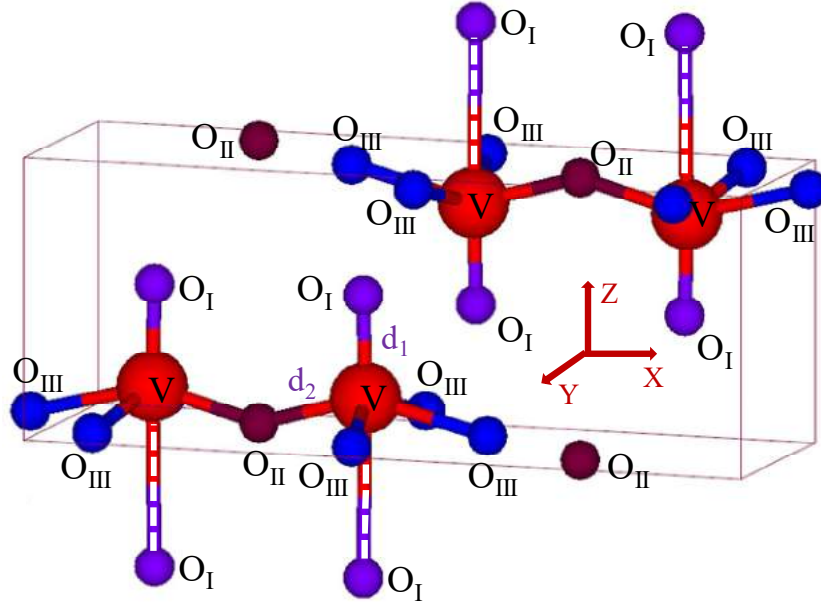
Figure 2.5 Schematic diagram of the V_2O_5 unit cell. Van der Waals bond between V and O_I is indicated by the white dashed line.

O_I is the terminal (vanadyl) oxygen with two different bond lengths; strong and short V-O_I bond is with length 1.577 Å (d_1), and a large and weak one is with a bond length of 2.793 Å. The later is of Van der Waals type bonding, which connects the two adjacent layers in the V_2O_5 structure. The two-fold coordinated bridging oxygen (O_{II}) connects two adjacent V atoms with V-O_{II} bond length of 1.78 Å (d_2). The ladder-shaped O_{III} atoms are the three-fold coordinated oxygen with three different V-O_{III} bond lengths of 1.88 (d_3), 1.88 (d_3), and 2.02 Å (d_4) [13]. V_2O_5 consists of layers connecting by a weak Van der Waals bond between V and O_I atom of the adjacent layer (shown by the white dashed line in Fig. 2.5). The highest frequency Raman mode at 993 cm^{-1} arises due to the vibration of terminal oxygen atoms along Z direction and is a signature peak for V_2O_5 [21]. The peak at 850 cm^{-1} is predicted to originate because of antiphase stretching mode of V-O_{II} bonds [22]. Displacement of O_{III} atoms in Y and X directions generates Raman modes at 701 and 523 cm^{-1}, respectively. The V-O_{II}-V bending deformation along Z direction gives rise to Raman mode at 483 cm^{-1}.

Modes at 403 and 283 cm^{-1} can be attributed to the oscillation of O$_I$ atoms along X and Y axes, respectively. One the other hand, displacement of O$_{II}$ atoms along Z-axis gives rise to Raman peak at 301 cm^{-1}. The low-frequency modes at 195, 144, and 102 cm^{-1} correspond to the X, Y, and Z displacements, respectively, of the whole chain of V-O$_{III}$ bonds [22,24]. The high intensity of 144 cm^{-1} peak indicates the long-range order of V-O layers in the XY plane [22]. The Raman mode at 850 cm^{-1} is reported not to be observed experimentally due to the pseudo-centrosymmetric nature of V-O$_{II}$-V bond [22]. However, we could observe the mode because of possible surface-enhanced Raman scattering due to the plasmonic effect of the Au NPs present (Fig. 2.2b) in the sample.

2.4   Phase Transition in V$_2$O$_5$:

2.4.1 Temperature-dependent electrical measurement

V$_2$O$_5$ is reported as a semiconductor with a large energy gap of 3.3 eV; within this gap, however, there exist two localized bands [25]. The schematic diagram of the electronic band structure of V$_2$O$_5$ is shown in figure 2.6a. V$_2$O$_5$ is a semiconductor with an indirect band gap value of 2.1 eV corresponding to a transition from R to Γ point in the first Brillouin zone [26]. The direct band gap at Γ point is reported ~2.5 eV [25,27]. Two split-off bands with a narrow bandwidth (~ 0.7 eV) below the conduction band at Γ point are also reported due to the overlapped O $2p$ and V $3d$ bands ($pd\pi$ bonds) [28,29].
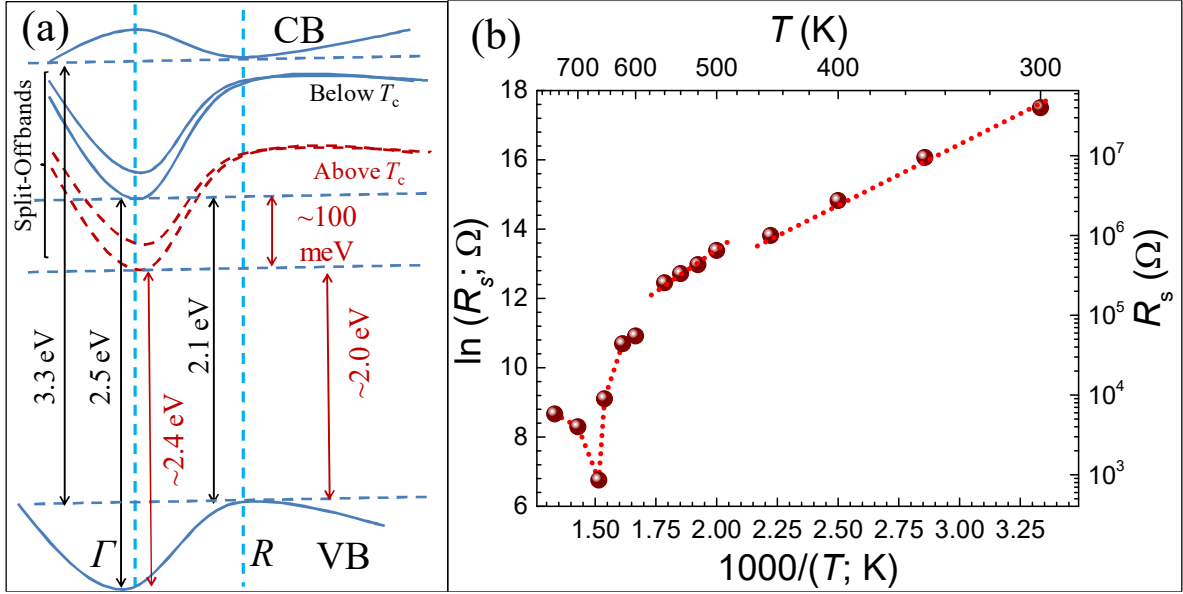
Figure 2.6 (a) Schematic electronic band structure of V_2O_5 indicating the possible transition. Solid and dashed split-off curves denote the electronic states below and above the transition temperature (T_c), respectively. (b) Change in the resistance with temperature in an ensemble of V_2O_5 nanostructure.

To study the MIT in V_2O_5, temperature-dependent resistivity measurement was carried out in a voltage range of 2 V using two Au coated contact tips and a source measurement unit (Agilent B2911A). We have also calculated the activation energy E_a from the slope of $\ln(R_s)$ vs. $(1/T)$ plot, using the formula $R_s = R_0 \exp(-E_a/K_B T)$; where K_B is the Boltzmann constant, R_0 is the resistance at temperature $T=0K$. The semi-log plot of resistance (R_s) *vs.* T^{-1} shows (Fig. 2.6b) that resistance decreases exponentially up to 450K with increasing temperature, indicating a semiconducting behavior leading to an activation energy of 0.29 ± 0.01 eV, which is slightly higher than the previously reported value (0.26 eV) for single crystalline V_2O_5, measured in the temperature range of 200-270K [30]. The most plausible reason for this low value of activation energy is due to the transition of electrons from localized split-off bands to main conduction band. In the temperature range of 500-550K, the slope of the plot

is increased with an activation energy of 0.4 ± 0.01 eV, which indicates the downward shift of split-off bands with increasing temperature. Above 550K, the slop falls rapidly disobeying the semiconducting nature and the plot shows metallic behavior of increasing resistance with increase in the temperature above 650K. The cause of the metallic behavior is still under debate [5,6,15-17]. The proposed metallic phase of metastable γ'-V_2O_5 in the structural phase transition model [17], is reported to convert to a stable semiconducting α-V_2O_5 phase above 613K [31]. In our study, however, the temperature-dependent electrical measurement shows (Fig. 2.6b) that the metallic character of the grown nanostructure sustains above 650K, which contradicts the formation of γ'-V_2O_5. Hence the reduction of V_2O_5 though O vacancy is likely in producing the metallic phase above the transition temperature [5]. However, the role of specific O is still not clear.

2.4.2 Temperature-dependent Raman spectroscopic measurement

A temperature-dependent Raman spectroscopic study (Fig. 2.7a) was conducted to address the role of specific O in producing the metallic phase. Temperature dependent Raman studies were performed by keeping the sample in the Linkam (THMS600) stage with an auto-controlled thermoelectric heating and cooling function within a temperature range of 80 to 650K. In temperature-dependent Raman study, the modes at 483 and 850 cm^{-1} are observed to disappear completely above the transition temperature of 530K and reappear again at the same temperature while cooling down. Moreover, a softening for all Raman modes was recorded with the increase in temperature except for the mode frequencies at 283, 403 and 993 cm^{-1}. Temperature dependence of frequencies for all the observed Raman modes is shown in figure 2.7b. With increasing temperature, the peak positions of the Raman modes, except for the three above mentioned modes, are red-shifted by an amount of 7 to 13

cm^{-1} in the temperature range from 300 to 650K. The intensity of the peak centered at 993 cm^{-1} is observed to decrease rapidly with the increase in temperature and regain almost its original intensity after cooling back to room temperature. The intensity ratio of the highest intense 144 cm^{-1} (B_{1g}/B_{3g}) Raman mode with 993 cm^{-1} (A_{1g}) mode with increasing temperature is shown in figure 2.7c.
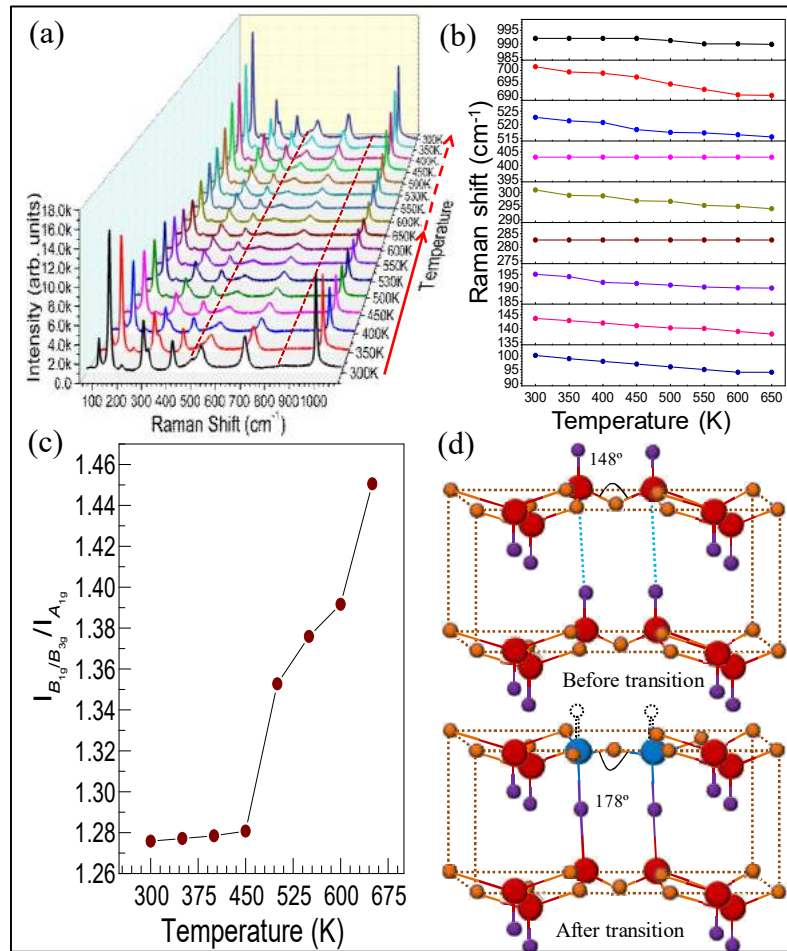
Figure 2.7 (a) Raman spectra of V$_2$O$_5$ nanostructures with increasing (denoted by solid arrow) and decreasing (denoted by the dashed arrow) temperature in the range of 300 to 650K (b) Change in vibrational frequency with temperature for each Raman mode. (c) Temperature dependence of the intensity ratio of the highest intense peak at 144 cm^{-1} ($I_{B_{1g}/B_{3g}}$) with the peak at 993 cm^{-1} ($I_{A_{1g}}$). (d) Schematic diagram of V$_2$O$_5$ unit cell at below and above the transition temperature.

450K indicating a significant decrease in the intensity of A_{1g} mode centered at 993 cm^{-1} as compared to that of B_{1g}/B_{3g} mode at 144 cm^{-1} around the transition temperature of 530K. The drastic fall in the intensity of A_{1g} mode, which is responsible for the vibration of vanadyl O_I atoms along the c-axis alone, signifies the possible loss of O_I atoms from the structure around the transition temperature. It may also be noted that the B_{1g}/B_{3g} mode frequency at 144 cm^{-1} is independent of the motion of O_I, so our inference about the role of O_I influencing the intensity of A_{1g} mode at 993 cm^{-1} is mutually exclusive. Moreover, it is reported that the vanadyl O_I is more prone to reduction, as the vacancy formation energy is lower for O_I atoms than the other two oxygen atoms (O_{II} and O_{III}) in V_2O_5 (001) oriented surface [32,33]. The modes at 483 and 850 cm^{-1}, arising due to V-O_{II}-V bending and stretching vibrations, respectively, disappeared above the transition temperature. It may be due to the relaxation of V_2O_5 structure initiated with the formation of vanadyl O_I vacancy (Fig. 2.7d). If one of the O_I atoms are removed from the surface, the V atom in its near vicinity projects inward for relaxation and the next right O_I atom relax upward to make a stiffer interlayer bond with decreased bond length (1.78 Å) [32]. Moreover, the V-O_{II}-V bond angle is also reported to increase to 178º, leading to almost a linear bond [32]. So, the disappearance of the modes at 483 and 850 cm^{-1} is in quite good agreement with the relaxation conditions. The absence of phonon softening with temperature for the Raman modes at 283, 403 and 993 cm^{-1}, which originates due to the Y, X and Z vibration of O_I atoms, respectively, may also be attributed to the structural relaxation as the V-O_I bonds become stiffer between the layers after the relaxation. The reversibility of the Raman modes with temperature can be explained by the excellent catalytic behavior of V_2O_5. The structural phase transition to γ'-V_2O_5 is further

ruled out with the absence of characteristic Raman mode at 602 cm^{-1} [34], in the studied temperature range of 300-650K (Fig. 2.7a).

2.4.3 Temperature-dependent UV-Vis absorption spectroscopic measurement

We have carried out the UV-Vis absorption spectroscopic studies in the reflection geometry to understand the optical properties in the light of electronic transitions. Absorption spectra were recorded using a UV-Vis absorption spectrometer (Avantes) in the range of 300-800 nm. A bare SiO_2/Si (100) wafer was used for reference to nullify the reflected contribution from the substrate. Figure 2.8a shows the UV-Vis absorption spectra of the sample. As there are Au NPs present in the sample, to investigate the role of Au in the absorption spectrum of V_2O_5, we performed the absorption studies for Au NPs as well as bulk V_2O_5 also. Au NPs of diameter ~ 40 nm shows a strong absorption peak at 528 nm, whereas bulk V_2O_5 shows four peaks around 560 to 630 nm. A faint absorption edge at ~ 342 nm may indicate the presence of theoretically forbidden interband transition in the bulk V_2O_5 powder [24,35]. The feature may have appeared because of the finite size of V_2O_5 powder and the measurements being performed at room temperature. On the other hand, V_2O_5 nanostructures in the presence of Au NPs show two strong absorption peaks at 342 and 565 nm. The peak at 565 nm (2.19 eV) matches with the previous report and can be attributed as the indirect transition from R to Γ point [24-29]. The peak at 342 nm (3.63 eV) may have shown its strong presence due to the plasmonic effect of Au NPs influencing the effective polarizability of the hybrid system [36]. Au NPs with a diameter of 40 nm on SiO_2 matrix is reported to show luminescence ~3.4 eV corresponding to energy gap at L –symmetry point [37]. To understand the origin of metallicity in V_2O_5, temperature-dependent UV-Vis absorption of the as-grown V_2O_5 nanostructures was studied. The Tauc's plot of the as-grown material, using *(αhν)$^{1/2}$* vs. *hν*

for indirect band gap semiconductor (absorption co-efficient, α; Planck's constant, h; frequency, v), at different temperatures ranging from 300 to 650K are shown in figure 2.8b.
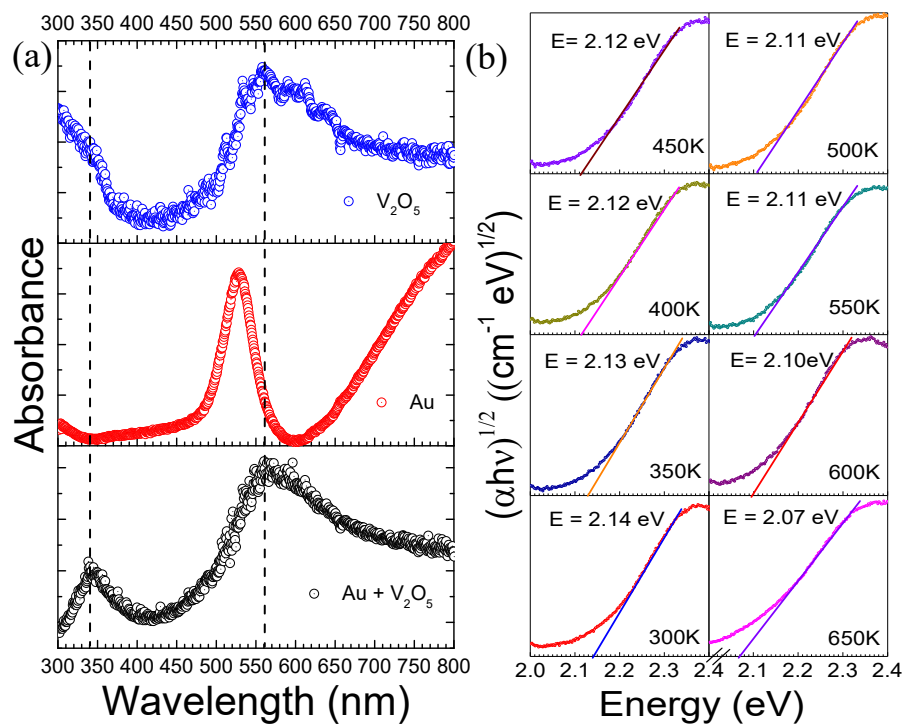
Figure 2.8 (a) UV–Vis absorption spectra of the grown sample, Au NPs, and bulk V_2O_5. (b) Tauc's plot of indirect band gap V_2O_5 nanostructures using UV-Vis spectra at different temperatures. The slopes are drawn to determine the band gap value, as inscribed in the insets for the plots at different temperatures.

An indirect band gap of 2.14 eV, which matches with the previously reported value of 2.1 eV for V_2O_5 [24], was recorded at 300K. The band gap decreases with increase in temperature and is measured to attain a value of 2.07 eV at 650K. The decrease in band gap by an amount of 70 meV indicates a downward shift of the split-off bands with an increase in temperature, as also inferred from the thermal activation energy analysis (Fig. 2.6b). Vanadyl O_I plays an important role in creating these split-off conduction bands [38,39]. Inspired by the O_I vacancy, the split-off conduction bands are reported to approach deeper down from the

conduction band at Γ point due to the breakdown of $pd\pi$ bond between O_I and nearest V

atom [14,38,39].

2.4.4 Temperature-dependent photoluminescence spectroscopic measurement

For further analysis, we carried out temperature-dependent photoluminescence (PL) studies

to examine the changes in electronic states with temperature. The PL spectra for the V_2O_5

nanostructures were recorded with an excitation laser of wavelength 325 nm (UV; He-Cd)

and 2400 gr.mm^{-1} grating using the same Raman spectrometer. In order to perform

temperature dependent measurements, the samples were kept in a Linkam (THMS600) stage.

Figure 2.9 shows PL spectra of V_2O_5 nanostructures with increasing temperature from 80 to

650K.
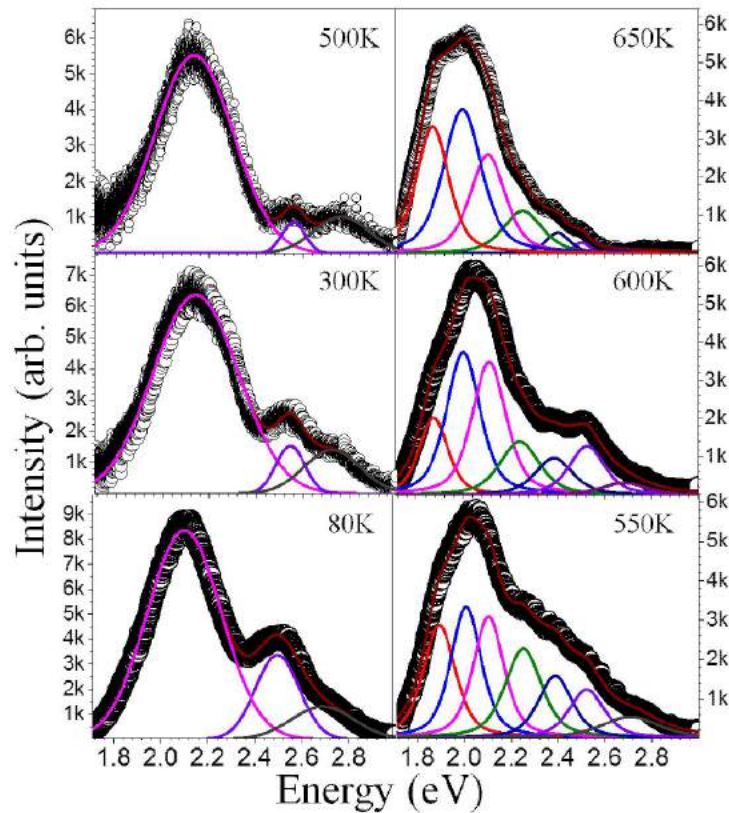
Figure 2.9 PL spectra at different temperatures ranging from 80 to 650K. Peaks are fitted with

Gaussian function. Symbols indicate data points, and lines indicate fitted curves.

We observed three sharp peaks at 2.1, 2.5 and 2.7 eV, recorded at 80K, which can be explained as an indirect transition from R to Γ point, a direct transition at Γ point and a direct transition at R point, respectively [24,40]. The observation of PL peaks for indirect transition in V_2O_5 is facilitated using the near resonance condition where laser excitation of 325 nm is selected close to the plasmonic assisted absorption peak of the hybrid system at 342 nm (Fig. 2.8a). At room temperature (300K), the peaks are blue shifted slightly to ~ 30 meV. The trend continues up to 500K, which is quite expected with increasing temperature. Surprisingly above the transition temperature at 550K, three new peaks arise around 1.89, 2.0, and 2.4 eV along with the previously observed peaks. With increasing temperature, the split-off conduction bands in the V_2O_5 electronic structure are found to approach deeper down from the conduction band around 70 to 100 meV at Γ point due to the breakdown of $pd\pi$ bond between O_I and nearest V atoms (Figs. 2.6a and 2.8b).[41] The origin of the newly evolved peaks can be understood because of the indirect transition from R to Γ point (1.89 and 2.0 eV for the two split-off bands) and a direct transition at Γ point (2.4 eV) of the new electronic levels, caused by oxygen vacancies (considering dotted split-off curves in Fig. 2.6a) [41,42]. With further increase in temperature up to 650K, the intensity of newly evolved low energy vacancy related peaks increases whereas, the intensity of band edge peaks decreases. Thus, the above observation supports the loss of O_I from the system with an increase in temperature [43,44] as also observed in the temperature-dependent Raman spectroscopic studies (Fig. 2.7). Reduction of an oxygen atom donates two electrons back to the structure. The breakdown of $pd\pi$ bond between O_I and nearest V atom results in delocalization of electrons towards neighboring V cation by occupying the partially filled V $3d$ states in the conduction band [45], leading to an increase in the number of carriers in

conduction band. The increased number of carriers in conduction band is responsible for the decrease in resistance above the transition temperature and the observed metallic behavior.

2.5 Summary:

V_2O_5 (001) nanostructures were grown by vapour transport mechanism using Au as catalyst. The Raman spectroscopic analysis and GIXRD measurements confirm the orthorhombic phase of the as-grown material. Temperature-dependent electrical properties showed a transition of semiconducting to metallic behavior at a temperature of 550K. Phonon softening behavior in the temperature-dependent Raman spectra indicated loss of vanadyl oxygen (O_I) as the possible reason for the observation of the metallic V_2O_5 phase above the transition temperature. Reduction of the band gap with increasing temperature, as observed in the Tauc's plot, with the appearance of new peaks in the PL spectra and in the thermal activation energy calculations, implies the downward movement of split-off bands from the conduction band. The downward shift of split-off bands with an increase in temperature is due to the breakdown of $pd\pi$ bond between O_I and nearest V atom, inspired by the formation of vanadyl O_I vacancy. The breakdown of $pd\pi$ bonds helps in accumulating electrons towards neighboring V atom to occupy the partially filled V $3d$ bands, leading to the increase in the number of carriers in the conduction band, which is finally made responsible for the decrease in the resistance and the observed metallic behavior.

2.6 References:

1. Poizot, P.; Laruelle, S.; Grugeon, S.; Dupont, L.; Tarascon, J. -M. Nano-Sized Transition Metal Oxides as Negative-Electrode Materials for Lithium-Ion Batteries. *Nature* **2000,** *407*, 496-499.

2. Rao, C. N. R. Transition Metal Oxides. *Annu. Rev. Phys. Chem.* **1989,** *40*, 291-326.

3. Pergament, A.; Stefanovich, G.; Andreev, V. Comment on "Metal-Insulator Transition without Structural Phase Transition in V_2O_5 Film" [Appl. Phys. Lett. 98, 131907 (2011)] *Appl. Phys. Lett.* 2013, *102*, 176101.

4. Nadkarni G. S.; Shirodkar, V. S. Experiment and Theory for Switching in $Al/V_2O_5/Al$ Devices. *Thin solid films* **1983**, *105*, 115-129.

5. Kang, M.; Kim, I.; Kim, S. W.; Ryu, J. -W.; Park, H. Y. Metal-Insulator Transition without Structural Phase Transition in V_2O_5 Film. *Appl. Phys. Lett.* **2011,** *98*, 131907-3.

6. Blum, R. -P.; Niehus, H.; Hucho, C.; Fortrie, R.; Ganduglia-Pirovano, M. V.; Sauer, J.; Shaikhutdinov, S.; Freund, H. -J. Surface Metal-Insulator Transition on a Vanadium Pentoxide (001) Single Crystal. *Phys. Rev. Lett.* **2007**, *9*, 226103-4.

7. Raible, I.; Burghard, M.; Schlecht, U.; Yasuda, A.; Vossmeyer, T. V_2O_5 Nanofibres: Novel Gas Sensors with Extremely High Sensitivity and Selectivity to Amines. *Sens. Actuators B* **2005**, *106*, 730-735.

8. Dhayal Raj, A.; Pazhanivel, T.; Kumar, P. S.; Mangalaraj, D.; Nataraj, D.; Ponpandian, N. Self Assembled V_2O_5 Nanorods for Gas Sensors. *Curr. Appl. Phys.* **2010**, *10*, 531-537.

9. Nishio, S.; Kakihana, M. Evidence for Visible Light Photochromism of V_2O_5. Chem. Mater. **2002**, *14*, 3730-3733.

10. Zuli, L.; Guojia, F.; Youqing, W.; Yandong, B. Laser-Induced Colouration of V_2O_5. *J. Phys. D: Appl. Phys.* **2000**, *33*, 2327-2332.

11. Krishnakumar, S.; Menon, C. S. Optical and Electrical Properties of Vanadium Pentoxide Thin Films. *phys. stat. sol. (a)* **1996**, *153*, 439-444.

12. Xie, S.; Iglesia, E.; Bell, A. T. Effects of Temperature on the Raman Spectra and Dispersed Oxides. *J. Phys. Chem. B* **2001**, *105*, 5144-5152.

13. Enjalbert, R.; Galy, J. A Refinement of the Structure of V_2O_5. *Acta Crystallogr., Sect. C: Cryst. Struct. Commun.***1986**, *42*, 1467-1469.

14. Lambrecht, W.; Djafari-Rouhani, B.; Vennik, J. Electronic Structure of Bulk and Surface Vanadyl Oxygen Vacancies in the Layer Compound V_2O_5. *Surf. Sci.* **1983**, *126*, 558-564.

15. Eon, J. G.; Olier R.; Volta, J. C. Oxidative Dehydrogenation of Propane on $\gamma\text{-}Al_2O_3$ Supported Vanadium Oxides. *J. Catal.* **1994**, *145*, 318-326.

16. Ramirez, R.; Casal, B.; Utrera, L.; Ruiz-Hitzky, E. Oxygen Reactivity in Vanadium Pentoxide: Electronic Structure and Infrared Spectroscopy Studies. *J. Phys. Chem.* **1990**, *94*, 8960-8965.

17. Rubin Aita, C. Additional Comment on "Metal-Insulator Transition without Structural Phase Transition in V_2O_5 Film" [Appl. Phys. Lett. 98, 131907 (2011)]. *Appl. Phys. Lett.* **2014**, *104*, 176101-2.

18. Wilhelmi, K. A.; Walterson, K. On the Crystal Structure of a New Vanadium Oxide, V_4O_9. *Acta. Chem. Scand.* **1970**, *24*, 3409-3411.

19. Chopra, K. L. *Thin film phenomena*, **1969**, 1st Ed., McGraw-Hill.

20. Drosos, C.; Jia, C.; Mathew, S.; Palgrave, R. G.; Moss, B.; Kafizas, A.; Vernardou, D. Aerosol-Assisted Chemical Vapor Deposition of V_2O_5 Cathodes With High Rate Capabilities For Magnesium-Ion Batteries. *J. Power Sources* **2018**, *384*, 355-359.

21. Abello, L.; Husson, E.; Repelin, Y.; Lucazeau, G. Vibrational Spectra and Valence Force Field of Crystalline V_2O_5. *Spectrochim. Acta, Part A: Mol. Spectrosc.* **1983**, *39*, 641-651.

22. Baddour-Hadjean, R.; Pereira-Ramos, J. P.; Navone, C.; Smirnov, M. Raman Microspectrometry Study of Electrochemical Lithium Intercalation into Sputtered Crystalline V_2O_5 Thin Films. *Chem. Mater.* **2008**, *20*, 1916-1923.

23. Bachmann, H. G.; Ahmed, F. R.; Barnes, W. H. The Crystal Structure of Vanadium Pentoxide. *Z. Kristallogr.* **1961**, *115*, 110-131.

24. Parker, J. C.; Lam, D. J.; Xu, Y. -N.; Ching, W. Y. Optical properties of vanadium pentoxide determined from ellipsometry and band-structure calculations. *Phys. Rev. B* **1990**, *42*, 5289-5293.

25. Khan, G. A.; Hogarth, C. A.; Electron Spin Resonance Studies of Evaporated V_2O_5 and Co-Evaporated V_2O_5/B_2O_3 Thin Films. *J. Mater. Sci.* **1991**, *26*, 2707-2710.

26. Clauws, P.; Broeckx, J.; Vennik, J. Lattice Vibrations of V_2O_5. Calculation of Normal Vibrations in a Urey-Bradley Force Field. *phys. stat. sol. (b)* **1985**, *131*, 459-473.

27. Chakrabarti, A.; Hermann, K.; Druzinic, R.; Witko, M.; Wagner, F.; Petersen, M. Geometric and Electronic Structure of Vanadium Pentoxide: A Density Functional Bulk and Surface Study. *Phys. Rev. B* **1999**, *59*, 10583-10590.

28. Eyert V.; Höck, K.-H. Electronic Structure of V_2O_5: Role of Octahedral Deformations. *Phys. Rev. B* **1998**, *57*, 12727-12737.

29. Atzkern, S.; Borisenko, S. V.; Knupfer, M.; Golden, M. S.; Fink, J.; Yaresko, A. N.; Antonov, V. N.; Klemm, M.; Horn, S. Valence-Band Excitations in V_2O_5. *Phys. Rev. B* **2000**, *61*, 12792-12798.

30. Karakotsou, Ch.; Kalomiros, J. A.; Hanias, M. P.; Anagnostopoulos, A. N.; Spyridelis, J. Nonlinear Electrical Conductivity of V_2O_5 Single Crystals. *Phys. Rev. B* **1992**, *45*, 11627-11631.

31. Cocciantelli, J. M.; Gravereau, P.; Doumerc, J. P.; Pouchard, M.; Hagenmuller, P. On the Preparation and Characterization of a New Polymorph of V_2O_5. *J. Solid State Chem.* **1991**, *93*, 497-502.

32. Ganduglia-Pirovano, M.; Sauer, J. Stability of Reduced V_2O_5 (001) Surfaces. *Phys. Rev. B* **2004**, *70*, 045422-13.

33. Sauer, J.; Dobler, J. Structure and Reactivity of V_2O_5: Bulk Solid, Nanosized Clusters, Species Supported on Silica and Alumina, Cluster Cations and Anions. *Dalton Trans.* **2004**, 3116-3121.

34. Baddour-Hadjean, R.; Smirnov, M. B.; Kazimirov, V. Y.; Smirnov, K. S.; Pereira-Ramos, J. -P. The Raman Spectrum of the γ'-V_2O_5 Polymorph: A Combined Experimental and DFT Study. *J. Raman Spectrosc.* **2015**, *46*, 406-412.

35. Kenny, N.; Kannewurf, C. R.; Whitmore, D. H. Optical Absorption Coefficients of Vanadium Pentoxide Single Crystals. *J. Phys. Chem. Solids.* **1966**, *27*, 1237-1246.

36. Sivadasan, A. K.; Parida, S.; Ghosh, S.; Pandian, R.; Dhara, S. Spectroscopically Forbidden Infra-Red Emission in Au-Vertical Graphene Hybrid Nanostructures. *Nanotechnology* **2017**, *28*, 465703.

37. Dhara, S.; Chandra, S.; Magudapathy, P.; Kalavathi, S.; Panigrahi, B. K.; Nair, K. G. M.; Sastry, V. S.; Hsu, C. W.; Wu, C. T.; Chen, K. H.; Chen, L. C. Blue Luminescence of Au Nanoclusters Embedded in Silica Matrix. *J. Chem. Phys.* **2004**, *121*, 12595-12599.

38. Lambrecht, W.; Djafari-Rouhani, B.; Vennik, J. On the Origin of the Split-Off Conduction Bands in V_2O_5. *J. Phys. C: Solid State Phys.* **1981**, *14*, 4785-4795.

39. Lambrecht, W.; Djafari-Rouhani, B.; Vennik, J. Theoretical Study of the Vanadyl-Oxygen Vacancy in V_2O_5: Tight-Binding Green Function Calculation, Optical Properties and Neutral Vacancy Ground-State Splitting. *J. Phys. C: Solid State Phys.* **1986**, *19*, 369-388.

40. Bhandari, C.; Lambrecht, W. R. L.; van Schilfgaarde, M. Quasiparticle Self-Consistent *GW* Calculations of the Electronic Band Structure of Bulk and Monolayer V_2O_5. *Phys. Rev. B* **2015**, *91*, 125116.

41. Basu, R.; Prasad, A. K.; Dhara, S.; Das, A. Role of Vanadyl Oxygen in Understanding Metallic Behavior of $V_2O_5(001)$ Nanorods. *J. Phys. Chem. C* **2016**, *120*, 26539-26543.

42. Wang, Y.; Li, Z.; Sheng, X.; Zhang, Z. Synthesis and optical properties of V_2O_5 nanorods. *J. Chem. Phys.* **2007**, *126*, 164701.

43. Díaz-Guerra, C.; Piqueras, J. Thermal Deposition Growth and Luminescence Properties of Single-Crystalline V_2O_5 Elongated Nanostructures. *Cryst. Growth Des.* **2008**, *8*, 1031-1034.

44. Basu, R.; Dhara, S. Spectroscopic Study of Native Defects in The Semiconductor to Metal Phase Transition in V_2O_5 Nanostructure. *J. Appl. Phys.* **2018**, *123*, 161550.

45. Wu, Q. -H.; Thissen, A.; Jaegermann, W.; Liu, M. Photoelectron Spectroscopy Study of Oxygen Vacancy on Vanadium Oxides Surface. *Appl. Surf. Sci.* **2004**, *236*, 473-478.

CHAPTER 3

STABILIZATION OF METASTABLE PHASES AT ROOM TEMPERATURE AND STRUCTURAL PHASE TRANSITION IN VO_2

"Change is more often a rapid transition between stable states than a continuous transformation at slow and steady rates."

— Isaac Asimov

3.1   Introduction:

Transition metal oxides are of great scientific as well as technological interest in developing the next generation of power-efficient electrical and optical devices [1]. Being a transition metal, most of the oxides of V undergo metal to insulator transition (MIT) as a function of temperature [2]. Among all oxides of V, however, VO_2 finds tremendous attraction and turns out to be the center of extensive research because of its first order, reversible MIT at the technologically important temperature of 340K, which is very close to room temperature [3,5]. A structural phase transition (SPT) from a low-temperature monoclinic M1 (space group $P2_1/c$) to a high-temperature rutile tetragonal R (space group $P4_2/mnm$) is also associated with the MIT [3-5]. Besides M1, another two metastable phases of monoclinic M2 (space group $C2/m$) and triclinic T (or monoclinic M3; space group $\overline{C}1$) are also reported to evolve during the phase transition from M1 to R [6]. The M2 and T phases can be stabilized at room temperature by doping with metals of lower valency than V^{4+}(e.g., Al^{+3}, Ga^{+3}, Cr^{+3}) [7-9]. The phase stabilization of the metastable phases is alternatively reported by applying tensile strain along the rutile c axis (c_R) [10,11]. In all the phases of VO_2, there are two interpenetrating parallel chains of V surrounded by six O atoms forming distorted octahedron. In the high temperature R phase, all the V chains are parallel and periodic [12]; whereas in the low temperature monoclinic M1, M2 and triclinic T phases there are significant differences in the arrangement of V along c_R axis. The V forms pair (dimerized)

and the pairs tilt along the c_R axis in the M1 phase, making the unit cell double of the unit cell in R phase (schematic in Fig. 3.1) with the approximate crystallographic relationship as $a_{M1} \leftrightarrow 2c_R$, $b_{M1} \leftrightarrow a_R$, and $c_{M1} \leftrightarrow b_R - c_R$ [7,13]. In the M2 phase, one set of V chains along with the c_R axis pairs without twisting, while the V ions in the nearest neighbor V chains, do not pair but twist away from c_R axis. The crystallographic relationship with the R phase is $b_{M2} \leftrightarrow 2c_R$, $a_{M2} \leftrightarrow 2a_R$, and $c_{M2} \leftrightarrow -b_R$ [13]. The triclinic T phase is intermediate between the M1 and M2 phases, in which paired V chains in the M2 phase are reported to be twisted slightly [14].
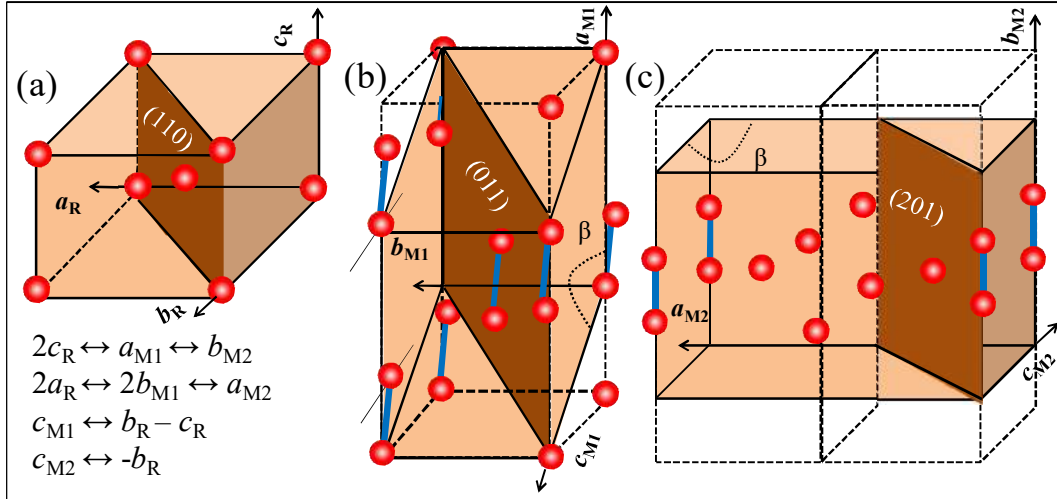
Figure 3.1 Schematic structural diagram of different phases of VO_2 (a) rutile tetragonal, R; (b) monoclinic, M1; and (c) monoclinic, M2. Red balls denote V atoms, each surrounded by O octahedra (not shown in the figure) with principal axis perpendicular to the shaded plane.

In addition to temperature, other driving forces such as external electric field [15], hydrostatic pressure [16], intense illumination [17], and strain [18] can also introduce phase transition in VO_2. Moreover, the transition temperature (T_c) tunes with the variation of carrier density [19], applied strain [20], or doping [21] showing significant change in the optical, thermal and electrical properties of VO_2. These characteristics make VO_2 a promising

material for various electrical, thermal and optical devices such as smart windows [22], gas sensors [23], electrical switches [24], and cathodes for Li-ion batteries [25]. Doping in bulk $M_xV_{(1-x)}O_2$ can lead to decrease in the T_c value for M = W^{+6}, Mo^{+6}, Ta^{+5}, Nb^{+5} [26], and an increase is reported in the T_c value for M = Al^{+3}, Ga^{+3}, Cr^{+3} [7-9].

The present chapter describes the growth and phase transformation among the various stable and metastable phases of VO_2 by external stimuli like temperature and pressure. The stabilization of the metastable phases of VO_2 at room temperature is made in a novel technique by introducing defects in the system, for the first time, via two ways: (i) hole doping by the creation of native vacancy defects and (ii) Mg doping with optimal proportion. Temperature and pressure induced phase transitions among the various phases of VO_2 are analyzed by synchrotron XRD and Raman spectroscopic measurements. We argue a first order MIT prompts a second order SPT without any latent energy leading to SPT and MIT observed at the same time in VO_2. Pressure and temperature dependent XRD and Raman spectroscopic studies along with the calculations of bulk modulus and mode Gruneisen parameters further help in finding the order of phase transition and the contribution of phonon modes towards thermal expansion. We have also performed a systemic study of the polarized tip-enhanced Raman spectroscopy (TERS) to explore the crystallographic orientation of VO_2 single nanorods as well as to identify the corresponding Raman mode frequencies. The assignment of phonon frequencies corresponding to each lattice vibration is made possible by density functional theory (DFT) calculations of phonon density of states using PHONOPY model. The phonon mode responsible for the phase transition is also identified using the polarized and high-temperature TERS measurements.

3.2 Growth of VO$_2$:

3.2.1 Hole doping by the creation of native vacancy defects

VO$_2$ nano and micro structures were grown on crystalline (*c*-)Si(111) substrate by vapor transport process using atmospheric pressure chemical vapor deposition (APCVD) technique as described in chapter 2; section 2.2.2. Bulk VO$_2$ powder (Sigma-Aldrich, 99%) was used as a source, and commercial Ar (99.9%) was used as the carrier gas. The source was placed in a high pure (99.99%) alumina boat inside a quartz tube. The reaction chamber was kept in a furnace and was pre-evacuated up to 10^{-3} mbar. Substrates were kept 10 mm away from the source in two positions, (i) parallel and (ii) normal to the stream of carrier gas. The temperature of the quartz tube was programmed to rise to the optimized growth temperature (1150K) with a ramp rate of 15K min^{-1}. The synthesis was carried for 4 h with different optimized O exposure by flowing 10, 20, 30 and 40 sccm (sample, S1, S2, S3, and S4, respectively) of Ar (99.9%) containing $\approx 2 \times 10^5$ ppm of O.

3.2.2 Mg doping with optimal proportions

V$_{1-x}$Mg$_x$O$_2$ nano- and micro-structures were grown by vapor transport process on high pure (99.99%) alumina boat using mixed VO$_2$ powder and Mg powder (Sigma-Aldrich, 99%) as the source and Ar (99.9%) as the carrier gas. Substrates were kept at 10 mm away from the source in two positions, (i) parallel and (ii) normal to the stream of carrier gas. The synthesis was carried out at 1100K for 3 h. The concentration of the Mg dopant was controlled by changing the flow rate of the carrier gas. The synthesis was carried with the optimized flow of Ar (99.9%), e.g., 20, 40, 60, 80, and 100 sccm (samples, S6, S7, S8, S9, and S10, respectively) in the presence of Mg powder. Sample S5 was prepared with the flow of 20 sccm Ar, keeping other growth conditions same except the Mg powder.

3.3   Phase Confirmation of the Pristine Samples:

3.3.1   Morphological analysis

The FESEM images of the pristine samples are shown in figure 3.2. The samples grown on the substrates parallel to the stream of carrier gas was found to form nanorods; whereas, those for normal to the stream of carrier gas found grow as micro-crystals. The average width of the micro-crystals is 2 to 5 μm (Fig. 3.2a). The insets of figure 3.2a show magnified images of microrod of width ~2±0.5 μm. On the other hand, figure 3.2b shows the nanorods of average width ~ 100 to 200 nm. The insets of figure 3.2b show typical nanorod of diameter 150±5 nm. We have used the micro-rods for pressure and temperature dependent Raman and XRD studies and a typical single nanorod (insets of Fig. 3.2b) for the polarized TERS studies.
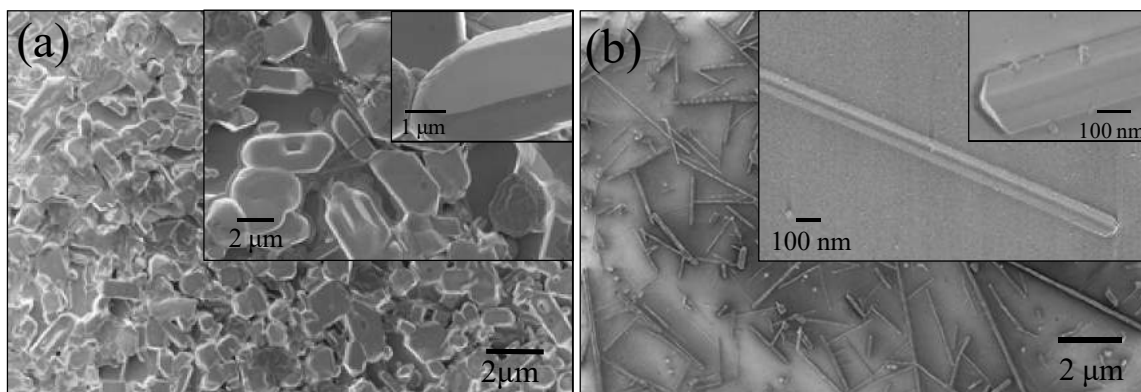
Figure 3.2 FESEM images of as-grown (a) micro and (b) nanorods. Insets show magnified images of micro and nanorods.

3.3.2   Structural analysis

Structural properties of the as-grown samples were studied using extreme conditions x-ray diffraction (ECXRD) in beamline-11, installed at Indus-2 synchrotron facility at Raja Ramanna Centre for Advanced Technology (RRCAT), India, with λ = 0.76089 Å using Si(111) channel-cut monochromator. A MAR345 image plate area detector was used to

collect two-dimensional (2-D) diffraction data. The sample to detector distance and the wavelength of the x-ray beam were calibrated using NIST standards of LaB6 and CeO_2. Calibration and conversion/integration of 2-D diffraction data to 1-D, intensity vs. 2θ, were carried out using the FIT2D software. The XRD pattern of the samples with different exposure to O is shown in figure 3.3a. In the case of samples S1 and S2, the diffraction peaks confirm the presence of monoclinic M1 phase of VO_2 (JCPDS # 04-007-1466) [27]. Whereas the diffraction peaks for samples S3 and S4 match with the T phase of VO_2 (JCPDS # 01-071-0289) [28].
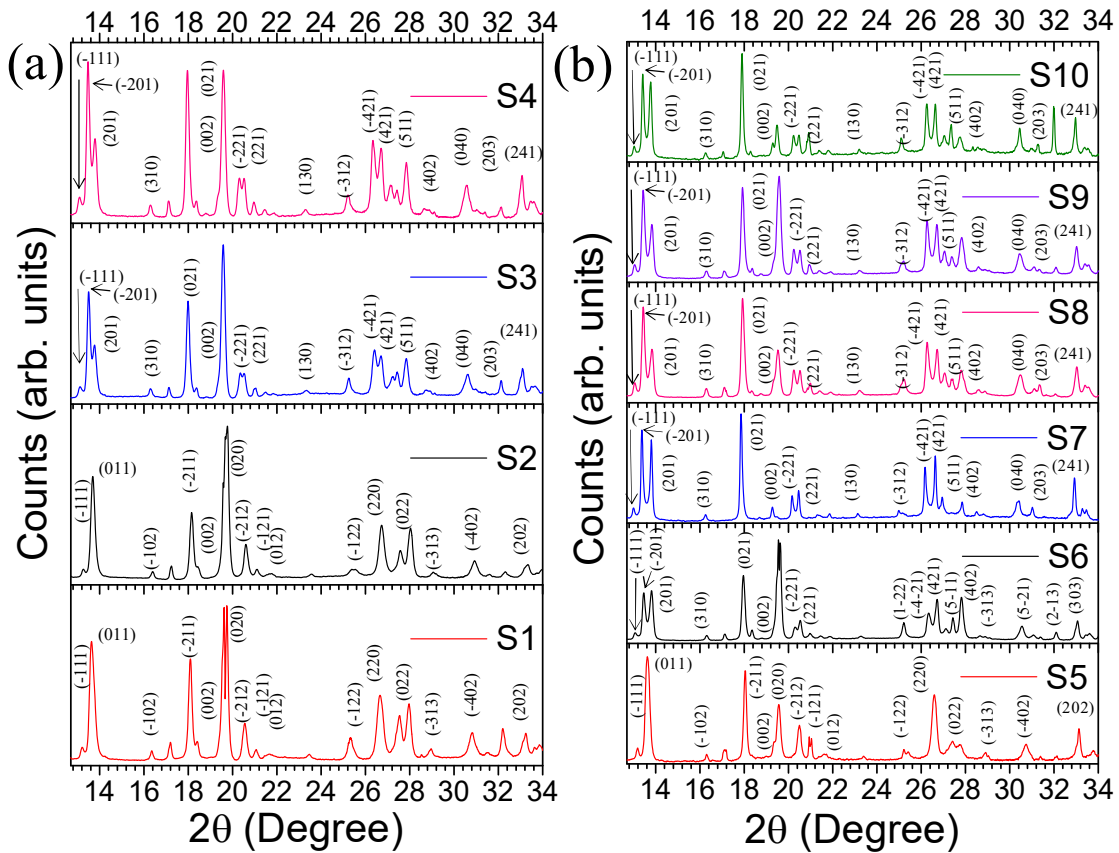
Figure 3.3 The XRD pattern of the pristine samples (a) S1, S2, S3 and S4 grown via hole doping and (b) S5 (control without Mg), and S6, S7, S8, S9 and S10 grown via Mg doping. The crystallographic (*hkl*) planes of the corresponding phases are indicated.

The x-ray crystallographic studies of the samples with different Mg dopant are shown in figure 3.3b. In sample S5, the diffraction peaks confirm the presence of monoclinic M1 phase of VO_2 (JCPDS # 04-007-1466) [27]. Whereas the diffraction peaks for sample S6 resemble the T phase of VO_2 (JCPDS # 01-071-0289) [28]. The samples S7 to S10 are found out as the M2 phase of VO_2 (JCPDS # 00-033-1441) [29].

While focusing on the diffraction peaks at lower 2θ values, the diffraction peak at $2\theta=13.67°$ represents the (011) plane corresponding to monoclinic M1 phase (equivalent to $(110)_R$ plane) of VO_2 for samples S1 and S5 [27]. In sample S4, the diffraction peak is observed at $2\theta=13.69°$, indicating a compression in (011) lattice plane. Compression in one direction generally is coupled to an expansion in the perpendicular direction. Thus, the compression in $(011)_{M1}$ plane leads to tensile strain along the c_R axis. In the case of samples S3, S4 and S6, two diffraction peaks observed at $2\theta = 13.47°$ and $13.81°$ may correspond to (-201) and (201) planes of T phase of VO_2. Similarly, for samples S7 to S10, the diffraction peaks equivalent to (-201) and (201) planes of the M2 phase of VO_2 are observed at around $2\theta = 13.38°$ and $13.84°$. The twin peaks in samples S6 to S10 are equivalent planes of $(110)_R$ phase, which are responsible for twin crystalline formation. The T and M2 phases of VO_2 are reported as the strained (tensile strain along the rutile c_R axis) stage for the M1 phase of VO_2 [11, 30]. In the present study, the role of substrate in introducing strain in these samples is ruled out as they all are synthesized on the same substrate [31]. Since, the samples S1 to S4 were grown for different percentage of the flow of Ar (containing $\approx 2\times 10^5$ ppm O); there would be a departure from perfect stoichiometry in VO_2, because of different amounts of O present in the carrier gas. Presence of excess O in the sample S4 is more probable, as it grows with the highest amount of O exposure at high temperature (1150K). We were unable to

stabilize M2 phase of VO_2 by varying O stoichiometry, as with the increase in Ar flow rate above 40 sscm the samples stabilized in the V_2O_5 phase. However, for the samples grown in the presence of Mg powder, with a different percentage of the flow of Ar, there would be a different percentage of Mg dopants present in the samples. The dopants can introduce strain in the sample and help in stabilizing the M2 phase of VO_2.

3.3.3 Raman spectroscopic analysis

Raman spectroscopic analysis was carried out to obtain further information about the phases present in the as-grown samples. The Raman spectra for the samples collected at room temperature are depicted in figure 3.4. Eighteen Raman-active phonon modes are predicted by Group theoretical analysis for all low-temperature phases of VO_2 (for M1: $9A_g+9B_g$, and for M2 and T: $10A_g+8B_g$) at Γ point with different symmetries [6,16].

However, we observed twelve vibrational modes for samples S1 and S5 (Fig. 3.4). Observed Raman modes at 141, 190(A_g), 225(A_g), 258 (either A_g or B_g,; A_g/B_g), 307(A_g/B_g), 335(A_g), 390(A_g/B_g), 440(A_g/B_g), 497(A_g/B_g), 611(A_g), 665(B_g), 823(B_g) cm^{-1} in case of sample S1 (Fig. 3.4a) confirms the presence of pure M1 phase of VO_2 [32,33]. All Raman modes in case of sample S1, except 141, 440 and 826 cm^{-1}, are blue shifted by an amount of ~2-3 cm^{-1} in sample S2. In case of sample S3, we observed thirteen Raman modes at 130 (A_g), 195 (A_g), 223 (A_g), 262 (A_g/B_g), 306 (A_g), 340 (A_g), 381 (A_g/B_g), 403 (A_g/B_g), 440 (A_g/B_g), 501 (A_g/B_g), 578, 622 (A_g), and 828 (B_g) cm^{-1}. In case of samples S4 and S6, thirteen mode frequencies are observed at 121, 201(A_g), 228(A_g), 267(A_g/B_g), 304(A_g), 343(A_g), 374(A_g/B_g), 413(B_g), 445(A_g/B_g), 503(A_g/B_g), 572(A_g), 636(A_g), and 828(B_g) cm^{-1} (Fig. 3.4), which resembles the reported data for T phase of VO_2 [6,19]. For samples S7 to S10, we observed eleven Raman modes at ~ 50, 203 (A_g), 217(A_g), 229(A_g), 273(A_g/B_g), 297(A_g),

$341(A_g)$, $432(A_g/B_g)$, $454(A_g/B_g)$, $651(A_g)$, and $831(B_g)$ cm^{-1} (Fig. 3.4b), which exactly resembled the reported M2 phase of VO$_2$ [6,19].
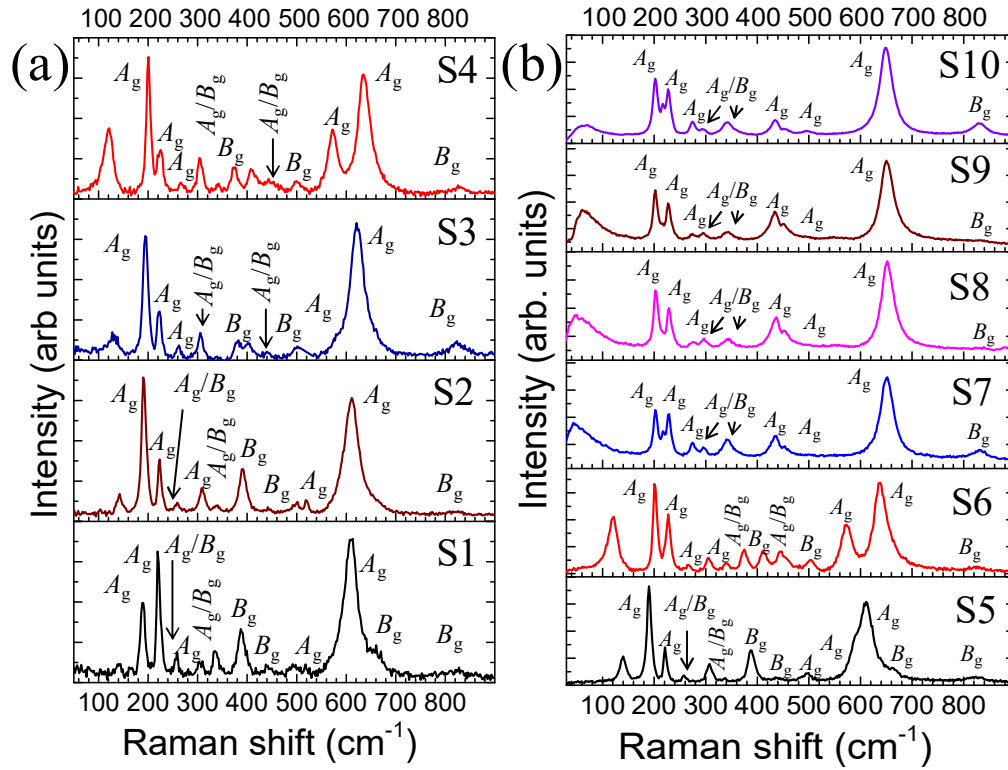
Figure 3.4 Raman spectra with proper symmetry notations of the pristine samples (a) S1, S2, S3 and S4 grown via hole doping and (b) S5 (control without Mg), and S6, S7, S8, S9 and S10 grown via Mg doping, collected at room temperature.

Raman spectroscopic studies confirm the presence of all the three different phases of pure VO$_2$, i.e., M1 phase in samples S1, S2, and S5, T phase in samples S3, S4, and S6, and M2 phase in samples S7, S8, S9, and S10.

3.4   Structural Phase Transition in VO$_2$:

3.4.1 Spectroscopic study of structural phase transition as a function of pressure

As metastable M2 phase is the maximum strained (tensile) phase of VO$_2$, compressive stress may lead to a structural transition to a stable phase of VO$_2$. To investigate the nature of

structural changes with stress, we performed the Raman spectroscopic studies at room temperature on samples S7, S8 and S9 (stabilized in M2 phase of VO₂) as a function of hydrostatic pressure.
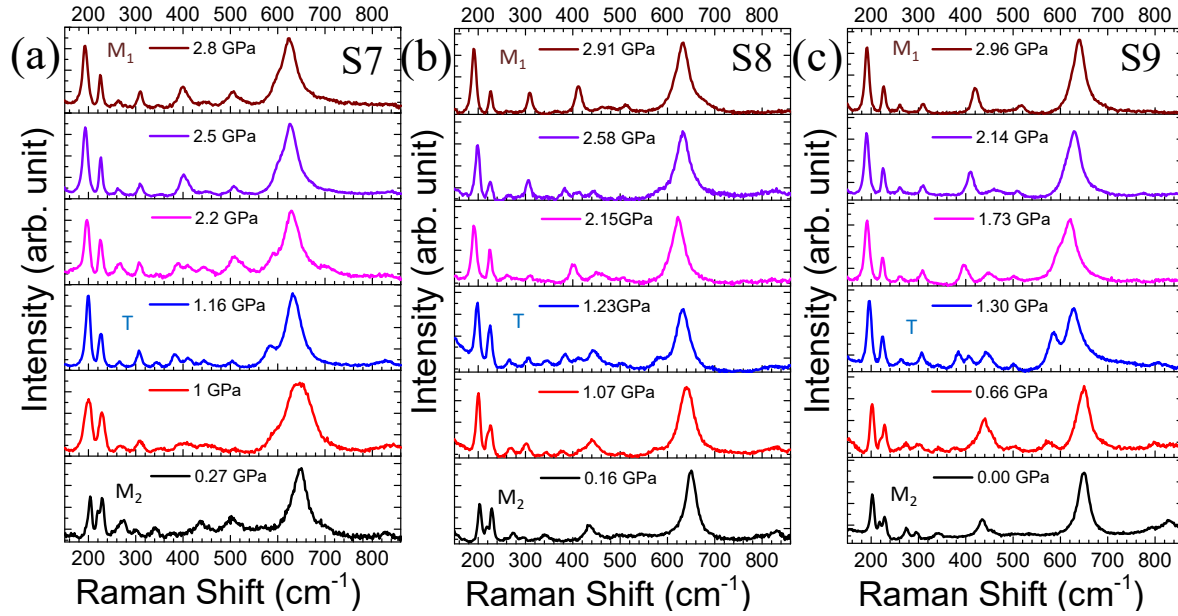
Figure 3.5 Raman spectra of samples (a) S7, (b) S8, and (c) S9 as a function of increasing hydrostatic pressure. The phases of VO₂ at the corresponding pressure are indicated.

At atmospheric pressure, the samples S7, S8, and S9 show Raman spectra corresponding to the M2 phase of VO₂ [6,19] (Fig. 3.5). With increasing hydrostatic pressure to 1.16 GPa the Raman spectra show peaks at 121, 201(A_g), 225(A_g), 267(A_g/B_g), 304(A_g), 343(A_g), 374(A_g/B_g), 409(A_g/B_g), 440(A_g/B_g), 501(A_g/B_g), 572(A_g), 636(A_g), and 828(B_g) cm^{-1} in sample S7, which resemble the reported data for the T phase [6,19]. With further increase in pressure to 2.8 GPa observed Raman bands at 140(A_g), 190(A_g), 221(A_g), 258 (A_g/B_g), 307(A_g/B_g), 335(A_g), 391(A_g/B_g), 440(A_g/B_g), 494(A_g/B_g), 621(A_g), 665(B_g), 823(B_g) cm^{-1} confirm the presence of pure M1 phase of VO₂ [32,33] (Fig. 3.5a). The structural phase transition from M2 to T and T to M1 proves the structural relaxation of the strained M2 phase stabilized by

Mg doping. For the sample S8, the structural transitions from M2 to T phase and T to M1 phase are observed at 1.23 and 2.91 GPa, respectively (Fig. 3.5b). The same for sample S9 is observed at 1.30 and 2.96 GPa, respectively (Fig. 3.5c). In the pressure releasing cycle, all three samples show reversible transitions from M1 $\rightarrow$ T $\rightarrow$ M2 with negligible hysteresis. The Raman spectra for sample S7 with complete pressure cycle is shown in figure 3.6a. As samples S8 and S9 are doped with higher percentages of Mg, they are expected to be under more tensile strain than sample S7, and the transition pressure is expected to be high according to the phase diagram of VO_2 [11]. We have plotted the Raman frequency shift with pressure. In the ω vs. P diagram (Fig. 3.6b), distinct changes are clearly observed in the spectra above 1.6 GPa for sample S7; (i) the Raman band at 218 cm^{-1} disappears, (ii) five new bands appear at 124, 378, 414, 504 and 576 cm^{-1}, (iii) the bands at 297, 341, and 435 cm^{-1} show blue shift, and (iv) the Raman bands at 203, 228, 273, 651, and 831 cm^{-1} show red shift. These are clear indications of a structural phase transformation from M2 to T phase of VO_2 [6,19]. With an increase in pressure ~2.8 GPa, again several changes are observed in the Raman spectra (Fig. 3.6b); (i) the bands at 341, 415, and 576 cm^{-1} disappear, (ii) the bands at 127, 409, 504, 576, and 636 cm^{-1} show red shift, and (iii) the 440 cm^{-1} band shows a blue shift. These changes indicate another structural phase transition from T to M1 phase of VO_2 [32,33]. The Raman band observed at 651 cm^{-1} arises due to V-O stretching vibration. The stretching mode is observed to shift from 651 to 636 cm^{-1} at 1.6 GPa due to transition from M2 to T phase and 636 to 621 cm^{-1} due to transition from T to M1 phase indicating the length of V-O bond to be relaxed from strain. Raman mode at 203 and 229 cm^{-1} correspond to the V-V vibration along and perpendicular to the c_R axis, respectively [34]. The observed shift of 2.95 cm^{-1}/GPa for the Raman mode at 203 cm^{-1} larger than that of 0.68 cm^{-1}/GPa for

229 cm^{-1} with pressure confirms that the distortion along the c_R axis is responsible for the phase transition. The Raman mode frequencies vary similarly with pressure for the samples S8 and S9 (not shown in the thesis), except for slightly higher values of transition pressure.
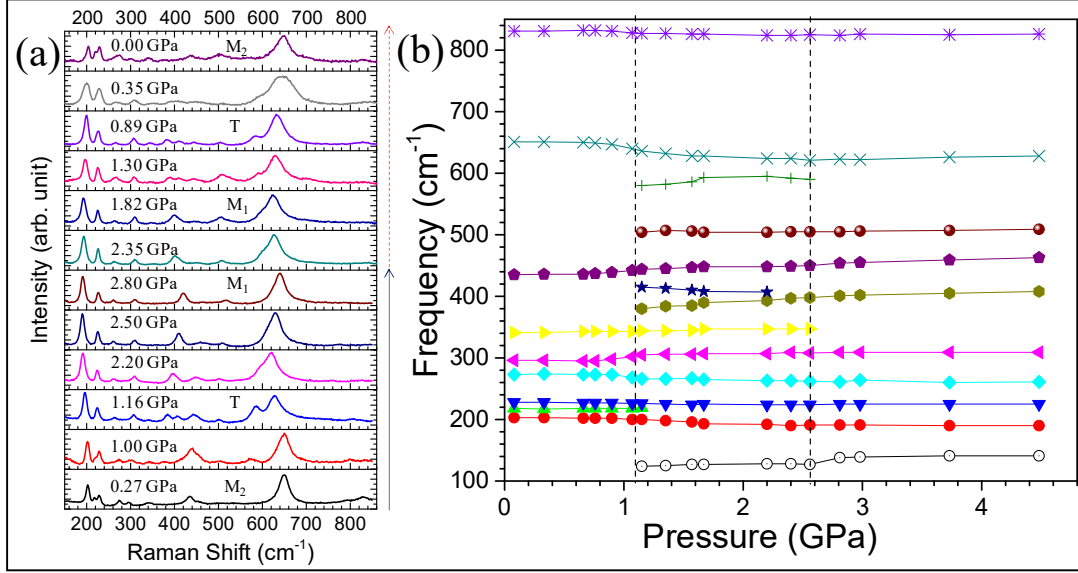
Figure 3.6 (a) Raman spectra of sample S7 as a function of hydrostatic pressure. The phases of VO_2 at corresponding pressure are indicated. Solid arrow and dashed arrow indicate increasing and decreasing pressure, respectively. (b) Raman mode frequency vs. pressure of sample S7. Changes in the spectral frequencies are recorded at 1.6 GPa and 2.8 GPa, signifying a phase transformation.

We have calculated the isothermal mode Gruneisen parameter [$\gamma_{iT} = (K/\omega_i)(d\omega_i/dP)|_T$; where K is the bulk modulus obtained from high-pressure XRD measurements described later] to find out the contribution from implicit anharmonicity of the Raman modes for sample S7. Table 3.1 lists the mode frequencies (ω_i) with the corresponding γ_{iT} with less than 10% error. Positive and negative values of Gruneisen parameters indicate the corresponding Raman modes contributing positively and negatively to thermal expansion, respectively [35]. The negative values of γ_{iT} for a few Raman modes in the M2 phase become zero or positive in the M1 phase indicating the complete relaxation of the phase from the strain.

Table 3.1 Frequencies (ω_i) and Gruneisen parameters (γ_{iT}) of Raman modes of sample S1.

M2		T		M1	
ω_i	γ_{iT}	ω_i	γ_{iT}	ω_i	γ_{iT}
203	-2.09	121	1.95	140	1.24
217	0.64	201	-3.58	190	0
229	-1.23	225	-0.87	221	0.15
273	-0.52	267	-1.48	258	0.25
297	2.86	304	0.82	307	0
341	0.83	343	0.71	335	0
432	2.27	374	4.27	391	1.44
651	-2.39	409	-1.56	440	1.81
831	-0.68	440	1.36	505	0.61
-	-	501	0.16	621	0.74
-	-	572	1.97	665	-
-	-	636	-1.86	823	0.08
-	-	828	-0.23	-	-

3.4.2 Crystallographic study of structural phase transition as a function of pressure

To confirm the structural phase transition, we performed XRD studies at room temperature as a function of hydrostatic pressure (Fig. 3.7). In the absence of any pressure, all the samples maintain the M2 phase of VO_2. Whereas, with an increase in pressure to 1.82 GPa in sample S7, the XRD pattern resembles the T phase of VO_2 (JCPDS # 01-071-0289) [28]. With further increase in pressure to 3.42 GPa, the XRD pattern resembles the M1 phase of VO_2 (JCPDS # 04-007-1466) [27] (Fig. 3.7a). This is similar as observed from high pressure Raman study. (Fig. 3.5a). In the case of sample S8, the structural phase transitions from M2 to T and T to M1 are observed at 1.85 and 3.85 GPa, respectively (Fig. 3.7b). The phase transition pressure for M2 to T and T to M1 in sample S9 are observed at 1.91 and 4.00 GPa,

respectively (Fig. 3.7c). The XRD patterns for these samples are compared after the pressure is released, and the initial structure is found to be recovered (Fig. 3.8a).
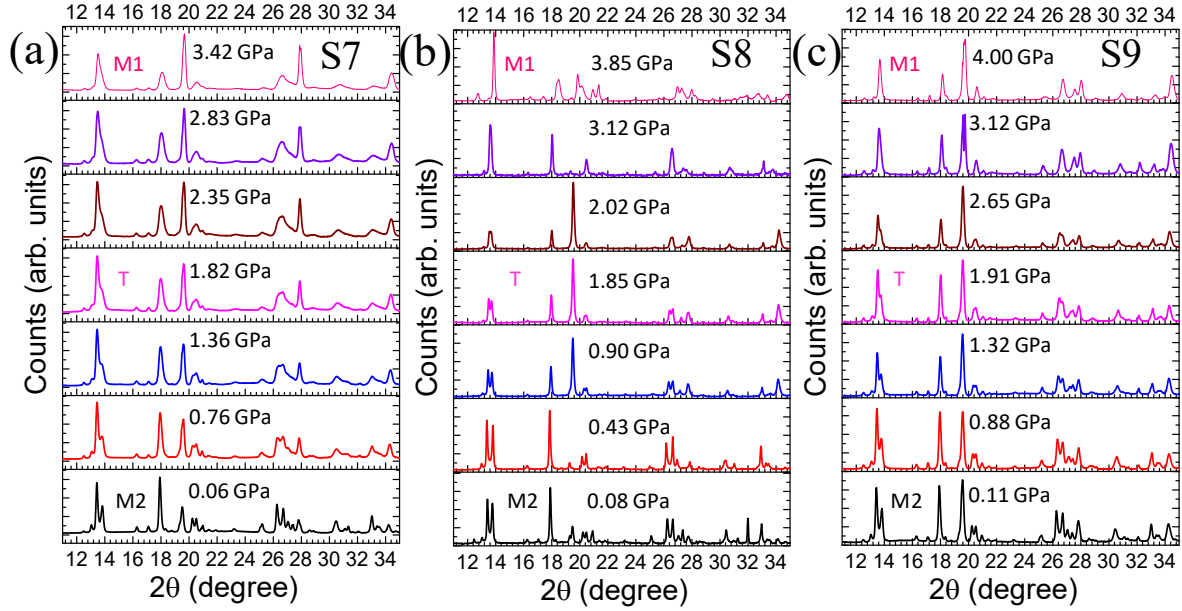
Figure 3.7 XRD pattern for samples (a) S7, (b) S8, and (c) S9 as a function of increasing pressure. The phases of VO_2 at corresponding pressure are indicated.

The structural transition from T to M1 is reported as the first order transition by Mitrano *et al*. [36] because of the observed mixed-phase behavior in XRD and Raman studies. They also reported that the normalized unit-cell volume did not show any discontinuity around the phase transition, which contradicted their claim of the first order phase transition. To understand the nature of the structural phase transition, we have plotted the normalized volume as a function of pressure (Fig. 3.8b). The normalized volume varies continuously with pressure, which resembles previous reports [36,37].
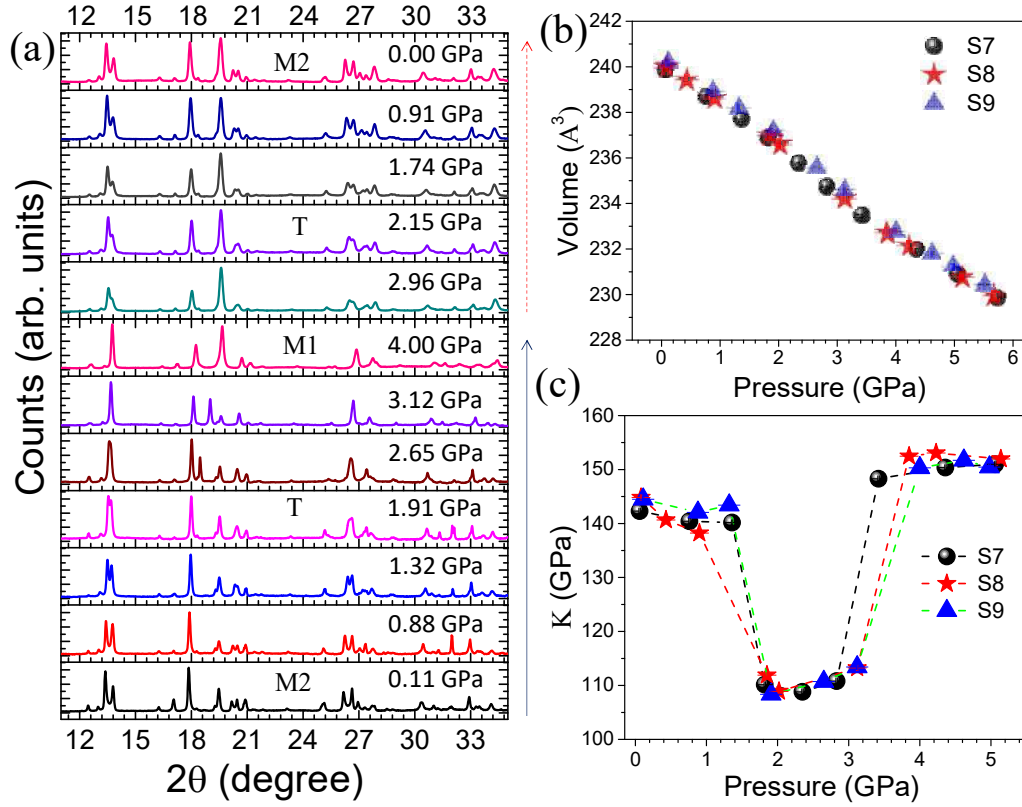
Figure 3.8 (a) XRD pattern for sample S7 as a function of hydrostatic pressure. The phases of VO₂ at corresponding pressure are indicated. Solid arrow and dashed arrow indicate increasing and decreasing pressure, respectively. Pressure dependence of the (b) unit-cell volume and (c) bulk modulus for samples S7, S8, and S9.

Considering the thermodynamic parameter volume (V) as the order parameter of the structural transition, we have calculated the first derivative of volume, bulk modulus $K = V(\mathrm{d}P/\mathrm{d}V)|_P$. The K vs. P curve shows discontinuity around the phase transition (Fig. 3.8c). The value of K for the M2 phase is ~ 140 GPa, which reduces to ~ 110 GPa for the T phase and again increases to ~150 GPa for the M1 phase of VO₂. We also found the values of bulk modulus, K from the pressure vs. volume plot in the individual phase fitted to a third order Birch-Murnaghan equation [38] (Fig. 3.9).
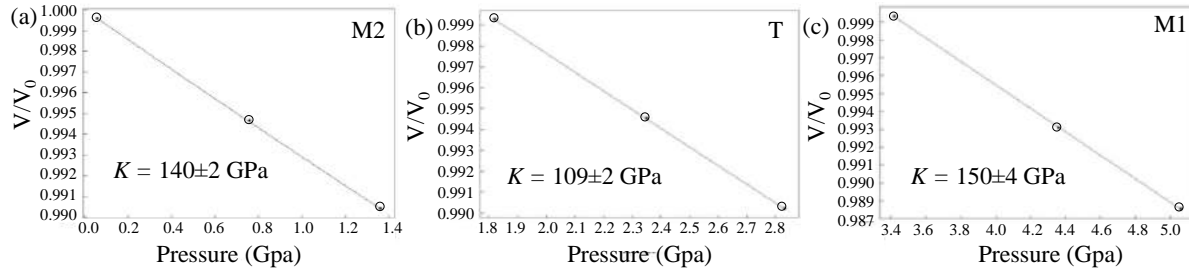
Figure 3.9 Pressure vs. reduced volume of sample S7 for (a) M2, (b) T, and (c) M1 phase. Data fitted to a third order Birch-Murnaghan equation result in $K = 140 \pm 2$ GPa for M2 phase, $K = 109 \pm 2$ GPa for T phase and $K = 150 \pm 4$ GPa for M1 phase.

The bulk modulus values were found out as 140 ± 2, 109 ± 2, and 150 ± 4 GPa for M2, T, and M1 phase, respectively. The values of K match well with the reported values [36]. We have also calculated the bulk modulus using electronic density functional theory, as implemented in the Vienna *ab initio* simulation package (VASP). The structure was first relaxed by relaxing the cell volume, then the cell shape and at last by the positions of atoms in at least four cycles. Moreover, minimum two more cycles were run using the converged *k*-grid and plane-wave energy cutoff to obtain the correct ground-state relaxed atomistic configurations, till the total energies converged to a precision of less than 10^{-10} eV/atom and the Hellmann-Feynman forces became less than 10^{-5} eV/Å. The bulk modulus for all the three phases of VO_2 was calculated using ELATE software using the Voigt, Reuss, and Hill methods. The values for bulk modulus were estimated as 257 ± 3 GPa for M2, 125 ± 4 GPa for T, and 254 ± 2 GPa for M1 phase of VO_2. The deviation of the estimated values of bulk modulus from the experimentally observed values may be because of the inherent non-stoichiometry in the oxide samples, and limitation of the methodology adopted in the present calculation. The calculated and experimentally observed values of bulk modulus for M1 and M2 phases are close to each other, whereas it decreases in the case of T phase. The volume per formula unit

is large in case of T phase, and thus the lesser value of bulk modulus is expected than that for M1 and M2 phases of VO_2. In view of these results, the structural phase transition from M2→T and T→M1 is seen as a continuous second order transition. Our observation supports the negligible latent heat value for M2→T and T→M1 transition measured by Pouget *et al.* [39] using differential scanning calorimetry. The observed mixed-phase behavior in some reports [40,41] may arise due to the coexistence of grains from both the phases with a variation of strain.

3.4.3 Spectroscopic study of structural phase transition as a function of temperature

To study the phase transition as a function of temperature, we have carried out the temperature-dependent Raman spectroscopy for the samples with different Mg concentration. Figure 3.10a shows the Raman spectra for sample S7 with increasing and decreasing temperature.
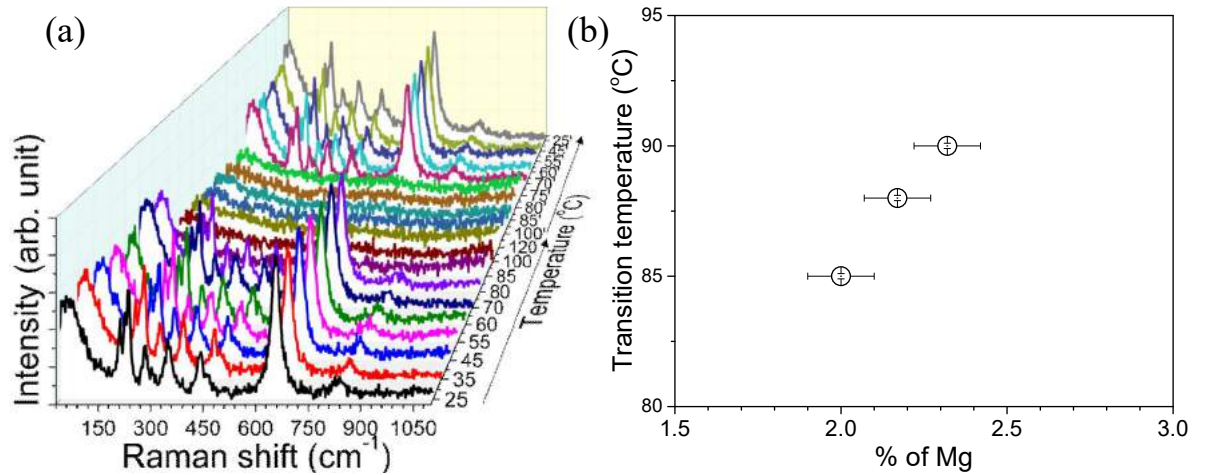
Figure 3.10 (a) Raman spectra for sample S7 as a function of increasing and decreasing temperature. (b) Variation of transition temperature for the samples S7, S8, and S9 with different Mg concentration.

All the Raman modes disappeared at 85 °C (358K), confirming the transition to the metallic R phase [31]. With a decrease in temperature, the Raman modes reappear with a hysteresis of 15 °C confirming the reversibility of the phase transition. Samples S8 and S9 also followed the same trend with a slight increase in the transition temperature. The transition temperatures for samples S8 and S9 are recorded as 88 (361K) and 90 °C (363K), respectively. The variation of transition temperature with Mg concentration is shown in figure 3.10b. The atomic percentage of Mg for the samples S7, S8, and S9 are calculated from x-ray photoelectron spectroscopy described in chapter 4.

To understand the electronic and structural contribution to the phase transition, we have plotted the shift in Raman frequency with temperature for sample S7 (Figure 3.11). All the Raman mode frequencies exhibit red shift with increasing temperature.
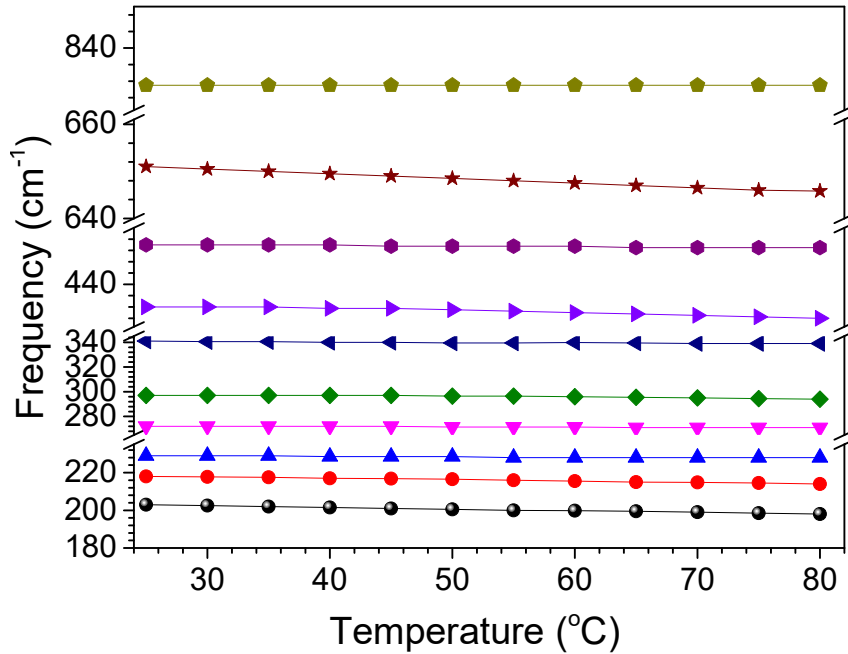
Figure 3.11 Raman mode frequency vs. temperature of sample S7.

The maximum frequency shift is observed for the Raman band at 203 cm^{-1} (V-V vibration) and 651 cm^{-1} (V-O vibration) indicating the reconstruction of V-V and V-O length along the

c_R axis [34]. We have calculated the isobaric mode Gruneisen parameter [γ_{iP} = (-$1/\alpha\omega_i)(d\omega_i/dT)|_P$]; where α (= 6×10^{-6} K^{-1}) is the thermal expansion coefficient obtained from high-temperature XRD measurements, which is close to the reported value of 5×10^{-6} K^{-1} [42] to find out the contribution from explicit/true anharmonicity of the Raman modes for sample S7 [43]. We also measure the ratio (η) of γ_{iT} and γ_{iP} to find out the relative contribution of implicit (volume dependent) and explicit (phonon-phonon interaction) anharmonicity. Table 3.2 lists the mode frequencies (ω_i) with the corresponding γ_{iP} and γ_{iT} values along with η (=$\gamma_{iT/}\gamma_{iP}$) value [43].

Table 3.2 Frequencies (ω_i) and relative contribution of isothermal (γ_{iT}) and isobaric (γ_{iP}) mode Gruneisen parameters of Raman modes for sample S7.

ω_i (cm^{-1})	γ_{iT} $(K/\omega_i)(d\omega_i/dP)|_T$	γ_{iP} $(-1/\alpha\omega_i)(d\omega_i/dT)|_P$	η (=$|\gamma_{iT/}\gamma_{iP}|$)
203	-2.1(±0.2)	74.6(±0.5)	0.03
217	0.6(±0.05)	55.6(±0.5)	0.01
229	-1.2(±0.1)	13.2(±0.2)	0.09
273	-0.5(±0.05)	11.1(±0.2)	0.05
297	2.9(±0.3)	30.6(±0.5)	0.09
341	0.8(±0.1)	17.8(±0.2)	0.04
432	2.3(±0.2)	28.0(±0.3)	0.08
651	-2.4(±0.2)	24.2(±0.2)	0.10
831	-0.7(±0.05)	3.6(±0.1)	0.09

For all the Raman modes, the value of η<<1, which implies most of the contribution is due to explicit anharmonicity. A similar trend is observed for samples S8 and S9 also (not shown in the thesis). From the above observations, it is clear that the frequency shift is dominated by phonon-phonon interaction.

3.4.4 Crystallographic study of structural phase transition as a function of temperature

We also carried out the temperature-dependent XRD measurements to examine the structural changes around MIT. Figure 3.12 shows the XRD patterns of sample S7 with increase and decrease in temperature. At room temperature (25 $^{\circ}$C), the samples maintain the M2 phase of VO_2 [27], whereas, with an increase in temperature to 70 $^{\circ}$C, the coexistence of both M2 and R phase of VO_2 is observed [44] (Figure 3.12a). With further increase in temperature to 85 $^{\circ}$C (358K), the XRD pattern resembles the pure R phase of VO_2 [45] confirming the structural phase transition. With a decrease in temperature, the sample returns to its original M2 phase with a hysteresis of 25 $^{\circ}$C.
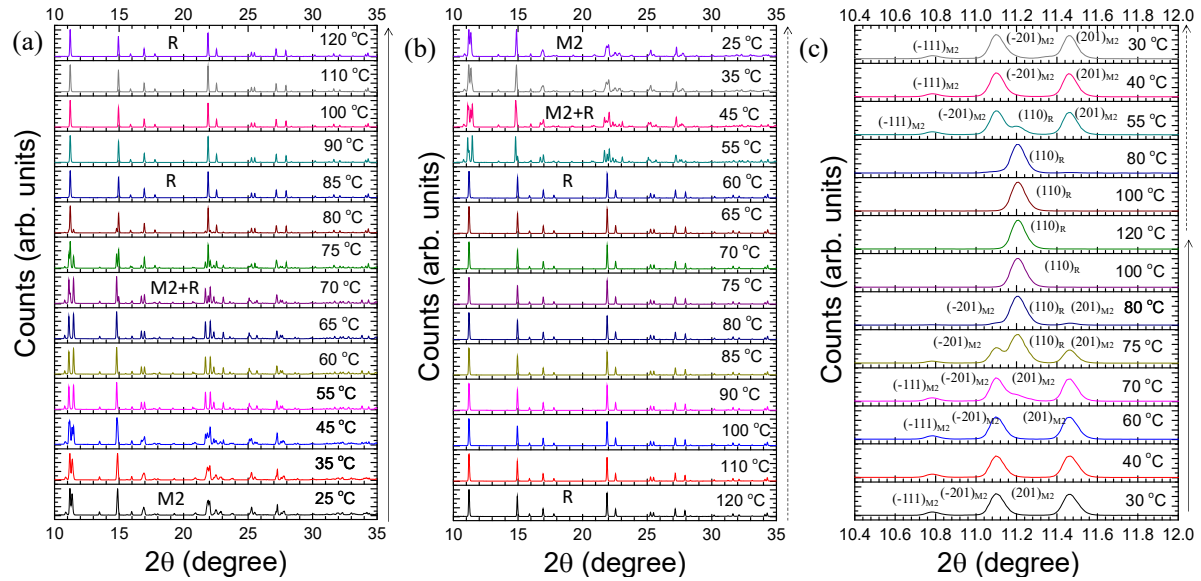
Figure 3.12 XRD pattern for sample S7 as a function of (a) increasing and (b) decreasing temperature. The phases of VO_2 at corresponding transition temperature are indicated. (c) Zoomed view of the XRD pattern at lower 2θ values with (*hkl*) indices showing the coexistence of M2 and R phase of VO_2. Solid and dashed arrows represent the increase and decrease in temperature, respectively.

We have plotted the diffraction pattern at lower 2θ values (Fig. 3.12c) with proper (*hkl*) notations to have a clear view of the coexistence of phases. The coexistence of both M2 and R phase for the temperature range 70 to 80 °C (343 to 353K) (increase in temperature) and 45 to 55 °C (318 to 328K) (decrease in temperature) confirms the M2→R transition as first order (Fig. 3.12). Samples S8 and S9 also followed the same trend with a slight increase in transition temperature (Fig. 3.13).
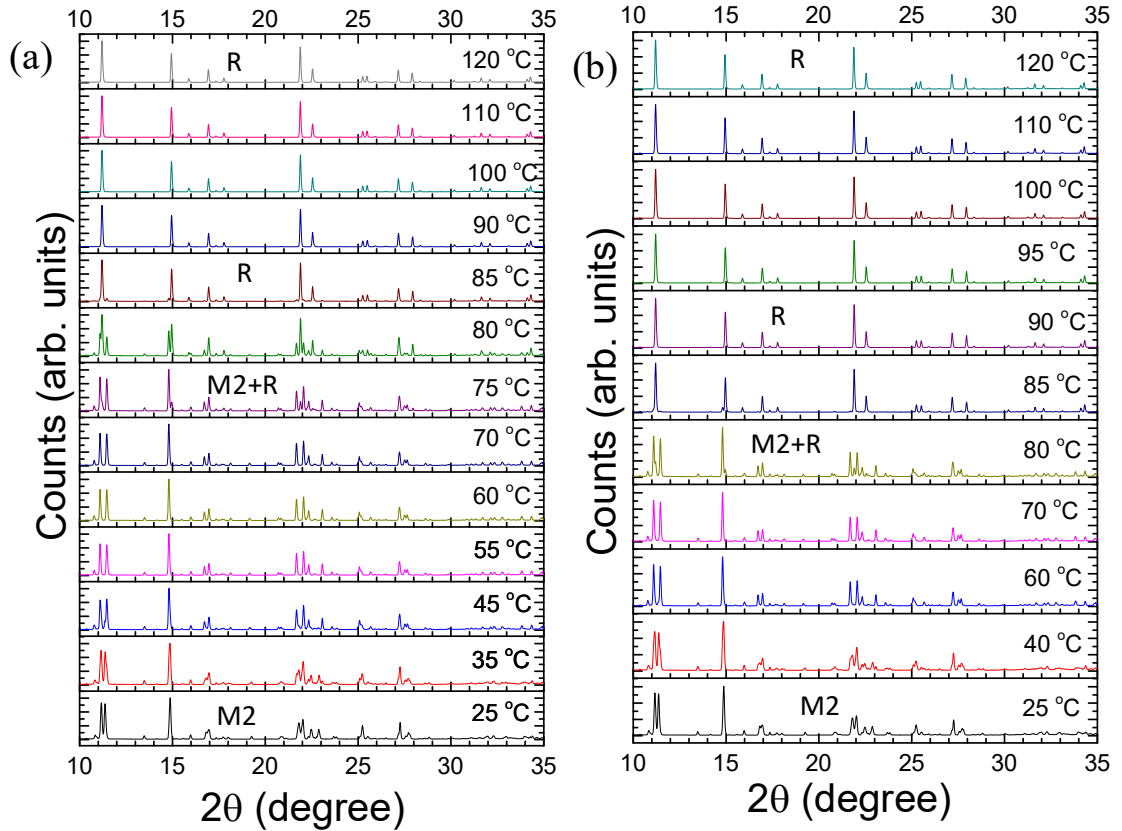
Figure 3.13 XRD pattern for samples (a) S8 and (b) S9 with temperature. The phases of VO$_2$ at corresponding transition temperature are indicated.

Thus, our observation also supports high latent heat value (770 cal/mole) for the M2→R transition measured by Pouget *et* al. [42] using differential scanning calorimetry as an indicative of first order phase transition.

3.5   Origin of Structural Phase Transition:

In general, phonons play a significant role in structural transitions. The role of phonons in the phase transition of VO_2 has been discussed by Yuan *et al.* [46], predicting that the breaking of the V-V bonds lead to an immediate electronic phase transition from an insulating to a metallic state while the crystal lattice remained monoclinic in shape. Whereas, Kim *et al.* [5] reported that the metallic R phase of VO_2 should not occur simultaneously with the first order MIT at ~ 340K. They considered a monoclinic and correlated metal (MCM) phase between the MIT and the SPT supporting the Mott phenomenon [47]. To understand the origin of the SPT, we have carried out TERS study on a typical horizontally lying VO_2 single nano-rod. Polarized Raman spectroscopy not only confirms the crystalline phase and crystallographic orientation of the sample but also helps in understanding the lattice dynamics by finding the mode symmetries. As TERS is accomplished with directional field enhancement, the identification of corresponding Raman mode frequency responsible for the structural phase transition is made possible using polarized and high-temperature TERS studies substantiated by DFT calculations for the phonon density of states.

3.5.1   Crystalline phase and crystallographic orientation of the VO_2 nanorod

We have chosen a typical nanorod of diameter ~150±5 nm (inset of Fig. 3.2b) for the polarized TERS study. The x-ray crystallographic structural study of nanorods using Cu K_α radiation source (λ=1.5406 Å) shows (011) plane analogous to the M1 phase of VO_2 (Fig. 3.14a) (JCPDS # 04-007-1466) [27]. The single peak at 27.98° in the GIXRD spectra suggests a preferential orientation of the VO_2 nanorods with the (011) plane parallel to the surface of the substrate. Observation of Raman modes at 141, 190(A_g), 225(A_g), 258 (either

A_g or B_g; A_g/B_g), 307(A_g/B_g), 335(A_g), 390(A_g/B_g), 440(A_g/B_g), 497(A_g/B_g), 611(A_g), 665(B_g),

823(B_g) cm^{-1} (Fig. 3.14b) confirm the presence of pure M1 phase of VO$_2$ [32,33].
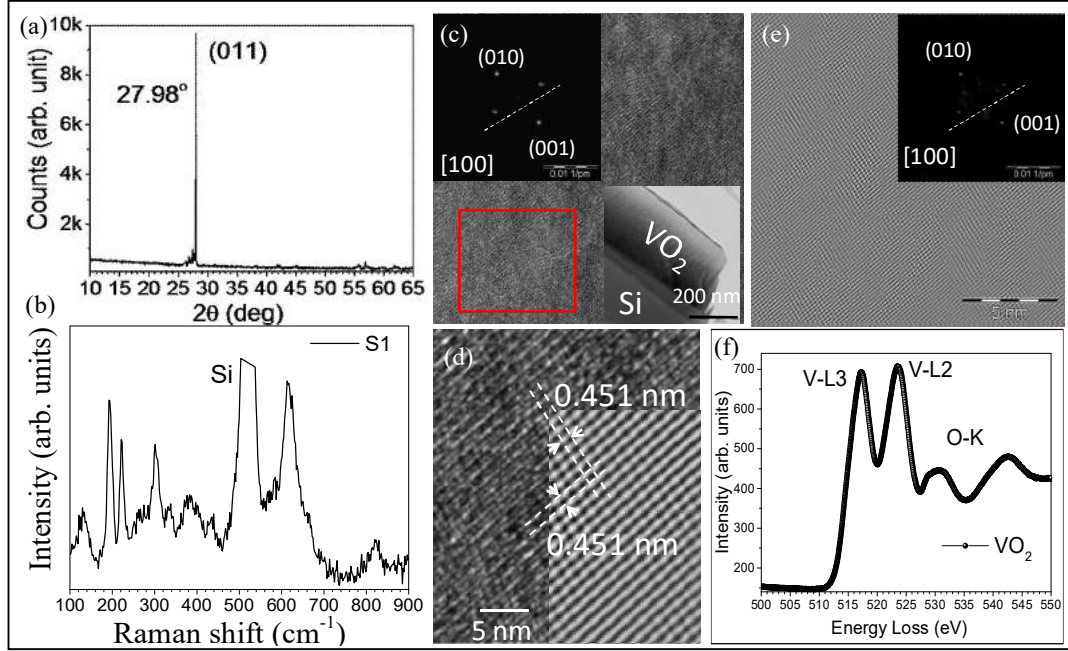
Figure 3.14 (a) GIXRD spectrum of the as-grown sample indicating crystalline (*hkl*) planes of (011) corresponding to the M1 phase of VO$_2$. (b) Raman spectrum collected from the single nanorod on Si substrate (c) The TEM image of a cross-section plane perpendicular to the VO$_2$ nanorod growth direction. Upper inset of (c) shows the SAED pattern of the selected portion (red box) with zone axis [100]. Lower inset of (c) shows the low magnification TEM image of the interface between VO$_2$ and Si substrate. (d) The HRTEM image of the VO$_2$ crystal taken along [100] zone axis. (e) FFT pattern (inset of 3(c)) and IFFT image of the nanorod indexed to the monoclinic phase of VO$_2$ with [100] zone axis. (f) EELS spectra of the VO$_2$ nanorod.

The TEM studies are performed for further confirmation of the crystalline orientation of VO$_2$ nanorod. Figure 3.14c shows the TEM image taken from the cross-section plane perpendicular to the growth direction of the VO$_2$ nanorod. A typical low-magnification TEM micrograph is shown (lower inset of Fig. 3.14c) for the interface between VO$_2$ and Si

substrate. The TEM image and corresponding selected area electron diffraction (SAED) pattern (inset of Fig. 3.14c) is indexed to the monoclinic phase of single-crystal VO_2 with zone axes along [100]. The HRTEM image (Fig. 3.14d) shows interplanar spacing of 0.451 nm corresponding to the inter-plane spacing of the (010) and (001) planes of monoclinic VO_2 crystals [48]. The inverse fast Fourier transformed (IFFT) image (Fig. 3.14e) of the FFT pattern (inset of Fig. 3.14e) of the selected area (in the red box of Fig. 3.14c) shows the same interplanar spacing of 0.451 nm (inset of Fig. 3.14d). The Fourier transformed clear lattice fringes confirm the good crystallinity of the nanorod. It is therefore confirmed that the nanorod is oriented by (011) face and its axis is along the $[100]_{M1}$ direction. Figure 3.14f shows a typical EELS spectrum of the nanorod. The unfilled $3d$ bands of V are strongly hybridized with O $2p$ bands in vanadium oxides. Therefore, both the V-$L_{2,3}$ edges and the O-K edge are expected to reflect the V oxidation state. The first two strong peaks around 517 and 523 eV are assigned as V-$L3$ and V-$L2$, and are attributed to excitation from V $2p_{3/2}$ and V $2p_{1/2}$ to unoccupied V $3d$ states, respectively. The doublets around 530 - 542 eV are attributed to the excitations from O $1s$ to hybridized O $2p$ - V $3d$ bands with t_{2g}, and, e_g symmetries, respectively [49,50]. The two well-separated O-K peaks confirm the oxidation state of V as +4 [51]. The EELS spectrum provides an estimation of ~1:2 for the atomic ratio of V/O, which suggests that the nanorods are VO_2 [52].

3.5.2 Polarized TERS study on the VO_2 nanorod

TERS is capable of enhancing the spatial resolution in the sub-diffraction limit [53,54]. The TERS study mainly utilizes the advantages of optical confinement using plasmonic metal nanostructures, especially Au and Ag [55,56]. The major reports based on TERS studies are mainly focused on covalently bonded materials such as bio-organic or carbon molecules with

an enhancement factor (EF) of eight orders [53,54]. However, it is being used extensively for characterizing non-carbonaceous materials, including partially ionic compounds [57-59]. Moreover, as the TERS is accomplished with directional field enhancement, the identification of corresponding phonon mode frequency is also made possible using polarized measurement [60].

The schematic of the TERS technique used for the investigation of phonon modes of VO$_2$ nanorods is shown in figure 3.15a. A surface probe microscopy (SPM) glass probe with an Au nanoparticle (~100 nm) attached at the tip, working in the tuning fork feedback mechanism (Fig. 3.15a), is used as the TERS probe. The excitation interaction volume generated due to the penetration of laser (far-field) and evanescent waves (near-field) in the nanorods are also schematically depicted in figure 3.15a. The growth direction of the nanorod (long axis) is chosen as the X direction, whereas the incident and the scattered light propagation direction is considered along with the Z direction. The parallel, $Z(XX)\bar{Z}$ and perpendicular, $Z(XY)\bar{Z}$ polarizations were configured using a half wave plate and a polarizer. The first and last letters in the Porto notation represents the direction of the propagation of the incident light (K_i) and scattered light (K_s), respectively. Whereas, the second and third letter inside the parenthesis represents the direction of the electric field polarization of the incident light (E_i) and the scattered light (E_s), respectively. The far-field and the near-field measurements were carried out at room temperature (300K) and were plotted in the same graph. The near and far-field Raman spectra of the VO$_2$ single crystal at two different conditions of parallel (XX) and cross (XY) polarization are shown in figures 3.15b and 3.15c, respectively. Among group theoretically predicted eighteen Raman active modes for M1 phase of VO$_2$ at Γ point ($9A_g+9B_g$) [16] we observed twelve modes at 140, 189, 220, 257,

306, 339, 390, 440, 495, 609, 662, and 821 cm^{-1}, which resemble well with the previously reported data [32,33]. The Raman modes observed at 189 and 220 cm^{-1} are reported to arise because of V-V vibration [16,34]. The intensity ratio of the two Raman modes around 200 cm^{-1} flips between parallel (*XX*) and cross (*XY*) polarization condition. The intensity flipping confirms that these two phonon modes are approximately perpendicular and parallel to the V-V dimer direction.
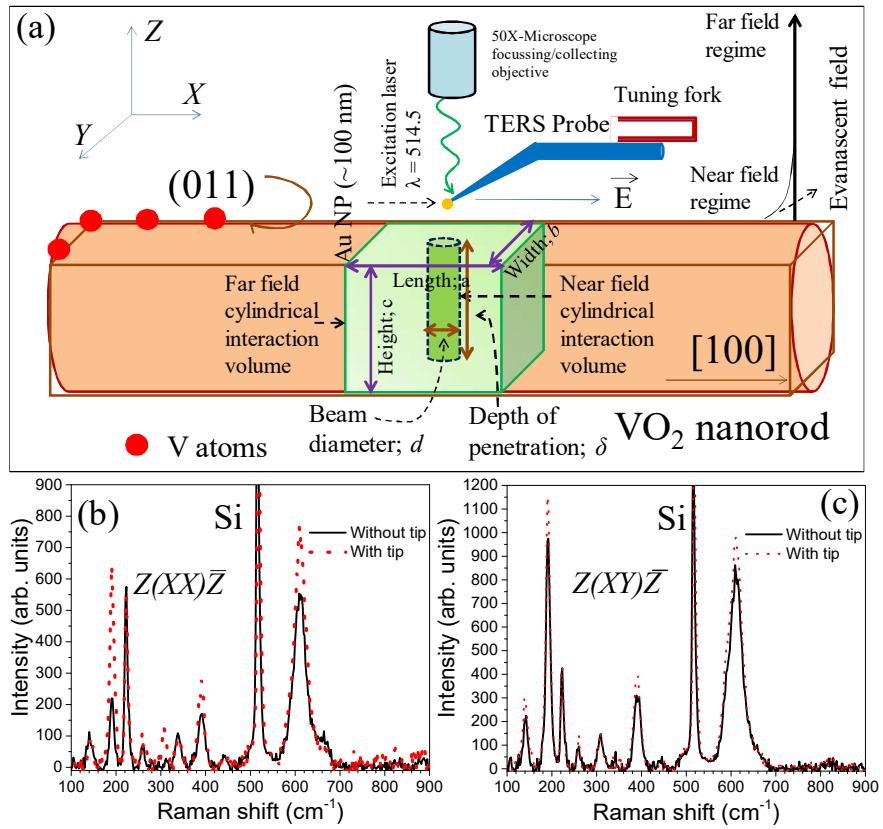
Figure 3.15 (a) Schematic representation of the experimental set up used for the near-field TERS measurements of VO$_2$ nanorod. (b) Raman spectra at parallel *Z(XX)Z̄* polarization with (dotted line) and without (solid line) TERS tip, and (c) Raman spectra at cross *Z(XY)Z̄* polarization with and without TERS tip.

The *EF* values for the recorded TERS spectra are estimated using the relation expressed in the equation 3.1 [61],

$$EF = \left(\frac{I_{with-tip}}{I_{without-tip}} - 1 \right) \frac{V_{FF}}{V_{NF}} \qquad \ldots\ldots\ldots\ldots\ldots\ldots\ldots\ldots\ldots\ldots\ldots\ldots (3.1)$$

where $I_{with-tip}$ and $I_{without-tip}$ are the recorded Raman mode intensities with and without the presence of TERS probe in the near- and the far-field regime of the sample, respectively. V_{FF} is the laser excitation interaction volume of the far-field configuration and V_{NF} is the effective interaction volume constituted by the near-field evanescent waves with the presence of TERS probe. We consider a cylindrical interaction volume (Fig. 3.15a) for the near-field configuration as $V = \pi(d/2)^2 \delta$, where, δ is the penetration depth of laser excitation through the sample and $d/2$ is the radius of the cylindrical interaction volume. In case of the near-field Raman spectral acquisition, presence of the TERS probe may confine the laser light and concentrate the field strength into a spot with a diameter ~100 nm (~size of Au nanoparticle). Therefore, V_{NF} is found to be ~2×10^6 nm^3 by assuming that the evanescent waves can penetrate the sample up to a distance of the order of a half-wavelength. However, for the far-field configuration, cylindrical interaction volume cannot be considered, as the focused laser beam diameter (~1.5 μ) is one order larger than the diameter of the nanorod (~150 nm). We have considered the interaction volume of the nanorod by the exposed laser beam as a rectangular prism of length a, width b, and height c. In the present study, a is the beam diameter; 1.5 μ, b is the width of nanorod; 150 nm, and c is the height of the nanorod ~300 nm as measured from low magnification TEM image of the interface between VO$_2$ and Si substrate (lower inset of Fig. 3.14b). Thus, V_{FF} is calculated ~6.8×10^7 nm^3 by considering the volume of the rectangular prism as $V = a \times b \times c$. The typical value of EF is calculated as ~66 (± 2), which is one order higher than that for without tip for the Raman mode at 189 cm^{-1} in the parallel (XX) polarization condition. The value of EF for the Raman mode at 189 cm^{-1} in

the cross (*XY*) polarization is calculated to be ~7. Whereas, in the case of Raman mode at 220 cm^{-1}, in both parallel and cross-polarization condition the value of *EF* is ~0. The value of *EF* (with less than 3% error) for all the Raman modes in *XX* and *XY* polarization configuration is listed in table 3.3.

Table 3.3 Raman enhancement factor (*EF*) for the observed phonon frequencies in recorded TERS spectra at different polarization conditions of *XX* and *XY*.

Frequency (cm^{-1})	EF_{XX}	EF_{XY}	Frequency (cm^{-1})	EF_{XX}	EF_{XY}
140	0	0	390	21	9
189	66	7	440	0	0
220	0	0	495	0	0
257	28	18	609	13	5
306	258	0	662	0	-
337	0	0	821	-	0

The maximum value of *EF* is found out as 258, which is two orders higher than that for without tip for the Raman mode observed at 306 cm^{-1}, in *XX* configuration. For all the Raman modes, the *EF* is higher in the case of the parallel (*XX*) polarization than that of the cross (*XY*) polarization condition (Table 3.3). As the TERS is capable of directional enhancement, it can be affirmed that the enhancing field vector is along the *X* direction, which is considered as the growth direction of the underlying 1-D VO$_2$ nanorod.

For further investigation, the electric field distribution for the TERS set up (Fig. 3.16a) is mapped by the 3D finite-difference time-domain (FDTD) method. The localized field distribution due to the TERS tip on VO$_2$ nanorod and the near-field intensity mapping for the system coupled with the TERS tip was simulated and extracted using the commercially available (Lumerical FDTD Solutions, Canada) numerical simulations. The TERS tip was designed by placing an Au sphere of diameter 100 nm on a conical glass tip. The coupled Au tip and VO$_2$ nanostructure system were excited by a plane wave source of

514.5 nm excitation wavelength injected along the *Z*-axis direction with a polarization in the *X*-axis direction. The perfectly matched-layer (PML) boundary conditions were used in the simulation with a simulation time of 1000 fs so that the energy field decayed fully. The mesh size was set as $2 \times 2 \times 1$ nm during all the numerical simulations. Further, the tip was positioned 10 nm above the sample surface to simulate the approximate gap expected during a typical scan. The near-field intensity maps for the VO_2 nanostructures were extracted and compared with the experimental data.
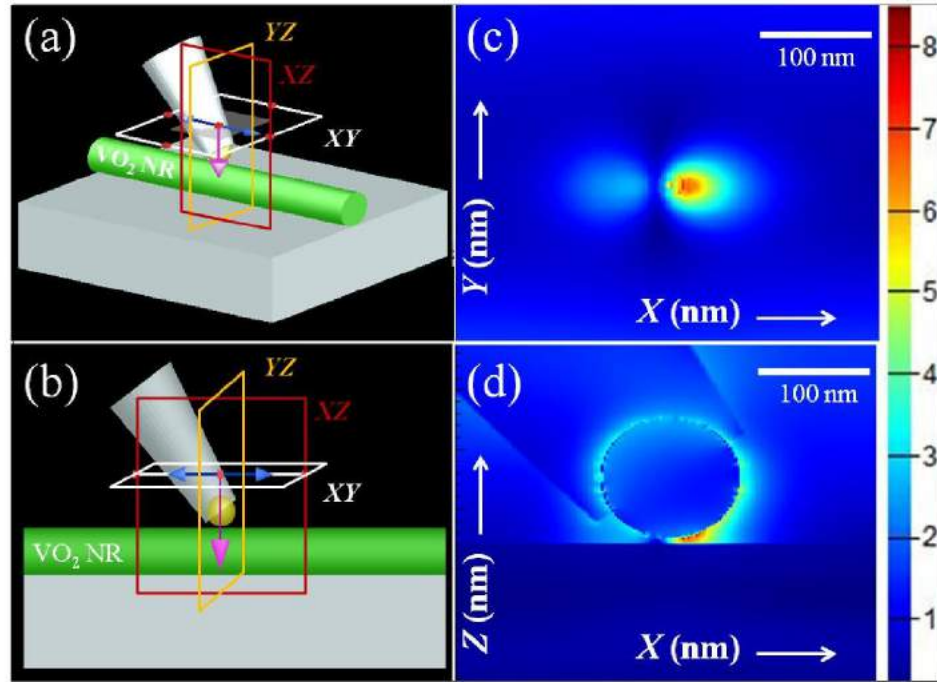
Figure 3.16 (a) The schematics of simulated structures projected in *XZ*–plane for coupled TERS tip with VO_2 nanorod and (b) The near-field distribution maps in *XY*–plane for VO_2 nanorod. The color bars indicate the relative strength of the field.

The schematics of the simulated structure for VO_2 nanorod (Fig. 3.16a) and its projection in *XZ*-plane (Fig. 3.16b) are shown. The near-field distribution map projected in *XY*-plane (Figure 3.16c) and *XZ*-plane (Fig. 3.16d) for coupled Au-VO_2 nanorod system

81

show that the field is confined at the interface along the *X*-axis, supporting our polarized TERS analysis.

3.5.3 Density function theory based PHONOPY calculation

Electronic density functional theory, as implemented in the Vienna *ab initio* simulation package (VASP) [62,63], was used for the total energy calculations. The projector augmented wave (PAW) pseudopotentials [64,65] in the Perdew-Burke-Erzenhoff (PBE) flavour to approximate the exchange-correlation functional, as supplied with VASP, were used for all the calculations. They were tested for convergence with respect to both the plane-wave energy cutoff and the *k*-grid. Gamma centered *k*-point meshes were used for all the systems. The converged plane-wave energy cutoff was 550 eV along with 5×5×5 *k*-point grid. The convergence of plane-wave energy cutoff and *k*-points were achieved to a precision of 0.1 meV/atom. The Methfessel-Paxton scheme of order two [66] was used for smearing the states with a smearing parameter of 0.2 eV. The structure was first relaxed by relaxing the cell volume, then the cell shape and at last by the positions of atoms in at least four cycles. Moreover, minimum two more cycles were run using the converged *k*-grid and plane-wave energy cutoff to obtain the correct ground-state relaxed atomistic configurations, till the total energies converged to a precision of less than 10^{-10} eV/atom and the Hellmann-Feynman forces became less than 10^{-5} eV/Å. The phonon dispersions were then calculated by the frozen phonon method with 2×2×2 supercells of the primitive cell of the Bravais lattice using PHONOPY code to carry out the pre- and post-processing of the calculations and plotting of the phonon dispersions [67]. The absence of any imaginary frequency confirms the structure as stable. The calculated and observed phonon modes are tabulated (Table 3.4). The phonon dispersion curve using the DFT of the phonon density of states is shown in figure 3.17a.

Table 3.4 Calculated and experimentally observed zone center optical modes in the M1 phase of VO_2

Calc. modes (cm^{-1})		Expt. Observe (cm^{-1})	Calc. modes (cm^{-1})		Expt. Observe (cm^{-1})
152	A_g	140	379	A_g	390
174	A_g	-	430	B_g	-
188	B_g	189	441	B_g	440
217	A_g	-	483	B_g	-
220	B_g	220	504	A_g	495
243	B_g	257	599	B_g	-
293	A_g	306	603	A_g	609
323	A_g	-	686	A_g	662
349	B_g	339	758	B_g	821

From the phonon dispersion curve, it is confirmed that the Raman modes around 200 cm^{-1} are dominated by V-V vibrations, as reported by experimental studies [16]. We observed two Raman modes at that frequency range; 189 and 220 cm^{-1} (Figs. 3.15b and 3.15c). The observed mode at 189 cm^{-1} can be compared with the calculated phonon frequency of 188 cm^{-1}; whereas the observed mode at 220 cm^{-1} can be assigned to the theoretically predicted phonon frequencies of either of 217 and 220 cm^{-1} or a cumulative contribution from both. The schematic atomic displacement of the Raman modes of 188, 217, and 220 cm^{-1} are shown in figure 3.17b. The Raman mode at 188 cm^{-1} is originated due to the V-V interaction along [100] direction of the M1 phase VO_2. On the other hand, the phonon vibrations at 217 and 220 cm^{-1} correspond to the vibration of V atoms at a direction, which is nearly perpendicular to that of 188 cm^{-1}. The 1-D VO_2 nanorod is oriented by (011) face, and its growth direction is along the [100]$_{M1}$ direction, as confirmed by GIXRD (Fig. 3.14a) are TEM (Figs. 3.14a-c) studies. So, the V-V interaction along [100] direction (crystallographic *X*-axis, used in Fig. 13.15a) is responsible for the Raman mode frequency observed at 189 cm^{-1}. Whereas, the V-V vibrations, nearly perpendicular to [100] axis, give rise to phonon frequency at ~220 cm^{-1}.
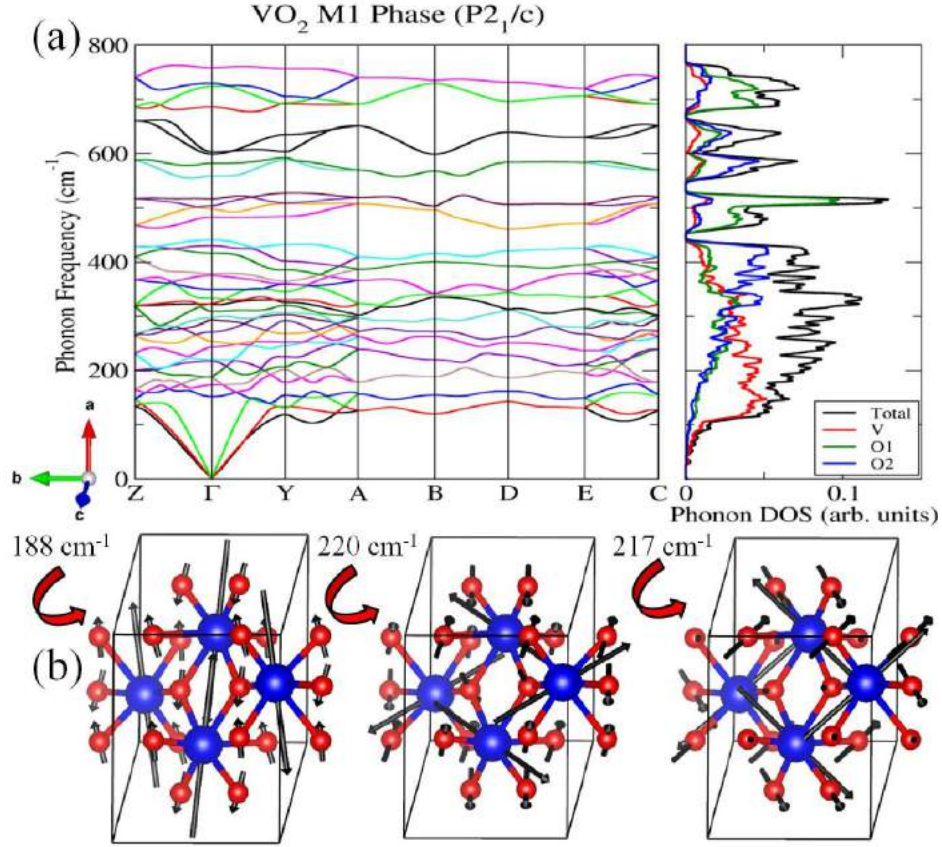
Figure 3.17 (a) Calculated phonon dispersions by the frozen phonon method with 2×2×2 supercells of the primitive cell of the Bravais lattice. (b) Schematic atomic displacement is shown for the 188, 217 and 220 cm^{-1} phonon modes. The directions of the displacements of atoms are shown by the arrows. The V and O atoms are shown with large (dark blue) and small (red) balls, respectively.

In the polarized TERS studies (Figs. 13.15b-c), the Raman mode at 189 cm^{-1} shows large enhancement in the parallel (*XX*) and less in the cross (*XY*) polarization conditions. Whereas, no enhancement is observed for the Raman mode at 220 cm^{-1}, in both the *XX* and the *XY* polarization conditions. Thus, the above studies confirm that the Raman modes at 189 cm^{-1} and 220 cm^{-1} are responsible for the vibration along *X* and *Y* axes, respectively using the unique property of directional enhancement in the TERS.

3.5.4 High-temperature TERS study

In order to study the role of phonons in the phase transition in VO_2, high-temperature TERS spectra were collected at a temperature range from 300 to 360K (Fig. 3.18). The Raman spectrum collected at 300K shows the vibrational modes for the pure M1 phase of VO_2 [32,33]. Whereas, at an intermediate temperature of 330K, we observed a rearrangement in the Raman spectra. The Raman modes at 199, 216, 222, 271, 293, 339, 432, 450, 650, and 831 cm^{-1} (Fig. 3.18) resemble with the reported M2 phase of VO_2 [6,19,68]. The structural change from M1 to M2 phase at a higher temperature is also observed by other groups [6,13]. The M2 phase sustained up to a temperature of 340K. However, all the Raman modes disappeared at 345K (metallic R phase), confirming the MIT in VO_2 [31,69].
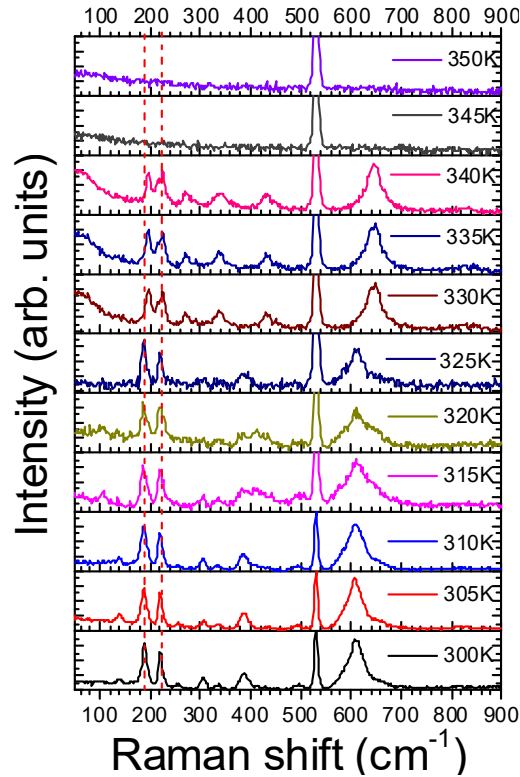
Figure 3.18 High-temperature TERS study on VO_2 nanorod with a temperature range from 300 to 360K.

We observed a shift in frequency ~ 2 cm^{-1} for the Raman mode at 220 cm^{-1}, which is quite expected due to thermal expansion of the lattice [70]. However, we observed a frequency shift of ~ 10 cm^{-1} in case of phonon mode 189 cm^{-1} in the same temperature range. Strelcov *et al.* [6] reported the same for the VO$_2$ nanostructures doped with Al. They observed no frequency shift for the mode $\sim$220 cm^{-1} in the structural transition from M1$\rightarrow$T$\rightarrow$M2 by doping, whereas the Raman mode of $\sim$189 cm^{-1} experienced a frequency shift of 10 cm^{-1}. The above observations demonstrate two facts: (i) The V-V interaction along [100] direction (corresponding Raman mode at 189 cm^{-1}) is responsible for the structural phase transition, and (ii) the MIT in VO$_2$ is not dominated by electron-lattice interaction, as one can still observe the insulating M2 phase in Raman spectra for a temperature range from 330 to 340K, in contrast to the report by Yuan *et al.* [46] The V-V dimers are reported to break and form a zig-zag pattern to stabilize the M2 phase [6,46]. The separation of V-V pairs due to increase in temperature only provokes the stabilization of intermediate M2 phase and does not prompt the metalicity in the system.

3.6 Summary:

Metastable phases of VO$_2$ were stabilized at room temperature by introducing defects in the system via two ways: (i) hole doping by native vacancy creation (M1 and T) and (ii) Mg doping with optimal proportion (M1, T, and M2). Pressure-induced structural phase transitions from M2 $\rightarrow$T$\rightarrow$M1 phases of VO$_2$ are observed in both XRD and Raman spectroscopic studies. The transition pressure for M2$\rightarrow$T and T$\rightarrow$M1 are observed to increase with the increase in doping concentration following the phase diagram of VO$_2$. The structural transition M2 $\rightarrow$T and T$\rightarrow$M1 is found to be second order continuous phase transition from the continuous change in the volume and a discontinuity in the bulk modulus

with hydrostatic pressure. However, the temperature-driven M2→R phase transition is found out as first order from the coexistence of both the phases for a narrow span of temperature. First order Mott-type MIT initiates a second order SPT without any latent energy leading to SPT and MIT observed simultaneously in VO_2. Further, the pressure and temperature dependent Raman spectroscopic studies help in finding the isothermal and isobaric Gruneisen parameters for the phonon modes and their relative contribution towards thermal expansion. The explicit anharmonicity (phonon-phonon interaction) is found to be dominant over the implicit (volume dependent) one for the M2 to R transition. In general, phonons play a significant role in structural transitions. The assignment of individual phonon mode, especially the one responsible for the structural phase transition in VO_2, is made possible using the directional field enhancement capability of TERS corroborated with FDTD and DFT calculations. Polarized TERS studies in the backscattering configuration confirmed the crystallographic orientation of VO_2 single nanorod, which was further reconfirmed by detailed high-resolution transmission electron microscopic analyses. High-temperature TERS studies confirm the fact that the separation of V-V dimers along [100] direction is responsible for the structural phase transition from M1 to M2 phase of VO_2 at 330K, but it does not induce metallicity in the system.

3.7 References:

1. Rao, C. N. R. Transition Metal Oxides. *Annu. Rev. Phys. Chem.* **1989,** *40*, 291-326.

2. Poizot, P.; Laruelle, S.; Grugeon, S.; Dupont, L.; Tarascon, J-M. Nano-Sized Transition Metal Oxides as Negative-Electrode Materials for Lithium-Ion Batteries. *Nature* **2000,** *407*, 496.

3. Morin, F. J. Oxides Which Show a Metal-to-Insulator Transition at the Neel Temperature. *Phys. Rev. Lett.* **1959**, *3*, 34.

4. Haverkort, M. W.; Hu, Z.; Tanaka, A.; Reichelt, W.; Streltsov, S. V.; Korotin, M. A.; Anisimov, V. I.; Hsieh, H. H.; Lin, H. -J.; Chen, C. T.; Khomskii, D. I.; Tjeng, L. H. Orbital-Assisted Metal-Insulator Transition in VO_2. *Phys. Rev. Lett.* **2005**, *95*, 196404.

5. Kim, H. -T.; Lee, Y. W.; Kim, B. -J.; Chae, B. -G.; Yun, S. J.; Kang, K. -Y.; Han, K. -J.; Yee K. -J.; Lim, Y. -S. Monoclinic and Correlated Metal Phase in VO_2 as Evidence of the Mott Transition: Coherent Phonon Analysis. *Phys. Rev. Lett*. **2006**, *97*, 266401.

6. Strelcov, E.; Tselev, A.; Ivanov, I.; Budai, J. D.; Zhang, J.; Tischler, J. Z.; Kravchenko, I.; Kalinin S. V.; Kolmakov, A. Doping-Based Stabilization of the M2 Phase in Free-Standing VO_2 Nanostructures at Room Temperature. *Nano Lett.* **2012**, *12*, 6198-6205.

7. Marezio M.; Dernier, P. D. Twinning in Cr-Doped VO_2. *Acta Cryst*. **1973,** *A29*, 618.

8. Villeneuve, G.; Drillon, M.; Hagenmuller, P.; Nygren, M.; Pouget, J. P.; Carmona F.; Delhaes, P. Magnetic and Structural Properties of Stoichiometric and Non-stoichiometric (V, Al) O_2 Alloys. *J. Phys. C: Solid State Phys*. **1977**, *10*, 3621.

9. Brückner, W.; Gerlach, U.; Moldenhauer, W.; Brückner, H. P.; Mattern, N.; Oppermann H.; Wolf, E. Phase Transitions and Semiconductor-Metal Transition in $V_{1-x}Ga_xO_2$ Single Crystals. *Phys. Status Solidi A* **1976**, *38*, 93-102.

10. Pouget, J. P.; Launois, H.; D'Haenens, J. P.; Merenda, P.; Rice, T. M. Electron Localization Induced by Uniaxial Stress in Pure VO_2. *Phys, Rev. Lett.* **1975**, *35*, 873-875.

11. Park, J. H.; Coy, J. M.; Kasirga, T. S.; Huang, C.; Fei, Z.; Hunter S.; Cobden D. H. Measurement of a Solid-State Triple Point at the Metal-Insulator Transition in VO_2. *Nature* **2013**, *500*, 431-434.

12. A. Zylbersztejn, A.; Mott, N. F. Metal-Insulator Transition in Vanadium Dioxide. *Phys. Rev. B* **1975**, *11*, 4383.

13. Goodenough, J. B. The Two Components of the crystallographic transition in VO_2. *J. Solid State Chem.* **1971**, *3*, 490-500.

14. Eyert, V. The Metal-Insulator Transitions of VO_2: A Band Theoretical Approach. *Ann. Phys. (Leipzig)* **2002**, *11*, 650-702.

15. Kim, D. H.; Kwok, H. S. Pulsed Laser Deposition of VO_2 Thin Films, *Appl. Phys. Lett*. **1994**, *65*, 3188.

16. Marini, C.; Arcangeletti, E.; Castro, D. D.; Baldassare, L.; Perucchi, A.; Lupi, S.; Malavasi, L.; Boeri, L.; Pomjakushina, E.; Conder K.; Postorino, P. Optical Properties of $V_{1-x}Cr_xO_2$ Compounds under High Pressure. *Phys. Rev. B* **2008**, *77*, 235111.

17. Cavalleri, A.; Dekorsy, T.; Chong, H. H. W.; Kieffer, J. C.; Schoenlein, R. W. Evidence for a Structurally-Driven Insulator-to-Metal Transition in VO_2: A View from the Ultrafast Timescale. *Phys. Rev. B* **2004**, *70*, 161102.

18. Kikuzuki, T.; Lippmaa, M. Characterizing a strain-driven phase transition in VO_2. *Appl. Phys. Lett*. **2010**, *96*, 132107.

19. Chen, C.; Zhao, Y.; Pan, X.; Kuryatkov, V.; Bernussi, A.; Holtz M.; Fan, Z. Influence of defects on structural and electrical properties of VO_2 thin films. *J. Appl. Phys*., **2011**, *110*, 023707.

20. Atkin, J. M.; Berweger, S.; Chavez, E. K.; Raschke, M. B.; Cao, J.; Fan, W.; Wu, J. Strain and temperature dependence of the insulating phases of VO_2 near the metal-insulator transition. *Phys. Rev. B* **2012**, 85, 020101.

21. Lee, S.; Cheng, C.; Guo, H.; Hippalgaonkar, K.; Wang, K.; Suh, J.; Liu, K.; Wu, J., Axially Engineered Metal–Insulator Phase Transition by Graded Doping VO_2 Nanowires. *J. Am. Chem. Soc.* **2013**, *135*, 4850-4855.

22. Mlyuka, N.; Niklasson, G.; Granqvist, C. -G.; Mg Doping of Thermochromic VO_2 Films Enhances the Optical Transmittance and Decreases the Metal-Insulator Transition Temperature. *Appl. Phys. lett*. **2009**, *95*, 171909.

23. Prasad, A. K.; Amirthapandian, S.; Dhara, S.; Dash, S.; Murali, N.; Tyagi, A. K. Novel Single Phase Vanadium Dioxide Nanostructured Films for Methane Sensing Near Room Temperature. *Sens. Actuators B* **2014**, *191*, 252-256.

24. Rajeswaran, B.; Umarji, A. M. Effect of W Addition on the Electrical Switching of VO_2 Thin Films. *AIP Adv*. **2016**, *6*, 035215.

25.   Nethravathi, C.; Rajamathi, C. R.; Rajamathi, M.; Gautam, U. K.; Wang, X.; Golberg, D.; Bando, Y. N-doped Graphene-VO_2 (B) Nanosheet-Built 3D Flower Hybrid for Lithium Ion Battery. *ACS Appl. Mater. Interfaces* **2013**, *5*, 2708-2714.

26.   Fisher, B. Electrical and Seebeck Effect Measurements in Nb Doped VO_2. *J. Phys. Chem. Solids* **1982**, *43*, 205-211.

27.   Goodenough, J.; Hong, H. Y. Structures and a Two-Band Model for the System $V_{1-x}Cr_xO_2$. *Phys. Rev. B* **1973**, *8*, 1323.

28.   Marezio, M.; McWhan, D. B.; Remeika, J. P; Dernier, P. D. Structural Aspects of the Metal-Insulator Transitions in Cr-Doped VO_2. *Phys. Rev. B* **1972**, *5*, 2541.

29.   Mitsuishi, T. On the Phase Transformation of VO_2. *Jpn. J. Appl. Phys.* **1967**, *6*, 1060.

30.   Nazari, M.; Zhao, Y.; Kuryatkov, V. V.; Fan, Z. Y.; Bernussi A. A.; Holtz, M. Temperature dependence of the optical properties of VO_2 deposited on sapphire with different orientations. *Phys. Rev. B* **2013**, *87*, 035142.

31.   Basu, R.; Sardar, M.; Bera, S.; Magudapathy, P.; Dhara, S. The Role of 1-D Finite Size Heisenberg Chains in Increasing the Metal to Insulator Transition Temperature in Hole Rich VO_2. *Nanoscale* **2017**, *9*, 6537.

32.   R. Srivastava and L. Chase, Raman Spectrum of Semiconducting and Metallic VO_2. *Phys. Rev. Lett.* **1971**, *27*, 727.

33.   Schilbe, P. Raman Scattering in VO_2. *Phys. B : Condensed Matter*, **2002**, *316*, 600-602.

34.   Basu, R.; Patsha, A.; Chandra, S.; Amirthapandian, S.; Raghavendra, K. G.; Dasgupta, A.; Dhara S. Polarized Tip-Enhanced Raman Spectroscopy in

Understanding Metal to Insulator and Structural Phase Transition in VO_2. *J. Phys. Chem. C* **2019**, *123*, 11189.

35. Kamali, K.; Ravindran, T. R.; Ravi, C.; Sorb, Y.; Subramanian, N.; Arora, A. K. Anharmonic Phonons of $NaZr_2(PO_4)_3$ Studied by Raman Spectroscopy, First-Principles Calculations, and X-Ray Diffractions. *Phys. Rev. B* **2012**, *86*, 144301.

36. Mitrano, M.; Maroni, B.; Marini, C.; Hanfland, M.; Joseph, B.; Postorino, P.; Malavasi, L. Anisotropic Compression in the High-Pressure Regime of Pure and Chromium-Doped Vanadium Dioxide. *Phys. Rev. B* **2012**, *85*, 184108.

37. Zhang, H.; Li, Q.; Cheng, B.; Guan, Z.; Liu, R.; Liu, B.; Liu, Z.; Li, X.; Cui T.; Liu, B. The Pressure-Induced Metallization of Monoclinic Vanadium Dioxide. *RSC Adv*., **2016**, *6*, 104949.

38. Birch, F. Finite Strain Isotherm and Velocities for Single-Crystal and Polycrystalline NaCl at High Pressures and 300°K. *J. Geophys. Res.* **1978**, *83*, 1257.

39. Pouget, J. P.; Launois, H.; Rice, T. M.; Dernier, P.; Gossard, A.; Villeneuve, G.; Hagenmuller P. Dimerization of a Linear Heisenberg Chain in the Insulating Phases of $V_{1-x}Cr_xO_2$. *Phys. Rev. B*, **1974**, *10*, 1801.

40. Jones, A. C.; Berweger, S.; Wei, J.; Cobden, D.; Raschke, M. B. Nano-Optical Investigations of the Metal−Insulator Phase Behavior of Individual VO_2 Microcrystals. *Nano Lett*. **2010**, *10*, 1574.

41. Sohn, J. I.; Joo, H. J.; Ahn, D.; Lee, H. H.; Porter, A. E.; Kim, K.; Kang, D. J.; Welland, M. E. Surface-Stress-Induced Mott Transition and Nature of Associated Spatial Phase Transition in Single Crystalline VO_2 Nanowires. *Nano Lett*. **2009**, *9*, 3392.

42. Chandrashekhar, G. V.; Barros, H. L. C.; Honig, J. M. Heat Capacity of VO_2 Single Crystals. *Mater. Res. Bull.* **1973**, *8*, 369-374.

43. Samanta, S.; Li, Q.; Cheng, B.; Huang, Y.; Pei, C.; Wang, Q.; Ma, Y.; Wang, L. Phase Coexistence and Pressure-Temperature Phase Evolution of VO_2 Nanorods Near the Semiconductor-Semiconductor Transition. *Phys. Rev. B* **2017**, *95*, 045135.

44. Okimura, K.; Watanabe, T.; Sakai, J. Stress-Induced VO_2 Films with M2 Monoclinic Phase Stable at Room Temperature Grown by Inductively Coupled Plasma-Assisted Reactive Sputtering. *J. Appl. Phys.* **2012**, *111*, 073514.

45. Rúa, A.; Cabrera, R.; Coy, H.; Merced, E.; Sepúlveda, N.; Fernández, F. E. Phase Transition Behavior in Microcantilevers Coated with M1-Phase VO_2 and M2-Phase VO_2:Cr Thin Films. *J. Appl. Phys.* **2012**, *111*, 104502.

46. Yuan, X.; Zhang, W.; Zhang, P. Hole-Lattice Coupling and Photoinduced Insulator-Metal Transition in VO_2. *Phys. Rev. B* **2013**, *88*, 035119-6.

47. Zhang, S; Chou, J. Y.; Lauhon L. J. Direct Correlation of Structural Domain Formation With the Metal Insulator Transition in a VO_2 Nanobeam. *Nano Lett.* **2009**, *9*, 4527-4532.

48. Cheng, C.; Guo, H.; Amini, A. Li, K.; Fu, D.; Zou, J.; Song, H. Self-Assembly and Horizontal Orientation Growth of VO_2 Nanowires. *Sci. Rep.* **2014**, *4*, 5456.

49. Khan, G. A.; Hogarth, C. A. A.C. Conduction through MIM Sandwich Samples of Evaporated Thin Films of V_2O_5 and V_2O_5/B_2O_3. *J. Mater. Sci.* **1991**, *26*, 1087-1092.

50. Mendialduaa, J.; Casanovaa, R.; Barbauxb, Y. XPS Studies of V_2O_5, V_6O_{13} , VO_2 and V_2O_3. *J. Electron Spectros. Relat. Phenom.* **1995**, *71*, 249-261.

51. Li, X.; Gloter, A.; Gu, H.; Luo, J.; Cao, X.; Jin, P.; Colliex, C. Discovery of Nanoscale Reduced Surfaces and Interfaces in VO_2 Thin Films as a Unique Case of Prewetting. *Scr. Mater.* **2014**, *78-79*, 41-44.

52. Wang, Y.; Zhang, Z. Synthesis and Field Emission Property of VO_2 Nanorods with a Body-Centered-Cubic Structure. *Physica E* **2009**, *41*, 548-551.

53. Chen, C.; Hayazawa, N.; Kawata, S. A 1.7 nm Resolution Chemical Analysis of Carbon Nanotubes by Tip-Enhanced Raman Imaging in the Ambient. *Nat. Commun.* **2014**, *5*, 3312.

54. Sonntag, M. D.; Klingsporn, J. M.; Garibay, L. K.; Roberts, J. M.; Dieringer, J. A.; Seideman, T.; Scheidt, K. A.; Jensen, L.; Schatz, G. C.; Van Duyne, R. P. Single-Molecule Tip-Enhanced Raman Spectroscopy. *J. Phys. Chem. C* **2012**, *116*, 478.

55. Polman, A. Plasmonics Applied. *Science* **2008**, *322*, 868-869.

56. Ozbay, E. Plasmonics: Merging Photonics and Electronics at Nanoscale Dimensions. *Science* **2006**, *311*, 189-193.

57. Patsha, A.; Dhara, S. Size Dependent Localized Phonon Population in Semiconducting Si Nanowires. *Nano Lett.* 2018, *18*, 7181.

58. Patsha, A.; Dhara, S.; Tyagi, A. K. Localized Tip Enhanced Raman Spectroscopic Study of Impurity Incorporated Single GaN Nanowire in the Sub-Diffraction Limit. *Appl. Phys. Lett.* 2015, **107**, 123108.

59. Sivadasan, A. K.; Patsha, A.; Maity, A.; Chini, T. K.; Dhara S. Effect of Scattering Efficiency in the Tip-Enhanced Raman Spectroscopic Imaging of Nanostructures In The Sub-Diffraction Limit. *J. Phys. Chem. C* **2017**, *121*, 26967.

60. Bailo, E.; Deckert, V. Tip-Enhanced Raman Scattering. *Chem. Soc. Rev.* **2008**, *37*, 921.

61. Kumar, N.; Rae, A.; Roy, D. Accurate Measurement of Enhancement Factor in Tip-Enhanced Raman Spectroscopy through Elimination of Far-Feld Artefacts. *Appl. Phys. Lett.* **2014**, *104*, 123106.

62. Kresse, G.; Hafner, J. Ab initio Molecular Dynamics for Liquid Metals. *Phys. Rev. B* **1993**, *47*, 558-561.

63. Kresse, G.; Furthmuller, J. Efficient Iterative Schemes for ab initio Total-Energy Calculations using a Plane-Wave Basis Set. *Phys. Rev. B* **1996**, *54*, 11169-11186.

64. Blochl, P. E. Projector Augmented-Wave Method. *Phys. Rev. B* **1994**, *50*, 17953-17980.

65. Kresse, G.; Joubert, D. From Ultrasoft Pseudopotentials to the Projector Augmented-Wave Method. *Phys. Rev. B* **1999**, *59*, 1758-1775.

66. Methfessel, M.; Paxton, A.T. High-Precision Sampling for Brillouin-Zone Integration in Metals. *Phys. Rev. B* **1989**, *40*, 3616-3621.

67. Togo, A.; Oba, F.; Tanaka, I. First-Principles Calculations of the Ferroelastic Transition Between Rutile-Type and CaCl$_2$-Type SiO$_2$ at High Pressures. *Phys. Rev. B* **2008**, *78*, 134106.

68. Basu, R.; Sardar, M.; Dhara, S. Origin of Phase Transition in VO$_2$. *AIP Conf. Proc.* **2018**, *1942***,** 030003.

69. Basu, R.; Magudapathy, P.; Sardar, M.; Pandian, R.; Dhara, S. VO$_2$ Microcrystals as Advanced Smart Window Material at Semiconductor to Metal Transition. *J. Phys. D : Appl. Phys.* **2017**, *50*, 465602.

70.   Suda, J.; Zverev, P.G. Temperature Dependence of Raman Frequency Shift in SrWO4 Crystal Studied by Lattice Dynamical Calculations. *Crystals* **2019**, *9*, 197.

CHAPTER 4

PHASE TRANSITION IN VO$_2$: METAL-TO-INSULATOR TRANSITION VS. STRUCTURAL PHASE TRANSITION

"Life is pleasant. Death is peaceful. It's the transition that's troublesome"

— Isaac Asimov

4.1   Introduction:

The metal-to-insulator transition (MIT) in vanadium dioxide gains tremendous attention in scientific society because it is accompanied by a structural phase transition (SPT) [1-3]. The simultaneous occurrence of MIT and SPT have led to a '*chicken-and-egg*' debate on the driving mechanism of the phase transition [4,5]. Biermann *et al*. [6] argued that VO$_2$ should be considered as a renormalized Peierls insulator (band-insulator) where the opening of the bonding-antibonding gap is driven by dimerization and renormalized down by interactions. Insulating and nonmagnetic nature of the M1 phase of VO$_2$ suggests that it may be a typical Peierls insulator with all the V chains dimerized [7]. However, it is also found that uniaxial strain [8], or doping of trivalent metals in VO$_2$ [7,9,10], leads to another monoclinic phase of VO$_2$ (M2), where V ions in alternate chains are only dimerized. Since the M2 phase with alternative non-dimerized V chains is also insulating, dimerization alone can not drive the MIT. According to Zylbersztejn and Mott [11], Sommers and Doniach [12], and Rice *et al*. [13], Coulomb repulsion is responsible for opening the energy gap in the semiconducting phases of VO$_2$. Qualitative proposal of electronic structures of VO$_2$ was reported long ago by Goodenough [14]. The O 2p orbitals stay 2.5 eV below the Fermi level in the electronic band structure of VO$_2$ [15,16] and form the valence band with π and σ bonds. In VO$_2$, there is one d electron per V atom, and the d levels of the V ions split into two states, namely, the lower-

lying triply degenerate t_{2g} and higher-lying doubly degenerate e_g^{σ} states (schematic in Fig. 4.1).
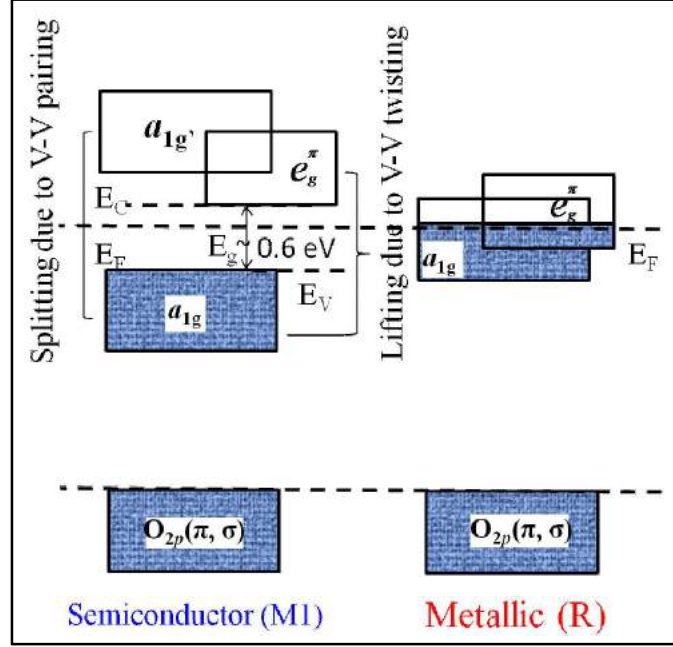
Figure 4.1 Schematic electronic band structures for the semiconducting and metallic phases of VO_2.

The t_{2g} multiplet splits again into an a_{1g} state (d_{xy}) and an e_g^{π} (d_{xz}, d_{yz}) doublet due to the tetragonal crystal field [14]. In the low-temperature semiconducting phase, V atoms form pairs in the rutile c (c_R) direction and split the a_{1g} bands into lower (bonding, a_{1g}) and upper (antibonding, $a_{1g'}$) bands. Moreover, the V-V pairs twist and thereby enhance the Vd-Op hybridization, which leads to a rise in the e_g^{π} band above the Fermi level. Thus, a gap of ~ 0.7 eV opens up to stabilize the insulating phase [4,14]. It is important to note that the density functional theory (DFT) with local density approximation (LDA) [4], however, fails to open the band gap between a_{1g} and e_g^{π} bands. On the other hand, LDA along with cluster dynamical mean field theory (C-DMFT) does manage to open up an energy gap of correct magnitude by taking account the correlation effects (Hubbard U) [6]. However, in the

metallic phase, the energy gap collapses and the Fermi level crosses partially filled a_{1g} and e_g^π bands. Thus, whether electron-phonon coupling or strong electron-electron correlation is responsible for triggering the phase transition in VO_2 is still under dispute; whether it can be understood in the Peierls scenario, or by invoking electronic correlation, indicating decisive role played by Mott physics.

The present chapter deals with the origin of the MIT and SPT in VO_2 and the correlation between them in details. We address the effect of defects in changing the transition temperature of VO_2 invoking dimensional reduction in V chains. The dimensional reduction leads to Mott-Hubbard MIT, and the insulating phase of VO_2 can be considered as one-dimensional (1-D) non-interacting Heisenberg spin ½ chains undergoing Peierls type SPT. The role of V vacancy (V_V) in increasing the transition temperature is discussed by introducing finite-size 1-D Heisenberg spin ½ chain model in the hole rich (acceptor doped) system. The correlation between MIT and SPT is analyzed by the observation of low-frequency collective spin excitation (spin-wave) in VO_2. As spin-wave propagates independently from the charge-density waves (spin-charge separation, according to Tomonaga-Luttinger (TL) liquid theory), the SPT and MIT are understood by separate phenomenological model. The experimentally observed Raman modes at low-frequency are compared with the calculated frequency for the spin-wave considering perturbation due to spin-lattice coupling. The significant deviation of Stokes to anti-Stokes intensity ratio of the low-frequency Raman mode from the usual thermal factor $\exp(h\nu/K_B T)$ disobeying Boltzmann's distribution law and the orthogonal dependency of the phonon and spinon vibration in the polarized Raman study confirm it to be originated from spin excitation. The role of doping in shifting the frequency of spin excitation as well as in increasing the

transition temperature while maintaining the same structural phase is discussed in details introducing finite-size 1-D Heisenberg spin ½ chain model.

4.2   Metal-to-Insulator Transition in VO_2:

4.2.1 Raman spectroscopic studies

In the previous chapter, we have seen that the variation in oxygen stoichiometry can stabilize the metastable phases of VO_2 at room temperature. From x-ray diffraction (Fig. 3.3a in chapter 3) and Raman spectroscopic measurements (Fig. 3.4a in chapter 3) we found that samples S1, S2, and S3, S4 were stabilized in M1 and T phases of VO_2, respectively. Presence of excess O in the samples S3 and S4 is probable, as they are grown with higher amount of O exposure at high temperature (1150K). The excess O creates V_V for maintaining the charge neutrality by the defect reaction (in Kroger-Vink notation),

$$O_2 => V_V^{4+} + 4h^+ + 2O^{-2} \dots\dots\dots\dots\dots\dots\dots\dots\dots\dots\dots\dots(4.1)$$

where O^{-2} are oxygen anions in the lattice and the four holes, h^+ are created at the V sites adjacent to the V_V site. These holes are trapped at the V sites of the neighboring chains by converting V^{4+} to V^{5+} or d^0 (spin $S = 0$) states leading to acceptor doping [17]. V^{4+} is located at the center of the oxygen octahedron with principal axes perpendicular to $(110)_{M1}$ lattice plane [4]. The V-O bond length is reduced as the V^{4+} is replaced by V^{5+}, and two apical O^{2-} of the octahedron shift closer to each other, which in turn reduce the (110) lattice plane spacing of M1 phase. In sample S2, the diffraction peak was observed at lower 2θ value than that of M1, indicating a compression in (011) lattice plane (Fig. 3.3a in chapter 3). Compression in one direction generally is coupled to an expansion in the perpendicular direction. Thus, the compression in $(011)_{M1}$ plane leads to tensile strain along the c_R axis.

The shortening of V-O bonds around each V^{5+} ion also reduces the twisting of V^{4+}-V^{4+} dimers (the spin-Peirls singlets of the $S = \frac{1}{2}$ chains) away from the c_R axis in its neighborhoods, which reflects in the hardening of the Raman modes 189 cm^{-1} (V-V), 220 cm^{-1} (V-V) and 609 cm^{-1} (V-O) from samples S1 to S4 (Fig. 3.4a in chapter 3). The increase in V_V introduced tensile strain along the c_R axis and produced the T phase.

To study the phase transition in the samples, we have carried out the temperature-dependent Raman spectroscopic study for the samples S1 to S4. Figure 4.2 shows the Raman spectra of the samples in the temperature range 300 - 360K using Linkam (THMS600) stage.
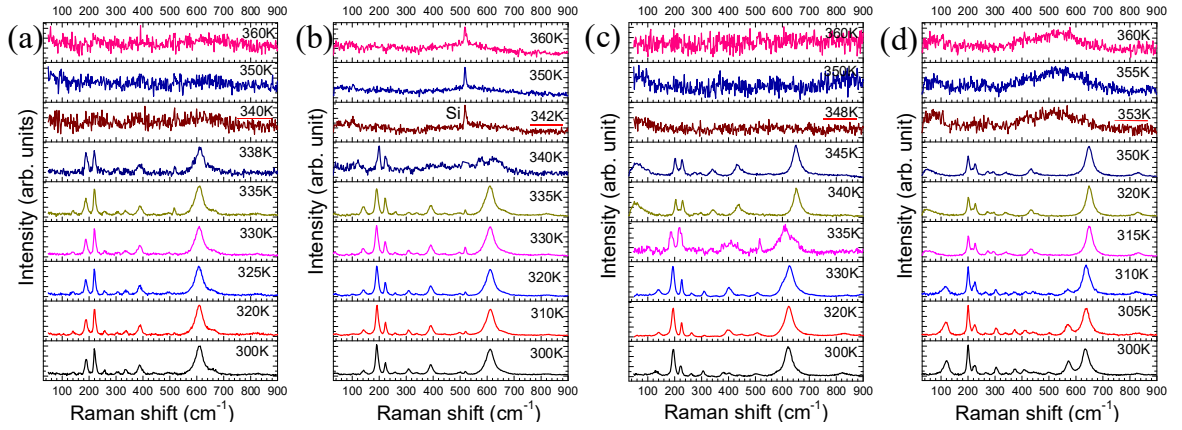
Figure 4.2 Raman spectra of the samples (a) S1, (b) S2 (c) S3, and (d) S4 as a function of temperature. Underlined temperatures denote the corresponding transition temperatures and phase reversibility. The peak observed at 521 cm^{-1} in (b) for sample S_2 above 340K correspond to Si substrate.

All the Raman modes disappear at 340, 342, 348 and 353K in samples S1 (Fig. 4.2a), S2 (Fig. 4.2b), S3 (Fig. 4.2fc), and S4 (Fig. 4.2d), respectively, confirming the transition (T_c) to metallic R phase for these samples at different temperatures. Going from S1 to S4, the T_c value increases by 13K. In samples S2 and S3, a noticeable change is observed in the Raman spectra indicating pure T phase for S2 and pure M2 phase for S3 at 340K [8,18]. All Raman

modes, however, disappeared at 342 and 348K leading to a transition from T→R and M2→R phase, respectively. So for sample S3, the phase evolution is T→M2→R with the rise in temperature. In sample S4, the T→M2 phase transition is observed at 320K and M2→R at 353K.
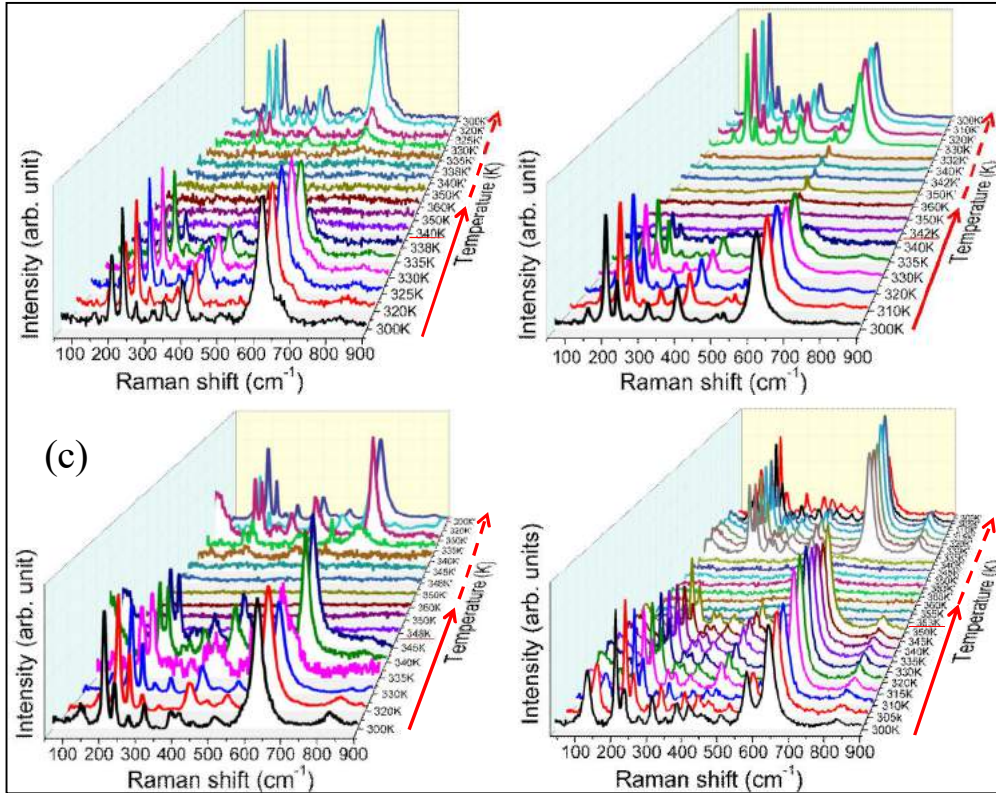
Figure 4.3 Raman spectra of the samples (a) S1, (b) S2 (c) S3 and (d) S4 with increase and decrease in temperature. Solid and dashed arrows denote the increase and decrease in temperature, respectively. Underlined temperatures denote the corresponding transition temperatures and phase reversibility.

All the four samples show reversible phase transition with a decrease in temperature with hysteresis values of 5, 10, 13 and 15K for samples S1, S2, S3, and S4, respectively (Figure 4.3). Hysteresis of values ranging from 3 to 40K depending on doping, size distribution, nucleation, and crystallographic orientation are reported for VO_2 [1-3].

4.2.2 Resistivity measurement

To study the MIT in VO_2, temperature-dependent resistance measurement was carried out in a voltage range of 2 V using two Au coated contact tips and a source measurement unit (Agilent B2911A). Temperature-dependent resistance measurement shows a sharp drop in the resistance value of four orders for all the samples S1 (at 342K), S2 (344K), S3 (352K) and S4 (355K) confirming the MIT in VO_2 (Figure 4.4a).
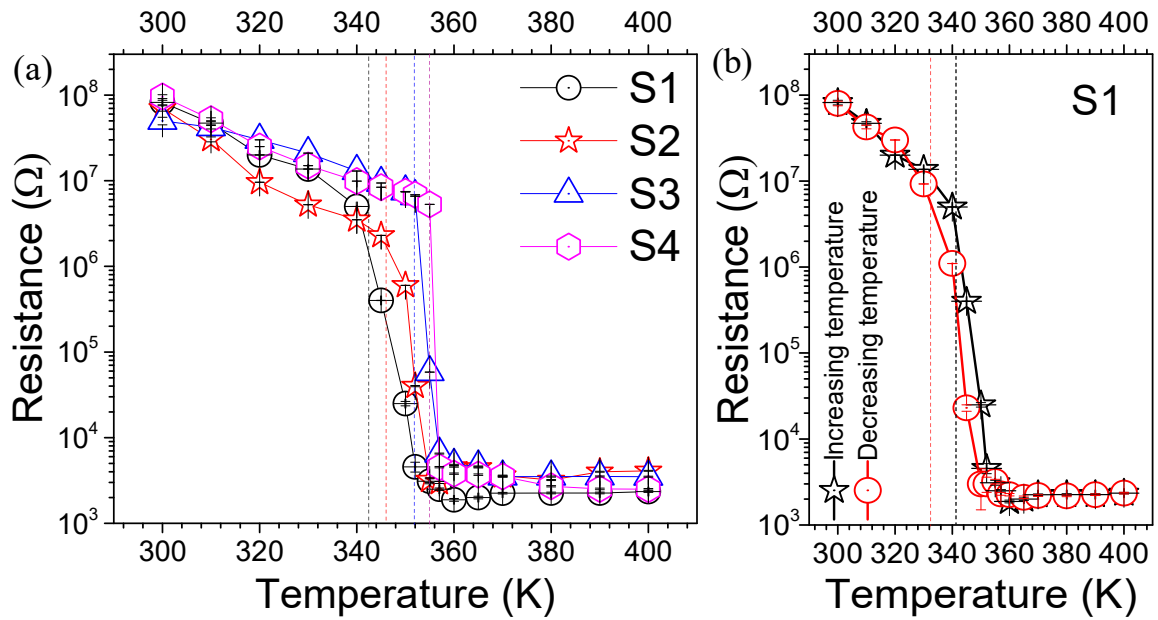
Figure 4.4 (a) Resistance measurements for the VO_2 samples S1, S2, S3 and S4 as a function of temperature showing a drop in resistance of four orders indicating metal-insulator transition (shown by vertical dashed lines). (b) Reversible temperature-dependent resistance measurement for sample S1 with a hysteresis value of ~8K (shown by vertical dashed lines). Symbols are for the experimental data, and connecting lines are guide to eyes.

The reversibility of MIT is shown for sample S1 in figure 4.4b with a hysteresis value of 8K. The hysteresis values for samples S2, S3, and S4 are found out as 10, 12, and 16K, respectively, which resemble the observed hysteresis in the Raman studies (Fig. 4.3).

4.2.3 X-ray photoelectron spectroscopic studies

In order to understand the reason behind the increase in T_c with an increase in oxygen exposure, x-ray photoelectron spectroscopic (XPS) studies were performed for all the samples. The Shirley type background-corrected XPS spectra for different elements and their characteristic electronic transitions for samples S1 to S4 are shown in figure 4.5.
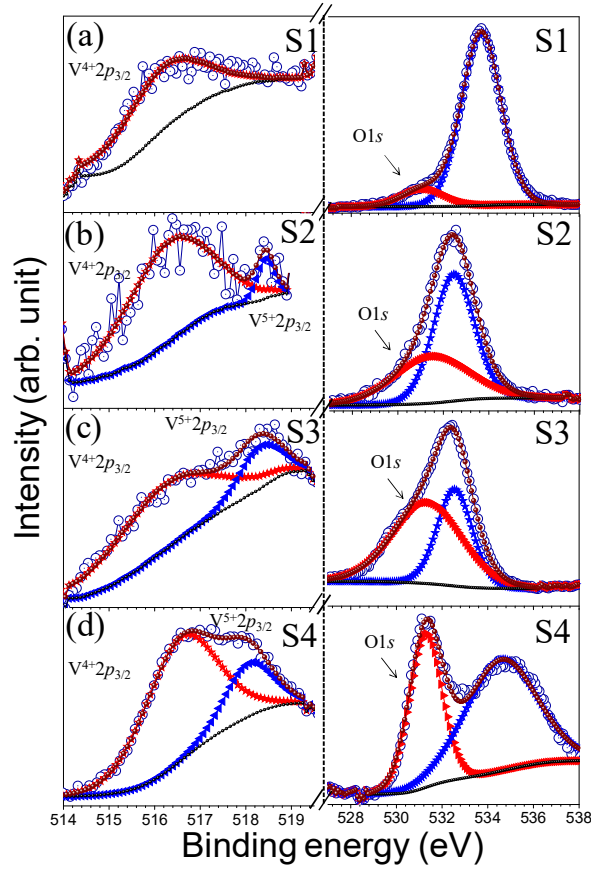
Figure 4.5 High-resolution XPS spectra of samples (a) S1, (b) S2, (c) S3, and (d) S4 with corresponding electronic transition of different elements. Open circles represent the data points, solid arrows and circles represent the fitted curves. In the left panel curves with red and blue arrows correspond to V^{4+} and V^{5+} oxidization states, respectively. In the right panel, red arrows correspond to lattice oxygen, and blue arrows correspond to oxygen from SiO_2 or absorbed oxygen species. Black small dots represent Shirley type background correction.

For sample S1, V $2p_{3/2}$ spin-orbit spectrum (Fig. 4.5a) can be fitted into a single peak with the binding energy (BE) value 516.2 eV and is assigned to V^{4+} oxidization state [19]. In sample S2, the spin-orbit spectrum can be fitted by two peaks with BE values 516.3 and 518.4 eV (Fig. 4.5b). The V $2p_{3/2}$ peak, observed at lower BE value of 516.3 eV for sample S2, can be assigned to V^{4+} oxidization state. The peak identified at higher BE value of 518.4 eV can be assigned to V^{5+} oxidization state [20]. These peaks are observed at 516.3 eV (V^{4+}) and 518.3 eV (V^{5+}) in sample S3 (Fig. 4.5c) and at 516.3 eV (V^{4+}) and 518.2 eV (V^{5+}) in sample S4 (Fig. 4.5d). The ratio of area under the curves of the two peaks can be a quantitative measure of the ratio V^{5+}/V^{4+}. This ratio increases progressively from samples S1 to S4. Table 4.1 contains the positions of the corresponding peaks and V^{5+}/V^{4+} ratio for all the four samples.

Table 4.1: Binding energy values of V^{4+} and V^{5+} and V^{5+}/V^{4+} ratio for samples S1 to S4.

Sample	V^{4+} (in eV)	V^{5+} (in eV)	V^{5+}/V^{4+}
S1	516.2	-	0
S2	516.3	518.4	0.083
S3	516.3	518.3	0.215
S4	516.3	518.2	0.279

Similarly, the oxygen spin-orbit spectrum for all the samples can be fitted by two peaks (Figs. 4.5a-d). O $1s$ peak for lower BE value at 531.2 eV (S1), and 531.3 eV (S2, S3, S4) are attributed to O in the lattice [19], and that of higher BE values at 532.5 to 534 eV correspond to O from SiO_2 [21,22] or absorbed O species. Significant increase in the amount of lattice O and V^{5+}/V^{4+} ratio from samples S1 to S4 indicates that increasing gas partial pressure leads to increasing oxygen excess (or equivalently increasing Vv concentrations, n_V). We have

already discussed how V_V is consistent with the increased tensile strain from samples S1 to S4 in section 4.2.1.

The V^{4+} $2p_{3/2}$ and O $1s$ peak are shifted towards higher BE in samples S2, S3, and S4 in comparison to sample S1. Higher oxidation states are reported to have larger chemical shifts of spin-orbit levels than lower oxidation states in comparison to neutral atom [17]. In samples S2 to S4, the existence of both V^{4+} and V^{5+} states is responsible for the shift in BE values towards higher energy values. In the V^{5+}–V^{4+} chain, V^{5+} is more electronegative due to the induced localized holes; therefore, V–O hybridization and strong V–V interaction results in the shifts of O $1s$ and V^{4+} $2p$ core levels toward higher BE values [17]. A plot of the T_c and Raman active modes frequencies vs. V^{5+}/V^{4+} ratios, which is eventually proportional to n_V, are shown in figure 4.6a.
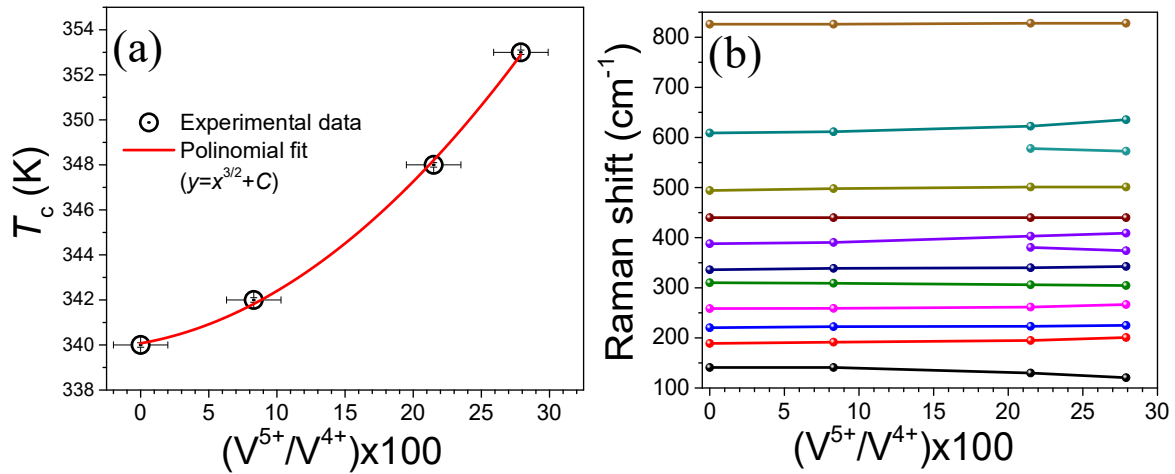
Figure 4.6 (a) Variation of transition temperature with V^{5+}/V^{4+} ratios ($\propto n_V$) with a polynomial fitting (red curve) exponent of 3/2 and a constant value C corresponding to T_C at $n_V = 0$ (340K). Bars denote errors in x and y axes. (b) Raman shift with V^{5+}/V^{4+} ratios for the four samples.

The transition temperature increases with V^{5+}/V^{4+} ratio of the samples S1 to S4 with a polynomial fitting exponent of 3/2 (Fig. 4.6a). The lowest frequency is red-shifted by an

amount of 20 cm^{-1}. On the other hand, most of the other modes are blue-shifted with the increase in V^{5+}/V^{4+} ratio (Fig. 4.6b), which confirms the role of V$_V$ concentration in increasing local strain.

4.2.4 Role of finite-sized Heisenberg spin ½ chain in modifying T$_c$

The insulating phases of VO$_2$ consist of dimerized 1-D long Heisenberg chains of V ions [4,17]. In the M1 phase, all V ions pair into dimers that are tilted away from c_R-axis. Excess oxygen, or equivalently V$_V$ leads to sites with V^{5+} or d^0 states (holes in the spin ½ chains). If the d^0 sites are pinned at the nearest neighbors of V$_V$ sites [17], they effectively cut off the 1-D spin chains into smaller fragments. The average size of the chains decreases with increase in V$_V$ concentration. Spin-Peierls transition temperature in the finite-size system is larger than the transition temperature in the infinite system. The correlation length of order parameter near phase transition temperature scales as,

$$\xi(T) \propto (T - T_{c0})^{-\nu} \quad \ldots\ldots\ldots\ldots\ldots\ldots\ldots\ldots\ldots\ldots\ldots\ldots\ldots(4.2)$$

where, $\xi(T)$ is the correlation length at temperature T, and T_{c0} is the thermodynamic (infinite system limit) transition temperature and ν is the critical exponent.

In a thermodynamic transition, correlation length diverges at the transition temperature. In a finite-size system, when the correlation length becomes of the order of the system size 'L' at a temperature $T_c > T_{c0}$, the phase transition occurs. Substituting $T=T_c$ and $\xi(T)=L$ (where L being the average length of the Heisenberg chains) in the scaling equation (4.2), we get

$$(T_c - T_{c0}) \propto L^{-1/\nu} \quad \ldots\ldots\ldots\ldots\ldots\ldots\ldots\ldots\ldots\ldots\ldots\ldots(4.3)$$

Since the average size of the chains is inversely proportional to the V$_V$ concentrations we get,

$$(T_c - T_{c0}) \propto n_V{}^{1/\nu} \quad \ldots\ldots\ldots\ldots\ldots\ldots\ldots\ldots\ldots\ldots\ldots\ldots(4.4)$$

It may be noted that n_V is proportional to the experimentally measured ratio of V^{+5} and V^{+4} ions (Table 4.1). From the experimental fit, we find $\nu = \frac{2}{3}$ (with $C = T_{c0} = 340K$ in Fig. 4.6a), which matches exactly with the theoretically predicted value of critical exponent for dimerization transition in finite-size spin ½ Heisenberg chain [23-25]. Increase in the T_c value with a decrease in sample size was also reported by few earlier workers in small particles [26], and thin films [27], invoking the presence of strain in the system. In our case, the particle size does not change, but the V_V concentration changes with the increase in oxygen exposure leading to the reduction of the effective lengths of the Heisenberg chains as described earlier. Different concentration of V_V essentially means different average length of the 1-D chains introducing finite-size effect on T_c. The concentration of d-electrons at V sites is the only crucial parameter determining the T_c. On the other hand, unrelaxed strains in the materials do not influence T_c. However, it profoundly affects the structural type of the insulating phase. Local strain prevents V-V dimers from twisting in one chain, and consequently de-pairing the dimers in adjacent chains, promoting M2 or T phase instead of M1 phase at intermediate temperatures. The T_c is reported to increase in Cr^{+3}, Al^{+3}, Ga^{+3} ions doped VO_2 [7-9]. These systems fall in the same universality class as our hole rich materials, because every trivalent metal ion also produces an adjacent V^{+5} site, just like every V_V induces adjacent d^0 sites. It is also significant that trivalent atom substitution stabilizes M2 and T phases [7-9], as observed in our materials, due to local lattice strains in the doped materials. So, the increase in T_c with increase in V_V concentration as well as the appearance of intermediate phases during phase transition can be understood as a finite size effect in 1-D half-filled band.

W^{+6}, Mo^{+6}, Ta^{+5}, Nb^{+5} doping in VO_2, on the other hand, reduce the T_c [28]. We speculate that substitution with metal ion having valency more than four leads to doubly occupied d^2 V sites. The doubly occupied sites can easily delocalize in the lattice (upper Hubbard band state), and one has to go down in temperature to arrest them into an insulating state, and thereby reducing the transition temperature in these materials. Thus, the reduction from three-band to one-band along with the dimensional reduction from 3-D to 1-D can explain both increase and decrease in the T_c value of VO_2 by doping with a metal having valency less and more than four, respectively.

4.3   Structural Phase Transition in VO_2:

The significant differences in the arrangement of V chains along c_R axis stabilize the insulating and metallic phases of VO_2. As discussed in chapter 3, the V chains are periodic and equally spaced with V-V separation of 2.86 Å in the high-temperature R phase [11]. On the other hand, the V atoms form dimers alternately and tilt along the c_R axis in the M1 phase with V-V separations of 2.65 (bonding) and 3.12 Å (anti-bonding) along $a_{M1} \leftrightarrow 2c_R$ axis [9,14]. In M2 phase, one set of V chains pair along the c_R axis without being twisted and the V-V separations being 2.53 Å (bonding) and 3.25 Å (anti-bonding) along $b_{M2} \leftrightarrow 2c_R$ axis; while the V ions in the nearest neighbor V chains do not form pair but twist with respect to the c_R axis with V-V separation of 2.93 Å [14]. The triclinic, T phase is reported as dimerized M2 phase [4]. To study the SPT in VO_2, we have chosen the samples grown via Mg doping as GIXRD (Fig. 3.3b in chapter 3) and Raman spectroscopic (Fig. 3.4b in chapter 3) studies confirm the presence of all the three different structural phases of pure VO_2 (M1 in sample S5, T in S6, and M2 in samples S7, S8, S9, and S10).

4.3.1 Stabilization of metastable phases

In order to determine the dopant percentage in the samples, the XPS studies were carried out for the samples S5, S6, and S7. The XPS spectra for different elements for samples S5 to S7 with the characteristic electronic transitions are shown in figure 4.7.

For sample S1, V 2p spin-orbit spectrum (Fig. 4.7a; 2nd panel) can be fitted with two curves with BE values of 516.3 and 523.7 eV, which are assigned as the transition from 2$p_{3/2}$ and 2$p_{1/2}$ spin-orbits of V^{4+} oxidization state, respectively [19, 20]. No trace of Mg was observed in sample S5 (Fig. 4.7a; 1st and 4th panels). In case of sample S6, Mg 1s and Mg Auger peaks are observed at 1304 and 306.1 eV, respectively [29], which are reported to be observed for the Mg ion bonded with O (Fig. 4.7b; 1st and 4th panels).
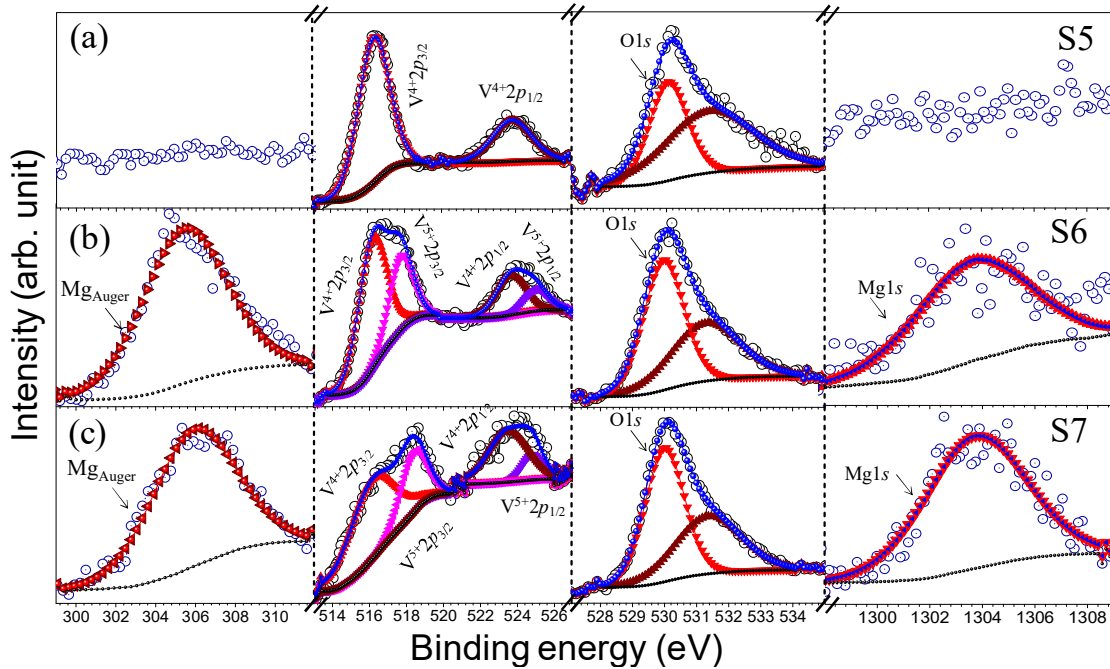
Figure 4.7 XPS spectra of the samples (a) S5, (b) S6, and (c) S7 denoted with the electronic transition of different elements. Open and solid symbols represent the data points and fitted curves, respectively. Black small dots represent Shirley type background correction.

110

The V 2p spin-orbit spectrum for sample S6 can be fitted by four peaks with BE values 516.2, 518.2, 523.6, and 524.8 eV (Fig. 4.7b; 2nd panel). The V 2$p_{1/2}$ and 2$p_{3/2}$ peak, observed at BE values of 516.2 and 523.6 eV, respectively for sample S6, can be assigned to V^{4+} oxidization state. The peaks observed at BE value of 518.2 and 524.8 eV can be assigned to 2$p_{1/2}$ and 2$p_{3/2}$ transitions for V^{5+} oxidization state [20]. In sample S7, the peaks are identified at 516.3 and 523.7 eV for 2$p_{1/2}$ and 2$p_{3/2}$ transition of V^{4+} oxidization states, respectively. Similarly, for V^{5+} oxidization state, the peaks are identified at 518.2 eV and 524.8 eV as 2$p_{1/2}$ and 2$p_{3/2}$ transitions in sample S7 (Fig. 4.7c; 2nd panel). The spin-orbit spectrum for Mg 1s and Mg Auger peak, in the case of sample S7, are observed at 1304 and 306 eV, respectively (Fig. 4.7b; 1st and 4th panels) [29]. On the other hand, for all the samples, O1s peak at low BE value (530 eV) is attributed to lattice O, and O1s peak with high BE value (531.5 eV) corresponds to absorbed O species (Fig. 4.7; 3rd panel) [21,22]. The atomic percentage (at. %) of Mg, V, and O are calculated from the area under the curves considering appropriate sensitivity factors for each element and are tabulated (Table 4.2).

Table 4.2 The atomic percentage of the elements and V^{5+}/V^{4+} ratio calculated from XPS spectra.

Sample	V^{4+} (at. %)	V^{5+} (at. %)	O (at. %)	Mg (at. %)	V^{5+}/V^{4+} ratio
S5	31.66	0	68.34	0	0
S6	21.42	8.19	69.57	0.81	0.38
S7	19.77	8.50	69.75	1.97	0.43

For the samples S8 to S10, we observed nearly similar results as that of sample S7 in XPS analysis except for a small increase in at. % of Mg. We have performed Laser-induced

breakdown spectroscopy (LIBS) to reconfirm the identification of the trace elements present in the samples (Fig. 4.8a). The plasma emission was produced in an air atmosphere using a Q-switched Nd: YAG laser (Quantel, Brilliant) operated at 532 nm, with a pulse duration of 8-10 ns and repetition rate of 10 Hz. The laser beam was focused at the target surface by a plano-convex quartz lens of focal length 15 cm; producing a spot size of about 400 μm in diameter. Plasma emission was collected at an angle by an optical fiber of 600 μm aperture (LTB, Germany), coupled to a fused silica collimator with a focal point of 8.7 mm and imaged onto the Aryelle 200 spectrometer (LTB, Germany). The dispersed light was detected by a CCD detector coupled to the spectrometer. We have performed LIBS to reconfirm the identification of the trace elements present in the samples.
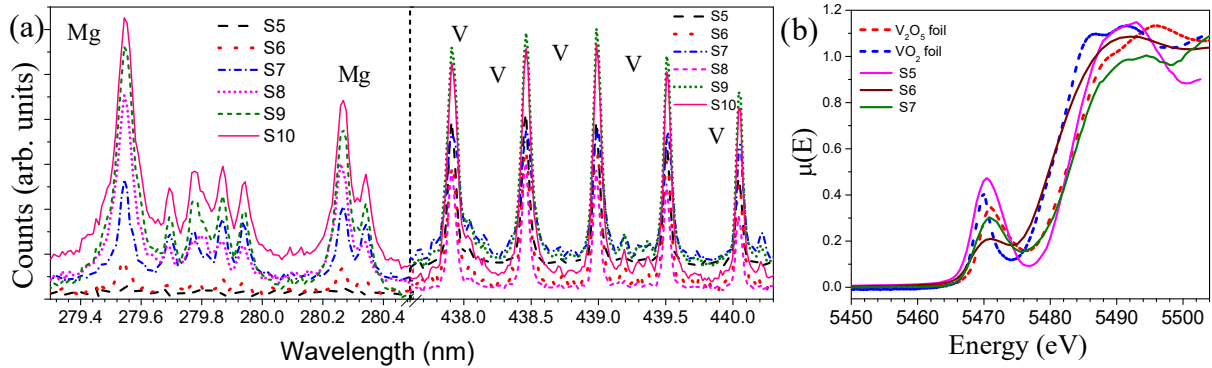
Figure 4.8 (a) LIBS spectra for the samples S5 to S10 showing peaks for V and Mg in VO_2 matrix. (b) Normalized XANES spectra at V K-edge for the samples S5 to S7 (solid lines). The XANES spectra for slandered VO_2 and V_2O_5 foils are also shown for comparison (dotted lines).

Figure 4.8a shows the LIBS spectra for the samples S5 to S10. In sample S5 there is no trace for Mg, whereas, in sample S6, the emission lines of Mg (II) at 279.55 and 280.27 nm proves the presence of Mg in the sample [30]. In the case of samples S7 to S10, the intensity of Mg lines increases simultaneously (Fig. 4.8a). The V lines were identified between 437 to 441

nm for all the samples [31]. The XPS and LIBS study confirm the presence of Mg in samples S6 to S10, which help in stabilizing the T and M2 phase of VO_2 by introducing strain in the system. The replacement of V^{4+} (d^1) by Mg ion is more likely to produce an adjacent V^{+5} (d^0) sites in the neighbouring chains. We have also carried out the x-ray absorption near edge structure (XANES) measurements to find out the oxidation state of the V in the samples (Fig. 4.8b). The x-ray absorption near-edge structure (XANES) measurement was performed at beamline-9 of Indus-2 synchrotron source at Vanadium K-edges in a transmission mode by putting the powder sample sandwiched between the scotch tapes. The removal of background and data normalization were performed using ATHENA software. The background removed extended x-ray absorption fine structure (EXAFS) data were fitted using ARTEMIS software. By comparing spectra, we confirm sample S5 is in +4 oxidation state, whereas samples S6 and S7 are in mixed +4 and +5 oxidation states (Fig. 4.8b).

4.3.2 Observation of collective spin excitation at low-frequency

In the Raman spectroscopic study of the samples S5 to S10 (Fig. 3.4b in chapter 3), we observed Raman peaks at the low-frequency side (~50 to 140 cm^{-1}) which were not predicted by the DFT calculation for phonon density of states (Table 3.4). The low-frequency modes for the samples are shown in figure 4.9. The 141 cm^{-1} band in sample S5 is reported as A_g mode in few of the earlier reports [32,33]. However, it is also reported as an external mode [34], which can be viewed as relative motions of structural units with respect to each other. The mode is observed at 121 cm^{-1} in sample S6 and ~ 50 cm^{-1} for samples S7-S10 (Fig. 4.9a). The low-frequency Raman mode for samples S7-S10 shows a continuous blue-shift (inset of Fig. 4.9b) with the increase in doping while the other Raman peaks do not show any shift in frequency (Fig. 4.9b) with doping.
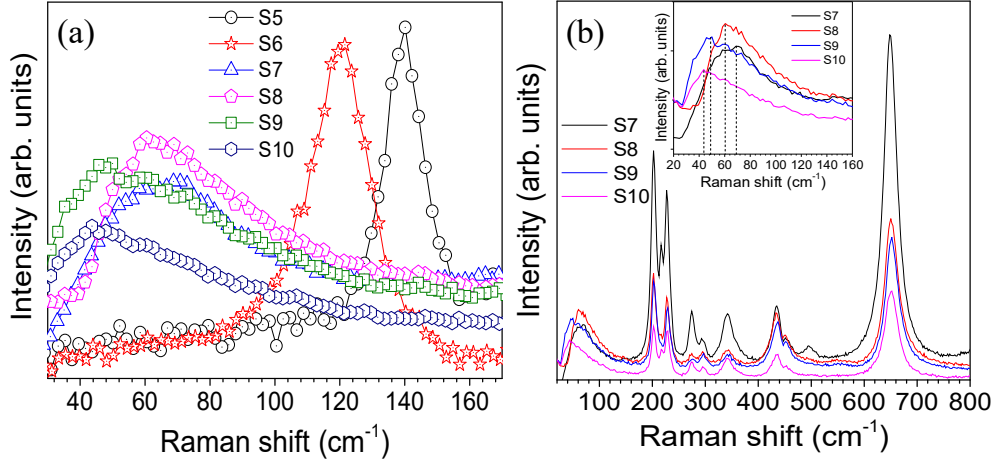
Figure 4.9 (a) Low-frequency Raman spectra of the samples S5 to S10. (b) Raman spectra for the samples S7 to S10. The inset in (b) shows Raman spectra for samples S7 to S10 at lower frequencies.

As discussed in section 4.2.1, the insulating phases of VO_2 consist of dimerized 1-D long Heisenberg chains of V ions [4,33]. In 1D spin ½ Heisenberg system, the Hamiltonian reads as,

$$H_0 = J \sum_j S_j . S_{j+1} \quad \text{………………………..……………… (4.5)}$$

where J (> 0) is the exchange interaction between neighbouring spins (S). The low-energy physics of this system is usually explained by a TL liquid with spinon excitation [35]. The Hamiltonian H_0 and the corresponding Raman operator R_0 commute with each other, and no Raman scattering is expected without additional perturbation. However, small perturbation v_0 exists due to spin-lattice coupling leading to the bond dimerization [36]. A perturbation due to static bond dimerization is termed as,

$$v_0 = \sum_j J (-1)^j u S_j . S_{j+1} \quad \text{………………………………... (4.6)}$$

where u is the distortion. Now the effective Hamiltonian becomes an exactly solvable Sine-Gordon (SG) model,

$$H' = H_0 + \int \frac{dx}{a_0} u d \sin (\sqrt{2\pi}\varphi) \quad \text{………………………………… (4.7)}$$

where $x = ja_0$; a_0 is the lattice spacing, and φ is the canonical part of Bosonic fields.

There are three kinds of spinon excitations; soliton (S), antisoliton (S'), and some breathers (B_n), which are the soliton-antisoliton bound states. The nth breather's mass E_n is related to E_s (mass of soliton) via,

$$E_n = 2E_s \sin [n\pi/(8/K-2)] \dots\dots\dots\dots\dots\dots\dots\dots\dots\dots \quad (4.8)$$

with $n = 1,\dots, [4/K-1]$ [37]. In SU(2)-symmetry, the soliton mass and second breather mass can be evaluated as

$$E_s \sim 1.5u^{2/3}J, \text{ and } E_2 = \sqrt{3}E_s \dots\dots\dots\dots\dots\dots\dots\dots\dots\dots \quad (4.9)$$

Soliton, antisoliton and the first breather form a spin-triplet with energy E_s. The second breather is a singlet excitation. Raman scattering from 1-D spin ½ chain is theoretically explored by Sato et $al.$[36] It is reported that in the case of dimerized chain, Raman intensity due to the triplets gives rise to a continuum background at frequencies $\omega \geq 2E_s$. Spin singlet breather B_2 appears as a δ-functional peak at $\omega=E_2$ using form-factor approach (provided T< J) [38,39]. However, in a practical case, a broadening in δ-functional peak is expected as the experiment is carried out at non-zero temperature. Pouget et $al.$ [40] reported the values of J for the different phases of VO_2 by the nuclear magnetic resonance (NMR) and susceptibility studies. The value of J for the M1, T, and M2 phases of VO_2 are found out as ~500K, ~350K, and ~320K, respectively [40]. The distortion (u) dependence of Raman mode due to spin-wave is also reported for $CuGeO_3$, TiOCr, and others [41-43]. We have calculated the distortion ($u=\Delta l/l$, where l is the distance between two spins) for the three samples S5(M1), S6(T) and S7(M2) as $u_1 = 0.07$, $u_2 = 0.08$, and $u_3 = 0.12$, respectively. The Raman mode frequencies for the samples in M1 (S5), T (S6), and M2 (S7) phases are calculated, using equation 4.9, as $\omega_1=152$ cm^{-1}, $\omega_2=117$ cm^{-1}, and $\omega_3=66$ cm^{-1}, respectively. The calculated and experimentally observed peaks are shown in figure 4.10a. The little

variation of experimental and calculated frequency is expected as the distortion u as well as exchange interaction J depends on doping concentration and temperature. Since the breather mode frequency is proportional to $u^{2/3}J$, where u is the dimerization order parameter, its variation with temperature mimics temperature dependence of order parameter. A background luminescence is observed in the case of sample S7 (Fig. 4.10a), which may be due to the tilted non-dimerized and randomly dimerized V- chains as reported by Sato *et al.* [36].
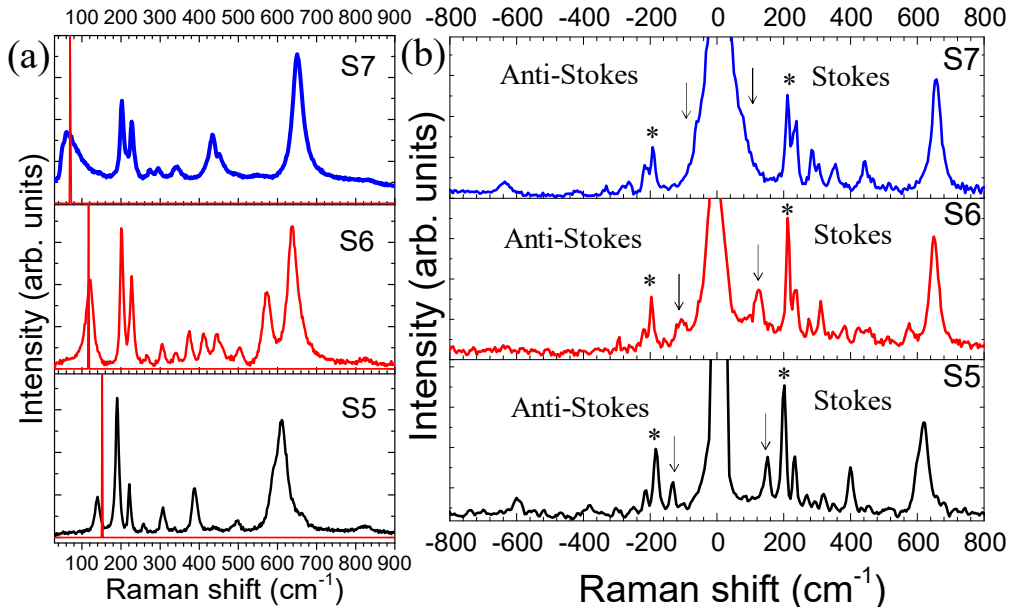
Figure 4.10 (a) Typical Raman spectra of all the samples S5, S6, and S7 and corresponding δ-functional peak at the calculated Raman mode frequency (b) Stokes and anti-Stokes spectra for the samples S5, S6, and S7. The spin-wave and the phonon mode used for calculation of (I_S/I_{AS}) ratio are denoted by arrow and star sign, respectively.

To reconfirm the origin of low-frequency Raman modes, we have calculated the intensity ratio of the Stokes to anti-Stokes (I_S/I_{AS}) Raman spectra for both the spin-wave and phonon vibration as a function of temperature. The Stokes and anti-Stokes Raman spectra collected at room temperature are shown in figure 4.10b. The presence of spin-wave in both

Stokes and anti-Stokes sides close to the Rayleigh line for all the three samples are denoted by an arrow mark (Fig. 4.10b). The frequency-shift, as well as the integrated I_S/I_{AS} ratio for the collective spin excitation at the lowest frequency and the closest phonon mode, originated due to V-V vibration ~200 cm^{-1} (denoted by '*' in Fig. 4.10b) are plotted as a function of temperature for all three samples (Fig. 4.11).
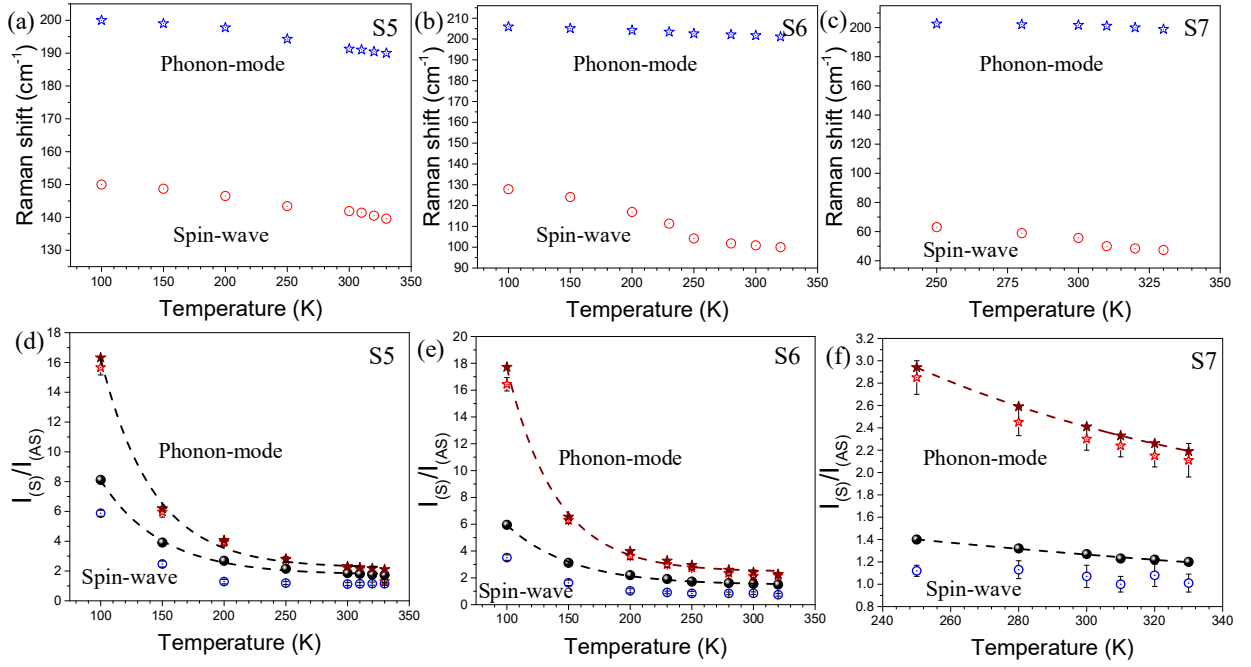
Figure 4.11 The frequency-shift with temperature for samples (a) S1, (b) S2, and (c) S3. The observed and calculated Stokes to anti-Stokes (I_S/I_{AS}) ratio with temperature for samples (d) S1, (e) S2, and (f) S3. The solid and empty symbols represent calculated and observed (I_S/I_{AS}) ratio, respectively, with corresponding error values.

The I_S/I_{AS} ratio is compared with the Boltzmann's distribution law:

$$\frac{I_S}{I_{AS}} = \left(\frac{\upsilon-\upsilon_m}{\upsilon+\upsilon_m}\right)^4 e^{\frac{h\upsilon_m}{K_B T}} \quad \dots\dots\dots\dots\dots\dots\dots\dots\dots\dots\dots \quad (4.10)$$

where υ is the excitation frequency, υ_m is the phonon frequency, h is the Planck's constant, K_B is the Boltzmann's constant, and T is the temperature. The calculated values from equation (4.10) and experimentally observed values of I_S/I_{AS} ratio for both the spin-wave and the

closest phonon mode are tabulated (Table 4.3). The calculated I_S/I_{AS} ratios are plotted in figure 4.11d-f as a function of temperature.

Table 4.3 Comparison between calculated and experimentally observed I_S/I_{AS} ratio for both the spin-wave and closest phonon mode with temperature in the three samples.

	Spin-wave			Phonon mode		
Sample S5						
T(K)	v (cm⁻¹)	$\dfrac{I_S}{I_{AS}}$	$\left(\dfrac{v-v_m}{v+v_m}\right)^4 e^{\frac{hv_m}{K_BT}}$	v (cm⁻¹)	$\dfrac{I_S}{I_{AS}}$	$\left(\dfrac{v-v_m}{v+v_m}\right)^4 e^{\frac{hv_m}{K_BT}}$
100	150±0.1	5.88±0.2	8.12	200±0.1	15.66±0.5	16.32
150	148.7±0.1	5.47±0.2	3.91	199±0.1	5.97±0.35	6.2
200	146.5±0.1	1.79±0.15	2.69	197.8±0.1	3.94±0.25	4.06
250	143.4±0.1	2.19±0.1	2.15	194.3±0.1	2.78±0.2	2.81
300	141.9±0.1	1.62±0.1	1.86	191.3±0.1	2.20±0.1	2.31
310	141.4±0.1	3.44±0.1	1.81	191±0.1	2.13±0.1	2.24
320	140.5±0.1	2.95±0.1	1.77	190.4±0.1	1.81±0.1	2.17
330	139.6±0.1	1.74±0.1	1.73	190±0.1	1.31±0.1	2.11
Sample S6						
T(K)	v (cm⁻¹)	$\dfrac{I_S}{I_{AS}}$	$\left(\dfrac{v-v_m}{v+v_m}\right)^4 e^{\frac{hv_m}{K_BT}}$	v (cm⁻¹)	$\dfrac{I_S}{I_{AS}}$	$\left(\dfrac{v-v_m}{v+v_m}\right)^4 e^{\frac{hv_m}{K_BT}}$
100	127.8±0.1	3.41±0.2	5.95	205.9±0.1	16.44±0.5	17.72
150	124.1±0.1	2.33±0.2	3.12	205.1±0.1	6.30±0.25	6.55
200	116.9±0.1	1.93±0.15	2.20	204.2±0.1	3.62±0.25	3.98
230	111.3±0.1	3.11±0.1	1.91	203.4±0.1	3.00±0.2	3.27
250	102.2±0.1	2.54±0.15	1.72	202.6±0.1	2.75±0.1	2.94
280	101.8±0.1	1.44±0.1	1.61	202.1±0.1	2.35±0.15	2.59
300	100.9±0.1	1.25±0.1	1.55	201.7±0.1	2.13±0.1	2.41
320	100.0±0.1	1.94±0.1	1.50	201.1±0.1	2.17±0.1	2.27
Sample S7						
T(K)	v (cm⁻¹)	$\dfrac{I_S}{I_{AS}}$	$\left(\dfrac{v-v_m}{v+v_m}\right)^4 e^{\frac{hv_m}{K_BT}}$	v (cm⁻¹)	$\dfrac{I_S}{I_{AS}}$	$\left(\dfrac{v-v_m}{v+v_m}\right)^4 e^{\frac{hv_m}{K_BT}}$
250	63.0±0.1	1.02±0.05	1.40	202.6±0.1	2.85±0.15	2.94
280	58.9±0.1	1.03±0.08	1.32	202.1±0.1	2.45±0.12	2.59
300	55.6±0.1	1.07±0.1	1.27	201.7±0.1	2.30±0.1	2.41
310	50.0±0.1	1.00±0.07	1.23	201.1±0.1	2.24±0.1	2.33
320	48.4±0.1	1.18±0.1	1.22	200.0±0.1	2.15±0.1	2.26
330	47.3±0.1	1.11±0.08	1.20	198.9±0.1	2.11±0.15	2.19

It is clear from figure 4.11 that though there is a continuous red-shift with an increase in temperature (Fig. 4.11a-c) for both the spin-wave and phonon mode, there is a significant

mismatch between the observed I_S/I_{AS} ratio and the calculated one for the spin-wave (Fig. 4.11d-f). However, I_S/I_{AS} ratio for the closest phonon mode ~ 200 cm^{-1} follows the usual thermal factor of $\exp(hv/K_BT)$ following Boltzmann's distribution law. Whereas, the lowest frequency mode for all the three samples shows a considerable deviation of I_S/I_{AS} ratio from the usual thermal factor $\exp(hv/K_BT)$ disobeying Boltzmann's law and thus confirming the mode to be originated from spin excitation [44,45].

We also performed the polarized Raman scattering on three single micro-rods of the samples S5, S6, and S7. The incident excitation wave is considered along the Z direction, whereas, the growth direction of the micro-rods (C_R axis) is chosen along the X-axis.
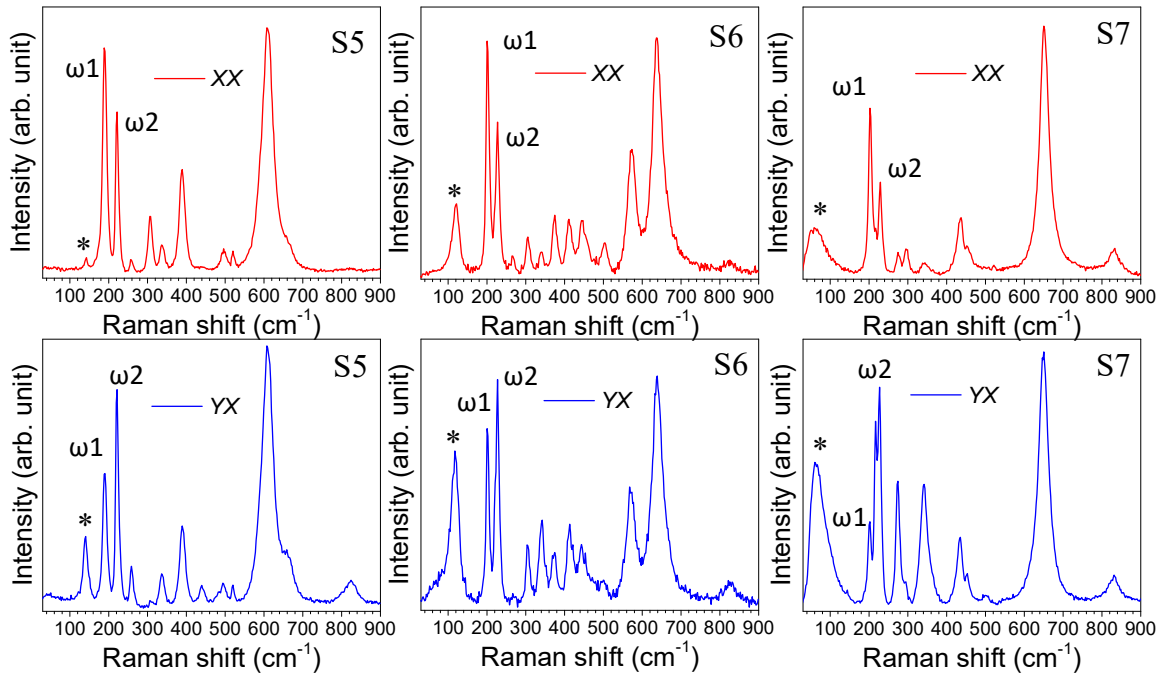
Figure 4.12 Raman spectra at parallel (*XX*) and cross (*YX*) polarization condition for the three samples S5, S6, and S7.

According to Porto notation, in the parallel, $Z(XX)\bar{Z}$ and perpendicular, $Z(YX)\bar{Z}$ polarization configurations, the first and fourth letters represent the direction of the propagation of the incident (K_i) and scattered light (K_s), respectively, whereas the second and third letter inside the parenthesis represents the direction of the electric field of the incident (E_i) and the scattered light (E_s), respectively. Figure 4.12 shows the Raman spectra with both parallel (*XX*) and cross (*YX*) polarization configurations for the three samples.

In case of parallel (*XX*) polarization, the intensity of the Raman mode arising due to V-V vibration parallel to C_R axis (denoted as ω1 in Fig. 4.12) is more than that of the mode arising due to perpendicular to the C_R axis (denoted as ω2 in Fig. 4.12) [4,18,46]. Whereas, the peak-intensity flips in case of cross (*YX*) polarization condition. The above observations imply the micro-rods are aligned along the X-axis, i.e., along the C_R direction [46]. However, the intensity of the low-frequency Raman-modes (denoted as '*' in Fig. 4.12) for all the three samples is observed to be high in case of cross-polarization condition (⊥ to C_R axis), and falls rapidly for parallel polarization (∥ to C_R axis). As the spin chains are aligned along the C_R direction, the spinon vibration is expected to be produced parallel to the *X*-axis.

In an electromagnetic (EM) wave, the electric field vector (***E***) and magnetic field vector (***B***) propagates orthogonally to each other. As the excitation EM wave was incident along *Z* direction; while the ***E*** field propagates along the *Y*-axis, the ***B*** field propagates along *X*-axis and vice-versa. The spins get excited by the magnetic field of the electromagnetic wave; therefore the maximum intensity is expected for the cross-polarization (*YX*) condition where ***E*** and ***B*** field propagates along the *Y*-axis and *X*-axis, respectively. Thus the orthogonal dependency of the phonon and spinon vibration in the polarized Raman study reconfirms the origin of the low-frequency Raman modes as spin excitation.

4.4   Metal-to-Insulator vs. Structural Phase Transition and the Origin of Phase Transition in VO_2:

We have carried out the temperature-dependent Raman spectroscopic analysis to study the phase transition of the $V_{1-x}Mg_xO_2$ samples. Figure 4.13a shows typical temperature-dependent Raman spectra for sample S5. All the Raman modes disappear at 340K for S5, 345K for S6, 348K for S7, 350K for S8, 355K for S9, 358K for S10 samples confirming the transition to metallic R phase [4,33]. The transition temperature is found to increase with an increase in Mg dopant (Fig. 4.13b).
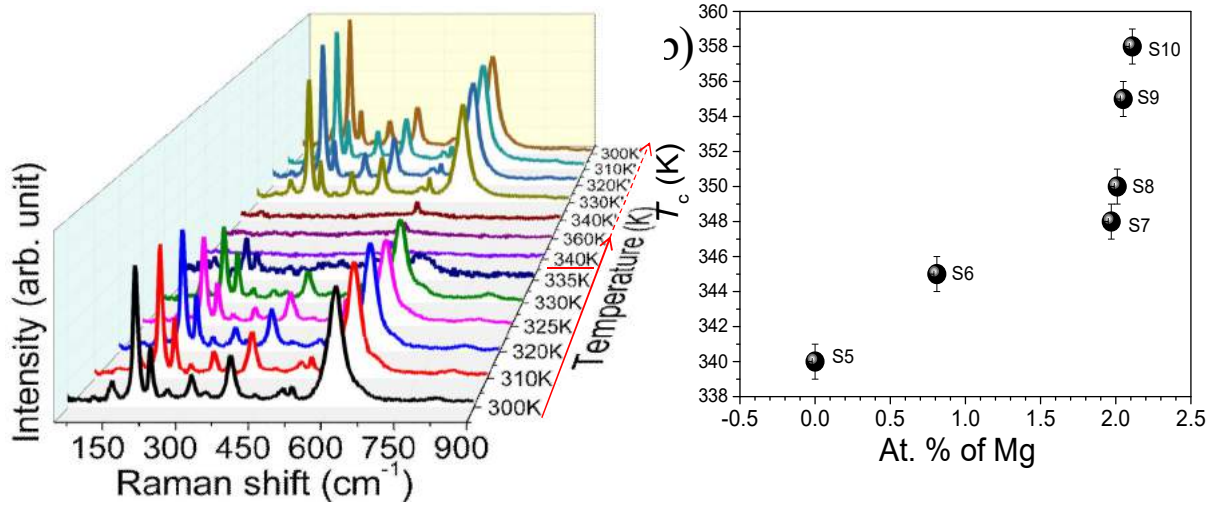
Fig. 4.13 (a) Raman spectra of the samples S5 as a function of temperature. The transition temperature is underlined. Solid and dashed arrows denote the increase and decrease in temperature, respectively, and (b) Variation of transition temperature with at. % of Mg dopant.

Doping of Mg leads to sites with V^{5+} or d^0 states (holes in the electron chains). The d^0 sites effectively cut down the length of the infinitely long 1-D spin chains into smaller fragments [33]. The average size, L of the spin-chains decreases with increase in d^0 states, i.e., with an increase in Mg dopant. The temperature for Spin-Peierls transition in the infinite-sized

system is lesser than that of in the finite-sized system as observed in the case of hole-doped samples S1 to S4. Takayoshi *et al*. [37] reported for 1D spin ½ Heisenberg chains that the finite energy gap increases linearly with $1/L$. As the doping concentration of Mg increases from samples S7 to S10, the average length of finite-sized spin ½ Heisenberg chains decreases, which in turn increases the factor $1/L$. The increase in $1/L$ results in an increase in E_s in SU(2) systems and thereby the Raman mode frequency ω increases as observed in figure 4.9b ($\omega = E_2$ and $E_2 = \sqrt{3}E_s$). The blue shift (inset of Fig. 4.9b) with an increase in doping is observed only for the low-frequency spin excitation, while the other vibrational modes remain unchanged (Fig. 4.9b) with doping. The variation in T_c with hole-doping, while maintaining the same monoclinic, M2 symmetry in samples S7-S10 (Fig. 4.9b), confirms that SPT does not have any role in MIT.

In the electronic band structure of VO_2 (Fig. 4.1), we have seen that Coulomb correlation may be sufficient to cause level repulsion between a_{1g} and overlapped $a_{1g'}$, e_g^π states, leading to an orbital selection and a half-filled a_{1g} band. The orbital nature of a_{1g} states is such that the hopping integral between V ions within a chain along c_R axis is larger compared to hopping in other two transverse directions (between V chains). In the high temperature metallic phase, three bands of different orbital characters overlap. The inter-orbital Coulomb repulsion pushes up the energy levels of the upper two bands, which leads to transfer of electrons from the upper two bands to the lowest band. The electron transfer process leads to further level separation between bands. This process stops when two upper bands become empty, and the lowest band becomes half filled. The changes in lattice parameters above transition temperature are driven by the changes in relative band fillings with temperature. As soon as the lower band becomes half filled, the intra-orbital local

Coulomb repulsion (Hubbard-type) takes over and drives a Mott-type MIT. The Mott insulating state is nothing but an assembly of parallel spin ½ antiferromagnetic Heisenberg chain. In 1-D, Heisenberg spin ½ chains are susceptible to spin-Pierls (dimerized phase) transition accompanying SPT. The electronic transition goes successively from, three-band, 3-D metal to a single half-filled band, then to 1-D Heisenberg chain and finally to the dimerized spin-Peierls insulator. Reduction to 1-D due to orbital selection is the reason for SPT and MIT to happen at the same time, in a discontinuous fashion.

4.5 Summary:

The transition temperature (T_c) of MIT is recorded to increase with the increase in oxygen content for samples grown with different oxygen exposure. The presence of V_V (with excess oxygen content) is found to generate unrelaxed local strain promoting T phase at the expense of the M1 phase in the samples S1 to S4. On the other hand, random local strain due to Mg doping is found out as the main cause for the evolution of the M1 phase into M2 and T phases. However, unrelaxed local strain is not the driving force for the observed MIT. From the spectroscopic analysis, we argue that the insulating phases of VO_2 should be viewed as a collection of V ions along c_R-axis of infinitely long Heisenberg spin ½ chains, which are non-interacting to each other. The Raman modes at low-frequency are observed for the first time in VO_2 and are explained by the soliton, anti-soliton and breathers vibrations of the dimerized 1-D spin ½ Heisenberg chains for the gapped case. The structural phase transition is explained by the observed low-frequency Raman modes ($\sim$ 50 to 140 cm^{-1}) and is compared with the calculated singlet breather mode of the 1-D vanadium chains. The orthogonal dependency of the phonon and spinon vibration in the polarized Raman study helps in finding the origin of the low-frequency Raman modes as spin excitation. Moreover,

it is found that the Stokes to anti-Stokes intensity ratio of the low-frequency Raman mode differs considerably from the Boltzmann's distribution law confirming it to be originated due to spinon vibration. The V_V creates d^0 sites (V^{5+}) at the nearest neighbours introducing finite-size scaling effect; as the d^0 sites reduce the effective length of the Heisenberg spin ½ chains. The increase in the T_c value with the concentration of V_V scales with a parametric value of ⅔, which matches with the reported scaling parameter of dimerized finite-sized Heisenberg spin ½ chains confirming our phenomenological model for the increase in the T_c value with doping. In fact, both the increase and decrease of T_c value by doping can also be explained from our reduced 1-D band model. As spin-wave propagates independently from the charge-density waves, the shift in the frequency of spin-wave with doping in the absence of any structural phase transition confirms that the SPT does not prompt the MIT. It is argued that MIT is driven by strong electronic correlation. The structural transition is of spin-Peierls type, which is initiated due to the dimerized spins resulting from Mott transition at a lower temperature. Mott type MIT prompts the spin–Peierls type structural transition because of reduced one-dimensionality achieved in the lowest half-filled band.

4.6 References:

1.   Morin, F. J. Oxides Which Show a Metal-to-Insulator Transition at the Neel Temperature. *Phys. Rev. Lett.* **1959**, *3*, 34.

2.   Haverkort, M. W.; Hu, Z.; Tanaka, A.; Reichelt, W.; Streltsov, S. V.; Korotin, M. A.; Anisimov, V. I.; Hsieh, H. H.; Lin, H. -J.; Chen, C. T.; Khomskii, D. I.; Tjeng, L. H. Orbital-Assisted Metal-Insulator Transition in VO_2. *Phys. Rev. Lett.* **2005**, *95*, 196404.

3.   Kim, H. -T.; Lee, Y. W.; Kim, B. -J.; Chae, B. -G.; Yun, S. J.; Kang, K. -Y.; Han, K. -J.; Yee K. -J.; Lim, Y. -S. Monoclinic and Correlated Metal Phase in VO_2 as Evidence of the Mott Transition: Coherent Phonon Analysis. *Phys. Rev. Lett.* **2006**, *97*, 266401.

4.   Eyert, V. The Metal-Insulator Transitions of VO_2: A Band Theoretical Approach. *Ann. Phys. (Leipzig)* **2002**, *11*, 650-702.

5.   Belozerov, A. S.; Korotin, M. A.; Anisimov, V. I.; Poteryaev, A. I. Monoclinic M1 Phase of VO_2: Mott-Hubbard Versus Band Insulator. *Phys. Rev. B* **2012**, *85*, 045109.

6.   Biermann, S.; Poteryaev, A.; Lichtenstein, A. I.; Georges, A. Dynamical Singlets and Correlation-Assisted Peierls Transition in VO_2. *Phys. Rev. Lett.* **2005**, *94*, 026404.

7.   Villeneuve, G.; Drillon, M.; Hagenmuller, P.; Nygren, M.; Pouget, J. P.; Carmona F.; Delhaes, P. Magnetic and Structural Properties of Stoichiometric and Non-Stoichiometric (V, Al) O_2 Alloys. *J. Phys. C: Solid State Phys*. **1977**, *10*, 3621.

8.   Marini, C.; Arcangeletti, E.; Castro, D. D.; Baldassare, L.; Perucchi, A.; Lupi, S.; Malavasi, L.; Boeri, L.; Pomjakushina, E.; Conder K.; Postorino, P. Optical

Properties of $V_{1-x}Cr_xO_2$ Compounds under High Pressure. *Phys. Rev. B* **2008**, *77*, 235111.

9.   Marezio M.; Dernier, P. D. Twinning in Cr-Doped VO_2. *Acta Cryst.* **1973,** *A29*, 618.

10.   Brückner, W.; Gerlach, U.; Moldenhauer, W.; Brückner, H. P.; Mattern, N.; Oppermann H.; Wolf, E. Phase Transitions and Semiconductor-Metal Transition in $V_{1-x}Ga_xO_2$ Single Crystals. *Phys. Status Solidi A* **1976**, *38*, 93-102.

11.   A. Zylbersztejn, A.; Mott, N. F. Metal-Insulator Transition in Vanadium Dioxide. *Phys. Rev. B* **1975**, *11*, 4383.

12.   Sommers, C.; Doniach, S. First Principles Calculation of the Intra-Atomic Correlation Energy in VO_2. *Solid State Communications* **1978**, *28*, 133-135.

13.   Rice, T. M.; Launois, H.; Pouget, J. P. Comment on "VO_2: Peierls or Mott-Hubbard? A View from Band Theory". *Phys. Rev. Lett.* **1994**, *73*, 3042-3042.

14.   Goodenough, J. B. The Two Components of the Crystallographic Transition in VO_2. *J. Solid State Chem.* **1971**, *3*, 490-500.

15.   Verleur, H. W.; Barker, Jr. A. S.; Berglund, C. N. Optical Properties of VO_2 between 0.25 and 5 eV. *Phys. Rev.* **1968**, *172*, 788.

16.   Powell, R. J.; Berglund, C. N.; Spicer, W. E. Photoemission from VO_2, *Phys. Rev.* **1969**, *178*, 1410.

17.   Chen, C.; Fan, Z. Changes in VO_2 Band Structure Induced by Charge Localization and Surface Segregation. *Appl. Phys. Lett.* **2009**, *95*, 262106.

18.   Strelcov, E.; Tselev, A.; Ivanov, I.; Budai, J. D.; Zhang, J.; Tischler, J. Z.; Kravchenko, I.; Kalinin S. V.; Kolmakov, A. Doping-Based Stabilization of the M2

Phase in Free-Standing VO$_2$ Nanostructures at Room Temperature. *Nano Lett.* **2012**, *12*, 6198-6205.

19. Colton, R. J.; Guzman, A. M.; Rabalais, J. W. Electrochromism in Some Thin-Film Transition-Metal Oxides Characterized by X-Ray Electron Spectroscopy. *J. Appl. Phys.* **1978**, *49*, 409-416.

20. Nag, N. K.; Massoth, F. E. Esca and Gravimetric Reduction Studies on V/Al$_2$O$_3$ and V/SiO$_2$ Catalysts. *J. Catal.* **1990**, *124*, 127-132.

21. Montero, I.; Galán, L.; de la Cal, E.; Albella, J. M.; Pivin, J. C. Incorporation of OH Radicals in Anodic Silicon Oxide Films Studied by Secondary-Ion Mass Spectroscopy, X-Ray Photoelectron Spectroscopy and Ir Analysis. *Thin Solid Films* **1990**, *193-194*, 325-332.

22. Carnera, A.; Mazzoldi, P.; Boscolo-Boscoletto, A.; Caccavale, F.; Bertoncello, R.; Granozzi, G.; Spagnol, I.; Battaglin, G. On the Formation of Silicon Oxynitride by Ion Implantation in Fused Silica. *J. Non-cryst. Solids* **1990**, *125*, 293-301.

23. Sólyom, J. Spin-Peierls Transition in Heisenberg Chains with Quantum Spin. *Phys. Rev. B* **1988**, *37*, 5781-5786.

24. Spronken, G.; Fourcade, B.; Lépine, Y. Finite-Size Study of the One-Dimensional Spin-(1/2) Dimerized Heisenberg Chain. *Phys. Rev. B* **1986**, *33*, 1886-1903.

25. Duffy, W.; Barr, K. P. Theory of Alternating Antiferromagnetic Heisenberg Linear Chains. *Phys. Rev.* **1968**, *165*, 647-654.

26. Nazari, M.; Zhao, Y.; Hallum, V.; Bernussi, A. A.; Fan, Z. Y.; Holtz, M. Finite Size Effect on the Phase Transition of Vanadium Dioxide. *Appl. Phys. Lett.* **2013**, *103*, 043108.

27.   Kim, H. K.; You, H.; Chiarello, R. P.; Chang, H. L. M.; Zhang, T. J.; Lam, D. J. Finite-Size Effect on the First-Order Metal-Insulator Transition in VO_2 Films Grown by Metal-Organic Chemical-Vapor Deposition. *Phys. Rev. B* **1993**, *47*, 12900-12907.

28.   Fisher, B. Electrical and Seebeck Effect Measurements in Nb Doped VO_2. *J. Phys. Chem. Solids* **1982**, *43*, 205-211.

29.   Seyama, H.; Soma, M. X-ray photoelectron spectroscopic study of montmorillonite containing exchangeable divalent cations. *J. Chem. Soc. Faraday Trans. I* **1984**, *80*, 237-248.

30.   Garcıa-Escarzaga, A.; Moncayo, S.; Gutierrez-Zugasti, I.; Gonzalez-Morales, M. R.; Martın-Chiveletc, J.; Caceres, J. O.; Anal. J. Mg/Ca Ratios Measured by Laser Induced Breakdown Spectroscopy (LIBS): A New Approach to Decipher Environmental Conditions. *At. Spectrom*. **2015**, *30*, 1913-1919.

31.   CRC Handbook for Chemistry and Physics, 62nd Edition, 1981-1982.

32.   Schilbe, P. Raman scattering in VO_2. *Phys. B : Condensed Matter* **2002**, *316*, 600-602.

33.   Basu, R.; Sardar, M.; Bera, S.; Magudapathy, P.; Dhara, S. The Role Of 1-D Finite Size Heisenberg Chains in Increasing the Metal to Insulator Transition Temperature in Hole Rich VO_2. *Nanoscale* **2017**, *9*, 6537.

34.   Wu, X.; Wu, Z.; Ji, C.; Zhang, H.; Su, Y.; Huang, Z.; Gou, J.; Wei, X.; Wang, J.; Jiang,   Y. THz Transmittance and Electrical Properties Tuning across IMT in Vanadium Dioxide Films by Al Doping. *ACS Appl. Mater. Interfaces* **2016**, *8*, 11842-11850.

35. Giamarchi, T. *Quantum Physics in One Dimension* (Oxford Univ. Press, New York, 2004).

36. Sato, M.; Katsura, H.; Nagaosa, N. Theory of Raman Scattering in One-Dimensional Quantum Spin-½ Antiferromagnets. *Phys. Rev. Lett*. **2012**, *108*, 237401.

37. Takayoshi, S.; Sato, M. Coefficients of Bosonized Dimer Operators in spin-½ XXZ Chains and Their Applications. *Phys. Rev. B* **2010**, *82*, 214420.

38. Essler F.H. L.; Konik, R. M. Applications of Massive Integrable Quantum Field Theories to Problems in Condensed Matter Physics. arXiv:*cond-mat*/0412421.

39. Kuzmenko I.; Essler, F. H. L. Dynamical Correlations of The Spin-½ Heisenberg XXZ Chain in a Staggered Field. *Phys. Rev. B* **2009**, *79*, 024402.

40. Pouget J. P.; Launois, H. Dimerization of a Linear Heisenberg Chain in the Insulating Phases of $V_{1-x}Cr_xO_2$ *Phys. Rev. B* **1974**, *10*, 1801.

41. Muthukumar, V. N.; Gros, C.; Wenzel, W.; Valenti, R.; Lemmens, P.; Eisener, B.; Gu¨ntherodt, G.; Weiden, M.; Geibel, C.; Steglich, F. Frustration-Induced Raman Scattering in $CuGeO_3$. *Phys. Rev. B* **1996**, *54*, R9635.

42. Van Loosdrecht, P. H. M.; Zeman, J.; Martinez, G.; Dhalenne, G.; Revcolevschi, A. Magnetic Interactions and the Pressure Phase Diagram of $CuGeO_3$. *Phys. Rev. Lett*. **1997**, *78*, 487.

43. Ruckamp, R.; Baier, J.; Kriener, M.; Haverkort, M. W.; Lorenz, T.; Uhrig, G. S.; Jongen, L.; Moller, A.; Meyer, G.; Gruninger, M. Zero-Field Incommensurate Spin-Peierls Phase with Interchain Frustration in TiOCl. *Phys. Rev. Lett*. **2005**, *95*, 097203.

44.   Bates, P. A.; Cottam, M. G.; Smith, S. R. P. "Anomalous" Behavior of the Anti-Stokes-Stokes Intensity Ratio for One-Magnon Raman Scattering in FeF_2. *Solid State Commun*. **1980**, *33*, 129.

45.   White, R. M.; Nemanich, R.; Herring, C. Light Scattering from Magnetic Excitations in Orthoferrites. *Phys. Rev. B* **1982**, *25*, 1822.

46.   Basu, R.; Patsha, A.; Chandra, S.; Amirthapandian, S.; Raghavendra, K. G.; Dasgupta, A.; Dhara S. Polarized Tip-Enhanced Raman Spectroscopy in Understanding Metal-to-Insulator and Structural Phase Transition in VO_2. *J. Phys. Chem. C* **2019**, *123*, 11189.

CHAPTER 5

APPLICATION OF VO$_2$ IN THE LIGHT OF PHASE TRANSITION

"*There are no such things as applied sciences, only applications of science.*"

— Louis Pasteur

5.1   Introduction:

Transition metal oxides play the key role as the next generation of power-efficient electrical and optical devices [1,2]. V is a transition metal ([Ar]$3d^3 4s^2$) having valences ranging between +2 to +5 with principal oxides in the form of VO, V$_2$O$_3$, VO$_2$, and V$_2$O$_5$, respectively [3]. However, the V-O phase diagram includes mixed-valence oxides containing two oxidation states, such as V$_4$O$_9$, V$_6$O$_{13}$, V$_8$O$_{15}$, V$_7$O$_{13}$, V$_6$O$_{11}$, and others allowing easy conversion between oxides of different stoichiometry. The oxides of V are classified into two groups, (i) Magneli phases (V$_n$O$_{2n-1}$) and (ii) Wadsley phases (V$_n$O$_{2n+1}$), respectively [4]. It is noteworthy that most of the Magneli phases undergoes a metal-to-insulator transition (MIT) at certain temperature, such as, V$_2$O$_3$ (~170K), V$_3$O$_5$ (~430K), V$_4$O$_7$ (250K), V$_5$O$_9$ (130K), V$_6$O$_{11}$ (170K), V$_8$O$_{15}$ (70K), and V$_9$O$_{17}$ (70K) [3,5]. The Wadsley phases, on the other hand, exhibit no MIT except for V$_6$O$_{13}$ (150K) [5]. VO$_2$ is particularly attractive among all the oxides of V because of the MIT being near to room temperature (340K) [6-8]. In addition, the MIT in VO$_2$ can not only be triggered by temperature but also with strain, pressure, chemical doping, as well as intense optical or electrostatic fields [9-12]. Along with MIT, significant changes also take place in the optical and structural properties of VO$_2$ [13,14]. The resistivity changes by four orders of magnitude through the transition [9], and the material reflects the electromagnetic radiation in the infrared (IR) region at high-temperature metallic phase, whereas it transmits IR at low-temperature semiconducting phase [13,15,16].

However, the material is known to be transparent in the visible region [17]. These interesting physical and chemical properties make VO_2 a promising material for electrochromic and thermochromic devices [18,19], supercapacitors [20,21], energy storage devices [22], batteries [23], bolometers [24], and chemical gas sensors [25-27].

In the present chapter we have explored three amongst the above-mentioned applications of VO_2; which are,

(i) Binder free supercapacitor, where we studied the influence of each structural phase and corresponding oxidation states of VO_2 nanoporous structures grown on carbon fiber on supercapacitor performance.

(ii) Advanced smart window, where we found VO_2 applicable for overall heat management of closure by filtering blue light along with the IR reflection above the transition temperature.

(iii) Methane (CH_4) sensing near room temperature, where the evaluation of sensing response of VO_2 around the transition temperature reveals a higher response for the semiconducting state than that of a metallic one. We extended the CH_4 sensing study towards the phase-pure Wadsley V_nO_{2n+1} (between VO_2 and V_2O_5) phases with in-situ oxidation to find the role of oxidation states and phase-purity of these materials while operating at high temperature.

5.2 VO_2 as Binder Free Supercapacitor:

Supercapacitors (SCs) are one of the emerging technologies for energy storage devices because of their longer cycle life, higher power density, and environmental friendliness compared to conventional batteries [28-30]. Carbon materials, metal oxide or hydroxide, and conducting polymer are choices of suitable candidates as electrodes for SC [31-33]. Carbon materials provide good conducting pathways to the electrolyte ion for electric double layer (EDL) formation, chemical stability, and excellent electrical conductivity [34]. However, the charge storage capacity is limited [31]. The conducting polymer is also an attractive choice

as a pseudo-capacitor [33], but the electrochemical stability is poor. In this context, transition metal oxides (TMOs) are fascinating candidates on account of their variable oxidation states and hence rapid redox kinetics [32]. There is an enormous impetus to improve the energy density for their commercialization. Even though the availability of other TMOs [35,36,37], such as RuO_2, MnO_2, Fe_2O_3, ZnO, In_2O_3, vanadium oxides are attractive candidates as SC electrode owing to their catalytic nature as well as low-cost and abundant storage on earth [38,39,40]. The poor charge storage properties and electrical conductivity of V-based materials can be overcome by fabricating directly on the current collector. There are several reports on SC properties of VO_x composites [33, 41-52]. VO_2 can be a good choice for electrode because of its higher electronic conductivity and structural stability due to the increased edge-sharing and the consequent resistance to lattice shearing during cycling as reported by Lampe-Onnerud *et al.* [53]. Issues related to the presence of multiple valence states of V [40], as well as its stability affecting capacitance retention and efficiency, is found to impede further utility in SCs. In this context, role of varied structural forms of VO_2 on super-capacitive behavior is yet to be understood. The present study not only stresses on the betterment of results with vanadium oxide but also attempts to provide insight into how different phases and metastable phases of VO_2 contribute and behave electrochemically.

5.2.1 Sample synthesis and phase confirmation

VO_2 samples were grown by vapor transport process using bulk V_2O_5 powder as source and Ar (99.9%) as a carrier gas. Carbon paper, composed of an open mesh of carbon fibers, was used as a substrate and placed on the high pure (99.99%) alumina boat inside a quartz tube. The source was placed in an alumina boat, which was kept in a furnace and was pre-evacuated up to 10^{-3} mbar. The substrate was kept above the source and downstream to the

Ar flow direction. The samples were prepared with Ar flow of 10, 20 and 30 sccm named as S11, S12, and S13, respectively. The synthesis was carried out for 3 hrs at an optimized growth temperature of 1150K. As-grown VO_2 structures on carbon paper were used as binder-free SC electrode. Noteworthy to mention that fabrication of the electrode did not require any additional steps such as preparing a slurry by mixing active material, binder and conductive additive in a solvent, coating slurry on a current collector and drying at a certain temperature for several hours.

To investigate the coating of VO_2 structure on the carbon fiber, FESEM analysis is performed, and a typical micrograph is shown in figure 5.1.
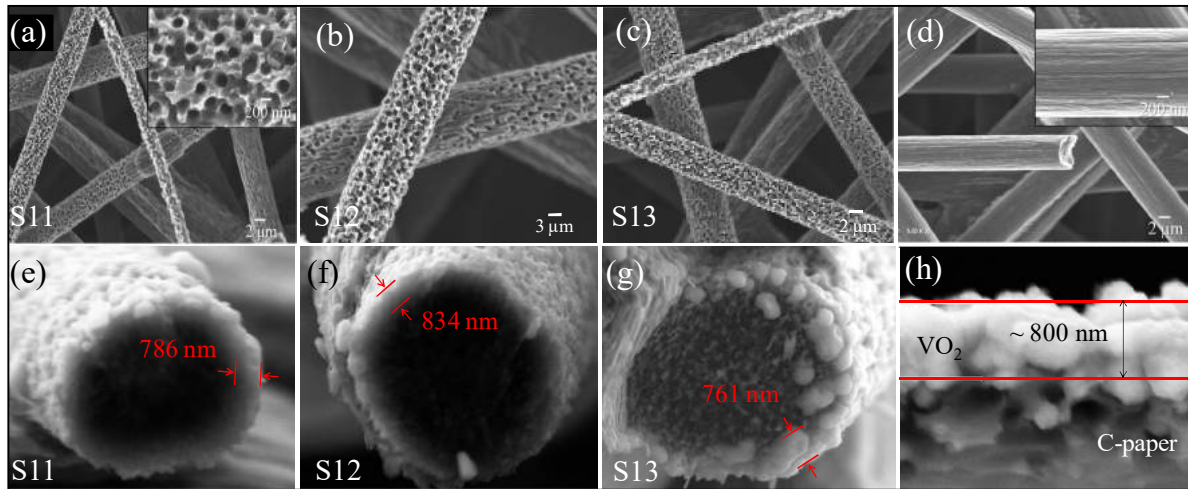
Figure 5.1 FESEM images of sample (a) S11, (b) S12, (c) S13, and (d) bare carbon fiber. Inset of (a) shows the magnified image with a typical pore diameter of approximately 200 nm. Inset of (d) shows the magnified image of bare carbon fiber. Cross-sectional FESEM images of sample (e) S11, (f) S12, and (g) S13 showing thickness of VO_2 layer around 800($\pm$50) nm. (h) Typical high magnification image for the sample S13 shows the thickness of VO_2 layer as approximately 800 nm.

The conformal coating of VO_2 porous structure on the carbon fiber for three grown samples S11 (Fig. 5.1a), S12 (Fig. 5.1b), and S13 (Fig. 5.1c) show similar morphology and average pore diameter. The structure consists of nanopores with pore diameters of

134

approximately ~200 nm, as observed from the inset of figure 5.1a. The cross-sectional FESEM images for the samples S11, S12, and S13, are shown in figures 5.1e-g, respectively. The thickness of the VO_2 nanoporous layer is found to be around 800($\pm$50) nm for all the samples (Fig. 5.1h for sample S13). FESEM image obtained from the bare carbon fiber shown in figure 5.1d ensures the porous nature VO_2 after the growth.

Expectedly, V_2O_5 gets reduced to VO_2 after reacting with C and releases CO_2 in forming nanoporous structure [54],

$$2V_2O_5 + C \rightarrow 4VO_2 + CO_2 \;…..………………………….(5.1)$$
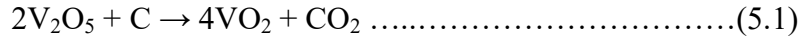
The ordered nanopores in the VO_2 structure can offer a large surface area and shortest channel/pathways for the electrolyte ions for enhanced SC performance.

The crystallographic structural analysis and phase confirmation of VO_2 were studied by glancing incidence x-ray diffractometer (GIXRD; Inel, Eqinox 2000) with a glancing angle (θ) of 0.5° in the θ-2θ mode and Cu K_α was used as the radiation source (λ=1.5406 Å). Crystallographic structural analyses are shown in figure 5.2a for samples grown with varying O content. The monoclinic M1 phase of VO_2 is confirmed in sample S11 from the diffraction peak at 2θ = 27.83°, which is assigned as (011) plane (JCPDS # 04-007-1466) [55]. Whereas sample S13 shows diffraction peaks and corresponding (*hkl*) planes at 27.58° (201) and 28.14° ($\bar{2}$01) plane (JCPDS # 01-071-0289) indicating the presence of T phase of VO_2 [56]. In case of sample S12, observation of diffraction peaks and corresponding crystalline planes at 2θ = 27.83° (011)$_{M1}$, 27.58° (201)$_{M2/T}$ and 28.14° ($\bar{2}$01) $_{M2/T}$ confirm the presence of both M1 and T phases of VO_2. The presence of the T phase in the O rich samples (S12 and S13) suggests that V^{4+} state is replaced by V^{5+}, as described in chapter 3 [57].

The mode of vibration and phase information of as-grown VO_2 structures are investigated by Raman spectroscopy. The typical Raman spectra for the samples S11, S12, and S13 at room temperature are shown in figure 5.2b.
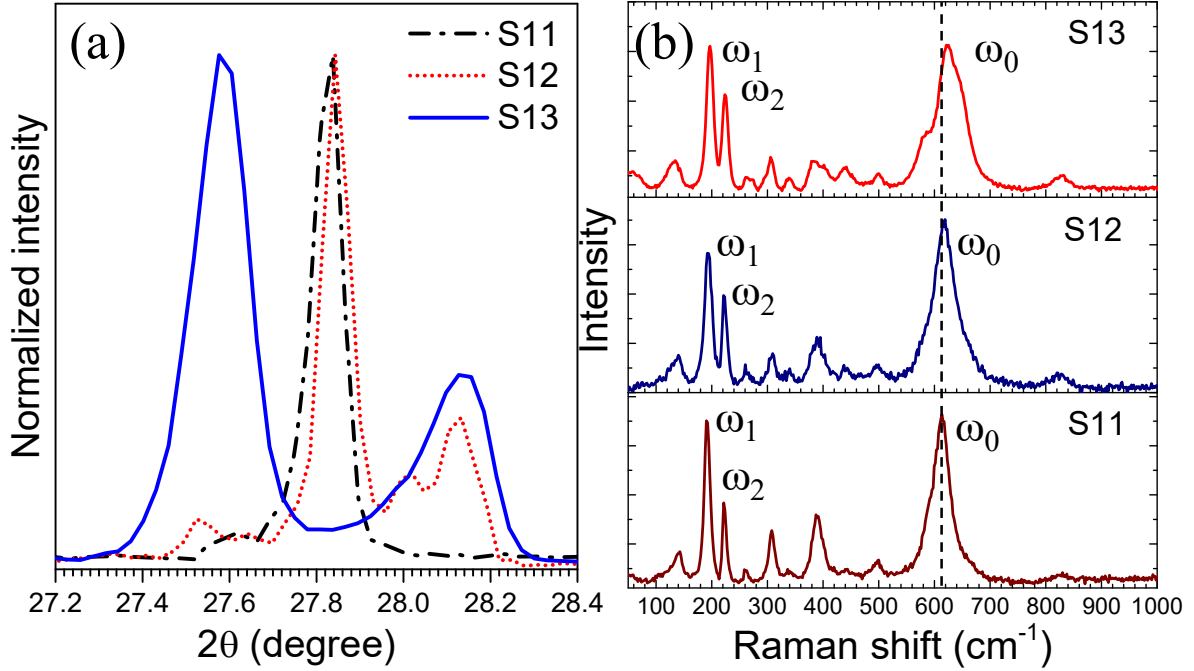
Figure 5.2 (a) GIXRD pattern and (b) Raman spectra of the pristine samples S11, S12, and S13.

Raman modes at 141 (A_g), 190 (A_g), 221 (A_g), 259 (either A_g or B_g; A_g/B_g), 308 (A_g), 339 (A_g), 389 (A_g/B_g), 440 (A_g/B_g), 498 (A_g/B_g), 612 (A_g), 829 (B_g) cm^{-1} confirm the presence of pure M1 phase of VO_2 in sample S11 and is in good agreement with earlier reports [58,59]. The Raman modes denoted as ω_0, ω_1, and ω_2 (Fig. 5.2b) correspond to V-O vibrations, the vibration of V ions in the transverse and vibration of V ions along the c axis, respectively [60]. The two major differences observed between the Raman spectra of the sample S11 and S13 are: (i) a blue shift of the Raman modes at 190 cm^{-1} (ω_1), and 221 cm^{-1} (ω_2) by an amount of 7 and 4 cm^{-1}, respectively; (ii) a significant blue shift of the Raman mode for 612 cm^{-1} (ω_0) and appearance of a new peak at 578 cm^{-1}, which indicates the signature for presence of the T phase of VO_2 [10]. We have collected confocal Raman spectra to confirm

the presence of pure VO_2 phases on the surfaces of the structures (Fig. 5.3). Raman signals arising from carbon paper beneath of VO_2 could easily be identified by adjusting the depth of focusing using confocal microscopy. The Raman modes below 1000 cm^{-1} correspond to VO_2 and above 1000 cm^{-1} are due to carbon paper.
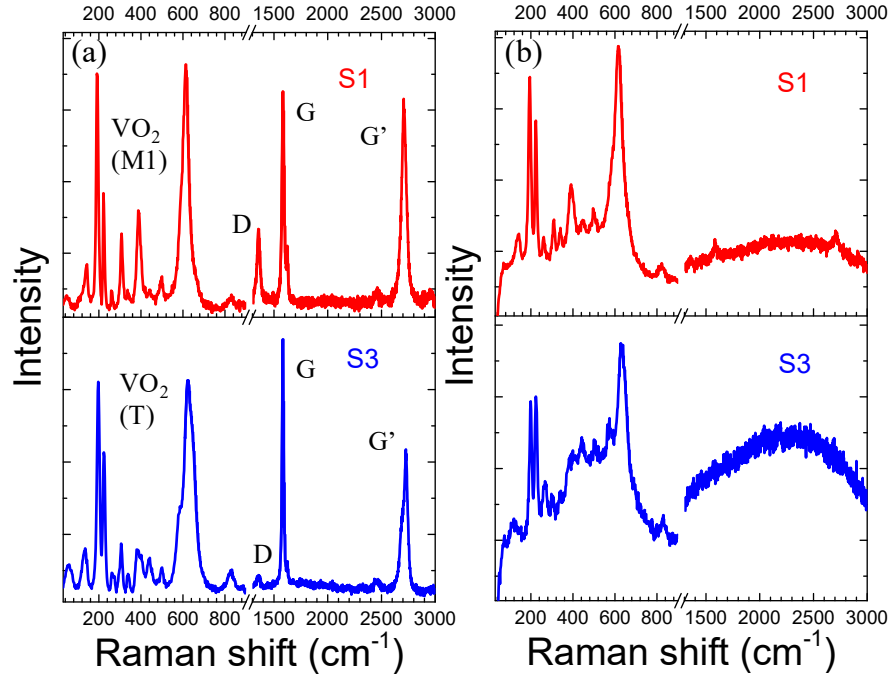
Figure 5.3 (a) Normal and (b) confocal Raman spectra of the pristine samples S11 and S13. The Raman modes below 1000 cm^{-1} correspond to VO_2 and above 1000 cm^{-1} are due to carbon paper.

The absence of Raman modes of carbon paper in confocal Raman spectroscopy confirms the surface of the material is constituted of pure VO_2.

In order to determine the chemical oxidation states of V and O, XPS study was employed on the VO_2 structures. The typical XPS spectra of V2$p_{3/2}$ and O1s peak of VO_2 are shown in figure 5.4. Details of XPS result for the samples grown on Si substrate are discussed in chapter 3, and we have shown that the substrate-induced strain effect plays no role in stabilizing the metastable phases [57].
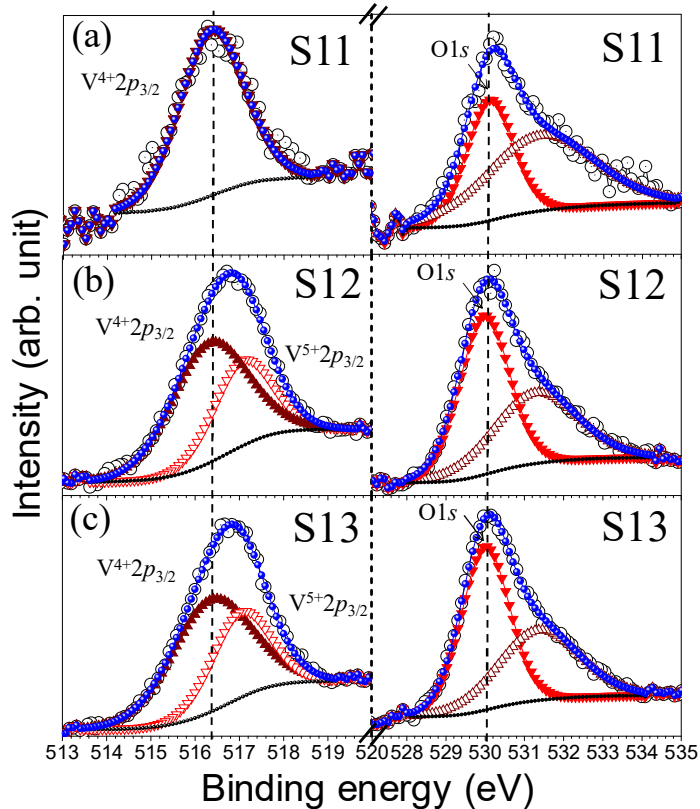
Figure 5.4 High resolution XPS spectra of sample (a) S11, (b) S12, and (c) S13. Open circles represent the data points, solid arrows and circles represent the fitted curves. In the left panel, solid and empty arrows correspond to V^{4+} and V^{5+} oxidization states, respectively. In the right panel, solid arrows correspond to lattice oxygen, and empty arrows correspond to oxygen from absorbed oxygen species. The vertical dashed lines denote the corresponding BE values for $V^{4+}2p_{3/2}$ and lattice O1s states. Black small dots represent Shirley type background correction.

The presence of $2p_{3/2}$ peak at 516.3 eV is assigned as a V^{4+} state, and only V^{4+} state is observed for sample S1. The full width half maxima (FWHM) of the peak corresponding to V $2p_{3/2}$ from sample S11 is found out as 1.7 eV (left panel Fig. 5.4a) which is increased to 2.0 (left panel Fig. 5.4b) and 2.1 eV (left panel Fig. 5.4c) in samples S12 and S13, respectively. The higher FWHM is attributed to the presence of additional chemical state in the samples. Hence, the peaks in sample S12 and S13 are deconvoluted, and a suitable peak fitting gives

rise to a peak at 517.1 eV in addition to the peak at 516.3 eV. The peak evolved at 517.1 eV is assigned as V^{5+} state in samples S12 to S13 as proposed in the XRD study. The ratio of the area under the curves of the two peaks, i.e., V^{5+}/V^{4+} increases progressively from S11 to S13. On the other hand, O1s peak at low BE value of 530 eV is attributed to O in the lattice, and that for high binding energy (BE) value at 531.5 eV corresponds to absorbed O species. The intensity and area under the curve of O1s are found to increase from sample S11 to S13 (right panel Fig. 5.4).

According to the phase-diagram of VO_2, metastable T phase evolves with an increase in temperature during the transition from monoclinic M1 to rutile R phase [61]. The zeta potential of the three samples is found out to be -35.6, -30.3, and -14.4 mV for samples S11, S12, and S13, respectively. The decrease in the value of zeta potential with an increase in the V^{5+}/V^{4+} ratio is in good agreement with the reported data [62]. The work functions of the samples are calculated from scanning Kelvin probe microscopy (SKPM) measurements using 20 nm conductive Pt-Ir coated Si tip. The work function of the tip was calibrated using Au reference and found out as 5.22 eV. Each line scan of SKPM mode is composed of a topography scan and a subsequent contact potential difference (CPD) measurement (Fig. 5.5). The work function of VO_2 is reported to decrease with increasing temperature and expected to be less in the T phase, than that of the M1 phase [63]. The work function of the three samples are calculated from SKPM measurements as 5.35, 4.81, and 4.8 eV for samples S11 in M1 phase, S12, and S13 with T phase, respectively, using the equation:

$$V_{CPD} = (\phi_M - \phi_S) / e \ldots\ldots\ldots\ldots\ldots\ldots\ldots\ldots\ldots\ldots\ldots \quad (5.2)$$

where ϕ_M and ϕ_S are work functions of the metal tip and the sample, respectively, and e is the elementary charge.
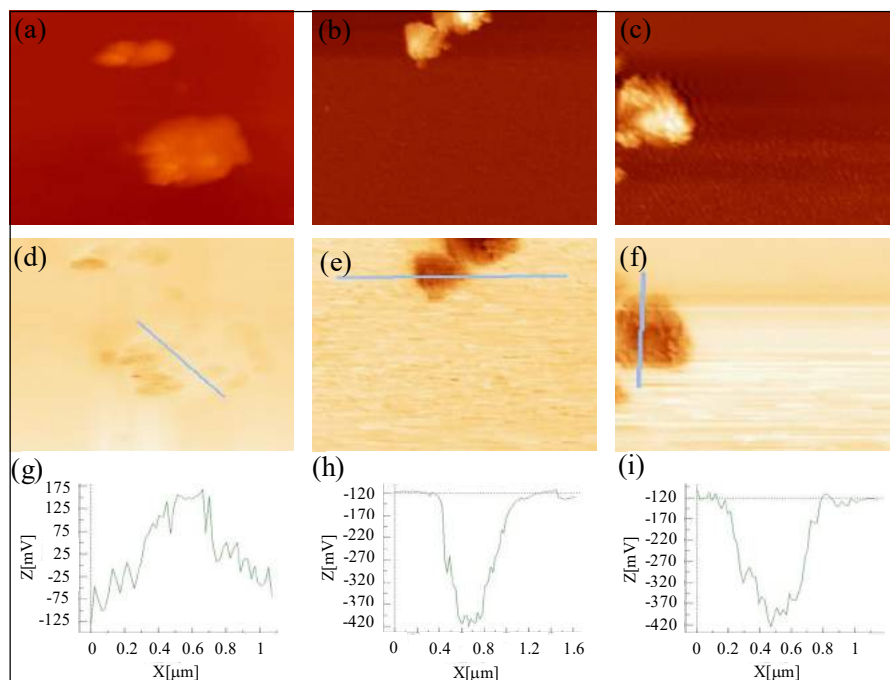
Figure 5.5 Topography of samples (a) S11, (b) S12, and (c) S13 with (d)-(f) and (g)-(i) showing corresponding SKPM images and the contact potential difference across the lines, respectively.

5.2.2 Supercapacitive performance

Supercapacitive performances of the VO$_2$ samples were investigated by cyclic voltammetry (CV), charge-discharge profile and electrochemical impedance spectroscopy (EIS) in three-electrode configuration using an electrochemical work station (Metrohm-Autolab, model PGSTAT302N). Ag/AgCl (3M KCl saturated) and Pt foil (1×1 cm^2) were used as reference and counter electrodes, respectively. A carbon paper (1 × 2 cm^2) was used as a substrate for growth of all the samples, where (1×1 cm^2) area was masked to avoid any VO$_2$ deposition and used for making electrical contact. The rest (1×1 cm^2) area, completely coated with VO$_2$, was used as working electrode. All the three electrodes were mounted by a lid and immersed vertically down in 1M Na$_2$SO$_4$ electrolyte media. The cell is assembled such that only the VO$_2$ coated area is exposed to the electrolyte

and the electrical contact area is away from the electrolyte level. The cyclic voltammetry behaviors at scan rates ranging from 10 to 100 mV/s and charge-discharge cycles at different current densities from 0.3 to 1.0 mA/cm^2 were carried out in a potential window of 0.5 V. EIS was performed in the frequency range 10 kHz to 0.001 Hz with open circuit potential, with an alternative current perturbation of 10 mV. The Nyquist plots were drawn from the impedance data and were fitted with a suitable equivalent electric circuit using EIS spectra analyzer software. Before, SC investigation, all samples were presoaked in the electrolyte for better wettability.

Investigation for the SC performance of the as-grown VO$_2$ samples is carried out in the three-electrode electrochemical cell. The specific capacitance is calculated using the given formula:

$$C = (\int I.dV)/v.A.V \text{ from cyclic voltammogram (CV)} \ldots\ldots\ldots\ldots\ldots(5.3)$$

$$C = (It_d)/V \quad \text{from charge-discharge} \quad \ldots\ldots\ldots\ldots\ldots\ldots\ldots (5.4)$$

where I is the current, v is scan rate; A is exposed area of the electrode in the electrolyte, t_d is discharge time, V is the potential window.

The cyclic voltammogram (CV) plots of the studied samples are carried out at potential scan rate from 10 to 100 mV/s at a potential window of 0.5 V (Figs. 5.6a-c). The near-rectangular CV with symmetrical shape is observed for the sample S11 at scan rates of 10 and 20 mV/s (Fig. 5.6a). The current density of the system is found to increase with increasing scan rate, suggesting fast kinetics and reversibility of the system. The absence of redox peak in sample S11 is attributed to mostly non-Faradic active sites for ion diffusion [64]. Hence, the obtained result ensures the fast electron transfer, which is facilitated by VO$_2$ nanoporous structure on the carbon fiber. The possible reactions are (i) surface

adsorption/desorption of electrolyte cations on the vanadium oxide (Eqn. 5.5) and (ii) intercalation/deintercalation of electrolyte cations in the bulk vanadium oxide (Eqn. 5.6):

$$(VO_2)_{surface} + Na^+ + e^- \leftrightarrow (VO_2{}^-Na^+)_{surface}\ldots\ldots\ldots\ldots\ldots\ldots\ldots\ldots\ldots(5.5)$$

$$VO_2 + Na^+ + e^- \leftrightarrow VO_2Na\ldots\ldots\ldots\ldots\ldots\ldots\ldots\ldots\ldots(5.6)$$
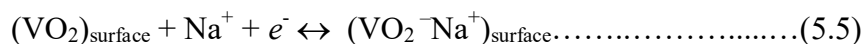
It is noteworthy that unlike sample S11, the signature of the oxidation peak is observed for both the samples S12 and S13 (Figs. 5.6b-c).
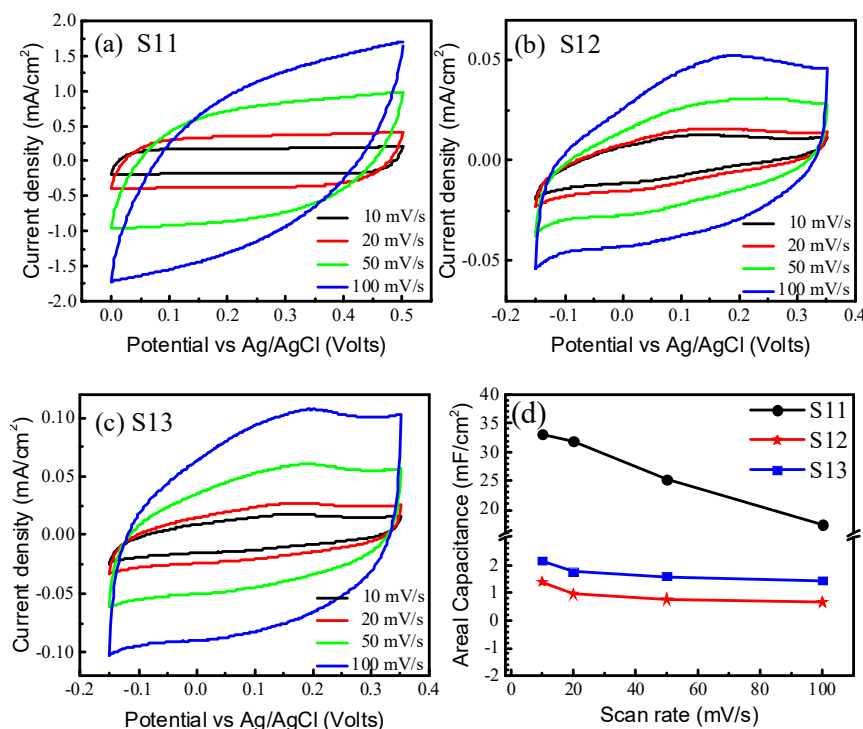
Figure 5.6 Cyclic voltammogram of (a) S11, (b) S12 and (c) S13. (d) Areal capacitance *versus* scan rate of the VO$_2$ samples.

The shape of CV plots for both the cases is unaltered with respect to the scan rate confirming its reversible nature. Redox reactions in sample S12 and S13 can be initiated due to the presence of mixed-valence states V^{4+} and V^{5+} in those samples. The areal capacitances of the samples are calculated using equation 5.3. The estimated areal capacitance of samples S11, S12 and S13 are 33.15±0.8, 1.39±0.06 and 2.16±0.04 mF/cm^2, respectively. The error

indicates the variation in collected data for spare samples of each type. The CV plot of the bare carbon paper was also carried out at the same potential window of 0.5 V *versus* Ag/AgCl, and the areal capacitance was found out to be 85 $\mu F/cm^2$ (not shown in figure). The value is significantly smaller than those for any of the VO_2 coated samples showing that the major contribution of areal capacitance is essentially from VO_2. According to equation 5.1, there was a loss of CO_2 from the substrate where the samples were synthesized by the CVD technique at 1150K for 3 hrs. The loss of CO_2 affects the weight of C paper. In that case, using weight of carbon paper as reference becomes ambiguous for measuring the weight of VO_2. So, following other references where active surface is taken for quantification [47, 65-69], the capacitance value is described in F/cm^2. Moreover, the surface area for all the samples is approximately same as shown from FESEM studies (Fig. 5.1). Sample S11 shows higher capacitance value than the reported values of other materials and the comparison is listed in table 5.1.

Table 5.1 Comparison of supercapacitive performance of VO_2 structures with other nanostructures

Sample	Areal Capacitance mF/cm^2	References
Multi-layer TiO_2 nanotube	0.06	Zheng *et al.* [65]
Carbon modified multi-layer TiO_2 nanotube	3.75	
Vertical graphene	0.56	Ghosh *et al.* [66]
MnO_2-Vertical graphene	5.64	
Al_2O_3-TiO_2	0.13	Du *et al.* [67]
Carbon nanotube	0.46	Zhou *et al.* [68]
Carbon nanotube/Polypyrrole	18.25	
TiVN	15	Achour *et al.* [69]
Monoclinic (M1) VO_2	33.15	Present work

Although capacitance values of S12 and S13 samples in T phase are higher than those of Al_2O_3-TiO_2, multi-layer TiO_2, carbon nanotube, and vertical graphene nanosheets, however, they are one order lower than that of sample S11 (M1 phase). The observed result, which matches well with the existing report by Tang *et al*. [46], is attributed to the O content of VO_2 structure. The quasi-rectangular shape of CV plots and decreased capacitance at higher scan rates (Fig. 5.6d) are attributed to the inaccessibility of electrolyte ion interior of the active material. The higher capacitance value for sample S11 can be understood from the formation of a double layer at the interface. The work function of sample S11 is found to be 5.35 eV, whereas, in case of samples S12 and S13, the work function values are ~ 4.8 eV (Fig. 5.5). As the work function of C is 4.81 eV [70], it is quite expected that at the interface of VO_2/C, there is a probability of formation of space charge region for sample S11 only. EDL at S11/C interface contributes to the space charge capacitance for sample S11.

The SC behavior of VO_2 nanoporous structures is also confirmed from the charge-discharge profile at different current density ranges from 0.3 to 1.0 mA/cm^2 (Figs. 5.7a-c). Excellent SC behavior includes a linear and symmetric charge-discharge profile for samples S11 and S12, as shown, respectively, in figures 5.7a and 5.7b. The insignificant potential drop of 0.03 V in discharge profile of sample S11 is attributed to the charge transfer resistance and electrode-electrolyte resistance (Fig. 5.7a). At a current density of 0.3 mA/cm^2, the specific capacitance of sample S11 is found to be 20.7 mF/cm^2. The reduced specific capacitance of 14.7 mF/cm^2 is observed at a higher current density of 1 mA/cm^2. However, a non-linear charging-discharging profile is observed for the sample S13, implying the poor surface charge capability in the sample, which may be correlated to the low value of zeta potential for this sample. Sample S13 is in the T phase of VO_2 containing the maximum

amount of V^{5+} (d^0) states (holes), and it can resort to the oxidation process easily to maintain charge neutrality. The obtained capacitance values of samples S12 and S13 are 0.47 and 0.68 mF/cm^2, respectively. Low capacitance values of samples S12 and S13, as compared to that for sample S11, match with CV results where one order higher value of areal capacitance is calculated for sample S11.
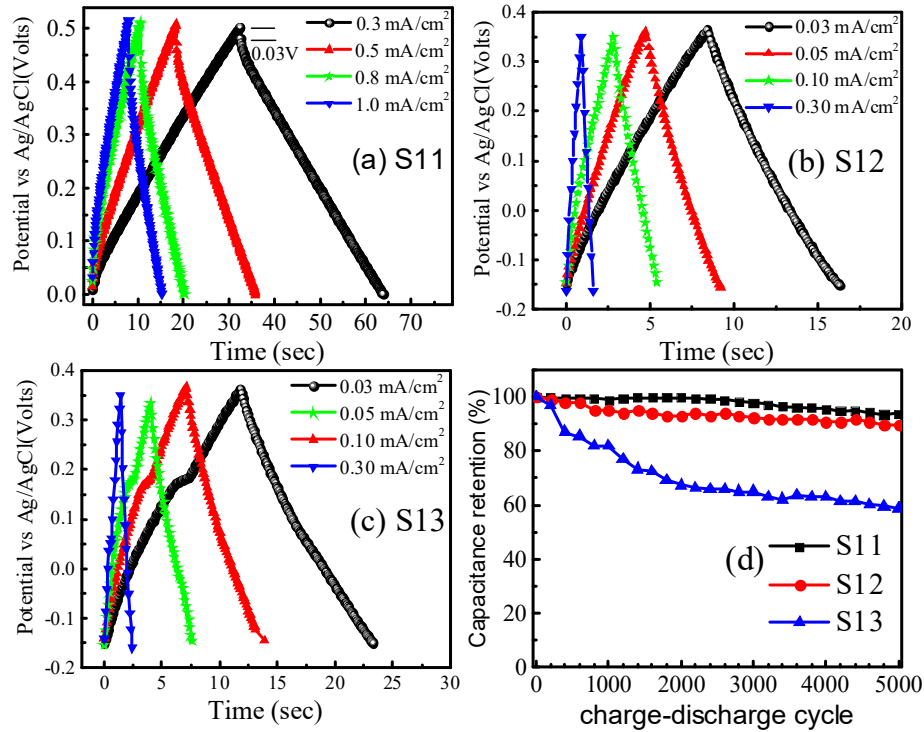
Figure 5.7 Charge-discharge profiles at current density of 0.3 to 1.0 mA/cm^2 (a) S11, (b) S12 and (c) S13 (d) capacitance retention of the samples with charge-discharge cycle.

The cyclic stability is one of the key parameters for high-performance SC. Coulombic efficiency of the samples is obtained from the equation,

$$\eta = t_{\mathrm{d}}/t_{\mathrm{c}} \quad \text{..} \quad (5.7)$$

where t_c is the charge time.

The capacitance retention of 93.7% with a Coulombic efficiency of 98.2% for 5000 charge-discharge cycles suggests excellent rate capability, reversibility, and durability of

sample S11 (Fig. 5.7d). The cyclic stability is found to be superior to recently studied $VO_2(B)/C$ core-shell by Zhang *et al*. [71]. Whereas, sample S12 shows capacitance retention of 89.8% with a Coulombic efficiency of 98.5% and sample S13 shows the capacitance retention of 58.9% with a Coulombic efficiency of 95.6%. The low value of capacitance retention in case of S13 (Fig. 5.7d) is because of poor surface charge potential as observed in charge-discharge profile. All the samples were re-examined by Raman spectroscopy and FESEM studies and found out to be stable after several runs.

To probe the frequency behavior of the VO_2 samples, EIS analysis is carried out, and the extracted result in terms of Nyquist and Bode plots are shown in figure 5.8. The steeper vertical line of sample S11 is observed form the Nyquist plot, as compared to those for samples S12 and S13. The results further support the superior SC behavior of sample S11, as compared to those for the other two samples. The intercept in real impedance axis is known as equivalent series resistance (R_s) which includes resistances contributed from solution, electrodes and electrode/electrolyte. The R_s is found to be 2.81 Ω for samples S12 and S13 and 46 Ω for sample S11 (Fig. 5.8a), representing good electrical contact between VO_2 and carbon paper. The semi-circular arc represents the double-layer formation [72] between active material and electrolyte. This signature is observed from the shape of CV plot (Fig. 5.6). However, a semicircular arc at high frequency is observed only for sample S11 from the Nyquist plot, as depicted in the inset of figure 5.8a. The disappearance of semicircular arc in samples S12 and S13 can be explained by the space charge polarization at the interface between VO_2 and carbon paper, as expected from SKPM results which indicate similar work functions for these samples and carbon.

The phase angle with respect to the frequency (Bode plot) is plotted in figure 5.8b. The phase angle of 81° at lower frequency region intuitively reveals the better-quality supercapacitive behavior in sample S11, as it approaches a phase angle of an ideal SC of 90°. Whereas, stability issue is observed for samples S12 and S13, which in-turn show reduced phase angle at a lower frequency. These results support our charge-discharge data (Fig. 5.7). The Bode plot (Fig. 5.8b) comprises a hump around 100 Hz for sample S11 confirming the excellent electrolyte ion accessibility and capacitance retention [73]. Moreover, the time constant of the system demarcating the power delivering capability is obtained from the Bode plot at a phase angle of 45°. Two-time constants are estimated for the sample S11 are 1.87 s and 5.8 ms, which again prove the contribution from space charge polarization at S11/C interface. Time constants for samples S12 and S13 are found to be 5.8 and 6.9 ms. The low time constants suggest the fast charge delivery capability of the VO_2/Na_2SO_4 system.
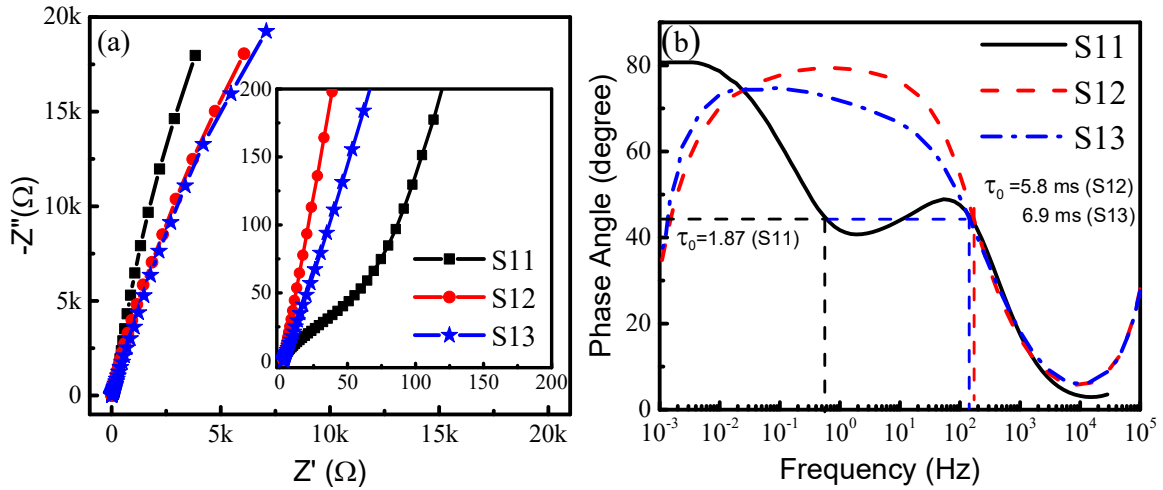
Figure 5.8 (a) Nyquist plot and (b) Bode plot of VO_2/Na_2SO_4 system

The specific (sp.) energy densities (E) and power densities (P) of the samples are calculated using equations (5.8) and (5.9).

$$E = CV^2/2 \quad \dots\dots\dots\dots\dots\dots\dots\dots\dots\dots\dots\dots \quad (5.8)$$

$$\text{and } P = E/t_d \quad \dots\dots\dots\dots\dots\dots\dots\dots\dots\dots\dots\dots \quad (5.9)$$

The sp. power densities for sample S11, S12, and S13 are found out as 129.3, 21.7, and 24.5

$\mu W/cm^2$, respectively. The dependence of areal energy density on areal power density is

shown in the Ragone plot (Fig. 5.9).
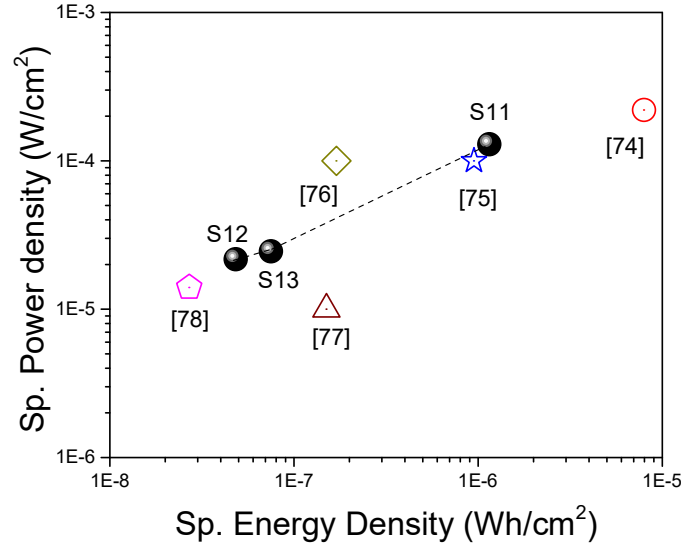
Figure 5.9 A Ragone plot of sp. energy density versus sp. power density for VO_2 nanoporous

structures. The data is compared with the published performance of other supercapacitors. Filled balls

represent the data points of this work for sample S11, S12, and S13. The dashed line guides to the

eye. The symbols represent the data from the literature with the corresponding references below.

The maximum measured energy density of the presently investigated supercapacitor for

sample S11 is 1.15 $\mu Wh/cm^2$, which is of same order to that for the flexible supercapacitors

comprising hierarchical nanostructures with carbon spheres and graphene oxide nanosheets

(7.96 $\mu Wh/cm^2$) [74], and is one order higher than Yarn supercapacitor based on

PANI/stainless steel (0.95 $\mu Wh/cm^2$) [75], graphene fiber supercapacitor (0.17 $\mu Wh/cm^2$)

[76], and Yarn supercapacitor based on CNT and Ti fibres (0.15 $\mu Wh/cm^2$) [77]. The energy

densities for sample S12 and S13 are 48 nWh/cm^2 and 75 nWh/cm^2, respectively, which are

two orders less compared to sample S11 but higher than ZnO nanowire/MnO_2 fiber

supercapacitor (27 nWh/cm^2) [78].

The supercapacitive study on the different structural phases of VO_2 nanoporous structure shows that VO_2 sample with all V in oxidation state +4 shows better SC performance because of the space charge region formed at the interface of VO_2 (M1) and carbon paper.

5.3 VO_2 as Advanced Smart-Window:

VO_2 is reported to transmit IR at low-temperature semiconducting phase and reflect IR at high-temperature metallic phase [13,15,16], whereas it is known to be transparent in the visible region [17]. However, we observed a change in color of the VO_2 microcrystals from white to cyan around the transition temperature. Generally, the optical property of a material depends on the response of electron and its transition between electronic states due to perturbation by the incident radiation. We performed temperature-dependent UV-Vis and photoluminescence (PL) spectroscopy on VO_2 microcrystals stabilized in M1 phase of VO_2 (sample, S1 as described in chapter 3) to study the change in the visible region around the phase transition of VO_2.

5.3.1 Temperature-dependent optical imaging

The optical images of the samples were captured at different temperatures using an optical microscope with a 50X objective with numerical aperture (N.A.) of 0.45 using a white light source. A change in color of the sample from white to cyan above transition temperature is observed from optical microscopic images (Fig. 5.10a). We collected simultaneous Raman spectra to monitor the phase transition. All Raman modes disappear at 340K (while increasing the temperature), confirming the MIT and reappear again at 330K (while decreasing the temperature), as shown in figure 5.10b.
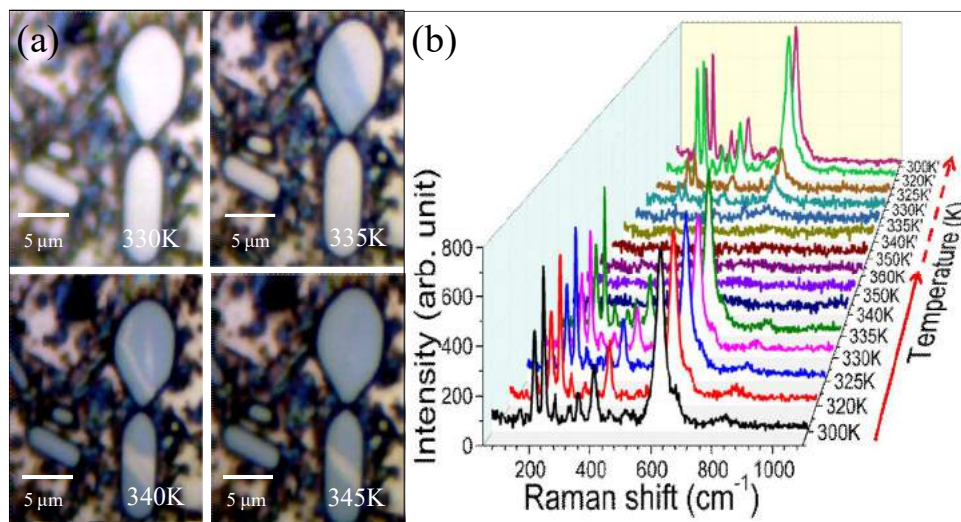
Figure 5.10 (a) Optical images of VO$_2$ micro-crystals at different temperatures and (b) Raman spectra of the sample at the temperature range 300 to 360K. Solid and dashed arrows denote increasing and decreasing temperatures, respectively.

To check whether there is any role of substrate in the observed colour change, we captured optical images of freestanding VO$_2$ crystals taken out from the Si substrate at different temperatures (Fig. 5.11).
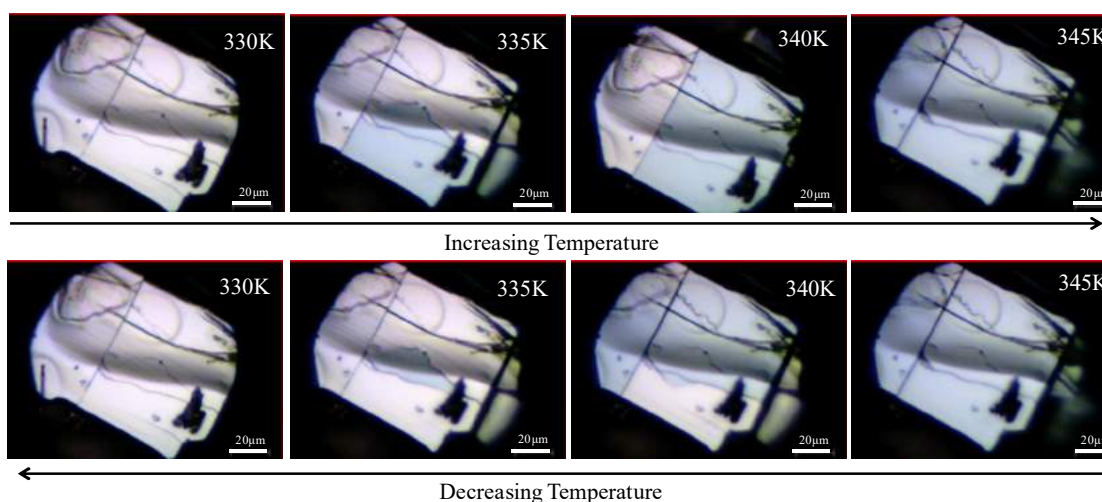
Figure 5.11 Optical images of free-standing VO$_2$ micro-crystals with increasing and decreasing temperature.

The free-standing crystals also undergo the same behavior as observed for the crystal grown on Si substrate, which confirms that optical changes at transition temperature is solely material property and does not depend on substrate. The colour of the microcrystals changed from white to cyan above transition temperature again retains their colour from cyan to white below the transition temperature.

5.3.2 Optical properties with the understanding of electronic band-structure

UV-Vis spectroscopy is one of the useful tools for the determination of colour for transition metal complexes. Transition metal ions can be colored (i.e., absorb visible light) because d electrons within the metal atoms can be excited from one electronic state to another [79,80]. For further analysis of the observed change in color during phase transition, temperature-dependent UV-Vis absorption spectra were recorded with the help of a light source of excitation wavelength in the range of 200 to 800 nm. Figure 5.12a shows UV-Vis absorption spectra at a different temperature ranging from 300 to 360K.
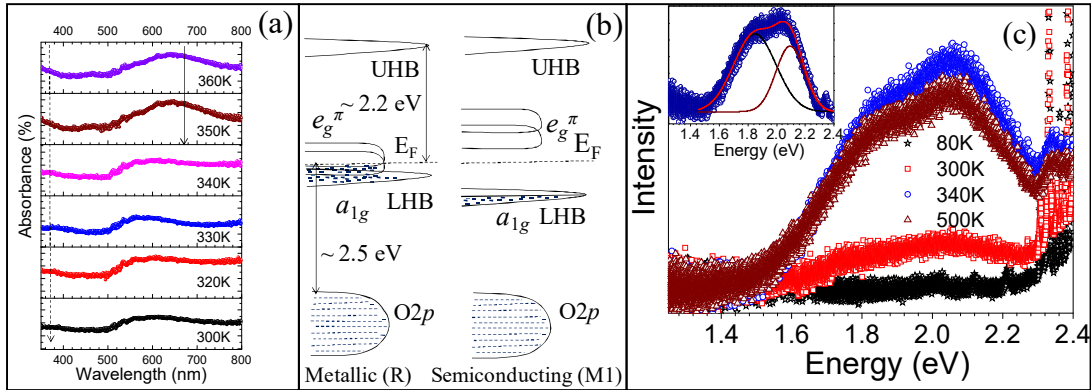
Figure 5.12 (a) UV-Vis absorption spectra of the grown sample with increasing temperature. The dashed line and solid line arrows indicate a change in slope and absorption tail, respectively, above the transition temperature. (b) Schematic electronic band structure for the semiconducting and metallic phases of VO_2 and (c) Photoluminescence (PL) spectra of the sample at different temperatures. Inset in (c) shows the deconvoluted PL spectra at 340K.

The broad absorption peak ranging the whole visible range for different temperatures of 300 to 340K can be explained as intra-band absorption [81]. A strong absorbance in the red region centered at ~ 650 nm is observed above the transition temperature ~350K. Absorption tail ~700 nm (indicated by solid arrow) is a clear indication of red light absorption above the transition temperature in the metallic phase. The alteration of the upward positive slope in the blue region below 400 nm (indicated by dashed arrow) to negative downward above the transition temperature confirms the reflection of blue light above the phase transition temperature.

The electronic band diagram of VO_2 is described in chapter 4 (Fig. 4.1). The observed colour change of the VO_2 micro-crystals is understood in the light of electronic transitions for VO_2. As discussed earlier, cluster dynamical mean field theory (C-DMFT) calculation using electronic correlation (Hubbard U) can only explain the opening of an energy gap in the low-temperature semiconducting phase of VO_2. Thus, it is important to choose the proper value of U to find the correct assessment of the energy gap. The typical value of U for transition metal oxides is ~3 to 4 eV [82]. With the intra-atomic Coulomb repulsion U set to 4.0 eV, Biermann *et al.* found out lower Hubbard band (LHB) about -1.8 eV below the Fermi level and upper Hubbard band (UHB) at about +2.2 eV [83]. The optical absorptions ~2 eV and below are attributed as an intraband transition or, free electron absorption in the previous reports [84,85]. We claim that the absorption at red region (~2 eV), as observed from the temperature-dependent UV-Vis spectra above the transition temperature, can be ascribed as transition from filled e_g^π bands to the UHB. We re-plotted the electronic band diagrams of VO_2 with LHB and UHB at low temperature insulating, and high-temperature metallic phases are shown schematically in figure 5.12b. For further analysis, temperature-dependent

photoluminescence (PL) spectroscopic studies were performed. Figure 5.12c shows the PL spectra of the as-grown sample in the temperature of 80-500K. At the lowest temperature of 80K no luminescence peak is observed with the laser excitation of 514.5 nm (2.41 eV), which is quite expected, as the valence band of VO_2 ($O2p$) is ~2.5 eV below the Fermi level in the semiconducting phase [84,85]. Although the half-filled lower-lying a_{1g} bands (LHB) may fall in the incident energy range, it will not participate in the PL process, as a single electron added to this band will jump to the UHB. The observed low intense broad peak at 300K may be attributed as the emission from UHB to e_g^π band as the e_g^π band is partially filled at room temperature [86]. At the transition temperature of 340K two broad peaks are observed at 1.85 and 2.09 eV (inset in Fig. 5.12c), which can be ascribed as transition from filled a_{1g} and e_g^π states, respectively, to the UHB which is ~2.2 eV above the Fermi level, E_F [83]. The intensity of the peaks decreases slightly with further increase in temperature up to 500K, which is natural for PL emission with increasing temperature. We carried out the PL studies for sample S2, S3, and S4 also, which were stabilized in metastable phases of VO_2 due to native defects (chapter 3). All of them show PL peaks at same energy value above the transition temperature only (not shown in figure). However, we failed to measure any PL peak up to the transition temperature starting form 80K, where defect may like to play a role also. Absence of PL emission at low temperature confirms that the PL peaks correspond to transition between band states instead of defects. The emission at ~2 eV above the transition temperature supports the absorption of light at red region, as observed from UV-Vis absorption spectroscopic study. As the color of material depends mostly on three primary colors red, green and blue (R+G+B), the absorption of red light makes the sample cyan

(G+B) above the transition temperature as observed from temperature-dependent optical microscopic images, captured above the transition temperature (Fig. 5.10a).

The thermochromism in VO_2 has been studied for smart window applications so far in the IR region, which supports the opening of the bandgap in the semiconducting phase. The filtering of the blue light along with reflection of infrared above the MIT temperature makes VO_2 applicable as advanced smart windows for overall heat management of a closure.

5.4 VO_2 as Methane Sensor:

Gas sensors with low operating temperature for detecting perilous gases are in great demand in the fields of environmental protection and human health. The identification of CH_4, the second-largest contributor to global warming after CO_2 [87], is difficult at temperatures lower than 200 °C within the safety limit of 1000 ppm for 8 h due to its high thermodynamic stability [88,89]. Catalytic materials, e.g., SnO_2 and ZnO, were used for CH_4 detection in the concentration range of a few hundreds of ppm [90-91]. However, high operating temperatures and low sensitivity remain a longstanding challenge in this area of research. In this regard, vanadium oxides form an interesting group of materials because of their varying oxidation states between V^{2+} and V^{5+}. VO_2 is particularly attractive because it exhibits a first order MIT near room temperature (340K) [6-8]. The resistance drops by four orders above the transition temperature [9]. As most of the metal-oxide gas-sensors works by resistance-based mechanism, a systemic study of CH_4 sensing behavior of VO_2 around the transition temperature needs to be probed. As VO_2 is extremely susceptible to change its oxidation state and forming various metastable phases in the presence of air, we extended the sensing study for the higher-order oxides of V than VO_2 (V_nO_{2n+1}). As most of the resistance-based gas sensors work at high temperatures in air background, the chance of oxidation is

very high, especially for multivalent oxide sensors [92]. Thus, the possibility of oxidation at a higher temperature and sensing behavior of the corresponding phase for V_nO_{2n+1} in the complete temperature range of gas sensing should be investigated systematically. We carried out brief analysis of the phase-pure Wadsley (V_nO_{2n+1}) nanoparticle as CH_4 sensor as a function of temperature and the role of oxidation state in sensing.

5.4.1 Methane sensing by VO_2 around the transition temperature

To study the CH_4 sensing behavior of VO_2 around the phase transition (340K), we have carried out the sensing performance at five different temperatures viz. 40 (313K), 50 (323K), 60 (333K), 70 (343K) and 80 °C (353K) for 50-500 ppm CH_4 (Fig. 5.13a). We prepared a pallet of VO_2 nanoparticles (sample S1) for the gas sensing experiments. The sensing was carried out in a custom-built exposure facility system using the chemiresistive method [93]. The sample was mounted on a PID controlled hot stage inside a double-walled stainless steel chamber. The gas flow rates were controlled using mass flow controllers. The sensor response upon exposure to gases was manifested as resistance changes, recorded in a standard two probe method. Commercially procured gas mixtures of ultra-high pure grade CH_4, diluted in N_2 carrier gas was used along with synthetic air background. N_2 gas is generated using TEXOL, laboratory N_2 generator. These gases were further passed through moisture traps to remove any residual humidity.

In order to ensure the reliability of the results, each gas-sensing investigation is repeated three times. There is hardly any response to CH_4 at room temperature, and it starts showing a significant change in resistance from 40 °C even for very low concentration of 50 ppm. It can be observed from the temperature-dependent resistance plot (Fig. 5.13b) that above 60 °C the resistance value decreased by four orders confirming the metal-to-insulator

phase transition in VO_2. As VO_2 is an *n*-type semiconductor; upon exposure to CH_4, the resistance of the VO_2 sensor shows a decrease in resistance [94]. The resistance drop on each exposure is consistent with the expected trend, and the magnitude of change increases with the concentration of the exposed gas.
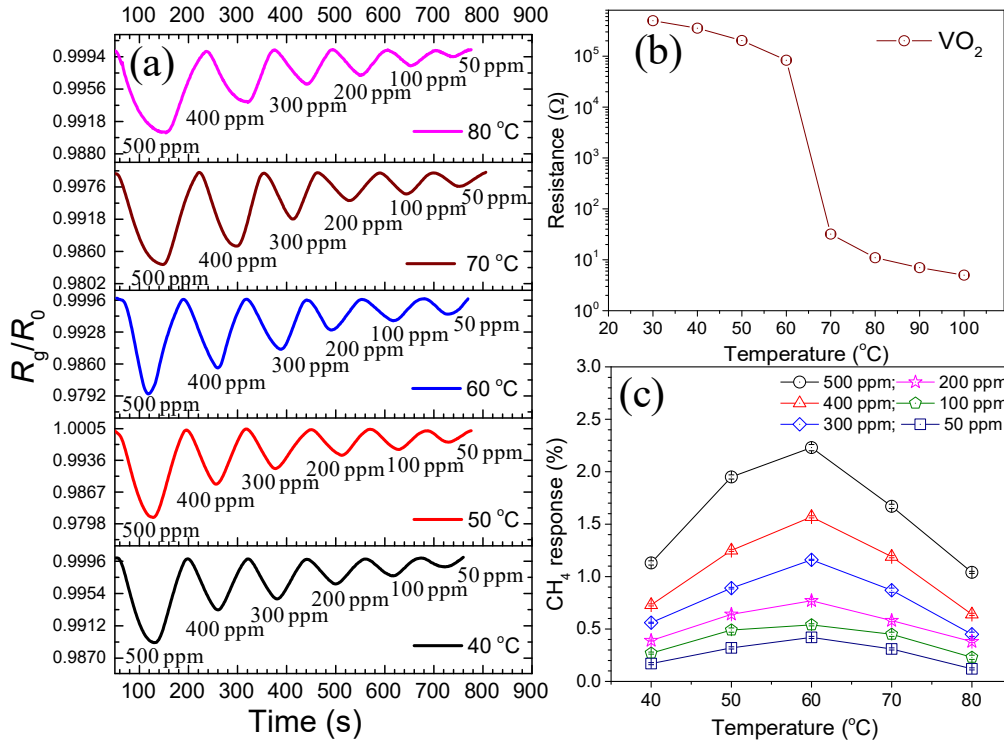
Figure 5.13 (a) Transient response curves of VO_2 towards CH_4 with temperature. Corresponding concentrations of gases are inscribed in the respective regions. (b) Base resistance (R_0) of the sample with temperature, and (c) Comparison of sensor response with operating temperatures. Estimated errors are within the size of data.

The reaction of CH_4 at the metal oxide surface happens by the chemisorption of oxygen followed by oxidation.

$$CH_4(g) + 2O_2^- \leftrightarrow CO_2 + 2H_2O + 4e^- \qquad \ldots\ldots\ldots\ldots(5.10)$$
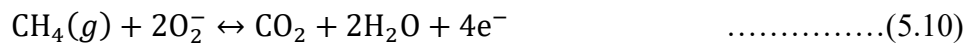
The sensor response expressed in % is defined as the ratio of change in resistance upon exposure to gas to the initial resistance; $(\Delta R/R_0)\times100$, where $\Delta R = (R_0 - R_g)$, R_g is the

resistance upon exposure to gas and R_0 is the initial resistance. The response and recovery times are calculated as the time used for changing the resistance from 10% to 90% of ΔR.

It is noteworthy that the response increases with an increase in temperature in the semiconducting phase up to 60 ^{o}C but decreases above the transition temperature (Fig. 5.13c), which can be attributed owing to the formation of the metallic state in the sample above the transition temperature. As the number of carriers increases in the metallic state, the relative change of resistance upon exposer to CH_4 decreases resulting in a drop in sensor response above the transition temperature. A maximum response value of 2.23% is obtained for 500 ppm of CH_4 at an operating temperature of 60 ^{o}C. The average response time and recovery time for 500 ppm gas at 60 °C are 55 s and 68 s, respectively. Pristine VO_2 is thus shown as a promising candidate for gas sensing applications in the semiconducting state near room temperature [27].

5.4.2 Oxidization of VO_2 to Wadsley V_nO_{2n+1} phases at higher temperatures

With an increase in temperature above 200 ^{o}C, an increase in resistance around three orders (Fig. 5.14a) is observed in contradiction with the metallic behavior of VO_2. As the resistance value of metallic VO_2 above transition temperature is in the orders of few Ohms; the sudden increase in resistance indicates the oxidation of VO_2 to other VO_x phases. To confirm the phase of the VO_x sample, we have collected the Raman spectra of the sample (Fig. 5.14b). The Raman peaks at 94, 137, 188, 275, 404, 475, 520, 685, and 990 cm^{-1}, confirm the presence of pure V_6O_{13} phase [95,96]. V_6O_{13} is known as a mixed-valence oxide as it exists between the V^{4+} and V^{5+} oxidation states and reported to be stabilized with oxidation of VO_2 at ~250 ^{o}C [97]. With further increase in temperature to 300 ^{o}C, the resistance of the sample

increases two orders unlike the semiconducting nature (Fig. 5.14a). The Raman spectrum of the sample at 300 °C (Fig.5.14b) resembles that of the V_4O_9 phase [95].
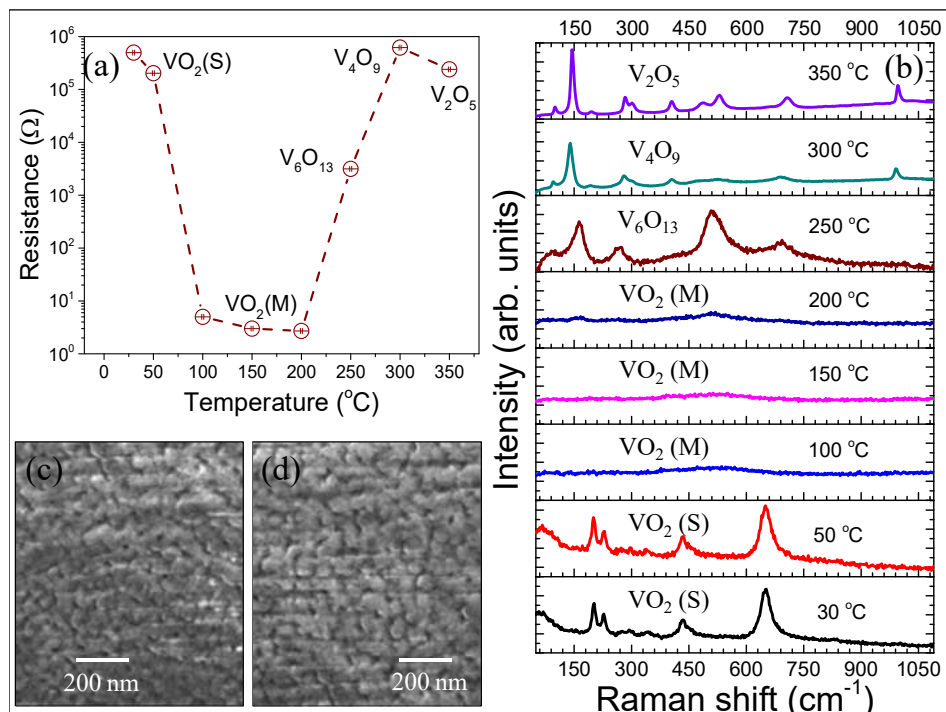
Figure 5.14 (a) The change in resistance with temperature (b) Raman spectra of the V_nO_{2n+1} sample with temperature ranging from 30 to 350 °C, and FESEM images of the sample (c) before and (d) after heating indicating the similar structure of nanoparticles with size ~50 nm.

The Raman spectrum for sample at 350 °C showing modes around 105 (A_g), 146 (B_{1g} or B_{2g}; B_{1g}/B_{2g}), 198 (A_g/B_{2g}), 286 (B_{1g}/B_{3g}), 305 (A_g), 405 (B_{1g}/B_{3g}), 485 (A_g), 529 (A_g), 703 (B_{1g}/B_{3g}) and 1006 (A_g) cm^{-1} confirms the presence of phase pure V_2O_5 (Fig. 5.14b) [98]. No further oxidation is observed with increasing temperature as the sample reaches its maximum oxidation state. All the V_nO_{2n+1} phases (n = 2, 4 and 6) are found to be stable after bringing back to room temperature, and we have studied the CH_4 sensing response in the range from 50 to 500 ppm at operating temperatures of 40, 50, 100, and 150 °C for each of the stable phases. The FESEM images collected before (Fig. 5.14c) and after (Fig. 5.14d) heating,

indicate the similar structure of nanoparticles with size ~50 nm, which confirms that there is no role of morphology in the variation of sensing response with heating.

5.4.3 Methane sensing by phase-pure Wadsley V_nO_{2n+1} nanoparticles

V_6O_{13} is known as a mixed-valence oxide as it exists between the V^{4+} and V^{5+} oxidation states with 2:1 ratio [99]. It undergoes an MIT at 150K and is reported to be quasi-metallic in nature at room temperature [99,100]. V_4O_9 is known as the missing link of the Wadsley phases having a similar structure of that for V_2O_5, but with the formal valence of $V^{4+}/V^{5+}=1$ [101]. The last member of the Wadsley family is V_2O_5 with the maximum oxidation state of +5. It forms a layered structure along the crystallographic c axis with vanadyl oxygen at the top-most plane [98].

The response transients of V_nO_{2n+1} towards CH_4 are studied as a function of temperature (Fig. 5.15) for six different concentrations from 50 to 500 ppm.
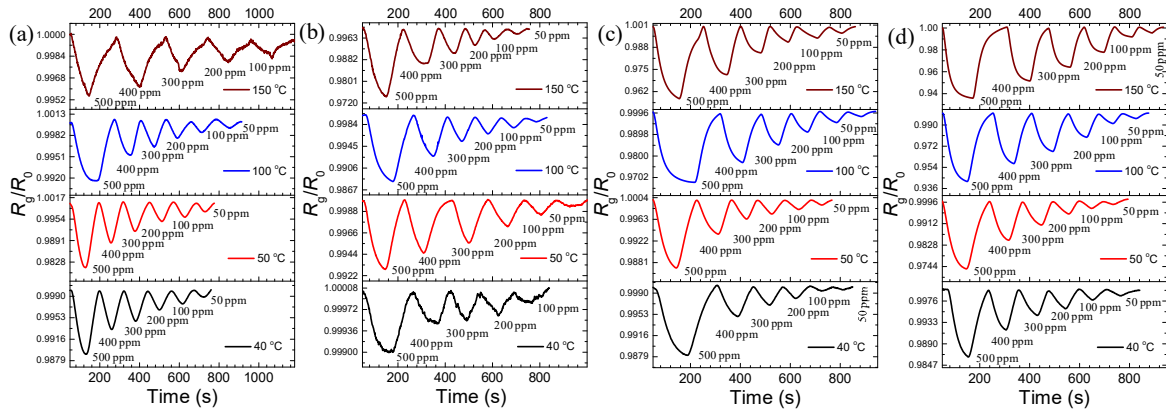
Figure 5.15 Transient response curves of (a) VO_2, (b) V_6O_{13}, (c) V_4O_9, and (d) V_2O_5 towards CH_4 with temperature. Corresponding concentrations of gases are inscribed in the respective regions.

From the slopes of the transient plots, it is observed that the response and recovery times for VO_2 (Fig. 5.15a) are very short for sensing performed at the semiconducting state. The response and recovery times increase as the temperature is raised above the transition

temperature of 340K (~70 $^{\circ}$C). The resistance drop on each exposure is consistent for all V_nO_{2n+1} phases, and the magnitude of change increases with the concentration of the exposed gas (Fig. 5.15).

The sensor response of the Wadsley phases towards CH_4 with different concentrations as a function of temperature is shown in figure 5.16. The response increases with increase in temperature for all the phases except for VO_2 (Fig. 5.16a) as it undergoes an MIT at a comparatively low temperature of 340K.
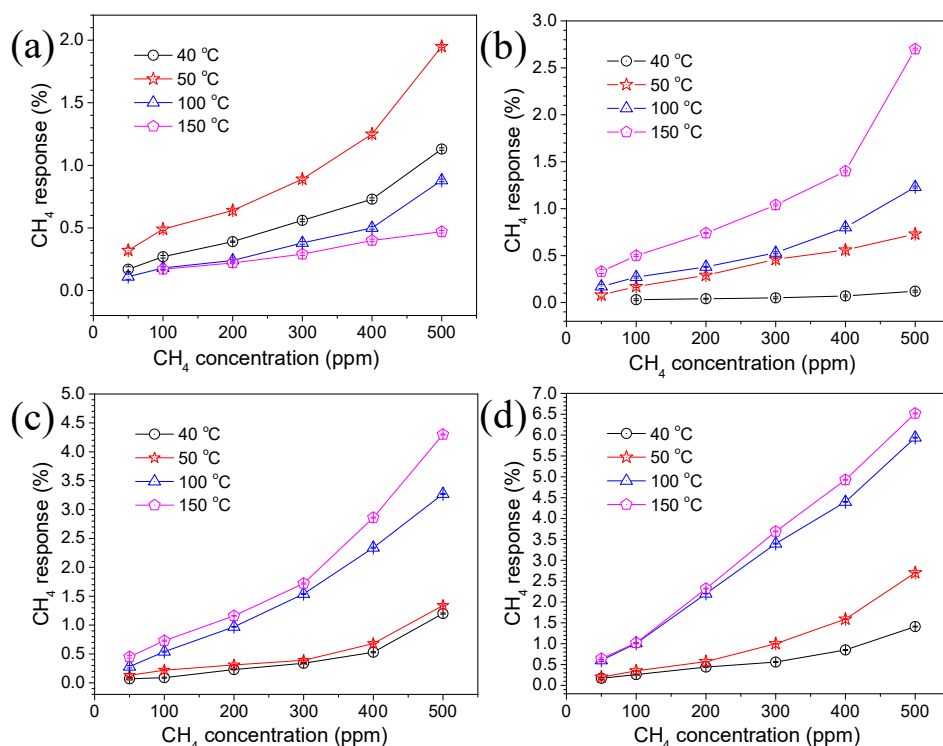
Figure 5.16 Comparison of sensor response of (a) VO_2, (b) V_6O_{13}, (c) V_4O_9 and (d) V_2O_5 towards CH_4 with operating temperatures for 50 to 500 ppm concentration.

The sample in the V_6O_{13} phase started showing a significant response at 40 $^{\circ}$C for 100 ppm concentration (Fig. 5.16b). The maximum response was observed at an operating temperature of 150 $^{\circ}$C for V_6O_{13} with response value of 2.7% for 500 ppm of CH_4. The average response time and recovery time for 500 ppm gas at 150 °C are 90 s and 88 s, respectively. The

comparatively less response of V_6O_{13} may be attributed due to its quasi-metallic nature above the transition temperature of 150K.
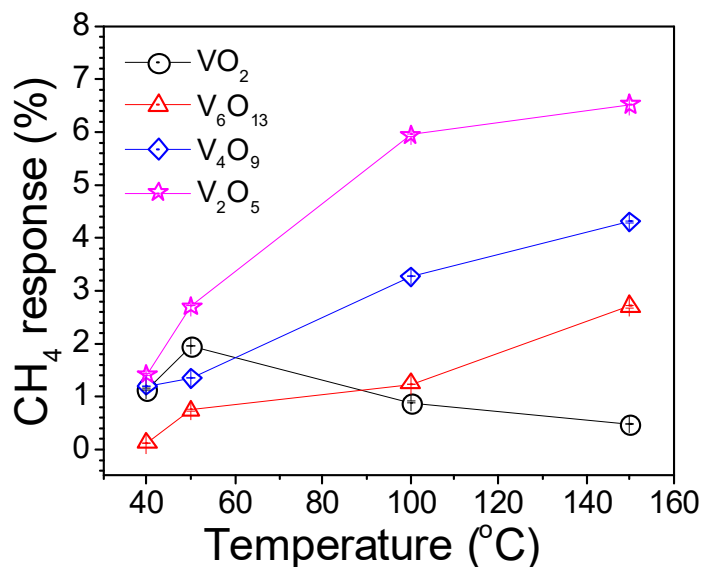
Figure 5.17 Comparison of sensor response of Wadsley phases towards CH_4 with operating temperatures for 500 ppm concentration. Estimated errors are within the size of data.

The response of V_4O_9 and V_2O_5 to CH_4 gas is found to be substantial at 40 °C, even for a very low concentration of 50 ppm (Fig. 5.16c). At 50 °C V_2O_5 shows a response towards CH_4 as 2.7%, which is more than that of VO_2 (1.95%) at that temperature (Fig. 5.16d). Higher responses were observed for V_4O_9 and V_2O_5 as 4.3 and 6.52%, respectively at an operating temperature of 150 °C. The average response and recovery time for 500 ppm gas at 150 °C are 80 s and 95 s for V_4O_9 and 100 s and 120 s for V_2O_5, respectively. V_4O_9 and V_2O_5 consist of shear structure, which opens more active sites that allow target objects to be inserted and extracted reversibly and thereby improving the sensor response. The top-most layer of V_2O_5 is composed of vanadyl oxygen, which forms dangling bonds at higher temperatures by creating oxygen vacancies. The vacancy acts as an active site in sensing, leading to an enhanced response at a higher temperature. The sensor response for VO_2, V_6O_{13}, V_4O_9 and

V_2O_5 phases with operating temperatures upon exposure to 500 ppm CH_4 is shown in figure 5.17. Among all the observed V_nO_{2n+1} phases, V_2O_5 is found out as the most suitable CH_4 sensing material at all operating temperatures (Fig. 5.17) not only for its layered structure but also for the non-availability of further oxidation state of V at a higher temperature. However, CH_4 sensing response in VO_2 is most suitable next to V_2O_5 at 50 ^oC (Fig. 5.17) for all measured concentrations (Fig. 5.16).

5.5 Summary:

Three of the various applications of VO_2 are studied in the light of its structural and metal-to-insulator phase transition.

The potential ability of different structural phases and corresponding oxidation states of VO_2 nanoporous structure for supercapacitor (SC) applications are studied. As VO_2 undergoes several structural phase transitions as a function of temperature, external electric field, hydrostatic pressure, intense illumination, and strain, our study provides insight on how different phases and metastable phases of VO_2 contribute and behave electrochemically. Monoclinic VO_2 sample with all V in oxidation state +4 shows better SC performance with the capacitance of 33 mF/cm^2, Coulombic efficiency of 98.2% and 93.7% capacitance retention after 5000 cycles, as compared to those for VO_2 samples with triclinic and mixed phases. A comparable high energy density is recorded for the sample with all V^{4+} in the Ragone plot. The power densities of the samples also show their mutual dependence indicating comparable values with the performance of other supercapacitors. The space charge region, formed at the interface of VO_2 and carbon paper, is found to contribute to the observed superior capacitance value for the pure M1 phase of VO_2 and ensures the potential of monoclinic-VO_2 nanostructure as a promising and next-generation SC.

The observed color change of the VO_2 microcrystals from white (R+G+B) to cyan (B+G) is explained by the absorption of red light (R) above the transition temperature and is analyzed with electronic band structure of VO_2 for both the semiconducting low and metallic high-temperature phases. These thermochromic properties make VO_2 applicable as advanced smart windows for overall heat management of a closure.

The comparison of CH_4 sensing response around the transition temperature of VO_2 reveals a higher response for the semiconducting state than that of a metallic one. The possibility of oxidation at a higher temperature and sensing behavior of the higher-order oxides of V than VO_2 were investigated systematically. The controlled in-situ oxidation of VO_2 to other Wadsley V_nO_{2n+1} phases, e.g., V_6O_{13}, V_4O_9 and V_2O_5, and their CH_4 sensing behavior show that V_2O_5 provides maximum response for CH_4 due to its sheer structure and thermal stability, whereas the fastest response and recovery is observed for VO_2 near room temperature (40 ^{o}C). VO_2 is also found most suitable CH_4 sensor after V_2O_5 close to room temperature (50 ^{o}C) for all measured concentrations.

5.6 Reference:

1.	Rao, C. N. R. Transition Metal Oxides. *Annu. Rev. Phys. Chem.* **1989,** *40*, 291-326.

2.	Poizot, P.; Laruelle, S.; Grugeon, S.; Dupont, L.; Tarascon, J-M. Nano-Sized Transition Metal Oxides as Negative-Electrode Materials for Lithium-Ion Batteries. *Nature* **2000,** *407*, 496.

3.	Liu, K.; Lee, S.; Yang, S.; Delaire, O.; Wu, J. Recent Progresses on Physics and Applications of Vanadium Dioxide. *Mater. Today* **2018**, *21*, 875-896.

4.	Bahlawane, N.; Lenoble, D. Vanadium Oxide Compounds: Structure, Properties, and Growth from the Gas Phase. *Chem. Vap. Depos.* **2014**, *20*, 299-311.

5.	Kachi, S.; Kosuge, K.; Okinaka, H. Metal-Insulator Transition in V_nO_{2n-1}. *J. Solid State Chem.* **1973**, *6*, 258-270.

6.	Morin, F. J. Oxides Which Show a Metal-to-Insulator Transition at the Neel Temperature. *Phys. Rev. Lett.* **1959**, *3*, 34.

7.	Haverkort, M. W.; Hu, Z.; Tanaka, A.; Reichelt, W.; Streltsov, S. V.; Korotin, M. A.; Anisimov, V. I.; Hsieh, H. H.; Lin, H. -J.; Chen, C. T.; Khomskii, D. I.; Tjeng, L. H. Orbital-Assisted Metal-Insulator Transition in VO_2. *Phys. Rev. Lett.* **2005**, *95*, 196404.

8.	Kim, H. -T.; Lee, Y. W.; Kim, B. -J.; Chae, B. -G.; Yun, S. J.; Kang, K. -Y.; Han, K. -J.; Yee K. -J.; Lim, Y. -S. Monoclinic and Correlated Metal Phase in VO_2 as Evidence of the Mott Transition: Coherent Phonon Analysis. *Phys. Rev. Lett*. **2006**, *97*, 266401.

9.	Kim, D. H.; Kwok, H. S. Pulsed Laser Deposition of VO_2 Thin Films, *Appl. Phys. Lett*., **1994**, *65*, 3188.

10. Marini, C.; Arcangeletti, E.; Castro, D. D.; Baldassare, L.; Perucchi, A.; Lupi, S.; Malavasi, L.; Boeri, L.; Pomjakushina, E.; Conder K.; Postorino, P. Optical Properties of $V_{1-x}Cr_xO_2$ Compounds under High Pressure. *Phys. Rev. B* **2008**, *77*, 235111.

11. Cavalleri, A.; Dekorsy, T.; Chong, H. H. W.; Kieffer, J. C.; Schoenlein, R. W. Evidence for a Structurally-Driven Insulator-to-Metal Transition in VO_2: A View from the Ultrafast Timescale. *Phys. Rev. B* **2004**, *70*, 161102.

12. Kikuzuki, T.; Lippmaa, M. Characterizing a Strain-Driven Phase Transition in VO_2. *Appl. Phys. Lett*. **2010**, *96*, 132107.

13. Mlyuka, N.; Niklasson, G.;. Granqvist, C. –G. Mg Doping of Thermochromic VO_2 Films Enhances the Optical Transmittance and Decreases the Metal-Insulator Transition Temperature, *Appl. Phys. lett.* **2009**, *95*, 171909.

14. Rajeswaran, B.; Umarji, A. M. Effect of W Addition on the Electrical Switching of VO_2 Thin Films, *AIP Adv* **2016**, *6*, 035215.

15. Roach, W. R. Holographic Storage in VO_2, *Appl. Phys. Lett.* **1971** *19*, 453.

16. Lu, S.; Hou, L.; Gan, F. Preparation and Optical Properties of Phase-Change VO_2 Thin Films, *J. Mater. Sci*. **1993**, *28*, 2169.

17. Zhou, J.; Gao, Y.; Liu, X.; Chen, Z.; Dai, L.; Cao, C.; Luo, H.; Kanahira, M.; Sun, C.; Yan, L. Mg-doped VO_2 Nanoparticles: Hydrothermal Synthesis, Enhanced Visible Transmittance and Decreased Metal-Insulator Transition Temperature, *Phys. Chem. Chem. Phys.* **2013**, *15*, 7505.

18. Basu, R.; Magudapathy, P.; Sardar, M.; Pandian, R.; Dhara, S. VO_2 Microcrystals as an Advanced Smart Window Material at Semiconductor to Metal Transition, *J. Phys. D: Appl. Phys*. **2017**, *50*, 465602.

19. Mjejri, I.; Rougier, A.; Gaudon, M. Low-Cost and Facile Synthesis of the Vanadium Oxides V_2O_3, VO_2, and V_2O_5 and Their Magnetic, Thermochromic and Electrochromic Properties, *Inorg. Chem.* **2017**, *56*, 1734-1741.

20. Basu, R.; Ghosh, S.; Bera, S.; Das, A.; Dhara, S. Phase-Pure VO_2 Nanoporous Structure for Binder-Free Supercapacitor Performances, *Sci. Rep*. **2019**, *9*, 46.

21. Jampani, P. H.; Velikokhatnyi, O.; Kadakia, K.; Hong, D. H.; Damle, S. S.; Poston, J. A.; Manivannan, A.; Kumta, P. N. High Energy Density Titanium Doped-Vanadium Oxide-Vertically Aligned CNT Composite Electrodes for Supercapacitor Applications, *J. Mater. Chem. A* **2015**, *3*, 8413-8432.

22. Ren, G.; Hoque, M. N. F.; Pan, X.; Warzywoda, J.; Fan, Z. Vertically Aligned VO_2(B) Nanobelt Forest and Its Three-Dimensional Structure on Oriented Graphene for Energy Storage, *J. Mater. Chem. A* **2015**, *3*, 10787-10794.

23. Mai, L.; Xu, L.; Han, C.; Xu, X.; Luo, Y.; Zhao, S.; Zhao, Y. Electrospun Ultralong Hierarchical Vanadium Oxide Nanowires With High Performance for Lithium Ion Batteries, *Nano Lett*. **2010**, *10*, 4750-4755.

24. Gou, J.; Wang, J.; Zheng, X.; Gu, D.; Yu, H.; Jiang, Y. Detection of Terahertz Radiation From 2.52 Thz CO_2 Laser Using a 320 × 240 Vanadium Oxide Microbolometer Focal Plane Array, *RSC Adv*. **2015**, *5*, 84252-84256.

25. Wang, Y. T.; Whang, W. T.; Chen, C. H. Hollow V_2O_5 Nanoassemblies for High-Performance Room-Temperature Hydrogen Sensors, *ACS Appl. Mater. Interfaces* **2015**, *7*, 8480-8487.

26. Mounasamy, V.; Mani, G. K.; Ponnusamy, D.; Tsuchiya, K.; Prasad, A. K.; Madanagurusamy, S. Template-Free Synthesis of Vanadium Sesquioxide (V_2O_3) Nanosheets and Their Room-Temperature Sensing Performance, *J. Mater. Chem. A* **2018**, *6*, 6402-6413.

27. Prasad, A. K.; Amirthapandian, S.; Dhara, S.; Dash, S.; Murali, N.; Tyagi, A. K. Novel Single Phase Vanadium Dioxide Nanostructured Films for Methane Sensing Near Room Temperature, *Sens. Act. B* **2014**, *191* 252-256.

28. Dubal, D. P.; Wu Y. P.; Holze, R. Supercapacitors: From the Leyden Jar to Electric Busses. *ChemTexts* **2016**, *2*,1-19.

29. Tiwari, J. N.; Tiwari, R. N.; Kim, K. S. Zero-Dimensional, One-Dimensional, Two-Dimensional and Three-Dimensional Nanostructured Materials for Advanced Electrochemical Energy Device. *Prog. Mater Sci.* **2012**, *57*, 724-803.

30. Conway, B.E. Electrochemical Supercapacitors: Scientific Fundamentals and Technological Applications. **1999**, *Kluwer Academic/Plenum Publishers*.

31. Inagaki, M.; Konno H.; Tanaike, O. Carbon Materials for Electrochemical Capacitors. *J. Power Sources* **2010**, *195*, 7880-7903.

32. Lokhande, C.; Dubal D.; Joo, O. -S. Metal Oxide Thin Film Based Supercapacitors. *Curr. Appl. Phys.* **2011**, *11*, 255-270.

33. Shown, I.; Ganguly, A.; Chen L. C.; Chen, K. H. Conducting Polymer-Based Flexible Supercapacitor. *Energy Sci. Eng.* **2015**, *3*, 2-26.

34. Zhao, T.; Ji, X.; Bi, P.; Jin, W.; Xiong, C.; Dang, A.; Li, H.; Li, T.; Shang, S.; Zhou, Z. In Situ Synthesis of Interlinked Three-Dimensional Graphene Foam/Polyaniline Nanorods Supercapacitor. *Electrochim. Acta* **2017**, *230*, 342-349.

35. Zhou, Z.; Zhang, Q.; Sun, J.; He, B.; Guo, J.; Li, Q.; Li, C.; Xie, L.; Yao, Y. Metal-Organic Framework Derived Spindle-like Carbon Incorporated α-Fe$_2$O$_3$ Grown on Carbon Nanotube Fiber as Anodes for High-Performance Wearable Asymmetric Supercapacitors. *ACS Nano* **2018**, *12*, 9333-9341.

36. Zhang, Q.; Xu, W.; Sun, J.; Pan, Z.; Zhao, J.; Wang, X.; Zhang, J.; Man, P.; Guo, J.; Zhou, Z.; He, B.; Zhang, Z.; Li, Q.; Zhang, Y.; Xu, L.; Yao, Y. Constructing Ultrahigh-Capacity Zinc–Nickel–Cobalt Oxide@Ni(OH)$_2$ Core-Shell Nanowire Arrays for High-Performance Coaxial Fiber-Shaped Asymmetric Supercapacitors. *Nano lett.* **2017**, *17* 7552-7560.

37. Zhang, Q.; Sun, J. ; Pan, Z. ; Zhang, J. ; Zhao, J. ; Wang, X. ; Zhang, C. ; Yao, Y. ; Lu, W. ; Li, Q. ; Zhang, Y. ; Zhang, Z. Stretchable Fiber-Shaped Asymmetric Supercapacitors with Ultrahigh Energy Density. *Nano Energy* **2017**, *39*, 219-228.

38. Yan, Y. ; Li, B. ; Guo, W.; Pang H.; Xue, H. *J.* Vanadium Based Materials as Electrode Materials for High Performance Supercapacitors. *Power Sources* **2016**, *329*, 148-169.

39. Man, P.; Zhang, Q.; Sun, J.; Guo, J.; Wang, X.; Zhou, Z.; He, B.; Li, Q.; Xie, L.; Zhao, J.; Li, C.; Li, Q.; Yao, Y. Hierarchically Structured VO$_2$@Ppy Core-Shell Nanowire Arrays Grown on Carbon Nanotube Fibers as Advanced Cathodes for High-Performance Wearable Asymmetric Supercapacitors, *Carbon* **2018**, *139*, 21-28.

40. Zhang, Q.; Wang, X.; Pan, Z.; Sun, J.; Zhao, J.; Zhang, J.; Zhang, C.; Tang, L.; Luo, J.; Song, B.; Zhang, Z.; Lu, W.; Li, Q.; Zhang, Y.; Yao, Y. Wrapping Aligned Carbon Nanotube Composite Sheets around Vanadium Nitride Nanowire Arrays for Asymmetric Coaxial Fiber-Shaped Supercapacitors with Ultrahigh Energy Density, *Nano lett*. **2017**, *17*, 2719-2726.

41. Ma, X.-J.; Zhang, W.-B.; Kong, L.-B.; Luo Y.-C.; Kang, L. VO_2: From Negative Electrode Material to Symmetric Electrochemical Capacitor. *RSC Adv.* **2015**, *5* ,97239-97247.

42. Hu, C.; Xu, H.; Liu, X.; Zou, F.; Qie, L.; Huang, Y.; Hu, X. VO_2/TiO_2 Nanosponges as Binder-Free Electrodes for High-Performance Supercapacitors. *Sci. Rep.* **2015**, *5*, 16012.

43. Lee, M.; Wee, B.-H.; Hong, J.-D. High Performance Flexible Supercapacitor Electrodes Composed of Ultralarge Graphene Sheets and Vanadium Dioxide. *Adv. Energy Mater.* **2015**, *5*, 1401890.

44. Senthilkumar, S. T.; Selvan, R. K.; Ponpandian, N.; Meloc, J. S.; Leed, Y. S. Improved Performance of Electric Double Layer Capacitor Using Redox Additive (VO^{2+}/VO_2^+) Aqueous Electrolyte. *J. Mater. Chem. A* **2013**, *1*, 7913-7919.

45. Huang, G.; Li, C.; Sun X.; Bai, J. Fabrication of Vanadium Oxide, With Different Valences of Vanadium, -Embedded Carbon Fibers and Their Electrochemical Performance for Supercapacitor. *New J. Chem.* **2017**, *41*, 8977-8984.

46. Tang, K.; Li, Y.; Li, Y.; Cao, H.; Zhang, Z.; Zhang, Y.; Yang, J. Self-Reduced VO/VO_x/Carbon Nanofiber Composite as Binder-Free Electrode for Supercapacitors. *Electrochim. Acta* **2016**, *209*, 709-718.

47. Wang, J.; Zhang, X.; Zhang, Y.; Abas, A.; Zhao, X.; Yang, Z.; Su, Q.; Lan, W.; Xie, E. Lightweight, Interconnected VO_2 Nanoflowers Hydrothermally Grown on 3D Graphene Networks for Wide-Voltage-Window Supercapacitors. *RSC Adv.* **2017**, *7*, 35558-35564.

48. Nie, G.; Lu, X.; Zhu, Y.; Chi, M.; Gao, M.; Chen, S.; Wang, C. Reactive Template Synthesis of Inorganic/Organic VO_2@Polyaniline Coaxial Nanobelts for High-Performance Supercapacitors. *ChemElectroChem* **2017**, *4*, 1095-1100.

49. Shao, J.; Li, X.; Qu, Q.; Zheng, H. One-step Hydrothermal Synthesis of Hexangular Starfruit-Like Vanadium Oxide for High Power Aqueous Supercapacitors. *J. Power Sources* **2012**, *219*, 253-257.

50. Hu, L.; Yu, L.; Zhao, C.; Long, X.; Chen, W. Synthesis and Characterization of VO_2/Mesoporous Carbon Composites for Hybrid Capacitors. *J. Wuhan Univ. Technol.-Mat. Sci. Edit.* **2010**, *25*, 574-578.

51. Li, M.; Sun, G.; Yin, P.; Ruan C.; Ai, K. Controlling The formation of Rodlike V_2O_5 Nanocrystals on Reduced Graphene Oxide for High-Performance Supercapacitors. *ACS Appl. Mater. Interfaces* **2013**, *5*, 11462-11470.

52. Zhu, J.; Cao, L.; Wu, Y.; Gong; Y., Liu; Z., Hoster; H. E.; Zhang, Y.; Zhang, S.; Yang, S.; Yan, Q.; Ajayan P. M.; Vajtai, R. Building 3D Structures of Vanadium Pentoxide Nanosheets and Application as Electrodes in Supercapacitors, *NanoLett.* **2013**, *13*, 5408-5413.

53. Lampe-onnerud, C.; Thomas, J. O.; Hardgrave, M.; Yde-Andersen, S. The Performance of Single-Phase in The Lithium/Polymer Electrolyte Battery. *J. Electrochem. Soc.* **1995**, *142*, 3648-3651.

54. Zhang, D. L.; Zhang, Y. J. Chemical Reactions Between Vanadium Oxides and Carbon During High Energy Ball Milling. *J. Mater. Sci*. **1998**, *17*, 1113-1115.

55. Goodenough, J.; Hong, H. Y. Structures and a Two-Band Model for the System $V_{1-x}Cr_xO_2$. *Phys. Rev. B* **1973**, *8*, 1323.

56. Marezio, M.; McWhan, D. B.; Remeika, J. P; Dernier, P. D. Structural Aspects of the Metal-Insulator Transitions in Cr-Doped VO_2. *Phys. Rev. B* **1972**, *5*, 2541.

57. Basu, R.; Sardar, M.; Bera, S.; Magudapathy, P.; Dhara, S. Role of 1-D Finite Size Heisenberg Chain in Increasing Metal to Insulator Transition Temperature in Hole Rich VO_2. *Nanoscale* **2017**, *9*, 6537-6544.

58. Srivastava R.; Chase, L. Raman Spectrum of Semiconducting and Metallic VO_2, Phys. Rev. Lett. **1971**, *27*, 727.

59. Schilbe, P. Raman Scattering in VO_2, *Phys. B : Condensed Matter*, **2002**, *316*, 600-602.

60. Basu, R.; Patsha, A.; Chandra, S.; Amirthapandian, S.; Raghavendra, K. G.; Dasgupta, A.; Dhara S. Polarized Tip-Enhanced Raman Spectroscopy in Understanding Metal to Insulator and Structural Phase Transition in VO_2, *J. Phys. Chem. C* **2019**, *123*, 11189.

61. Park, J. H.; Coy, J. M.; Kasirga, T. S.; Huang, C.; Fei, Z.; Hunter S.; Cobden, D. H. Measurement of a Solid-State Triple Point at the Metal–Insulator Transition in VO_2. *Nature*, **2013**, *500*, 431-434.

62. Ji, S.; Zhang F.; Jin, P. Phase Transition of Single Crystal $VO_2(R)$ Nanorods in Solution Revealed by Reversible Change in Surface Charge State and Structure. *Mater. Lett.* **2011**, *65*, 708-711.

63. Sohn, A.; Kim, H.; Kim, D.-W.; Ko, C.; Ramanathan, S.; Park, J.; Seo, G.; Kim, B.-J.; Shin J.-H.; Kim, H.-T. Evolution of Local Work Function in Epitaxial VO_2 Thin Films Spanning the Metal-Insulator Transition. *Appl. Phys. Lett.* **2012**, *101*, 191605-3.

64. Al-Asadi, A. S.; Henley, L. A.; Wasala, M.; Muchharla, B.; Perea-Lopez, N.; Carozo, V.; Lin, Z.; Terrones, M.; Mondal K.; Kordas, K. Aligned Carbon Nanotube/Zinc Oxide Nanowire Hybrids as High Performance Electrodes for Supercapacitor Applications. *J. Appl. Phys.* **2017**, *121*, 124303.

65. Zheng, L.; Dong, Y.; Bian, H.; Lee, C.; Lu, J.; Li, Y. Y. Self-Ordered Nanotubular TiO_2 Multilayers for High-Performance Photocatalysts and Supercapacitors. *Electrochim. Acta* **2016**, *203*, 257-264.

66. Ghosh, S.; Gupta, B.; Ganesan, K.; Das, A.; Kamruddin, M.; Dash S.; Tyagi, A. K. MnO_2-Vertical Graphene Nanosheets Composite Electrodes for Energy Storage Devices. *Mater Today Proc.* **2016**, *3*, 1686-1692.

67. Du, X.; Lin, B.; Li, B.; Feng, T.; Mao S.; Xu, Y. Surface Modification of Al Foils for Aluminum Electrolytic Capacitor. *Adv. Funct. Mater.* **2017**, *27*, 1606042.

68. Zhou, Y.; Hu, X.; Shang, Y.; Hua, C.; Song, P.; Li, X.; Zhang Y.; Cao, A. Highly Flexible All-Solid-State Supercapacitors Based on Carbon Nanotube/Polypyrrole Composite Films and Fibers. *RSC Adv.* **2016**, *6*, 62062-62070.

69. Achour, A.; Lucio-Porto, R.; Chaker, M.; Arman, A.; Ahmadpourian, A.; Soussou, M.; Boujtita, M.; Le Brizoual, L.; Djouadi M.; Brousse, T. Titanium Vanadium Nitride Electrode for Micro-Supercapacitors. *Electrochem. Commun.* **2017**, *77*, 40-43.

70. Liu, P.; Sun, Q.; Zhu, F.; Liu, K.; Jiang, K.; Liu, L.; Li Q.; Fan, S. Measuring the Work Function of Carbon Nanotubes with Thermionic Method. *Nano Lett.* **2008**, *8*, 647-651.

71. Zhang, Y.; Zheng, J.; Hu, T.; Tian F.; Meng, C. Synthesis and Supercapacitor Electrode of $VO_2(B)/C$ Core-Shell Composites with a Pseudocapacitance in Aqueous Solution. *Appl. Surf. Sci.* **2016**, *371*, 189-195.

72. Hanumantha, P. J.; Datta, M. K.; Kadakia, K. S.; Hong, D. H.; Chung, S. J.; Tam, M. C.; Poston, J. A.; Manivannan A.; Kumta, P. N. A Simple Low Temperature Synthesis of Nanostructured Vanadium Nitride for Supercapacitor Applications. *J. Electrochem. Soc.* **2013**, *160*, A2195-A2206.

73. Adhikari, A. D.; Oraon, R.; Tiwari, S.K.; Lee, J. H.; Kim, N. H.; Nayak, G. C. A V_2O_5 Nanorod Decorated Graphene/Polypyrrole Hybrid Electrode: A Potential Candidate for Supercapacitors. *New J. Chem.* **2017**, *41*, 1704-1713.

74. Zhang, X.; Lai, Y.; Ge, M.; Zheng, Y.; Zhang, K.-Q.; Lin, Z. Fibrous and Flexible Supercapacitors Comprising Hierarchical Nanostructures with Carbon Spheres and Graphene Oxide Nanosheets. *J. Mater. Chem. A* **2015**, *3*, 12761-12768.

75. Fu, Y.; Wu, H.; Ye, S.; Cai, X.; Yu, X.; Hou, S.; Kafafy, H.; Zou, D. Integrated Power Fibre for Energy Conversion and Storage. *Energ. Environ. Sci.* **2013**, *6*, 805-812.

76. Meng, Y.; Zhao, Y.; Hu, C.; Cheng, H.; Hu, Y.; Zhang, Z.; Shi, G.; Qu, L. All-Graphene Core-Sheath Microfibers for All-Solid-State, Stretchable Fibriform Supercapacitors and Wearable Electronic Textiles. *Adv. Mater.* **2013**, *25*, 2326.

77. Chen, T.; Qiu, L.; Yang, Z.; Cai, Z.; Ren, J.; Li, H.; Lin, H.; Sun, X.; Peng, H. An Integrated 'Energy Wire' for Both Photoelectric Conversion and Energy Storage. *Angew. Chem. Int. Ed.* **2012**, *51*, 11977-11980.

78. Bae, J.; Song, M. K.; Park, Y. J.; Kim, J. M.; Liu, M.; Wang, Z. L. Fiber Supercapacitors Made of Nanowire-Fiber Hybrid Structures for Wearable/Flexible Energy Storage. *Angew. Chem. Int. Ed.,* **2011**, *50*, 1683.

79. Brisdon, A. K. Inorganic Spectroscopic Methods. **1998**, *Oxford: Oxford UP*.

80. Housecroft, C. E.; Sharpe, A. G. Inorganic Chemistry. **2005**. Harlow, England: Pearson Prentice Hall.

81. Peterseim, T.; Dressel, M.; Dietrich, M.; Polity, A. Optical Properties of VO_2 Films at the Phase Transition: Influence of Substrate and Electronic Correlations, *J. Appl. Phys.* **2016**, *120*, 075102.

82. Anderson, P. W. New Approach to the Theory of Superexchange Interactions, *Phys. Rev.* **1959**, *115*, 1.

83. Biermann, S.; Poteryaev, A.; Lichtenstein, A. I.; Georges, A. Dynamical Singlets and Correlation-Assisted Peierls Transition in VO_2, *Phys. Rev. Lett.* **2005**, *94*, 026404.

84. Goodenough, J. B. The Two Components of the Crystallographic Transition in VO_2, *J. Solid State Chem.* **1971**, *3*, 490.

85. Verleur, H. W.; Jr. Barker, A. S.; Berglund, C. N. Optical Properties of VO_2 between 0.25 and 5 eV, *Phys. Rev.* **1968**, *172*, 788.

86. Nazari, M.; Zhao, Y.; Kuryatkov, V. V.; Fan, Z. Y.; Bernussi, A. A.; Holtz, M.; Temperature Dependence of the Optical Properties of VO_2 Deposited on Sapphire with Different Orientations, *Phys. Rev. B* **2013**, *87*, 035142.

87. Wetchakun, K.; Samerjaia, T.; Tamaekonga, N.; Liewhiran, C.; Siriwong, C.; Kruefu, V.; Wisitsoraat, A.; Tuantranont, A.; Phanichphant, S. Semiconducting Metal Oxides as Sensors for Environmentally Hazardous Gases, *Sens. Actuators, B* **2011**, *160* 580-591.

88. Das, A.; Bonu, V.; Prasad, A. K.; Panda, D.; Dhara, S.; Tyagi, A. K. The Role of SnO_2 Quantum Dots in Improved CH_4 Sensing at Low Temperature, *J. Mater. Chem. C* **2014**, *2* 164-171.

89. Quaranta, F.; Rella, R.; Siciliano, P.; Capone, S.; Epifani M.; Vasanelli, L.; Licciulli, A.; Zocco, A.; A Novel Gas Sensor Based on SnO_2/O_s Thin Film for the Detection of Methane at Low Temperature, *Sens. Actuators, B* **1999**, *58*, 350.

90. Haridas, D.; Gupta, V. Enhanced Response Characteristics of SnO_2 Thin Film Based Sensors Loaded with Pd Clusters for Methane Detection, *Sens. Actuators, B* **2012**, *166/167*, 156-164.

91. Basu, P. K.; Bhattacharyya, P.; Saha, N.; Saha, H.; Basu, S. The Superior Performance of the Electrochemically Grown Zno Thin Films as Methane Sensor, *Sens. Actuators, B* **2008**, *133*, 357-363.

92. Kang, Y. B. Critical Evaluation and Thermodynamic Optimization of the $VO-VO_{2.5}$ System, J. Eur. Ceram. Soc. **2012**, *32*, 3187-3198

93. Prasad, A. K.; Dhonge, B. P.; Mathews, T.; Dash, S.; Tyagi, A. K.; Shwathy, R.; Murali, N. International Conference on Nanoscience, Engineering and Technology (ICONSET), **2011** IEEE Xplore, Chennai, 73-77.

94. Schilling, O.; Colbow, K. A Mechanism for Sensing Reducing Gases with Vanadium Pentoxide Films. *Sens. Actuators*, B **1994**, *21*, 151-157.

95.   Shibuya, K.; Sawa, A. Optimization of Conditions for Growth of Vanadium Dioxide Thin Films on Silicon by Pulsed-Laser Deposition, *AIP Adv.* **2015**, *5*, 107118-10.

96.   Li, H.; Wang, T.; Wang, Y.; Wang, S.; Su, P.; Yang, Y. Intrinsic Triple-Enzyme Mimetic Activity of V_6O_{13} Nanotextiles: Mechanism Investigation and Colorimetric and Fluorescent Detections, *Ind. Eng. Chem. Res*. **2018**, *57*, 2416-2425

97.   Akande, A. A.; Linganiso, E. C.; Dhonge, B. P.; Rammutla, K. E.; Machatine, A.; Prinsloo, L.; Kunert, H.; Mwakikunga, B. W. Phase Evolution of Vanadium Oxides Obtained through Temperature Programmed Calcinations of Ammonium Vanadate in Hydrogen Atmosphere and Their Humidity Sensing Properties, *Mater. Chem. Phys*. **2015**, *151*, 206-214.

98.   Basu, R.; Prasad, A. K.; Dhara, S.; Das, A. Role of Vanadyl Oxygen in Understanding Metallic Behavior of V_2O_5 (001) Nanostructure *J. Phys. Chem. C* **2016**, *120*, 26539.

99.   Toriyama, T.; Nakayama, T.; Konishi, T.; Ohta, Y. Charge and Orbital Orderings Associated with Metal-Insulator Transition in V_6O_{13}. *Phys. Rev. B* **2014**, *90*, 085131.

100.   Kawashima, K.; Ueda, Y.; Kosuge, K.; Kachi, S. Crystal Growth and Some Electric Properties of V_6O_{13}. *J. Cryst. Growth* **1974**, *26*, 321-322.

101.   Yamazaki, S.; Li, C.; Ohoyama, K.; Nishi, M.; Ichihara, M.; Ueda, H.; Ueda, Y., Synthesis, Structure and Magnetic Properties of V_4O_9-A Missing Link in Binary Vanadium Oxides. *J. Solid State Chem.* **2010**, *183*, 1496-1503.

CHAPTER 6

SUMMARY AND FUTURE SCOPE

"Why should we look to the past in order to prepare for the future?
-     *Because there is nowhere else to look."*

— James Burke

The Thesis principally described the metal to insulator (MIT) as well as structural phase transitions (SPT) of the vanadium oxides nano and micro-structures (VO_2 and V_2O_5), the origin of the phase transitions and finally the applications of the materials in the light of phase transformation. In the beginning, after a brief introduction of both the oxides, the conflicts on the phase transition mechanism, change in the structure and properties around the transition are discussed in detail. The role of vanadyl O_I oxide in initiating the MIT of V_2O_5 nanostructures and the post-transition structural relaxation of the sample are deliberated. The stabilization of various phases of VO_2 by doping and transformation between the phases by external stimuli like temperature and pressure are carried out to analyse the SPT in VO_2. The reason for the MIT and SPT in VO_2 and the correlation between them is studied to resolve the long-lasting debate on the origin of phase transition in this material. The applications of VO_2 in the light of phase transition have also been probed.

6.1 Summary of the Thesis:

6.1.1 Chapter 1

➢   Introduction of the transition metal oxides, especially V_2O_5 and VO_2, with the basic structure and properties.

➢   The change in physical properties and structural relaxation of V_2O_5 after a transition is discussed.

➤ The electronic, optical and structural properties of various phases of VO_2 are discussed in detail.

➤ To understand the conflict in the origin behind the phase transformation, brief introductions of the proposed phase transition mechanisms, *e.g.*, Mott and Peierls transitions, are reviewed.

➤ The applications of VO_2 due to the interesting physical and chemical properties are explored in the light of phase transition.

6.1.2 Chapter-2

➤ The metallic behaviour in V_2O_5 above transition temperature was observed from the temperature-dependent current-voltage measurements and is discussed considering the observed emission peaks in the temperature-dependent photoluminescence (PL) spectroscopic studies.

➤ The newly evolved PL emission above the transition temperature was understood in terms of creation of defect states leading to the modification of conduction bands in the V_2O_5 electronic structure.

➤ The reversible temperature-dependent Raman spectra were analyzed for the allowed vibrational modes of semiconducting and metallic V_2O_5 phases to identify the vanadyl oxygen responsible for the transition as well as to understand the relaxed structure after the transition.

➤ The change in electronic band structure after the reduction of V_2O_5, prompting the metallicity in the sample, is discussed using temperature-dependent UV-Visible absorption spectroscopic studies and thermal activation energy calculations.

➢   The breakdown of $pd\pi$ (V-O$_I$) bonds helps in accumulating electrons towards neighboring V atom to occupy the partially filled V $3d$ bands, leading to the increase in the number of carriers in the conduction band, which is finally made responsible for the observed metallic behavior.

6.1.3 Chapter-3

➢   The stabilization of metastable phases of VO$_2$ was made possible in a novel technique by introducing defects in the system, for the first time, via two ways: (i) hole doping by native vacancy creation and (ii) Mg doping with optimal proportion.

➢   Temperature- and pressure-induced phase transitions among the various phases of VO$_2$ was analyzed by synchrotron XRD and Raman spectroscopic measurements.

➢   The structural transitions M2 →T and T→M1 were found to be continuous (second order) phase transition from the continuous change in the volume and a discontinuity in the bulk modulus with hydrostatic pressure.

➢   The temperature-driven M2→R phase transition was found out as first order from the coexistence of both the phases for a narrow span of temperature.

➢   The explicit anharmonicity (phonon-phonon interaction) was found to be dominant over the implicit (volume dependent) one for the M2 to R transition.

➢   A systemic study of the polarized tip-enhanced Raman spectroscopy (TERS) was carried out to explore the crystallographic orientation of VO$_2$ single nanorods as well as to identify the corresponding phonon vibrations.

➢   The assignment of phonon frequencies corresponding to each lattice vibration was made possible by density functional theory calculations of phonon density of states. The

phonon mode responsible for the structural phase transition was also identified using the polarized and high-temperature TERS measurements.

6.1.4 Chapter-4

➢ The effect of defects in changing the transition temperature of VO_2 was demonstrated by invoking dimensional reduction in V chains.

➢ The role of V vacancy in increasing the transition temperature is discussed by introducing finite-size 1-D Heisenberg spin ½ chain model in the hole rich (acceptor doped) system.

➢ The correlation between MIT and SPT was analyzed by the observation of low-frequency spin excitation (spin-wave) in VO_2. As spin-wave propagates independently from the charge-density waves (spin-charge separation according to Tomonaga-Luttinger liquid theory), the SPT and MIT were understood by separate phenomenological model.

➢ The experimentally observed Raman modes at low-frequency were compared with the calculated frequency for the singlet breather mode considering perturbation due to spin-lattice coupling.

➢ The significant deviation of Stokes to anti-Stokes intensity ratio of the low-frequency Raman mode from the usual thermal factor $\exp(hv/K_B T)$ disobeying Boltzmann's distribution law and the orthogonal dependency of the phonon and spinon vibration in the polarized Raman study confirmed it to be originated from spinon vibration.

➢ The role of doping in shifting the frequency of collective spin excitation as well as in increasing the transition temperature while maintaining the same structural phase is discussed in detail introducing finite-size 1-D Heisenberg spin ½ chain model.

➤ The phase transition in VO_2 was understood by the 1st order MIT driven by Mott physics (R to M2) prompting the 2nd order Peierls-type SPT (M2 to T and T to M1).

6.1.5 Chapter-5

➤ The three imperative applications of VO_2 were explored in the light of its phase transition; (i) Binder free supercapacitor, (ii) Advanced smart window, and (iii) Methane sensing near room temperature.

➤ Each structural phase and corresponding oxidation states of VO_2 nanoporous structures grown on carbon fiber was compared based on their supercapacitor performance.

➤ Among other structural phases of VO_2, the M1 phase was found out as the most suitable candidate for the supercapacitor applications with a specific capacitance value of 33 mF/cm^2.

➤ VO_2 was found out as an eligible candidate for overall heat management of a closure by filtering blue light along with the IR reflection above the transition temperature.

➤ The evaluation of sensing response of VO_2 around the transition temperature revealed a higher response for the semiconducting state.

➤ Methane sensing performance of the phase-pure Wadsley V_nO_{2n+1} (between VO_2 and V_2O_5) phases with in-situ oxidation were analysed to find the role of oxidation states and phase-purity of these materials while operating at high temperature.

➤ V_2O_5 with the highest oxidation state of V^{5+} showed superior sensor response towards CH_4 than other Wadsley phases.

➤ CH_4 sensing response in VO_2 is most suitable next to V_2O_5 at 50 ^oC for all measured concentrations.

6.2 Future Scope:

➢   Study of the MIT in the other vanadium oxides such as VO, V_2O_3, V_6O_{13}.

➢   As the origin of MIT in VO_2 is found out as Mott type and SPT can be separated from the MIT, the application of VO_2 as Mott transistor can be probed.

➢   Doping with a metal having valency greater than V^{4+} (Nb, W) reduces the transition temperature in VO_2. Efforts need to be done to initiate the transition at room temperature with minimal energy.

➢   As VO_2 is an *n*-type semiconductor, coupling with *p*-type semiconductor like CuO can be composed to form a *pn*-junction diode, which above the transition temperature can act as a Schottky diode.